Durham E-Theses

Geochemistry and economic significance of the pindos ophiolite mantle sequence.

Mansolas, Ioannis

Geochemistry and Economic Significance of the Pindos Ophiolite Mantle Sequence.

Ioannis Mansolas
December 1991

Department of Geological Sciences

University of Durham
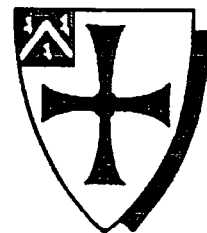
Geochemistry and Economic Significance of the Pindos Ophiolite Mantle Sequence.

A thesis presented for the degree of

Doctor of Philosophy

by

Ioannis Mansolas

B. Sc. Athens University

Department of Geological Sciences

University of Durham

December 1991

Abstract

In the Pindos ophiolite complex of northwestern Greece, mantle sequence peridotites comprise more than 90% of the exposed lithologies. At central Pindos, the complex is divided into two parts, northern and southern. Harzburgites, with little or no free clinopyroxene, are dominant in the latter, while clinopyroxene-bearing harzburgites are present in the former. The Moho is exposed in the southeast part of the southern block where cumulate rocks are in contact with mantle peridotite. The Moho has a transitional character and is characterized by increased abundance of discordant dunites, extensive emplacement of dykes of variable mineralogy, and the pervasive impregnation of the depleted harzburgite by basaltic melt. The cumulate rocks near this transition are dominated by dunite with subordinate troctolite and gabbro and minor wehrlite. There is no evidence of a well-developed magma chamber, with cumulates mostly appearing as sill-like bodies in a series of intrusions. Away from the Moho, cumulate olivine and two-pyroxene gabbros become abundant.

Serpentinization has variably affected the peridotites but has not changed their major-element composition appreciably except for the addition of H_2O. A small depletion in the MgO wt.% content of the rocks is observed with increasing alteration, as well as mobilization of sulphur and re-distribution of sulphides.

The complex has experienced two stages of re-equilibration at low pressures (<10 kb), the first between 850-950°C, recorded by mineral equilibria with high-blocking temperatures, and the second at ~750°C, recorded by olivine-spinel pairs. The harzburgites show slightly elevated oxygen fugacities between QFM and QFM+1.5 (log units).

The chemistry of the Pindos peridotites is quite variable. Comparison with peridotites from various geotectonic settings shows that the northern part of the complex has fairly uniform composition and experienced smaller degrees of partial melting in a mid-ocean ridge environment. The southern part is more depleted and resembles peridotites dredged from present-day intra-oceanic subduction zones. This is also supported by modelling of residues of partial melting of spinel lherzolite using temperature- and pressure-dependent major-element distribution coefficients, showing degrees of melt extraction of the order of ~12-15% and ~20%-40% for the northern and southern part respectively.

The PGE content of the harzburgites is fairly uniform and similar to that of mantle-derived rocks world-wide. The abundance of the PGE is controlled by residual sulphides, while a small depletion in Pd is consistent with the presence of residual alloys. Chromitites have more variable PGE abundances and show both positive and gentle negative patterns. Oxygen fugacity and sulphide saturation are the controlling parameters of the abundances and patterns of the PGE.
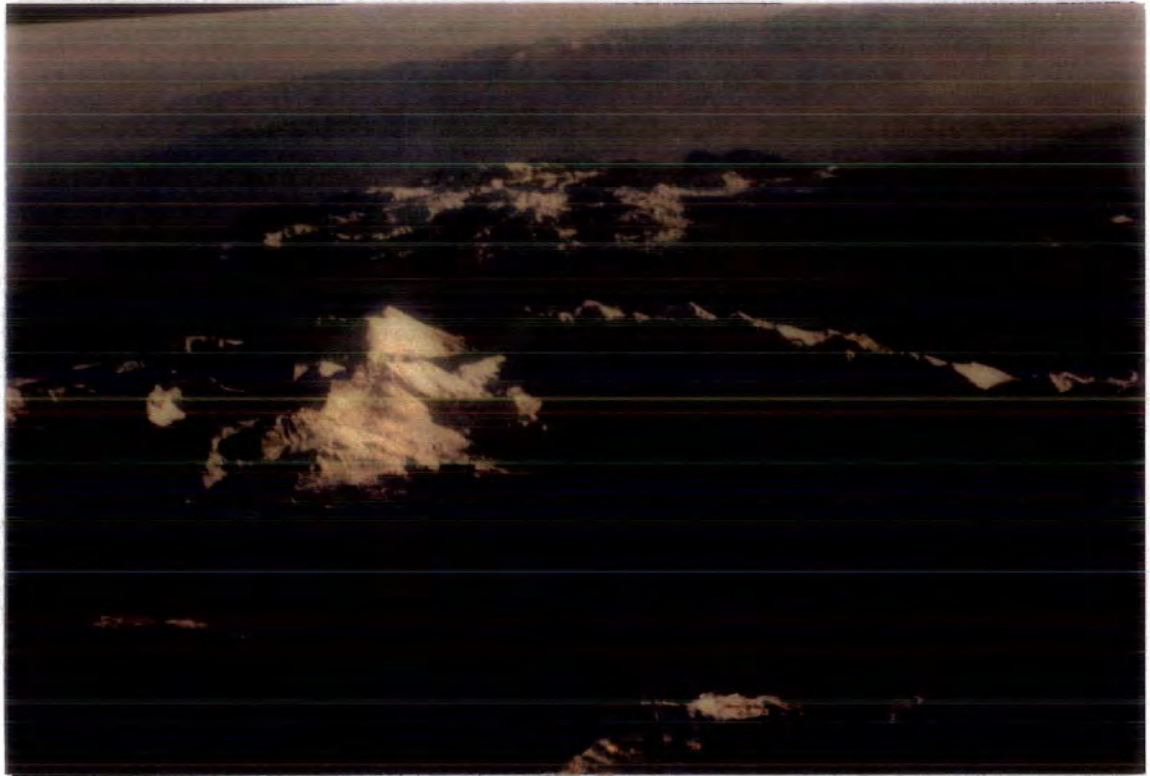
FRONTISPIECE.

The Pindos mountains viewed from the southwest at an altitude of 10,000 feet. The south slopes of Mt. Avgo and the southwest slopes of Mt. Mavrovouni are visible.

Table of contents

List of Tables

List of Plates

List of abbreviations

Fo	Forsterite
En	Enstatite
Di	Diopside
Fs	Ferrosilite
Hd	Hedenbergite
Sp	Spinel
Chr	Chromite
Ol	Olivine
Opx	Orthopyroxene
Cpx	Clinopyroxene

Mg#	Mg/(Mg+Fe*)
Cr#	Cr/(Cr+Al)
$Y^{R^{3+}}_{sp}$	$R^{3+}/\Sigma R^{3+}$, R^{3+}=Cr, Al, Fe^{3+} fraction in spinel
Fe* or Fe_{tot}	Total iron as FeO or Fe_2O_3

PGE	Platinum-group elements
PGM	Platinum-group minerals

T	Temperature
°C	Degrees Celsius
°K	Degrees Kelvin
P	Pressure
GPa	Gigapascal
kb	kilobar
f_{O_2}	Oxygen fugacity
f_{S_2}	Sulphur fugacity

Chapter 1. Field relations

1.1. Introduction

The term "ophiolite" is derived from the Greek words "ophis" (= snake) and "lithos" (= rock) and was used by early workers to describe the shiny green rocks now termed serpentinites (Brogniart, 1813, cited in Nicolas, 1989b). The frequent association of these serpentinites with pillow basalt and radiolarite was noticed in the early 20th century (Steinman, 1927) and the term ophiolite was extended to indicate this particular rock association. The link between ophiolites and the oceanic environment was thus made.

Since the prevalent geological concept at the time was that of the geosyncline, ophiolites were interpreted as part of the eugeosynclinal development (Steinman, op. cit.; Brunn, 1960, 1961; Aubouin, 1965). In the Sixties, however, sea-floor spreading was recognized as an ongoing process of sea-floor generation and refined models of a dynamic regenerative oceanic crust were developed (e.g. Cann 1970, 1974).

Meanwhile work on ophiolites (mainly the Troodos massif) (Gass and Masson Smith, 1963; Gass, 1968; Moores, 1969; Moores and Vine, 1971) led to the realization that they represent fragments of oceanic lithosphere, thus opening a vast array of opportunities to study at close range otherwise inaccessible magmatic processes.

In 1972 the term "ophiolite" was redefined by the participants of the Penrose Conference of the Geological Society of America (Coleman, 1977):

"Ophiolite refers to a distinctive assemblage of mafic to ultramafic rocks. It should not be used as a rock name or as a lithologic unit in mapping. In a completely developed ophiolite the rock types occur in the following sequence, starting from the bottom and working up:

(i) an ultramafic complex, consisting of variable proportions of harzburgite, lherzolite and dunite, usually with a metamorphic tectonic fabric (more or less serpentinized).

(ii) a gabbroic complex, ordinarily with cumulus textures commonly containing peridotites and pyroxenites and usually less deformed than the ultramafic complex.

(iii) a mafic sheeted dyke complex.

(iv) a mafic volcanic complex, commonly pillowed.

Associated rock types include:

(1) an overlying sedimentary section typically including ribbon cherts, thin shale interbeds, and minor limestones;

(2) podiform bodies of chromite generally associated with dunite;

(3) sodic felsic intrusive and extrusive rocks.

Faulted contacts between mappable units are common. Whole sections may be missing. An ophiolite may he incomplete, dismembered, or metamorphosed. Although ophiolite generally is interpreted to be oceanic crust and upper mantle, the use of the terms should be independent of its supposed origin."

Participants of the G. S. A. Penrose Conference.

A new debate about whether ophiolites are truly representative of oceanic crust and mantle was prompted by Miyashiro (1973). Based on geochemical evidence from major and trace elements in basalts, he claimed that the Troodos complex, the show case of ongoing research in ophiolites, was formed in an island arc and not in a mid-ocean ridge environment. This was also confirmed by Pearce and Cann (1973). At the same time the development of discriminant diagrams for lavas based on minor and trace elements (e.g. Pearce and Cann, 1973; Pearce and Norry, 1977) pointed to distinct differences between many ophiolites from mid-ocean ridge basalts and those with affinities with supra-subduction zone (SSZ) magmas. Since then an increasing number of ophiolites has been ascribed (at least partly) an SSZ origin (e.g. Vourinos, Noiret et al., 1981; Oman, Pearce et al., 1984; Josephine, Harper, 1984; Pindos, Kostopoulos, 1988).

1.2. Ophiolitic mantle sequences

The tectonite peridotites form a floor to the crustal magma chamber in which the overlying peridotites and gabbros are formed. The chemical and textural similarities between

the ophiolitic tectonites and the Alpine-type ultramafic bodies was early noted (Thayer, 1960) and are assumed of similar origin. Some investigators suggested a cumulative formation of the peridotites by crystal settling from a basaltic magma during formation of the oceanic crust (e.g. Thayer, 1964, 1967; McTaggart, 1971). This hypothesis, however, was incompatible with some characteristics of the tectonites, namely, the high proportion of peridotite to overlying cumulates and the lack of mineralogical or chemical cryptic variation within the peridotites. In addition, experimental melting studies showed that the co-precipitation of olivine and orthopyroxene, which constitute 85-99% of the peridotites, is prevented at low pressures by the reaction relationship between olivine and orthopyroxene (Kushiro et al., 1968). The suggestions for a cumulative origin have been superseded by chemical, structural, and experimental studies of the peridotites, which prove that they represent residual mantle after almost complete melt extraction after partial fusion of primary mantle (e.g. Hess, 1964; Green and Ringwood, 1967; Menzies and Allen, 1974; Dick, 1977; Nicolas et al., 1980; Jaques and Green, 1981; Falloon and Green, 1987, 1988). In addition, the continuing discovery of serpentinites and gabbros at oceanic fracture zones (e.g. Miyashiro et al., 1969; Aumento and Lubat, 1971; Sinton, 1978; Hamlyn and Bonatti, 1980; Dick, 1989) further strengthens the links to the oceanic environment.

The origin of dunite patches and veins that, almost invariably, are found in association with the tectonite peridotites is somewhat controversial. Some workers (e.g. Moores and Vine, 1971; Cassard et al., 1981; Nicolas et al., 1980; Nicolas and Prinzhofer, 1983) group these dunites with the harzburgites as residues of melting from a pristine mantle, while others propose a magmatic origin as crystal fractionates from ascending liquids during the mantle convective ascent (e.g. O'Hara, 1968; Malpas, 1978; Furnes et al., 1988). The controversy is not yet resolved, but it is unlikely that a universal process can explain the origin of all dunites types (see Nicolas, 1989b, for a review). It will be noted that the proponents of the residual theory rely mostly on structural arguments and that geochemical criteria for a residual origin are not easy to meet, since extreme degrees of melting are required to remove orthopyroxene from the residue (Kostopoulos, 1991).
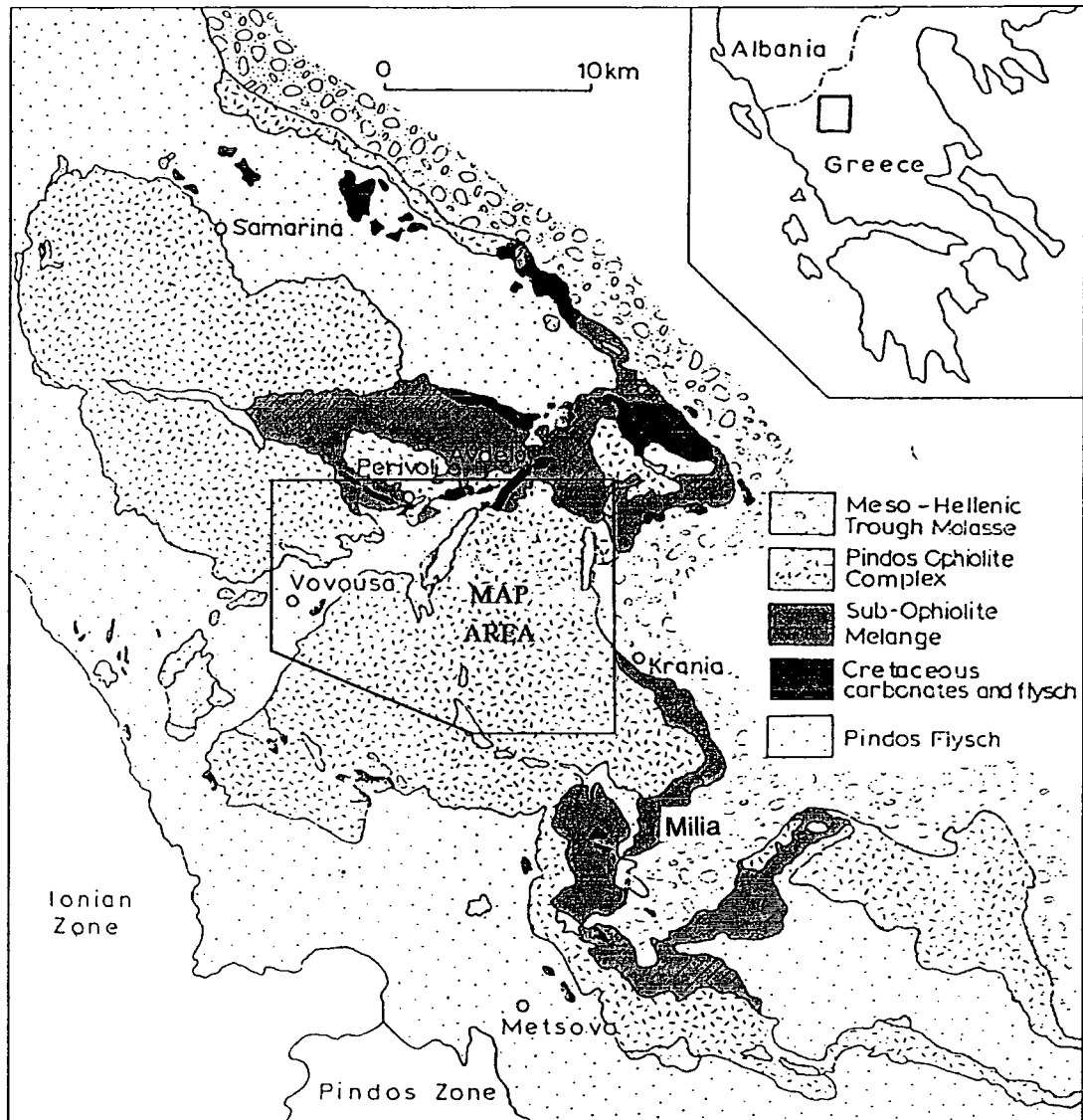
Figure (1.1) General geology of Pindos. The box marked "MAP AREA" delineates the area mapped in Figure 1.2. Inset shows the location of the Pindos complex in Greece. From Rassios (1989).

1.3. Regional setting

The Pindos ophiolite occupies an area of ca. 700 km^2 in NW Greece between the villages of Samarina, Vovousa, Krania and Metsovo (Figure 1.1). It is situated within the Pindos mountain range, which is a part of the Dinaro-Hellenides chain. The ophiolite is part of a NW-SE trending zone that includes the Koziakas and Othris ophiolites to the southeast and Vourinos to the east. The complex rests on the flysch of the Pindos zone to the west and is partially covered by the molassic sediments of the Mesohellenic trough to the east. The ophiolite is separated in two parts by the Aoos valley, trending ENE-WSW, which exposes the

underlying flysch near the village of Vovousa. The study area is confined to the north part of the southern block, between the villages Milia and Perivoli and Mt. Avgo, and to the southernmost part of the northern block, north of the village of Vovousa (Figure 1.1). Field mapping and sample collection were carried out during two field seasons in the summers of 1987 and 1988. The study area was mapped on a scale of 1:20,000. A 1:50,000 version of the map is shown in Figure 1.2, including a part of the Aspropotamos complex that was mapped by Kostopoulos (1988).

1.4. Previous work

The regional geology of Pindos was examined by Brunn (1956), Parrot (1967), Terry (1971, 1972, 1973, 1975), Kemp and McKaig (1984) and Jones (1990). Sideris (1968), Sideris and Baltatzis (1979), Montigny et al (1973), Paraskevopoulos (1975), Terry (1974, 1979), Capedri et al (1978, 1980, 1981, 1982), Bebien et al (1980), Dupuy et al (1984) and Kostopoulos (1988) have examined the petrography and geochemistry of magmatic rocks. Studies on mineralisation (e.g. sulphides, oxides) include those of Melidonis and Dimou (1978), Skounakis et al. (1984), Lorand and Pinet (1984), Kantza (in prep.) and Valsami (1991). In addition there is an ongoing research program on the exploration for chromite deposits by the Institute of Geological and Mineral Research of Greece. As yet no economic-scale chromite deposits are known in Pindos.

1.5. Sedimentary and metamorphic rocks

A variety of sedimentary and metamorphic rocks are exposed around the study area. These lie structurally beneath the ophiolite, with the exception of the molasse. The lithologies and field relations have been described by Kostopoulos (1988) and Jones (1990) and only a brief description will be given here.

1.5.1. Metamorphic rocks

The metamorphic sole of the ophiolite (Loumnitsa unit of Jones, 1990) is found in contact with ultramafic rocks and in detached blocks in the mélange (Jones, 1990). Lithologies include amphibolites, epidote-amphibolites, garnet-mica schists, marble inliers,

calc-phyllites and (sheared) metabasites usually in this order from the peridotite downward (Kostopoulos, 1988). The rocks display an inverted metamorphic grade and are similar in this respect to the metamorphic sole found underneath most ophiolites. The protoliths of the metamorphic rocks are usually basalts, although they have been found to grade downward to sediments in the mélange (Jones, 1990). ^{40}Ar-^{39}Ar radiometric dating of hornblende crystals from amphibolites have given an age of 165.3 Ma (Spray et al., 1984), suggesting that obduction occurred during the uppermost mid-Jurassic. However the ophiolite itself is thrust onto Eocene turbidites implying that emplacement was completed only after 120 Ma from the time of initial detachment (Kostopoulos, 1988).

1.5.2.The tectonic and sedimentary mélange.

This unit outcrops extensively near the Avdela and Perivoli villages. It consists of a mosaic of lithologies of variable age, type and chemistry that have been brought together by tectonic processes. Its field appearance is a chaotic mixture of centimetre to >100-metre sized clasts set in a deformed mudstone-siltstone matrix. Kostopoulos (1988) identified clasts of Triassic carbonates, chert, pillow lavas, ophiolite fragments, and debris flows consisting of ophiolite derived clasts. He further divided the lavas, based on their field appearance and chemistry, into Triassic alkalic within-plate basalts (Avdela Unit), transitional mid-ocean ridge basalts (Aspri Petra Unit) and normal mid-ocean ridge tholeiites of Triassic age (Strangopetra Unit). The mélange was probably formed by accretionary processes over a subducting oceanic plate.

1.5.3.The Dio Dendra group

Jones (1990) described this unit of pelagic and turbiditic sediments and distinguished four formations of Late Jurassic to Late Cretaceous age. These are, in order of decreasing age, the Karamoula, Agios Nicolaos, Krevati, and Zygourogreko formations. The Dio Dendra group occurs as discontinuous but extensive thrust sheets that do not contain complete successions of these formations and it lies structurally between the mélange and the Pindos flysch. In Figure 1.2 it is included in the mélange.

1.5.4. The Pindos flysch

The Pindos ophiolite and attached rocks are thrust on the Late Cretaceous-Eocene flysch of the Pindos zone (Aubouin et al., 1970). The flysch is composed of quartzo-feldspathic, medium- to fine-grained turbidites with common redeposited carbonates (Jones, 1990).

1.5.5. The molasse

The ophiolite is overlain by the Eocene to Miocene molassic sediments of the Meso-Hellenic trough (Brunn, 1956, Soliman and Zygoyiannis, 1979). Where the molasse directly overlies the ophiolite, it consists of a basal conglomerate mainly composed of ophiolitic clasts, which may reach several metres in size near the contact and grades upwards via fine conglomerates and coarse sands to shales and marls. The strata near the contact are tilted to near vertical and thrusts have been developed in the molasse due to backthrusting of the ophiolite.

1.6. Ophiolitic rocks

The Pindos ophiolite is characterized by the overwhelming abundance of mantle over crustal rocks. The mantle sequence consists of tectonized harzburgite with subordinate dunite and a variety of dykes. Crustal rocks are exposed in the southeastern part of the study area in contact with mantle rocks (Figure 1.2). The ophiolite forms a large thrust sheet up to ~700 m thick, structurally overlying all the previously described units except the molasse. Internal thrusting and faulting have displaced, and possibly rotated, large blocks of the ophiolite and their original relation is not easily recognized due to the lithologic monotony of the rocks.

Abelia

Dramala

KALDA

1758 ×

MICRO-LIVADO

57′

39°
59′

Gucamisios

Tripimeni

1285

1924 ×

1967

Pyrostia

1887

Kyra Kali

1433 ×

55′

Krania

1525 ×

Simadro

2190

2013 ×

-angle fault

Livadi

1 2 3 4 km

...vousa, Perivoli, Microlivado, and Krania.

Kontoyianni

PERIVOLI

Kodaro

VOVOUSA

×
1158

×
1187

Avgo

▲
2177

Zioga

×
1911

×
1878

Peridotite

Dunite

Transition zone

Pyroxenite

Cumulates (Dunitic)

Cumulates (Gabbroic)

Wherlite

Lavas and dykes

Metamorphic sole

Chert, limestone   (Mélange)
mudstone, shale

Flysch

Molasse

Cumulate layering

Orthopyroxene folia

Figure (1.2) Geologic map of the Pindos ophiolite between
Kostopoúlos (1988), Rassios (1989); this work.

1.6.1. The mantle sequence

The mantle sequence is composed of harzburgite with variable amounts of subordinate dunite. The harzburgite is composed of olivine and pyroxene in approximately 4:1 ratio and displays a compositional layering defined by orthopyroxene poor and rich layers (Plate 1.2). Minor clinopyroxene (2-4%), as green chrome diopside grains, occurs only in the Vovousa peridotite. Chromite is a constant accessory mineral at 1-2% of the mode.

In the field the harzburgite weathers to an orange-brown colour against which the black chromite grains stand out. The weathering rind usually persists for a couple of centimetres and fresh harzburgite surfaces have a green colour. Orthopyroxene has a larger resistance to weathering than olivine and this gives harzburgites a rough surface that contrasts with the smooth surfaces of adjacent dunites. A foliation is developed by the clustering of orthopyroxene grains in clots 2-5 cm long (Plates 1.2 and 1.3). The deformation of the orthopyroxene is apparent in hand specimen by the bent surfaces of the grains.

Dunite forms between 1 and 10% of the exposure and occurs either as layers, mostly parallel or sub-parallel to the foliation of the enveloping harzburgite (concordant dunite), or as pods, the boundaries of which transect the foliation of the tectonite host. Dunite usually consists of olivine and variable amounts of chrome spinel (2-5%) dispersed throughout the rock. Occasionally chromite grains cluster together to form stringers, 2-5mm thick and a few tens of centimetres long. If the dunite is of the concordant type, so that its thickness and relation to the tectonite foliation can be determined, these stringers are usually found near the centre of the layer and are parallel to the dunite walls and the foliation of the enclosing harzburgite. The amount and type of dunite is not uniform throughout the mantle sequence, as dunite becomes more abundant towards the Moho and discordant dunite becomes the only type present.

Another feature of the harzburgite that signifies approach to the Moho is the occurrence of veins and dykes. These are mostly gabbro pegmatite dykes of variable thickness (5-50 cm) and orientation that are invariably rodingitized. Troctolite and dolerite dykes are less abundant, but pyroxenites dominate in some areas (notably Dramala, Figure

1.2). These occur as 10 cm to 3 m thick dykes or boudins and consist almost solely of large (up to 8 cm) tabular crystals of pyroxenes, with small amounts of chromite and scarce olivine.

The harzburgite has been deformed in the plastic and brittle deformation fields (Rassios, 1989) and there is evidence of isoclinal folding (Plate 1.1). Rassios (pers. comm.) noted that the harzburgite fabric can be classified with respect to the intensity of deformation using a fabric "scale" based on the elongation of the orthopyroxene. The divisions of this scale are as follows:

#0: The peridotite has no discernible foliation (Plate 1.2).

#1: Weak foliation of blocky orthopyroxene.

#2: Strong foliation of almond-shaped to elongated orthopyroxene.

#3: Plastic deformation of orthopyroxenes into augen shapes or elongation up to 5:1 (Plate 1.3)

#4: Orthopyroxene elongated in excess to 5:1. Grades to fine-grained mylonites.

Rassios and Grivas (1988) and Rassios (1989) have mapped the peridotite deformation using this scale in the Dramala area (Figure 1.3). Rassios (1989) found that petrofabric evaluations show correlation between fabric types and deformation mechanism. In brief, weakly foliated fabrics represent high temperature peridotite structures (1200°C, Nicolas, 1989a), while elongated orthopyroxene fabrics tend to signify lower temperature deformation. Rassios (1989) suggested that the former correspond to diapiric and near-ridge fabrics (Nicolas et al., 1980; Ross et al., 1980) while the latter correspond to mylonite development at 800-900°C (Ross and Zimmerman, 1982).

Together with peridotite fabrics Rassios (1989) also mapped the orthopyroxene foliations and lineations, the spinel foliations, and the contacts of dunites with surrounding harzburgite in the Dramala peridotite (Figures 1.4 and 1.5). She found that the orthopyroxene foliations show two maxima, one at ~125°/50°-60°S and one at 040°/50°-60°S. The orthopyroxene lineations are show a uniform orientation at 020°/30°-30°S, probably the result of the intersection of the two orthopyroxene foliations. The orientations of the spinel foliation show essentially the same geometry as orthopyroxene foliations.
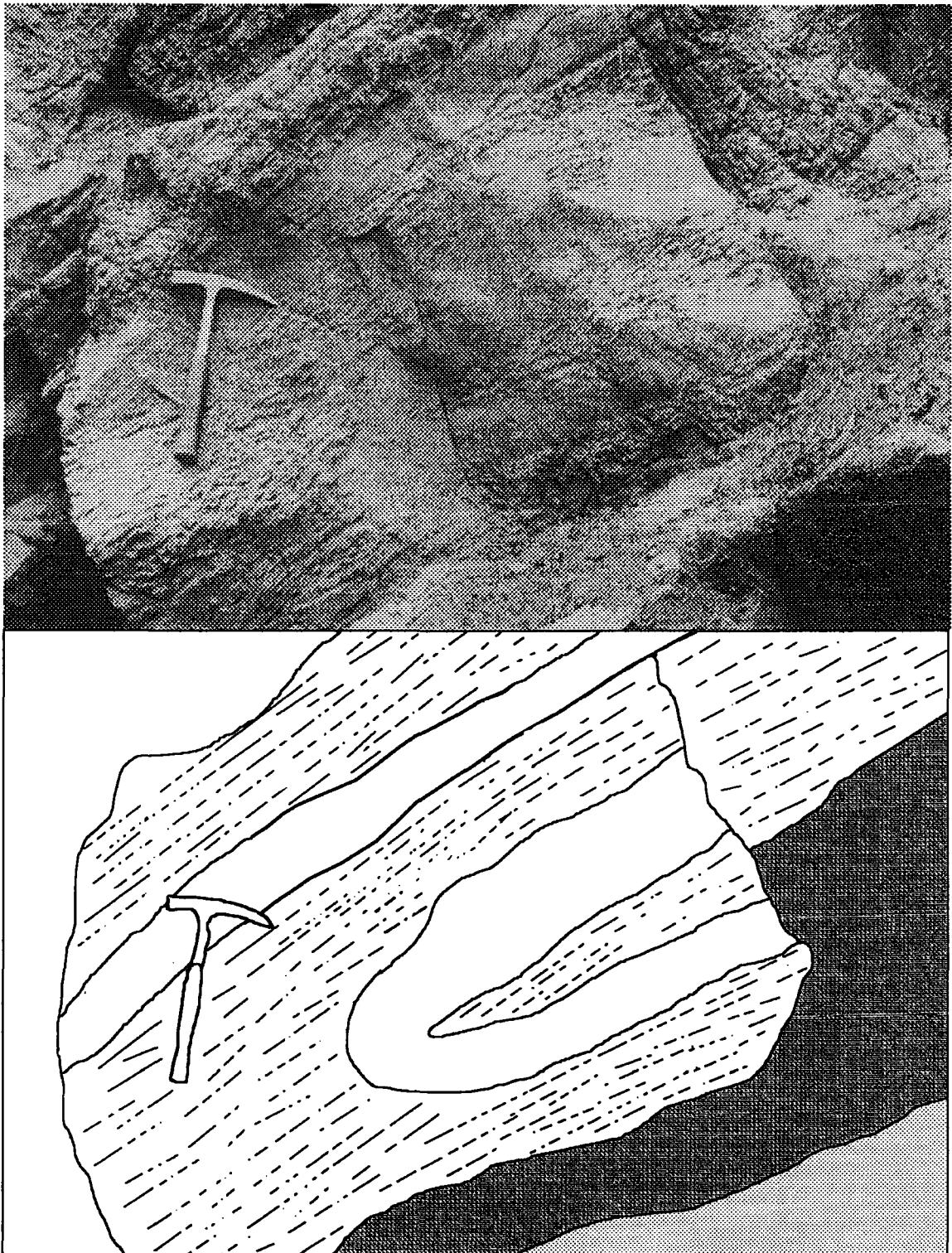
Plate (1.1) Isoclinal folding in mantle sequence harzburgite. Note that the orthopyroxene foliation is sub-parallel to the axial plane of the fold.
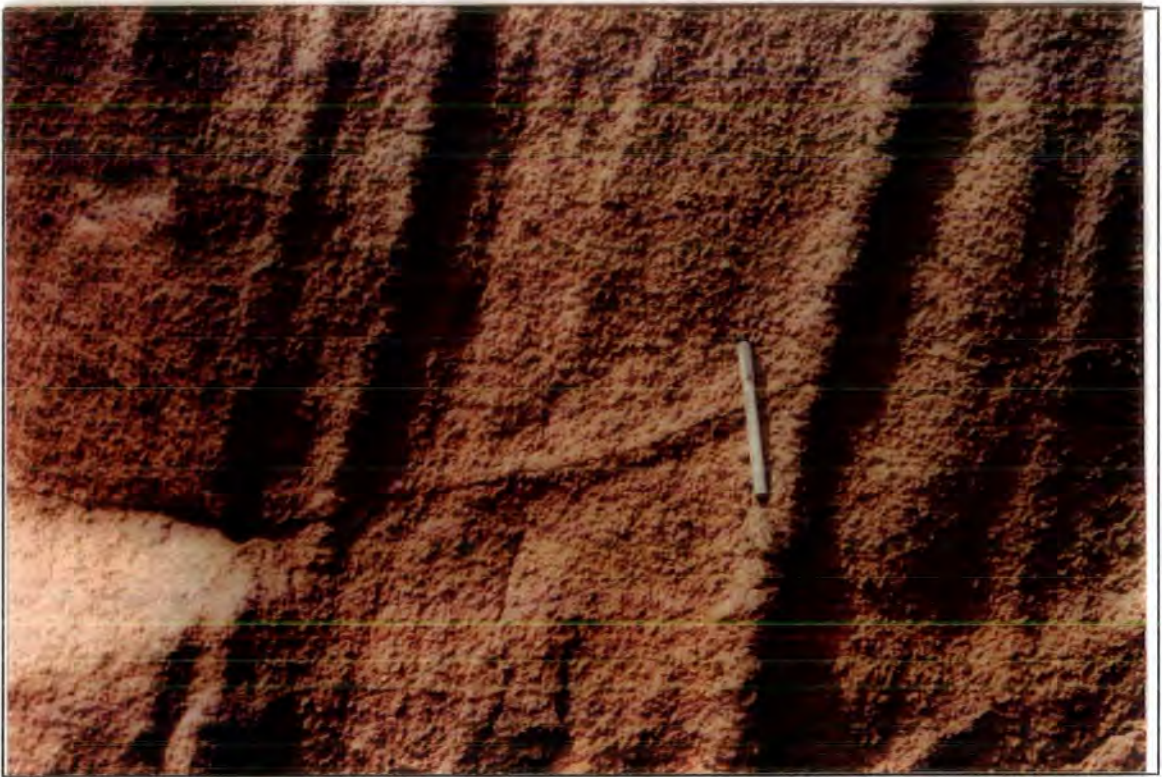
Plate (1.2) Pyroxene-rich and pyroxene-poor bands in mantle sequence harzburgite. The pen is 3.5 cm long.

Plate (1.3) Intensely tectonized harzburgite. Note elongation of orthopyroxene parallel to the pen.
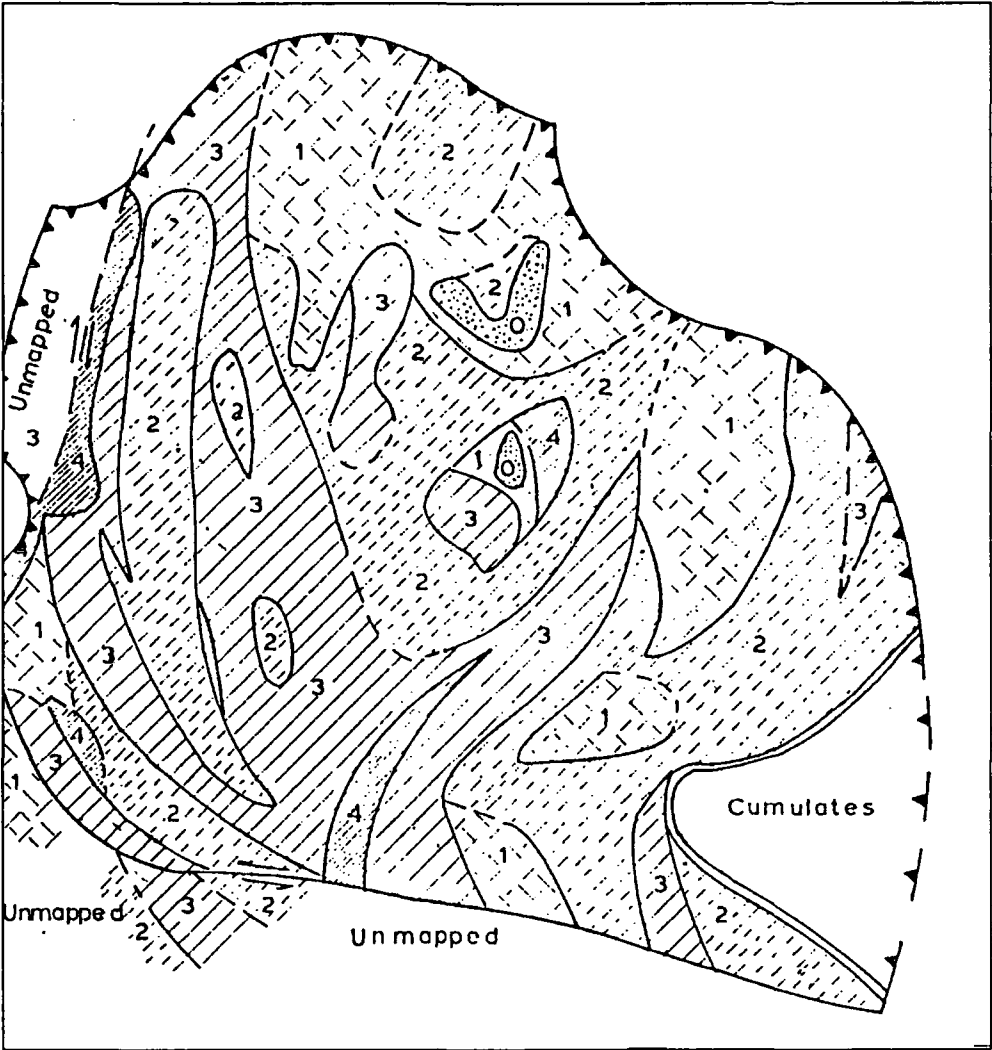
Figure (1.3) Areal distribution of peridotite fabric types in the Dramala area (Rassios, 1989).
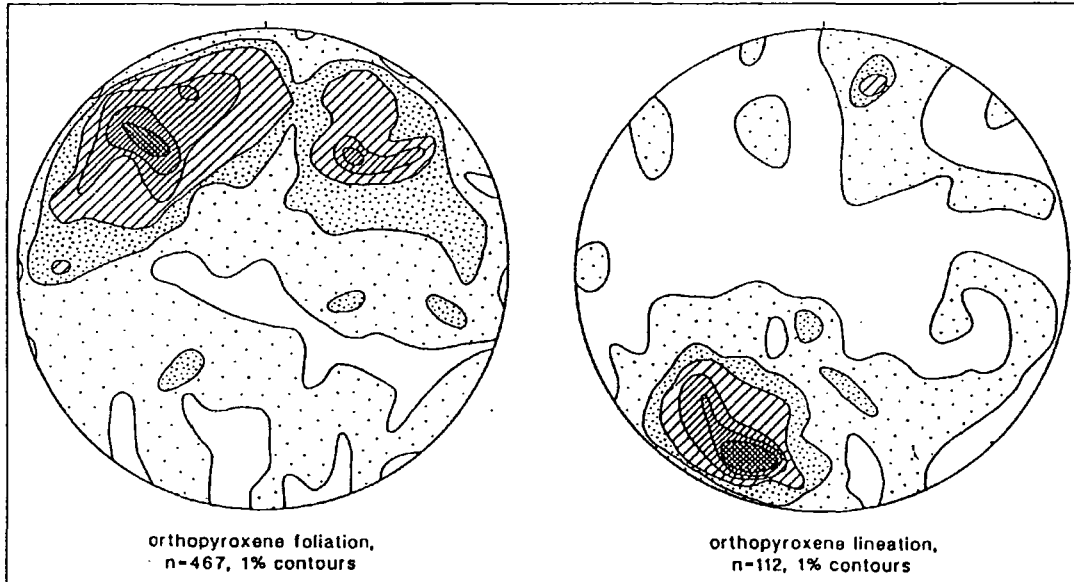
Figure (1.4) Orthopyroxene foliations and lineations in the Dramala peridotite (Rassios, 1989).
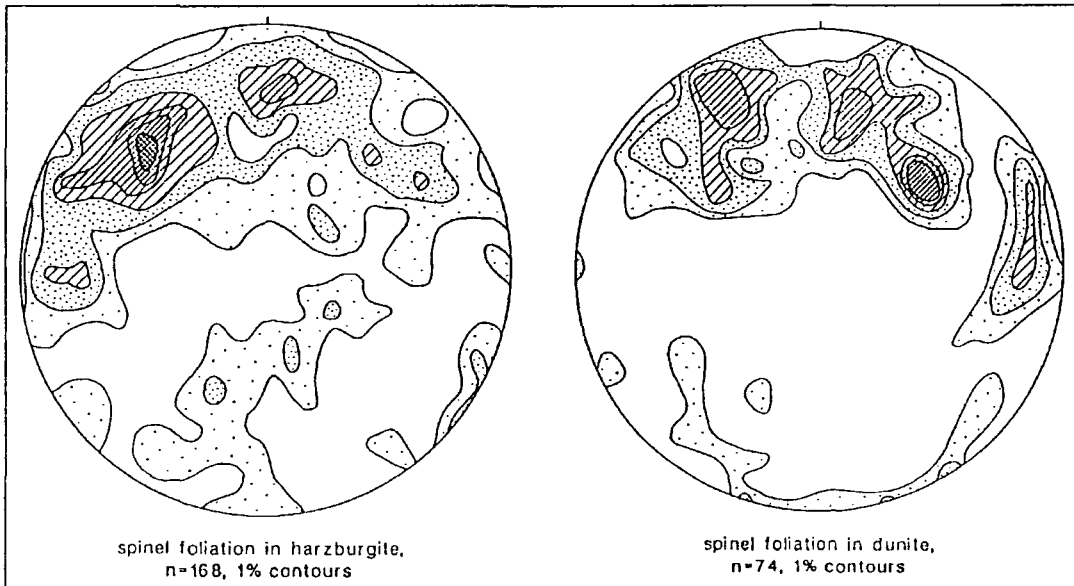
Figure (1.5) Spinel foliations   in the Dramala peridotite (Rassios, 1989).

Based on the relations of these two orientations with mylonites and brittle shears, Rassios (1989) ascribed an early high temperature origin to the 125°/S fabrics as opposed to a late, low temperature origin for the 040°/S structures. She also noted a correspondence of the 125°/S foliation with high-temperature peridotite fabrics (types #1 and #2, 1200°C) and of the 040/S foliation with granulation fabrics (types #3 and #4, 900°C), which supports her conclusion.

Rassios (1989) proposed a model for the genesis and emplacement of the Dramala peridotite, where the old, high-temperature 125°/S corresponds to a mantle diapir at a near-ridge environment, while the younger, low-temperature 040°/S represents the transition of the ophiolite from oceanic to obducting environment.

1.6.2. The transition from mantle to cumulate rocks

In the southeast part of the study area (Figure 1.2) the tectonized harzburgite comes in contact with cumulate rocks. This transition corresponds to the petrological Moho of ophiolites (Moores and Vine, 1971). In contrast to some ophiolites that have a quite sharp Moho (e.g. Vourinos, Harkins et al., 1980; Oman, Browning, 1984), with the transition of mantle to cumulate lithologies occurring within a few meters, in Pindos this transition is in most places gradual, occurring over a distance of 50-300 m. Thus, a mixed zone is developed between mantle tectonite and cumulate rocks, that is characterized by a, sometimes chaotic, mixture of tectonite harzburgite, discordant dunite, cumulates and dykes. Similar gradual transitions from mantle to cumulate lithologies have been described in a variety of ophiolites (review in Coleman, 1977. Transition zone of Nicolas and Prinzoffer, 1983). Common characteristics of these transition zones (including Pindos) are the irregular geometry and the gradational nature in terms of mineralogy of their lower contact with the underlying harzburgite and their essentially dunitic nature. Their thickness varies widely between different complexes, but, with a few exceptions, is fairly constant within a given massif (Nicolas and Prinzoffer, 1983).

East of the Kyra Kali ridge the transition zone is horizontal or gently inclined (Figure 1.2), but west of the ridge the mixed zone (and overlying cumulates) has been deformed by a

NW-SE trending steep shear zone, that has rotated the mixed zone-cumulate contact to near vertical. As a result of this deformation the thickness of the mixed zone is highly attenuated in places and the mantle harzburgite comes in tectonic contact with cumulate rocks.

The transition from mantle to cumulate lithologies is characterized by the increasingly abundant presence of dykes (plagioclase dunites, troctolites, pyroxenites, dolerites, but mostly gabbroic pegmatites, as described earlier), the decreasing proportion of harzburgite and its replacement by untectonized, almost solely discordant dunites, and the erratic but ubiquitous presence of plagioclase in the harzburgite. The latter has three modes of occurrence:

a: it occasionally forms diffuse, 2-5 cm thick, margin to intrusive dykes (Plate 1.4)

b: as 2 to 20 cm thick layers of plagioclase harzburgite with sharp contacts with the surrounding ordinary harzburgite (Plate 1.4)

c: as irregular meter-sized patches of plagioclase harzburgite in otherwise normal harzburgite (Plate 1.5)

The plagioclase invariably occurs as lobate grains surrounding olivine crystals (Plate 1.6). Sometimes the flattening and elongation of plagioclase laths define a foliation or lineation. Plagioclase-bearing harzburgites are texturally indistinguishable from plagioclase-free tectonite harzburgites, preserving their foliation and compositional layering. In thin section the plagioclase is often associated with clinopyroxene, both occurring in drop-like inclusions surrounding olivine grains, in a texture reminiscent of the cumulate poikilitic texture. In contrast to the olivine and orthopyroxene, the plagioclase and clinopyroxene do not show any evidence of strain (Plate 3.8).
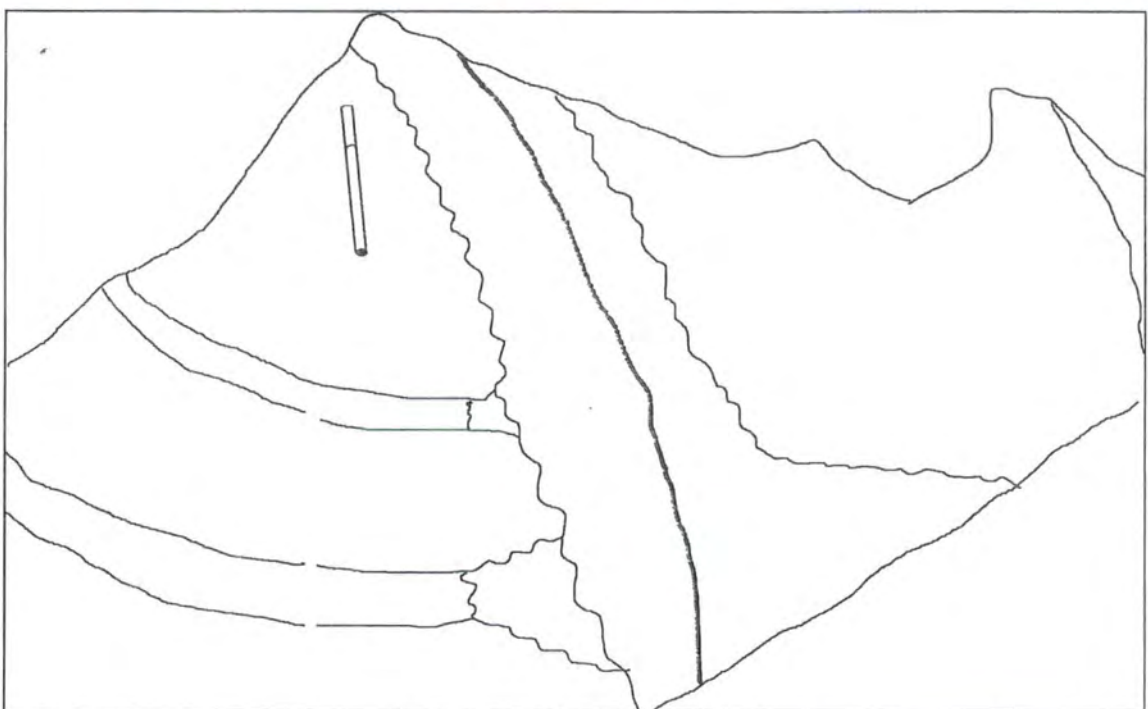
Plate (1.4) Transition-zone harzburgite cut by plagioclase-bearing dunitic dykes. The veinlet in the middle of the picture has created an impregnation zone, marked with wavy boundaries, around 15 cm. thick. In the left part of the picture two almost horizontal plagioclase-bearing veins show a homogeneous distribution of plagioclase and have well defined boundaries against the harzburgite.
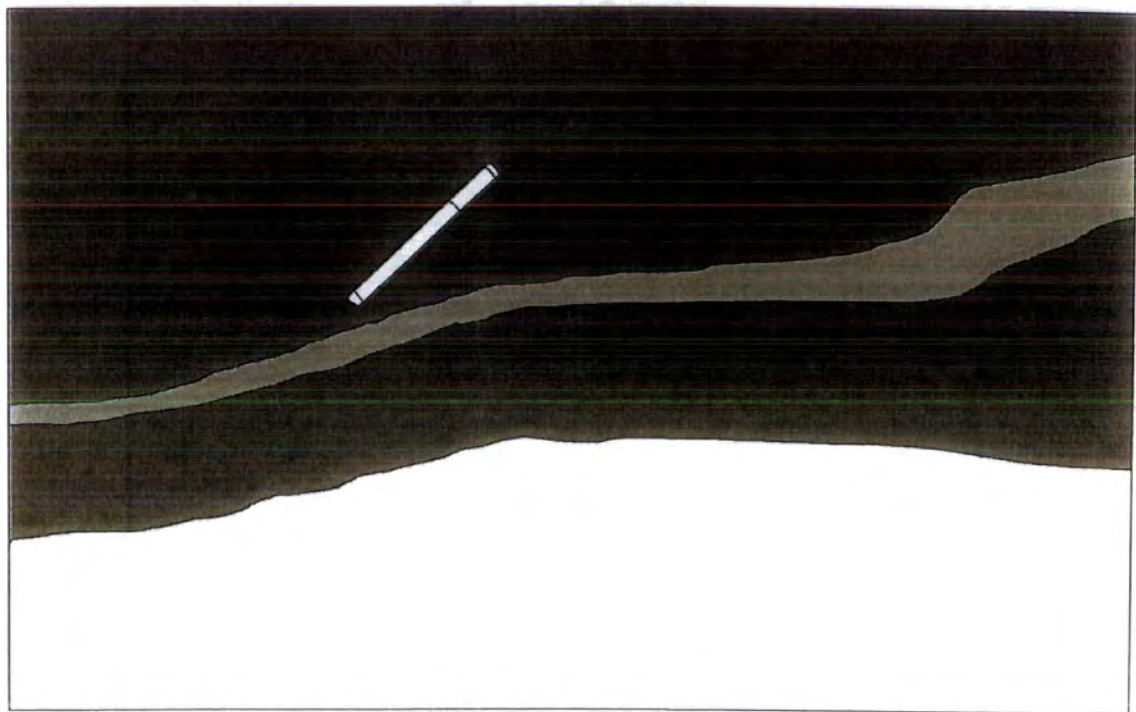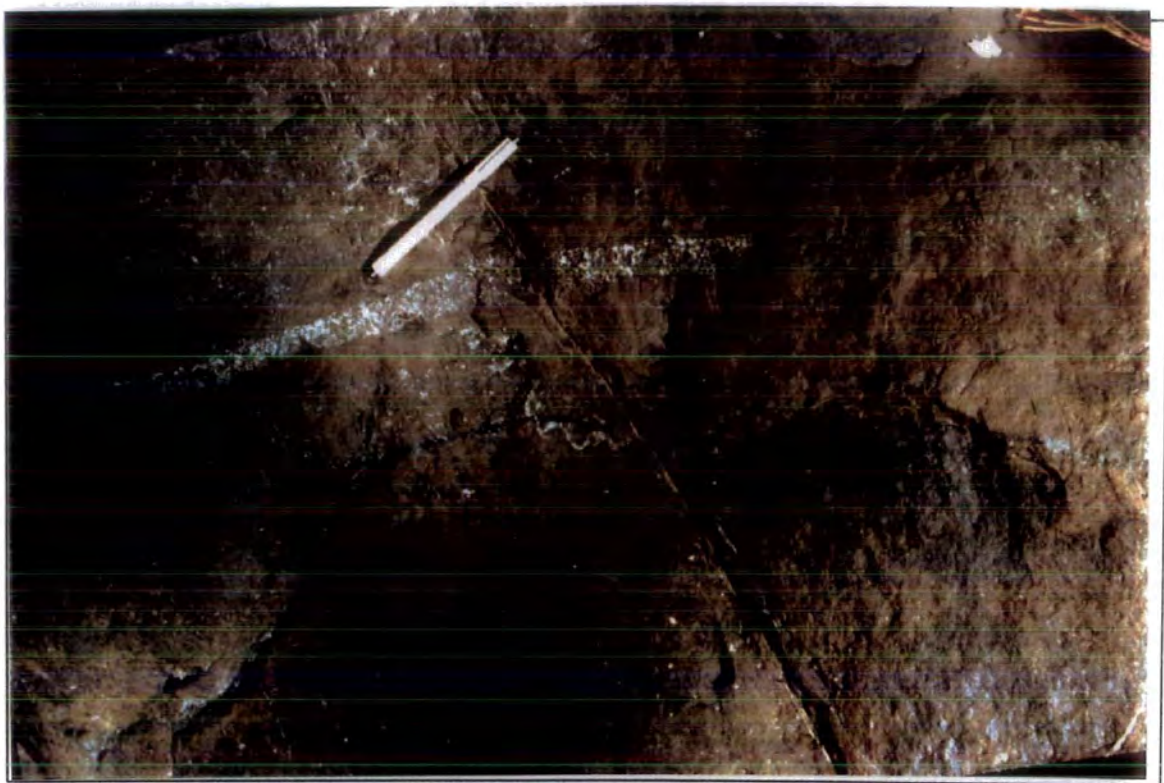
Plate (1.5) Transition-zone harzburgite cut by a plagioclase-bearing dunitic dyke. In the lower part of the picture the harzburgite is free of impregnation. The upper part (shaded) is plagioclase-impegnated harzburgite.
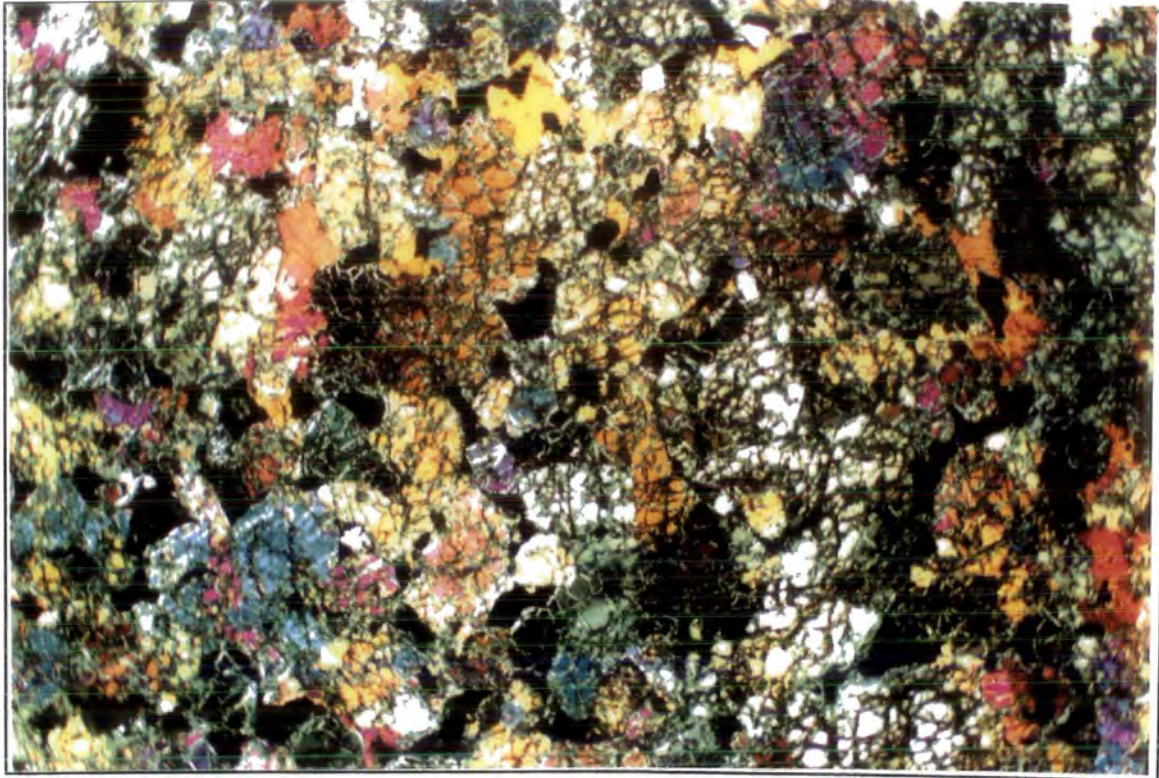
Plate (1.6) Plagioclase impregnation in dunite. The plagioclase is located at olivine grain boundaries and is in extinction because it is replaced by hydrogrossular. Crossed nicols, field of view 13 mm.

A similar transition from tectonite harzburgite to plagioclase harzburgite to ultramafic cumulates has been described by Terry (1974). This occurs in the northern block of the ophiolite near the village of Smixi and probably represents the Moho in that part of the ophiolite.

Plagioclase and clinopyroxene impregnation of dunites and harzburgites by percolating magma is now a well documented process in both ophiolites and abyssal peridotites (Dick, 1977; Nicolas et al., 1980; Nicolas and Prinzhofer, 1983; Dick, 1984, 1989; Evans, 1985; Miller and Mogk, 1987; Cannat et al., 1990). Although a magmatic origin for plagioclase peridotite massifs (e.g. Othrys, Menzies and Allen, 1974; western Alps, Bodinier et al., 1988) or peridotites slowly equilibrated in the plagioclase lherzolite stability fields (Evans and Girardeau, 1988) is undisputed, the field and textural evidence for the plagioclase peridotites in the Pindos transition zone is entirely consistent with an origin by melt impregnation.

Plagioclase also occurs in dunites of the transition zone, but it is not easy to distinguish between plagioclase-impregnated mantle dunite and cumulate dunite.

1.6.3. Cumulate rocks

Cumulate magmatic rocks are exposed in an area of ~15 km² in the southeast of the study area (Figure 1.2). They are bounded to the west and north by mantle and transition zone peridotite, and are terminated against the molasse basal conglomerate to the east. They have been divided into dunitic and gabbroic cumulates according to the lithology that dominates the outcrop.

1.6.3.1. Dunitic cumulates

This unit is dominated by olivine-rich rocks. These include dunites, troctolites, wehrlites, and olivine gabbros. The dunites dominate near the transition zone but the amount of plagioclase present in the rocks increases with distance from the Moho. The dunites consist of olivine with minor amounts of chromite dispersed throughout the rock. Plagioclase is frequently present, occurring as lobate grains that surround olivine crystals. Clinopyroxene occurs as large (up to 5 cm) oikocrysts enclosing olivine. Locally the amount of plagioclase

increases and dunite grades to troctolite. A weakly orientated cumulate layering is sometimes defined by segregations of plagioclase (1-5 cm thick) that persist for up to ~1 m.

Dykes similar to those occurring in the transition zone persist within this unit. Pyroxenites are scarce, but troctolitic, doleritic and gabbro pegmatitic dykes are still abundant although their frequency is diminished with increasing distance from the Moho.

A particular characteristic of this unit is the repetition of the sequence dunite-troctolite-gabbro that occurs in series of sill-like bodies of variable thickness. Lithologies within these sills rarely show well defined boundaries and mostly grade into each other in an irregular manner. The relative proportions of the lithologies also shows wide variation. Smaller-sized sills frequently show fine-grained margins, mixing and flow-induced deformation structures. The repetition of these sills in an outcrop resembles cumulate layering but the irregularity of their occurrence precludes their origin in a single, well-developed magma chamber. More likely they represent series of small scale intrusions injected between the cooling, but still plastically deformable, large dunite bodies.

True rhythmic layering is displayed in a wehrlite body that outcrops south of the Kyra Kali ridge (Figure 1.2, Plate 1.7). The rocks consist of olivine and clinopyroxene with a small (<1%) amount of spinel and virtually no plagioclase. The variation in the relative amounts of olivine and clinopyroxene define parallel layers of constant thickness (1-5 cm) (Plate 1.8). The rocks are fractured by jointing, but the layers can be traced laterally for several meters. A maximum thickness for these wehrlites of ~10 m can be observed before exposure is obscured.

1.6.3.2. Gabbroic cumulates

This unit is characterized by the predominance of plagioclase-rich rocks, i.e. troctolites and gabbros. The boundary between this and the previously described unit is somewhat arbitrary, since it is based on the relative proportions of the two lithologies on the outcrop and should not be interpreted as sharp contact. Nevertheless, there is a real decrease of the amount of dunites and troctolites and an increase of gabbros with distance from the transition zone.

Plate (1.7) Wehrlite showing centimetre-scale cumulate layering of alternating olivine-rich and olivine-poor layers. The clinopyroxene-rich layers are more resistant to alteration and stand out.

Plate (1.8) A closer view of the preceding wehrlite showing the poikilitic texture of the clinopyroxene.

Olivine and two-pyroxene gabbros are abundant, the latter becoming dominant towards the contact with the molasse to the east. These become locally plagioclase-rich and may grade to anorthosites. The gabbros sometimes display cumulate lamination, marked by the weak orientation of pyroxene. The cumulate characteristics are better developed in this unit marked by the varying proportions of olivine, pyroxene and plagioclase in 5-30 cm bands that define cumulate layering. The cumulate characteristics become less well developed towards the east where the gabbros are terminated against the basal conglomerate of the molasse. No higher level rocks were found in this part of the ophiolite.

1.7. Summary

The Pindos ophiolite is exposed in the Central Pindos mountain range, which is a part of the Dinaro-Hellenides chain. The ophiolite comprises a large thrust sheet of almost exclusively mantle-derived rocks over an area of ca. 700 km^2, and is divided in two parts, North and South, by the Aoos valley. Harzburgites, with little or no free clinopyroxene, dominate the south part of the ophiolite, while clinopyroxene-bearing harzburgites are present in the northern part. The Moho is exposed in the southeast part of the south block, where cumulate rocks are in contact with mantle sequence lithologies. The Moho has a transitional character and is characterized by the increased abundance of discordant dunites, extensive emplacement of dykes of variable mineralogy, and the pervasive impregnation of the depleted harzburgite by basaltic melt. The cumulate rocks near this transition are dominated by dunite with subordinate troctolite and gabbro and minor wehrlite. Away from the Moho, cumulate olivine and two-pyroxene gabbros become abundant.

Chapter 2. Serpentinization

2.1. Introduction

The ultramafic rocks of this study, in common with similar rocks world-wide, have been affected, to a smaller or larger degree, by interaction with fluids. This process has destroyed the original textures, produced new minerals, and may have changed the chemical composition of the rocks. The purpose of this chapter is to examine the conditions of serpentinization and establish how this alteration affects the chemical composition of a rock, i.e. which elements are mobilized or not, and how the original rock composition can be reproduced.

2.2. Field description

Two main types of serpentine can be distinguished in the field by their physical appearance.

I. Massive serpentinite: This is formed from dunite or harzburgite protolith and retains the petrographic texture of the original rock. In outcrop, dunites and harzburgites develop a weathering rind of yellowish-brown colour and thickness varying up to 2 cm. Orthopyroxene weathers slower than olivine and this gives harzburgites a rough surface compared to the smooth surface of the dunites. Freshly broken surfaces of both serpentinized harzburgites and dunites are dark green and have a conchoidal fracture. The colour of the freshly broken rock is a good indicator of the degree of serpentinization, ranging from light gray-green for the unaltered rock and becoming progressively greenish-black for the completely serpentinized rock.

II. Sheared serpentinite: This occurs in regions of massive serpentine and is associated with tectonic movements (faults, thrusts). The rock is usually fragmented and displays anastomosing cleavage and slickenslide surfaces. Its colour varies from yellow-green to olive-gray. The characteristic brown weathering rind of blocky serpentine is typically absent here. Asbestos slip-fibres are sometimes developed on the slickenslide surfaces of sheared serpentinites, with their orientation controlled by the direction of tectonic movement.

It will be noted that asbestos veins of appreciable size (i.e. larger than 2-3 mm width) have not been found anywhere in the Pindos ophiolite as yet, nor have any magnesite or calcite veins been observed.

2.3. Microscopic features

Olivine alteration initiates along fractures and grain boundaries where it comes in contact with serpentinizing fluids. This process finally leads to the characteristic mesh and hourglass textures. The serpentinization of olivine produces a characteristic pseudomorphic texture; in thin section it appears as an irregular tesselation of polygonal cells each of which consists of a centre composed of serpentine or relict olivine, surrounded by an outer zone of apparently[1] fibrous serpentine. The limits of this outer zone are defined by an original fracture or grain boundary. The apparent fibres of serpentine in the outer zone are aligned at approximately right angles to the trace of the original fracture. Wicks et al. (1977) termed this pseudomorphic texture a mesh texture, the centre of each cell a mesh centre, the outer zone a mesh rim and the original fracture the central parting of the mesh rim. Wicks et al. (op. cit.) presented an idealized model for this process, whereby olivine is represented by orthogonally stacked cubes and serpentinization starts with the growth of apparent serpentine fibres normal to the grain's surfaces. After this initial stage three possibilities exist:

a) the serpentine apparent fibres continue to grow until olivine is completely replaced;

b) the alteration stops before the olivine grain is consumed;

c) fibre growth is arrested and olivine is replaced by randomly orientated fine-grained serpentine.

Case (a) above will mainly produce hourglass textures. Case (b) will produce a mesh texture with olivine mesh centres, whereas case (c) will produce a mesh texture with isotropic mesh centres and minor hourglass textures. In reality, these textures are rarely repeated over

---

[1]The term apparent is used in reference to the serpentine habit because, although serpentine may appear fibrous, it is in fact a phyllosilicate mineral. Of the three polymorphs (antigorite, lizardite, chrysotile) only chrysotile usually develops fibrous crystals.

a long range because of the irregularity of fracture spacing and pattern, but textures that resemble the ideal ones can usually be found. The reason that this type of serpentinization appears to be a two-stage process, may reflect two distinct reaction intervals or the change of the reaction from being interface controlled to being diffusion controlled (Wicks and Whittacker, 1977).

Since the majority of the Pindos rocks are only partly serpentinized, the most commonly observed texture is serpentine mesh rims with olivine mesh centres (Plate 2.1), although the relative proportions of olivine and serpentine can vary a lot according to the degree of alteration. When olivine is completely replaced, the resulting texture in most cases is mesh rims with fine-grained serpentine mesh centres (Plate 2.2). Hourglass mesh centres are rather infrequent and appear to be restricted to the rocks of the transition zone, whereas pure hourglass textures (i.e. mesh hourglass textures without mesh rims) have not been observed at all.

Pyroxene is altered in the same manner as olivine, with serpentine replacement progressing around the grain's rim and along fractures and cleavage planes (Plate 2.5). Serpentine pseudomorphs after pyroxene are termed **bastites** and the term has been applied to pseudomorphs after amphibole as well. Wicks and Whittacker (1977) found that when replacement of the original mineral was complete, talc, chlorite and phlogopite bastites were indistinguishable from those derived from chain silicates and proposed the inclusion of sheet silicates' pseudomorphs in the definition of bastite. In contrast to olivine, mesh textures are not observed in pyroxene bastites, and although the alteration may have started along a rectangular set of fractures, the serpentine apparent fibres are arranged parallel to the original cleavage of the mineral.

Orthopyroxene bastites are far more common than clinopyroxene bastites, reflecting not only the relative frequency of occurrence of the two minerals but also the resistance of clinopyroxene to serpentinization. It is not unusual for clinopyroxene exsolution lamellae in orthopyroxene, to be preserved after complete replacement of their host by serpentine.

Spinel is the most resilient mineral during serpentinization of ultramafic rocks and is often preserved intact even after complete serpentinization of the original rock. It commonly develops a thin magnetite rim that is easily distinguished in translucent spinel grains because it is opaque (Plate 2.6).

In addition to pseudomorphic textures, serpentine veins are present in most samples. Four types of these veins can be distinguished:

i   veins of featureless serpentine (Plate 2.7);

ii   banded veins, that resemble those of type (i) except for the existence of two symmetrical bands of serpentine parallel to the walls of the vein, while the centre is filled with serpentine that has opposite extinction to that of the walls;

iii   veins of cross-fibre serpentine (Plate 2.8), that may or may not have a centre of featureless serpentine;

iv   veins of interlocking serpentine (Plate 2.9).

Veins of types (i) and (ii) may crosscut existing mesh textures or bastites but are usually parallel or branching with each other, whereas veins of type (iii) and (iv) crosscut existing pseudomorphic textures as well as veins of type (i) and (ii).
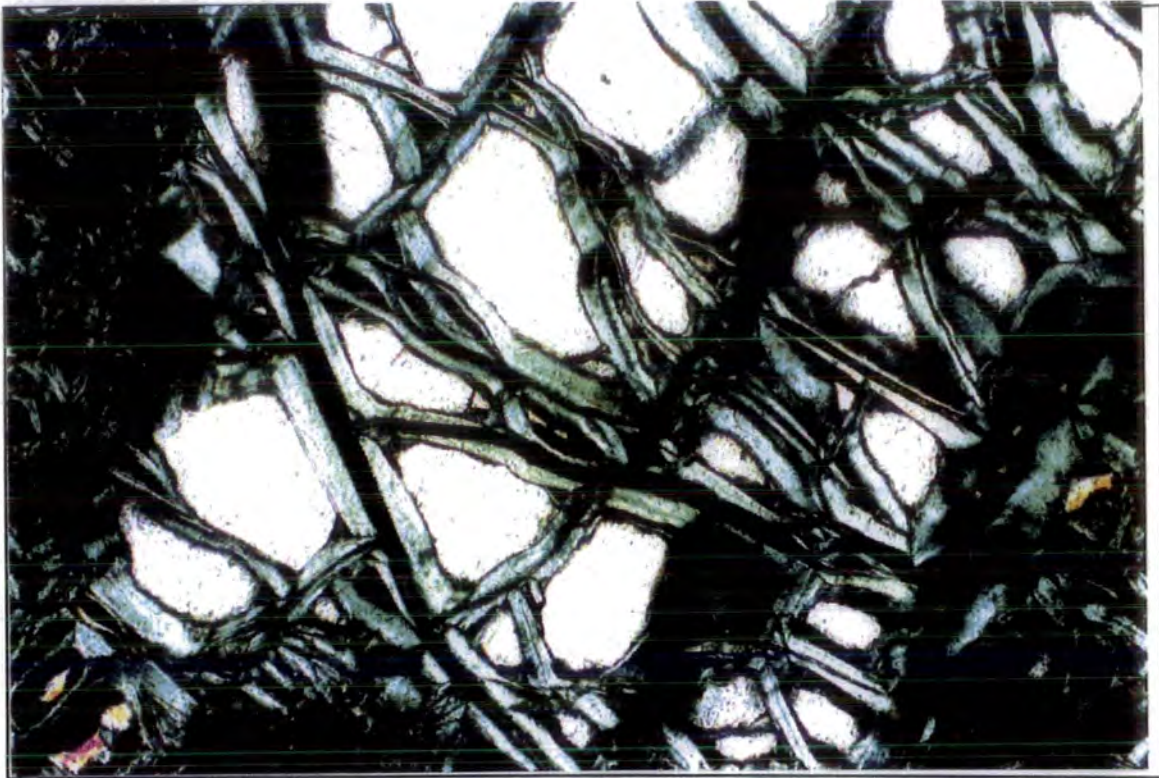
Plate (2.1) Mesh texture with serpentine mesh rims and olivine mesh centres. Crossed nicols, field of view 1.3 mm.
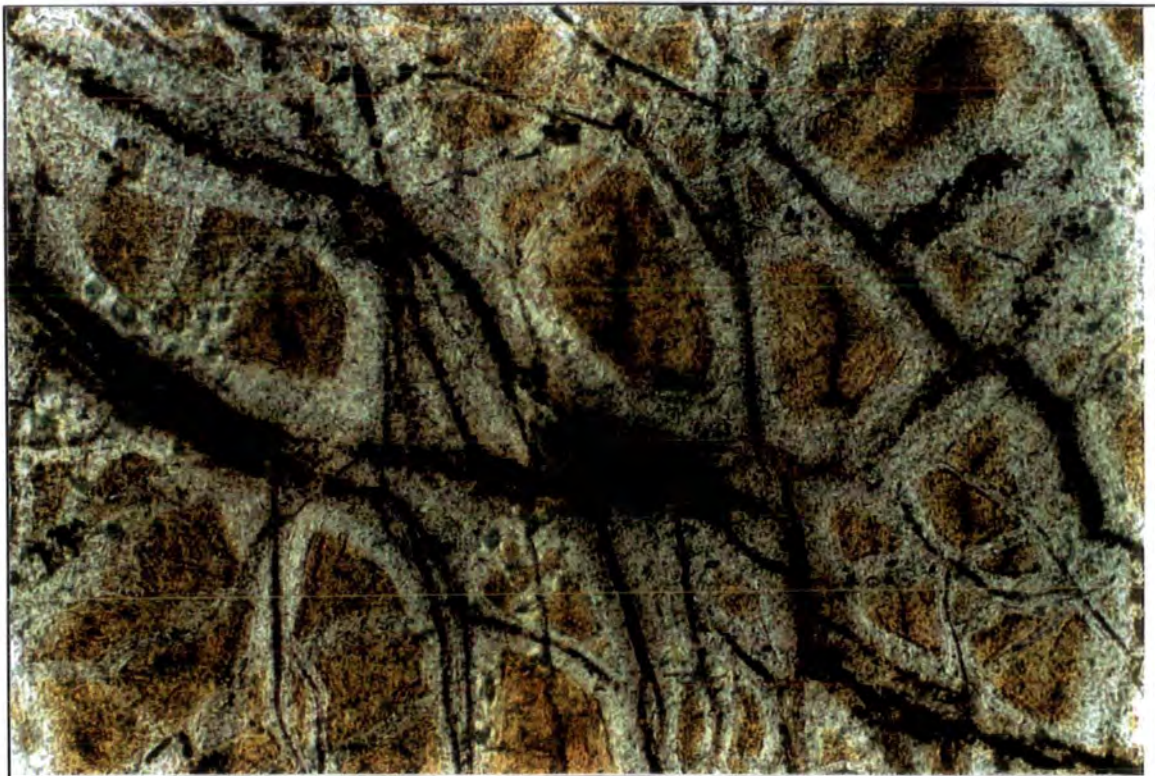
Plate (2.2) Mesh texture with serpentine mesh rims and fine-grained serpentine mesh centres. Note migration of magnetite along the central parting. Plain polarized light, field of view 13 mm.

Plate (2.3) The central parting of a bipartite. Crossed nicols, field of view 0.3 mm.
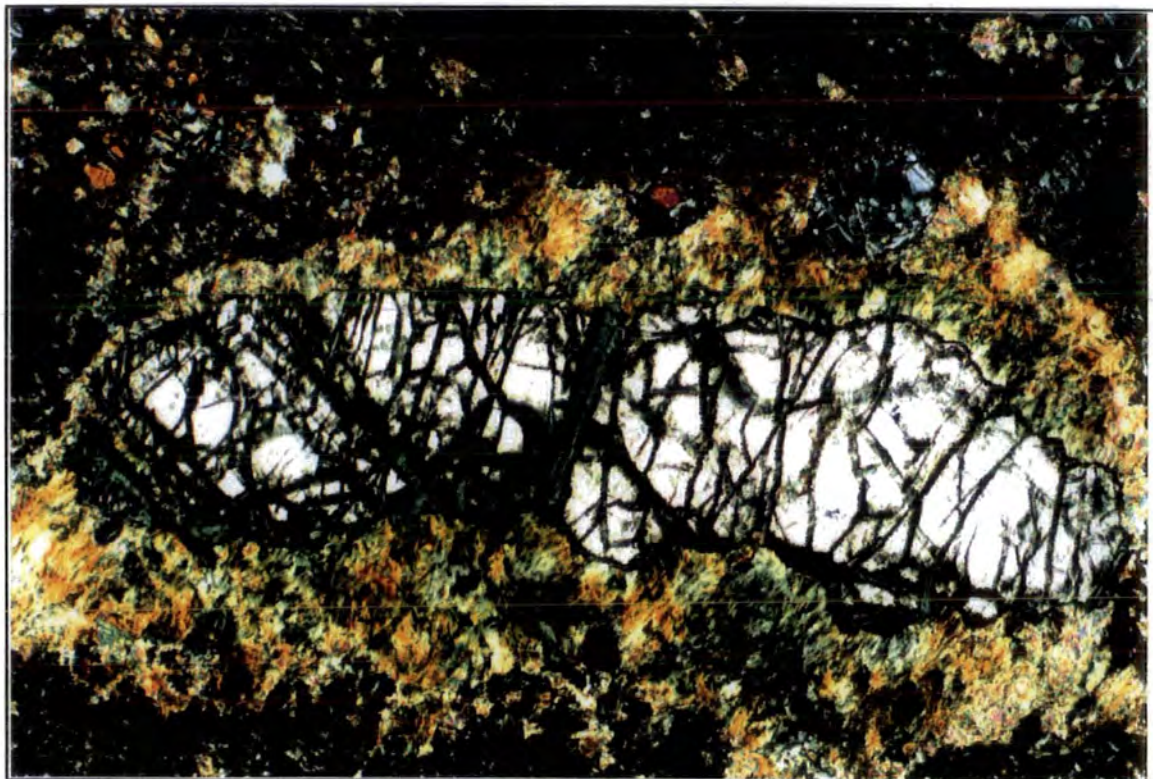
Plate (2.4) Talc reaction rim with enstatite. Note replacement of talc by serpentine (lower right). Crossed nicols, field of view 1.3 mm.
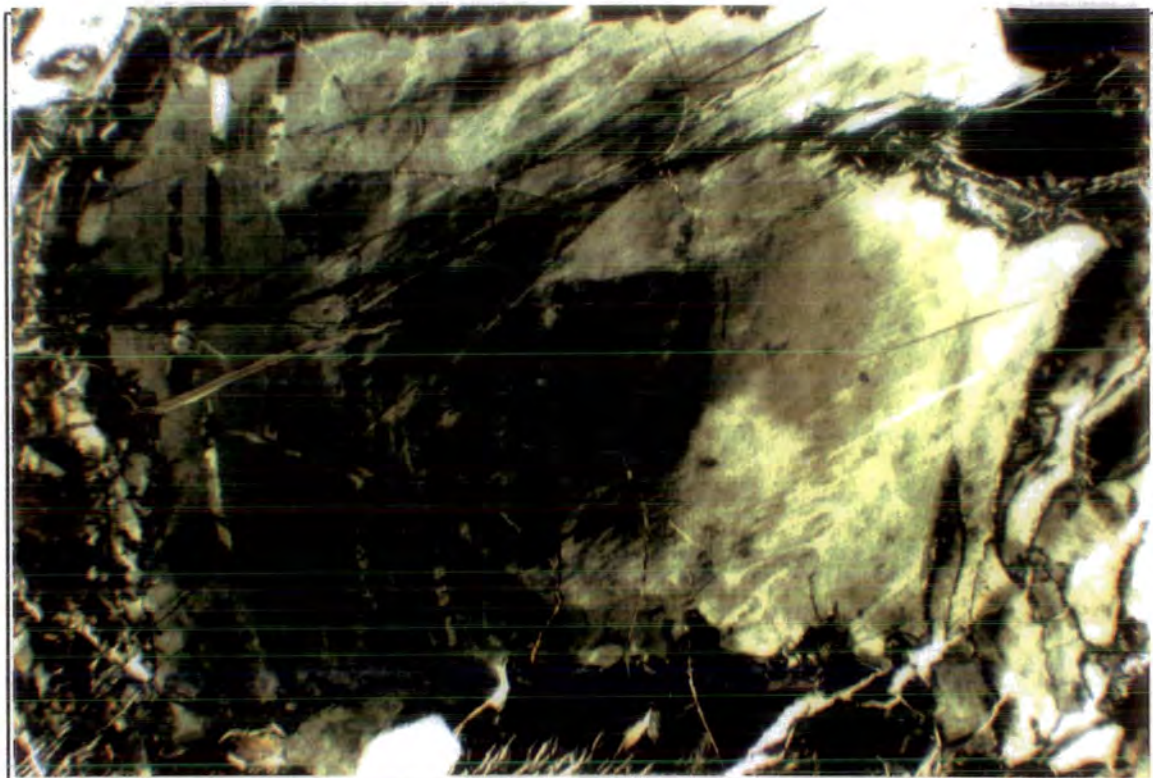
Plate (2.5) A complex bastite after orthopyroxene. Note the different extinction of the central part. Crossed nicols, field of view 2.5 mm.

Plate (2.6) Magnetite rim in spinel. Note expansion cracks in spinel filled with serpentine. Plain polarized light, field of view 1.3 mm.

Plate (2.7) Fracture filling vein of featureless serpentine. Crossed nicols, field of view 0.6 mm.

Plate (2.8) Fracture filling vein with walls of cross-fibre serpentine and centre of featureless serpentine. Crossed nicols, field of view 0.6 mm.
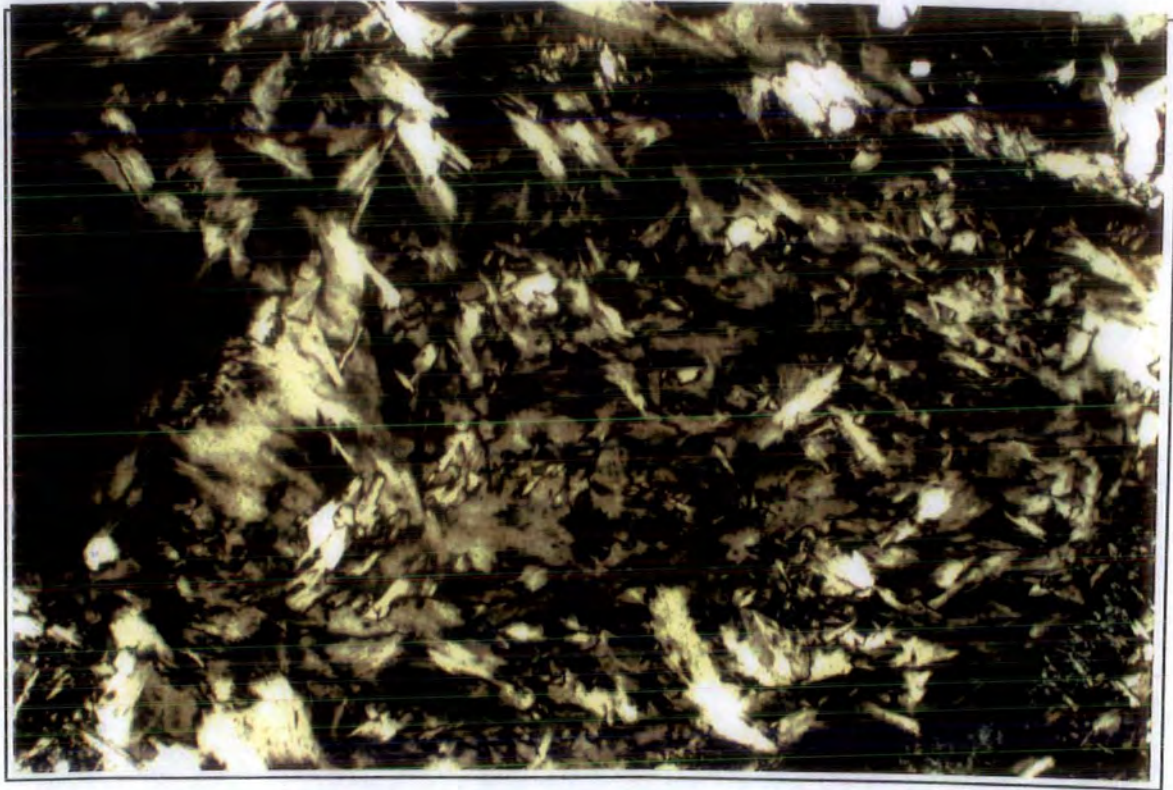
Plate (2.9) Fracture filling vein composed of interlocking serpentine. Crossed nicols, field of view 1.3 mm.

SAMPLE	Rock	Original mineralogy	Alteration products	Estimated serpentine%	LOI
GM4	D	ol,cpx,pl	l-b	100	12.08
AG882	D	ol,chr	l-b	70	8.37
DR1	D	ol,chr	l-b	90	13.05
DR16	D	ol,chr	l	95	13.51
DR19D	D	ol,chr	l-b		6.05
DR20	D	ol,chr	l-cht-b	60	9.95
DR35	D	ol,chr	l-cht-b		11.59
DR8	D	ol,chr	l-cht	90	11.03
LI881	D	ol,opx,chr	l-b		7.79
LI8810	D	ol,chr	l-b		12.28
LI8815	D	ol,chr	l-b		4.67
LI8816	D	ol,opx,chr	l-b	45	6.74
LI8823	D	ol,chr	l-b		10.82
LI8824	D	ol,chr	l-b	65	8.30
LI8827D	D	ol,chr	l		7.18
LI883	D	ol,chr	l-b		4.66
SI18	D	ol,chr	l-cht-b	100	13.99
SI19	D	ol,pl	l-b	100	14.40
KK886	D	ol,cpx,pl	l-cht-b		10.47
KK887	D	ol,cpx,pl	l-b		12.12
SI36	Gb	cpx,ol,pl	l-br(?)		1.79
AG2	Hz	ol,opx,chr	ta-l-cht(?)	40	1.57
AG3	Hz	ol,opx,chr	ta-l-cht(?)	20	2.05
AG883	Hz	ol,opx,chr	l-b+cht	80	7.08
DR11	Hz	ol,opx,chr	l-b(?)	50	6.83
DR14	Hz	ol,opx,chr	l-b		11.18
DR18	Hz	ol,opx,chr	l		3.09
DR19H	Hz	ol,opx,chr	ta-l		3.08
DR3	Hz	ol,opx,chr	l-b	80	10.24
DR32	Hz	ol,opx,chr	l-b		6.23
DR36	Hz	ol,opx,chr	l-b		3.86
DR9	Hz	ol,opx,chr	ta l-b	90	10.53
KK8820	Hz	ol,opx,chr	l		10.17
LI8811	Hz	ol,opx,chr	l	50	6.31
LI8812	Hz	ol,opx,chr	l-b(?)		5.23
LI8813	Hz	ol,opx,chr	l	30	3.76
LI886	Hz	ol,opx,chr	l		3.03
SI13	Hz	ol,opx,chr	l-b	75	9.69
SI16	Hz	ol,opx,chr	l-cht		
SI17	Hz	ol,opx,chr	l-cht	95	12.15
SI21	Hz	ol,opx,chr	ta	85	12.01
SI27	Hz	ol,opx,chr	ta	55	6.41
SI31	Hz	ol,opx,chr	l-cht-b		10.22
SI33	Hz	ol,opx,chr	l-cht	95	12.23
SI43	Hz	ol,opx,chr	l-b	80	10.17
KK46	Tr	ol,pl	l-(cht?)		8.65
SI6	Tr	ol,pl,chr	l-b	80	8.35
KK18	Lhr	ol,opx,cpx,pl	l	70	8.94
KK33	Whr	ol,cpx,pl	l-cht		7.62
KK36	Whr	ol,cpx,pl	l -		9.67
SI41	Lhr	ol,opx,cpx,pl	l	90	9.63

Table (2.1) The most common lithologies of the Pindos ultramafics and their alteration products. D=dunite, Hz=harzburgite, Tr=troctolite, Lhr=lherzolite, Whr=wehrlite, opx=orthopyroxene, cpx=clinopyroxene, chr=chromite, pl=plagioclase, l=lizardite, cht=chrysotile, ta=talc, b=brucite. LOI=loss on ignition. Serpentine in volume%. All samples include magnetite.

2.4. Mineralogy

The alteration mineralogy of the serpentinized rocks of Pindos was studied by whole rock XRD and optical microscopy and is presented in Table 2.1. Serpentine, brucite, talc and magnetite have all been identified and are described below.

The structural classification of serpentine $(Mg_3Si_2O_5(OH)_4)$ was undertaken by Wicks and Whittaker (1975), who revised the existing classification at the time and divided the serpentine polymorphs into two types: those of flat layered structure (**lizardites**) and those of cylindrical structure (**chrysotiles**) (Table 2.2). The polymorphs identified in this study by XRD spectra are lizardite-1T and chrysotile 2Mc1. Only in one sample was lizardite-6H present in sufficient amount to be detected. It will be noted that, according to this classification, antigorite is not regarded as a serpentine polymorph because of its different structure.

LIZARDITE - flat layered serpentines (1, 2, or multilayered)	
polytypes	mineral name
Group C - 1T	lizardite
D - 2H	2-layer serpentine
A - 3T	3-layer serpentine
B - 6H	6-layer serpentine
CHRYSOTILE - cylindrical structures	
polytypes	mineral name
$2M_{c1}$	clinochrysotile
$2Or_{c1}$	orthochrysotile
$1M_{c1}$	one-layer clinochrysotile

Table (2.2) The revised classification of serpentine minerals after Wicks and Whittaker (1975).

Lizardite is present in all serpentinized studied samples, whereas **chrysotile** was detected only in 25% of the samples (Table 2.1). Determining the relative proportions of these two polymorphs by X-ray techniques is unreliable because sample orientation may randomly amplify or suppress reflections. It is clear, however, that the amount of chrysotile never exceeds the amount of lizardite and that, in the majority of the samples, it constitutes only a small proportion of the total serpentine present.

Texture	Optical Character	Mineralogy
PSEUDOMORPHIC TEXTURES		
mesh rim	α	lizardite + brucite
	γ	lizardite, antigorite or chrysotile
mesh centre	α,γ+is	commonly lizardite + brucite, rarely antigorite or chrysotile + brucite
hourglass	α	lizardite + brucite
	γ	antigorite or chrysotile
orthopyroxene bastite	α	lizardite rarely with brucite
	γ	lizardite rarely with brucite
clinopyroxene bastite	α	lizardite
	γ	lizardite
amphibole bastite	α	lizardite rarely with brucite
	γ	lizardite rarely with brucite
phlogopite bastite	α	not found
	γ	lizardite rarely with brucite
talc bastite	α	not found
	γ	lizardite rarely with brucite
chlorite bastite	α	not found
	γ	antigorite or lizardite
NON-PSEUDOMORPHIC TEXTURES		
interlocking	α	lizardite 1T or multilayer polytype, possibly with some chrysotile
	γ	chrysotile and/or lizardite or antigorite
interpenetrating	α	not found
	γ	commonly antigorite, less commonly chrysotile and/or lizardite
serrate veins	α	not found
	γ	commonly chrysotile, less commonly antigorite
VEIN SERPENTINE		
asbestos cross-fibre	α	not found
	γ	chrysotile
asbestos slip-fibre	α	not found
	γ	chrysotile
non-asbestiform (fracture filling)	α	lizardite 1T or multilayer polytypes
	γ	chrysotile and/or lizardite or antigorite + brucite
	is	chrysotile and/or lizardite + brucite
non-asbestiform (slip)	α	not found
	γ	chrysotile and/or lizardite or antigorite + brucite
	is	chrysotile and/or lizardite + brucite

Table (2.3) A guide to serpentine minerals according to their textures (from Wicks and Whittaker, 1977). is=isotropic.

Optically, the two polymorphs are virtually indistinguishable. Nevertheless, serpentine textures may be used to identify individual minerals. Wicks and Whittacker (1977) have proposed a "texture guide" to serpentine mineralogy which is reproduced here as Table 2.3. It is apparent that pseudomorphic textures mainly indicate the presence of lizardite 1T, which explains the predominance of this polymorph in the Pindos rocks.

It will be emphasized here that antigorite has not been identified in any X-ray trace studied. Thus, in the absence of any texture that can signify its presence, it can safely be suggested that it is unlikely that antigorite occurs in Pindos. This does not exclude the possibility that antigorite could have been formed during a previous stage of alteration and was subsequently replaced by lizardite or chrysotile. This, nonetheless, seems unlikely as this process would have produced peculiar textures and would have left relict antigorite grains (e.g. Coleman and Keith, 1971; Moody, 1976b), as in the case of talc replacement by serpentine (see below).

Brucite ($Mg(OH)_2$) has been identified by its 100 reflection in X-ray spectra and is present in 60% of the samples. When determining the abundance of brucite from the intensity of its major reflection, the same problem as with serpentine exists, but it is likely that brucite does not form in great quantities. Because brucite has a large structural water content (~30 wt.%) its presence in substantial amounts would be reflected in a high loss on ignition (L.O.I.) value. Instead, the maximum L.O.I. value, found in totally serpentinized samples, is 14.4 wt.% (Table 2.1). Assuming a serpentine H_2O content of 12.7 wt.% (ideal serpentine formula) the maximum amount of brucite required to supply the additional water to 14.4 wt.% is ca. 10%.

Brucite is very difficult to distinguish from serpentine in thin section because both are found as fine-grained intergrowths (Wicks and Whittaker, 1977). When brucite appears in distinct grains, it is readily identifiable by its positive uniaxial character. With the aid of Table 2.3, it may be suggested that brucite mostly occurs with lizardite in pseudomorphic textures but rarely, if ever, in bastites.

Talc ($Mg_3Si_4O_{10}(OH)_2$) has been identified in only a few samples (4) by XRD or optical methods. It replaces orthopyroxene, typically as a reaction rim around the latter (Plate 2.4).

Talc itself is replaced by serpentine, although this replacement is not complete and perfect pseudomorphs of serpentine after talc (talc bastites) have not been observed.

Magnetite (Fe_3O_4) is always present in serpentinized ultramafic rocks. Its mode of occurrence seems to be related to the intensity of the alteration. During the early stages of serpentinization, magnetite is usually found as submicroscopic grains uniformly dispersed throughout the rock. As serpentinization progresses magnetite grains tend to cluster or create stringers, usually along fractures (Plate 2.6). Magnetite can also be seen in rims around chromite grains, where it is formed at the expense of chromite (Plate 2.6).

The mineralogy of serpentine veins cannot be deduced with great certainty from Table 2.3. The serpentine of type (iii) veins (cross-fibre) is almost always chrysotile, but types (i) and (ii) (featureless or banded serpentine) and type (iv) (interlocking serpentine) can be either lizardite or chrysotile. It will be noted that, although most veins are filling fractures or replace pre-existing minerals randomly, not all veins signify transportation of material; veins of types (i) and (ii) can be seen some times to have a central parting, an indication that they were produced by a mechanism that was similar, if not the same, as that which created the mesh textures. In addition, a single thin section usually has a small number of veins (less than five) which contribute a very small percentage of the mass of a sample. Veins may become significant towards the fractured surfaces of the rock (joints, slickenslides) but, as Wicks and Whittaker (1977) pointed out, these parts are either difficult to section or are usually discarded altogether.

The occurrence of lizardite chiefly in pseudomorphic textures, and of chrysotile in late veins or replacing lizardite or antigorite (Wicks and Whittaker, op. cit.), suggests that lizardite is the first serpentine mineral to form during serpentinization. Moody (1976a) observed that although both lizardite and chrysotile form during experiments, SEM photographs showed that lizardite forms first on olivine and was later replaced by chrysotile. In a petrographic study of ocean peridotites and ophiolites, Prichard (1979) showed that, in pseudomorphic textures, lizardite is always the first polymorph to be formed and only when very little olivine remains is chrysotile formed, mainly in cross-cutting veins. Figure 2.2 shows that chrysotile is present in partially, as well as completely, serpentinized samples.

Other minerals have been reported in studies of alteration of ultramafic rocks: chlorite and Cr-enriched spinel in high temperature hydrothermal alteration (Kimball, 1988,1990), ferritchromite and antigorite in prograde metamorphosed rocks (Moody, 1976; Wicks and Whittaker, 1977) and carbonates (usually magnesite) but none have been detected in the Pindos samples.

2.5. Phase relations

The system SiO_2-Al_2O_3-FeO-MgO-CaO-H_2O-CO_2 can be used to describe in detail the majority of ultramafic rocks in the presence of a fluid phase. Experimental work or thermodynamic modelling have been used to investigate phase relationships in this system or its sub-systems (e.g. Bowen and Tuttle, 1949; Johannes, 1969; Moody, 1976a; Hemley et al., 1977a,b; Jenkins, 1981; Trommsdorf and Conolly, 1990; Will et al., 1990). The restricted mineralogy of the alteration minerals allows the elimination of some components of this system when considering phase relationships in the rocks of this study. The fluid that was involved in the serpentinization of the Pindos ultramafics can be assumed with certainty to have been H_2O with no, or very little, CO_2. This conclusion is drawn from the absence of CO_2-bearing minerals, such as magnesite. The reaction brucite + CO_2 = magnesite is very sensitive to the presence of CO_2 in the fluid phase, even when its partial pressure is very low and brucite is unstable at $X_{CO_2} > 0.05$ (e.g. Johannes, 1969). Since CaO and Al_2O_3 have very low abundances and do not form individual phases, it can be reasonably assumed that their effect on the equilibrium conditions is negligible. Consequently, the experimental work that is best suited to describe the Pindos ultramafics is experiments in the system SiO_2-MgO-FeO-H_2O.

The serpentinization assemblage serpentine+-brucite+magnetite has been studied in terms of the P,T phase relations by a number of authors. The univariant equilibrium curve for the reaction:

$$serpentine + brucite = olivine + water \qquad (2.1)$$

was first studied in the system $MgO\text{-}SiO_2\text{-}H_2O$ by Bowen and Tuttle (1949), who established

what is effectively the hydration conditions for olivine. They found that serpentine+brucite

forms from olivine in the presence of water vapour at pressures less than 1 Kb at 400°C and

at pressures of 3 Kb at 450°C. Pistorius (1963) extended the experimental work to 50 Kb,

where serpentine + brucite form at ca. 475°C. The work of Page (1967) showed that in an

iron-bearing system these temperatures are somewhat lower: 300°C at pressures less than 1

Kb and ca. 325°C at a pressure of 3 Kb. Johannes (1968) found that earlier experimental

work on the reaction was in error and lowered the equilibrium temperatures by 60°C at the

same H_2O pressures. Later work by Hemley et al. (1977) established the equilibrium for the

same reaction at 370°C at 1 Kb (Figure 2.1).

The presence of talc, even in small amounts, is significant because it defines a

different regime of pressure and temperature. The stability field of talc in the system $MgO\text{-}$

$SiO_2\text{-}H_2O$ can be bounded by the work of Hemley et al. (1977a,b), who determined the

thermal dehydration temperature at a water pressure of 1kb for the assemblage talc-

forsterite-enstatite at 643°C and the assemblage chrysotile-forsterite-talc at 441°C (Figure

2.1). Although talc may decompose to a variety of minerals (e.g. anthophyllite, antigorite),

the reactions mentioned are consistent with the observed assemblages. It will be noted that

the serpentine polymorph in Figure 2.1 is chrysotile. This is because Hemley et al. (1977a,b),

in common with many other studies (e.g. Johannes, 1969, Chernosky, 1973), used chrysotile

as starting material for their experiments. Although this might pose a question about the

applicability of these experiments to lizardite assemblages, it is generally considered that the

thermodynamic properties of the two polymorphs are similar and that differences in

equilibrium temperatures are not significant.

It is clear from Figure 2.1 that talc is stable at much higher temperatures than

serpentine and it cannot be in equilibrium with serpentine and enstatite. Talc is unstable at

the conditions that serpentine formed, as is evident from the fact that it being replaced by

serpentine (Plate 2.4). Coleman and Keith (1971) interpreted a similar occurrence of talc

reaction rims around enstatite in the Burro Mountain Dunite as a localised effect due to the

high activity of silica near enstatite grains, and not as an indication that the ultramafic body

had experienced high temperatures at some stage during its history. If this was the case with

Pindos, however, then serpentine and talc would not show the observed reaction relationship.

Therefore, the presence of talc is interpreted as an indication that rock-fluid interaction started

at high temperatures (>600°C). However, the scarcity of talc in the Pindos rocks suggests

that this interaction was short-lived and the temperature fell quickly to levels where talc

formation is arrested.
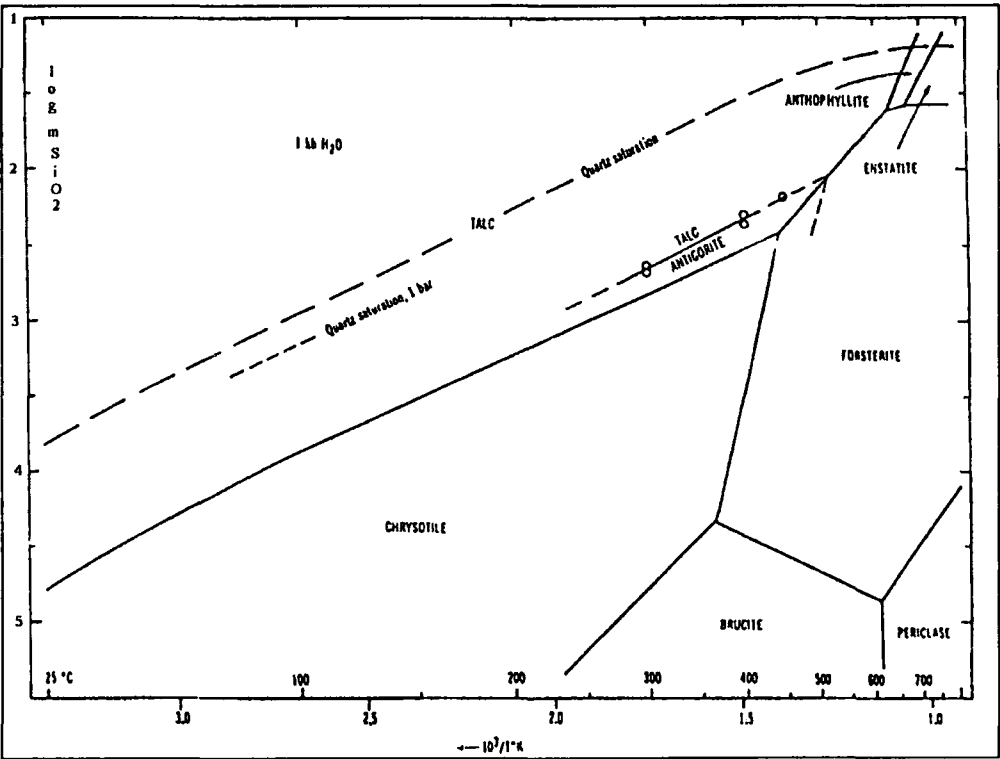
Figure (2.1) Experimental (talc) and calculated (chrysotile, forsterite, brucite, periclase) equilibria in the system SiO_2-MgO-H_2O. Dashed lines represent uncertainty bands. (from Hemley et al., 1977b).

2.6. Chemical effects of serpentinization

Serpentinization is a process that involves the destruction of existing magmatic

minerals (olivine, pyroxene etc.) and the formation of new ones (serpentine, brucite etc.). The

ability of the new minerals to accept various elements in their lattice is an important aspect of

the study of the mobility or immobility of these elements. Wicks and Whittaker (1975), in their

study of serpentine mineral structures, examined the effect of different elements substituting

in the lizardite and chrysotile structure. They showed that lizardite can accommodate substantial amounts of Al^{3+} and Fe^{3+} in its lattice and that Ni^{2+} can freely substitute for Mg^{2+}. This is demonstrated by the occurrence of end-member composition minerals with the lizardite structure, namely amesite, $Mg_2Al(SiAl)O_5(OH)_4$, greenalite, $Fe_3Si_2O_5(OH)_4$, cronstendite, $Fe_2Fe_2Si_2O_5(OH)_4$, and nepouite, $Ni_3Si_2O_5(OH)_4$. In addition, Co^{3+}, Mn^{3+} and Cr^{3+} can substitute for Mg^{2+} to a limited extent. The same elements can enter the chrysotile structure, although substitution is more restricted and only the Ni-serpentine intermediate composition garnierite, $(Mg,Ni)_3Si_2O_5(OH)_4$, and end-member composition percoraite, $Ni_3Si_2O_5(OH)_4$, may coexist with the chrysotile structure. Table 2.4 shows the composition of an ideal serpentine with the same Mg# as Fo_{90} and En_{90}. It can be seen that serpentine has MgO, FeO_{tot} and SiO_2 contents intermediate between the olivine and enstatite values. It is possible for a forsterite-enstatite assemblage to produce serpentine without any loss of mass according to the reaction :

$$Mg_2SiO_4 + MgSiO_3 + 2H_2O = Mg_3Si_2O_5(OH)_4 \qquad (2.2)$$
olivine   enstatite   serpentine
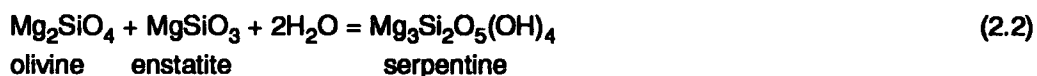
This however requires olivine and pyroxene to be present in equimolar proportions (or approximately 60% olivine 40% pyroxene by weight), a condition that is met only in a few pyroxene-rich harzburgites. If olivine is present in larger amounts, the silica available in the rock is not enough to combine with all magnesium, which may enter the solution according to the reaction :

$$2Mg_2SiO_4 + 2H^+ + H_2O = Mg_3Si_2O_5(OH)_4 + Mg^+ \qquad (2.3)$$
olivine   serpentine
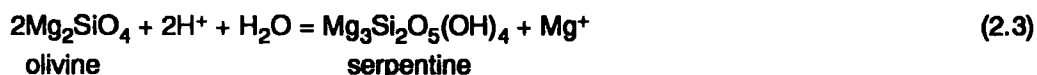
or precipitate as brucite according to the reaction :

$$2Mg_2SiO_4 + 3H_2O = Mg_3Si_2O_5(OH)_4 + Mg(OH)_2 \qquad (2.4)$$
olivine   serpentine   brucite
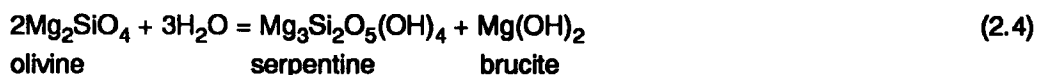
It is apparent that the presence of enstatite reduces the amount of brucite by providing the silica to form serpentine. This has been observed by Coleman and Keith (1971) in the Burro Mountain dunite and the same can be seen in Table 2.1. This seems to support the notion that silica only goes into solution when there is insufficient MgO available to combine with it. It also means that, during serpentinization, the composition of the rock will remain unchanged with respect to SiO_2 and MgO until all pyroxene is consumed. Beyond this point, and in the case of dunites, magnesium will either enter the solution or precipitate as brucite.

The presence of iron in solid solution in olivine and pyroxene changes the reaction from simple hydration to a redox reaction. Formation of magnetite (Fe_3O_4) requires the oxidation of ferrous iron in the silicates. Less obvious is the oxidation of iron that is present in serpentine, since most of this iron can be in the trivalent state (Table 2.5). It has been mentioned earlier that serpentine can accept substantial amounts of Fe^{3+} (Wicks and Whittaker, 1975), but this requires substitution of Si^{4+} by Al^{3+} to achieve charge balance. Since aluminium is present in the serpentine of Pindos rocks (Table 2.4), then at least part of the iron present must be in the trivalent state, but since this iron was derived from the primary ferromagnesian minerals, no distinction will be made between Fe^{2+} and Fe^{3+} in subsequent calculations and total iron will be calculated as FeO. A general reaction can be written as:

$$Fe\text{-olivine} + Fe\text{-enstatite} = Fe\text{-serpentine} + Fe\text{-brucite} + magnetite \qquad (2.5)$$
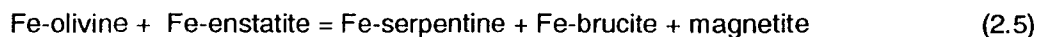
The actual amount of magnetite formed depends not only on the available iron but, more crucially, on the amount of iron that serpentine and brucite can accommodate in their lattices. Coleman and Keith (1971) noted an inverse correlation between the amounts of magnetite and brucite which they attributed to the inclusion of iron in the brucite. The substitution of iron in brucite has been established by many authors (see Moody, 1976b for a review) who also showed that: a) brucite has more iron than co-existing lizardite; b) brucite usually has more iron than the parent olivine; c) lizardite may have more or less iron than the

parent olivine, the amount being controlled by the co-existing brucite and/or magnetite. The experiments of Moody (1976a) on iron-bearing olivines suggest that magnetite formation is favoured over iron substitution in brucite by higher temperatures. Janecky and Seyfried (1986) noted that during seawater interaction with peridotite, magnetite formation was correlated with increase of the pH of the solution, whereas low pH favoured the accommodation of iron in the fluid phase and in the serpentine.

Magnetite also forms from the alteration of chromite, although its distribution suggests that it formed by a different process in this case (Plate 2.6). Magnetite can be observed to replace chromite grains around the rim and along fractures, probably by the removal of Cr, Al and Mg from the spinel and not by the precipitation of magnetite from solution.

The fluid that caused the serpentinization of the Pindos ophiolite cannot be characterized without isotopic evidence. However, it was noted that, during probing of serpentines, the Cl line was frequently detected and was very strong when a fluid inclusion was accidentally hit. Although this may suggest the trapping of high-chlorinity fluids derived from seawater, it should be noted that oxygen isotope studies of other ophiolites and in particular Vourinos (Wenner and Taylor, 1973; Magaritz and Taylor, 1974) have shown that meteoric water was involved in serpentinization.

	CMT731	LI8819	LI8819	AG2	LI8826	SI23	Serpentine
SiO_2	48.96	51.17	47.07	44.21	49.27	49.03	47.94
Al_2O_3	0.14	0.76	0.26	0.15	0.26	0.35	
Cr_2O_3	0.07	n.d.	0.10	0.04	0.11	0.04	
FeO*	6.04	3.06	5.04	8.51	5.82	6.34	8.58**
MnO	0.11	0.03	n.d.	0.11	0.21	0.04	
MgO	43.27	44.45	47.08	46.02	44.09	43.48	43.48
CaO	0.18	0.03	0.05	0.15	0.17	0.11	
NiO	0.55	0.29	0.15	0.31	0.00	0.21	
Total	75.22	82.91	80.67	79.52	79.74	81.94	87.4
Mg#	0.928	0.963	0.944	0.906	0.931	0.925	0.90
Fo	0.921	0.910	0.910	0.912	0.916		

Table (2.4) Electron probe analyses of serpentines. CMT731 and SI23 are analyses of lizardite pseudomorphs (mesh textures). The rest are analyses of featureless vein serpentine. Fo is the forsterite fraction of fresh olivine. Last column is ideal serpentine composition with Mg#=0.90. The low totals result from burning of the grains during probing. All analyses (including last column) are recalculated to 100%. *Total iron as FeO.**Calculated for an Mg#=0.90

	Lizardites Average of 6	Lizardite bastites Average of 23	Chrysotile Average of 7	Ideal composition
SiO_2	41.58	41.46	42.02	41.9
Al_2O_3	0.82	2.76	0.47	
Fe_2O_3	3.22		0.79	
FeO	0.08	3.74**	0.25	7.5**
MgO	40.59	38.34	41.63	38.0
H2O+	13.41	13.1	13.62	12.6
Total	99.70	99.4	98.78	100.0

Table (2.5) Compilation of serpentine analyses by Moody (1976b). Ideal composition is $Mg_3Si_2O_5(OH)_4$.**Total iron as FeO calculated for an Mg#=0.90

2.6.1. The effect of serpentinization on the chemistry of the ultramafics

It would be safe to assume that the original mineralogy of the Pindos ultramafics does not include any hydrous minerals. Although primary amphibole and phlogopite peridotites exist, there is no evidence to suggest that such peridotites exist in Pindos. It follows, then, that any structural water that appears in the analysis of a sample should be due to the presence of alteration minerals. Furthermore, the amount of water should correlate with the abundance of H_2O-bearing minerals. It has been shown so far that the principal alteration mineral in Pindos is serpentine. Figure 2.2 shows a plot of the loss on ignition against the amount of serpentine, as was visually estimated under the microscope, for the ultramafic rocks of Table 2.1. The good positive correlation displayed further suggests that brucite and talc are not present in large amounts. This allows the use of the loss on ignition as an index of the degree of serpentinization, so that differences in sample composition can be related to the degree of alteration.

In Figures 2.3a-h SiO_2, Al_2O_3, total iron as Fe_2O_3, MgO, CaO, Ni, and Cr are plotted against loss on ignition. TiO_2 and MnO have very restricted compositional ranges (0.00-0.03 wt.% and 0.10-0.13 wt.% respectively) and do not show any variation, while Na_2O, K_2O and P_2O_5 are below the limit of detection. All oxides have been recalculated to anhydrous to cancel the diluting effect of water. Both harzburgites and dunites are included in the plots, but it will be noted that the latter are cumulates, representing varying degrees of fractionation, which adds some complexity to the interpretations.

In order to quantitatively assess the variation of any element with alteration, least-squares regressions were calculated separately for harzburgites and dunites. Also shown in Figures 2.3a-h are the approximate positions of the main silicate minerals. i.e. olivine, orthopyroxene, and serpentine, the latter also recalculated as volatile-free. The range of compositions represents the observed variation in Pindos rocks.
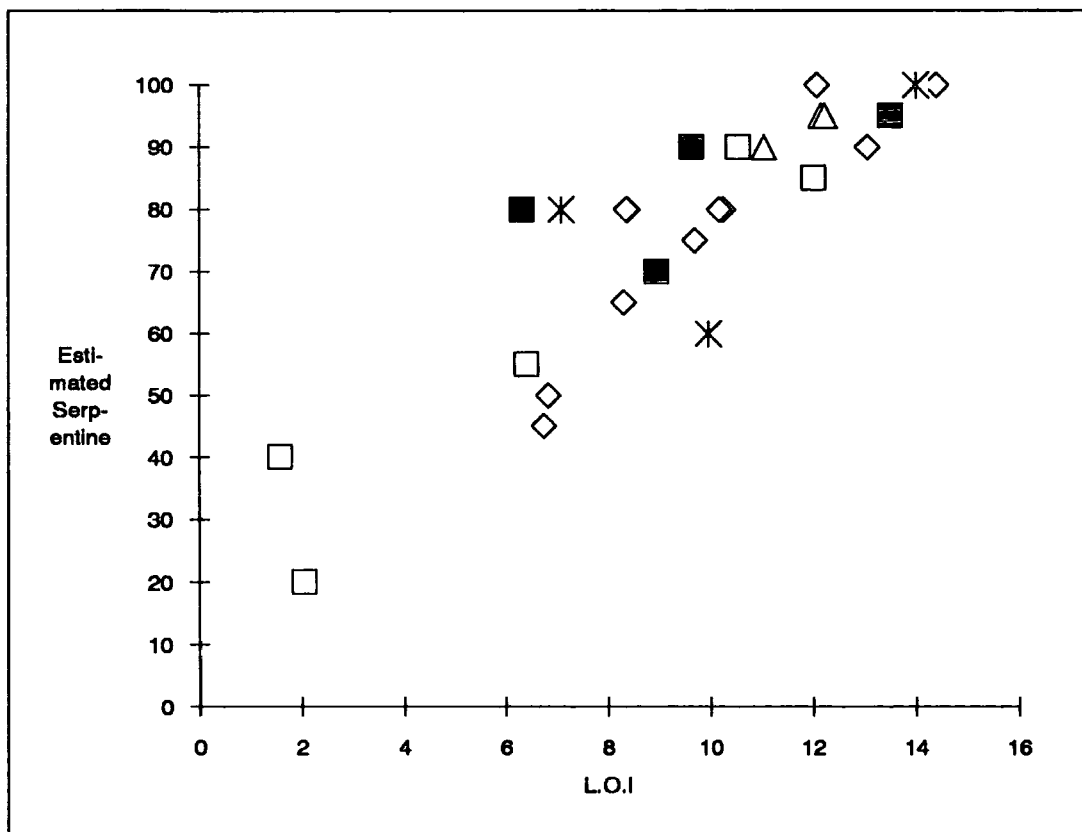
Figure (2.2) Plot of the estimated percentage of serpentine against loss on ignition (L.O.I.). Symbols denote the alteration minerals as determined by XRD. All samples include magnetite. Solid square: lizardite, diamond: lizardite and brucite, triangle: lizardite and chrysotile, star: lizardite, chrysotile and brucite, open square: talc and serpentine.
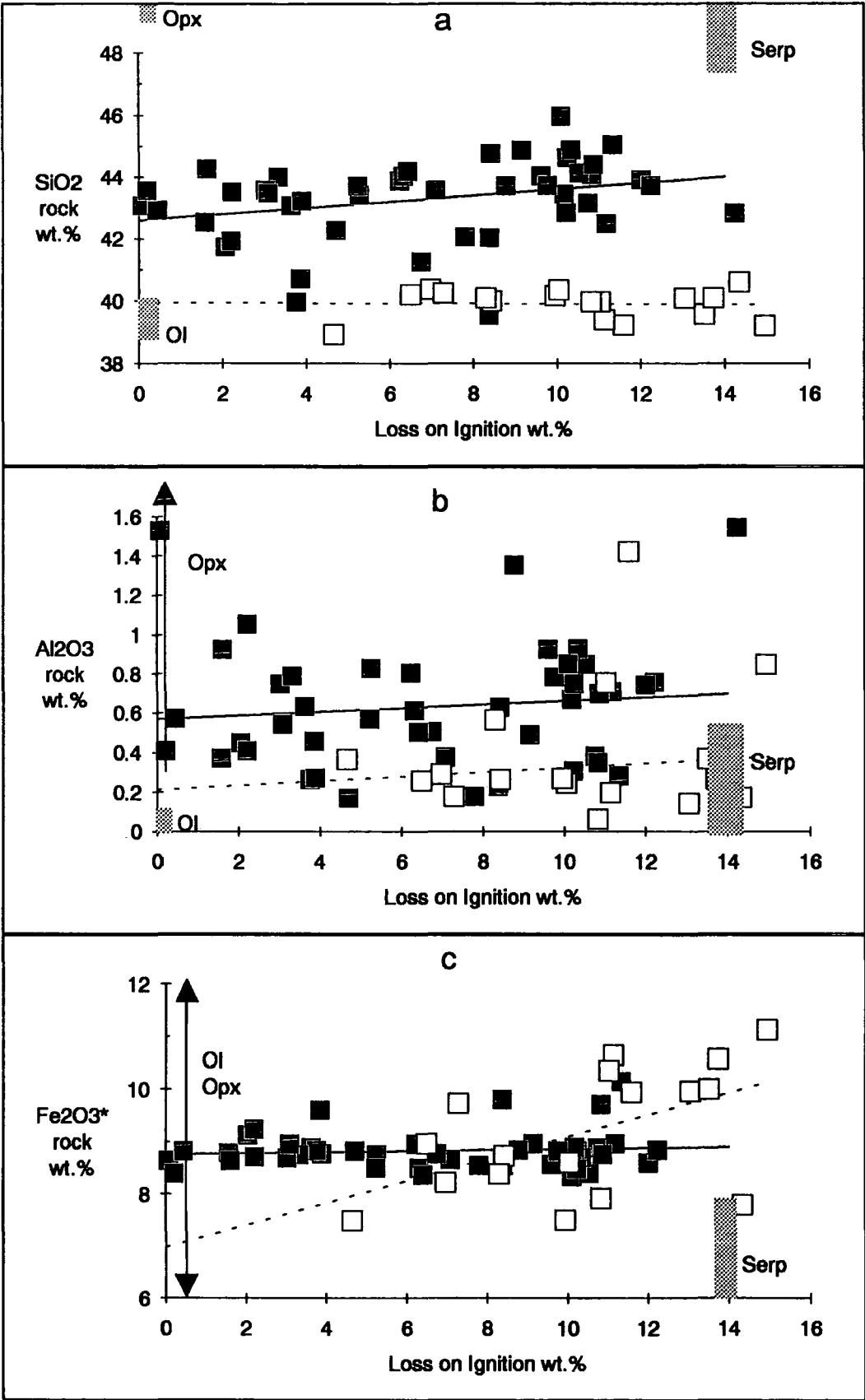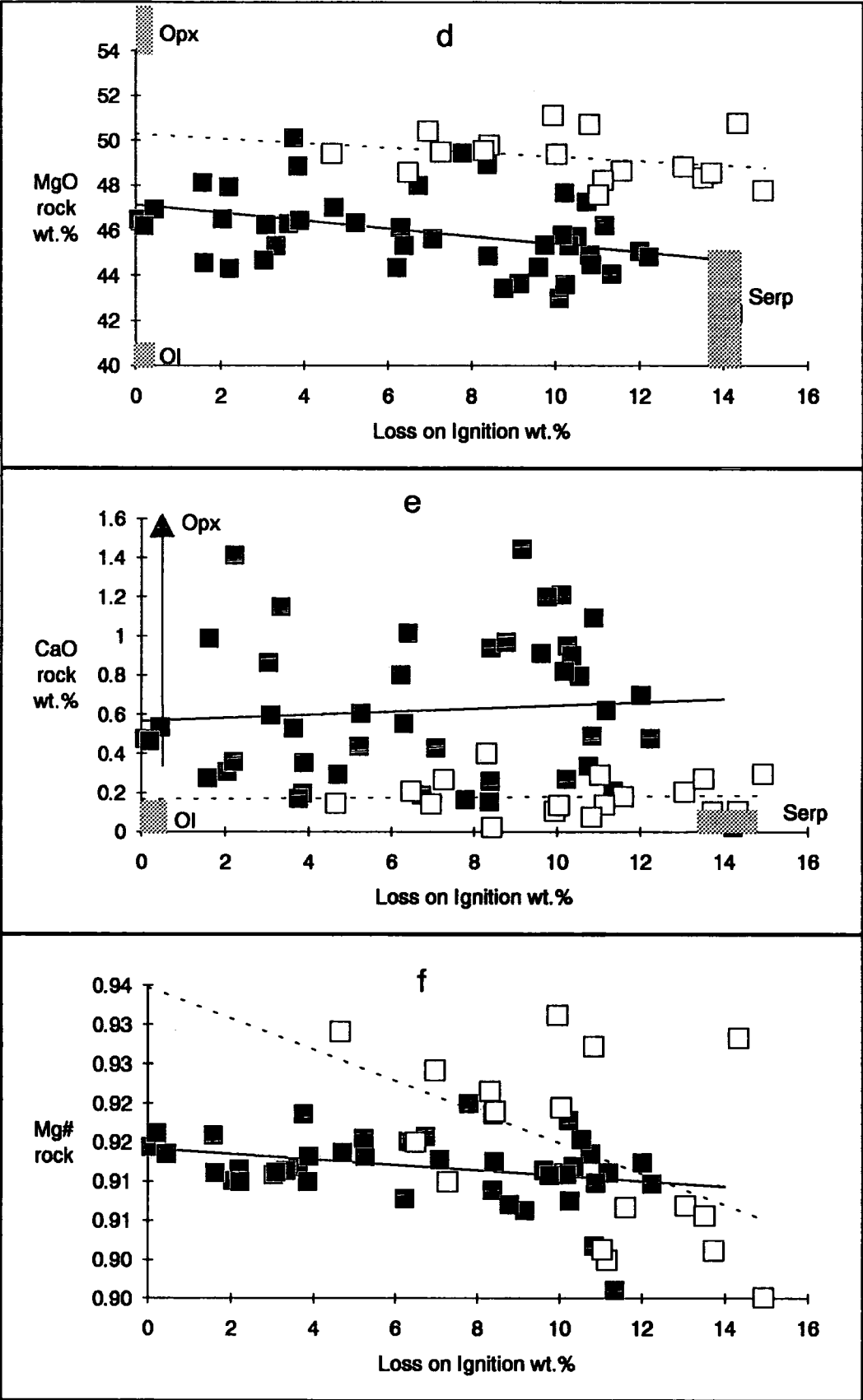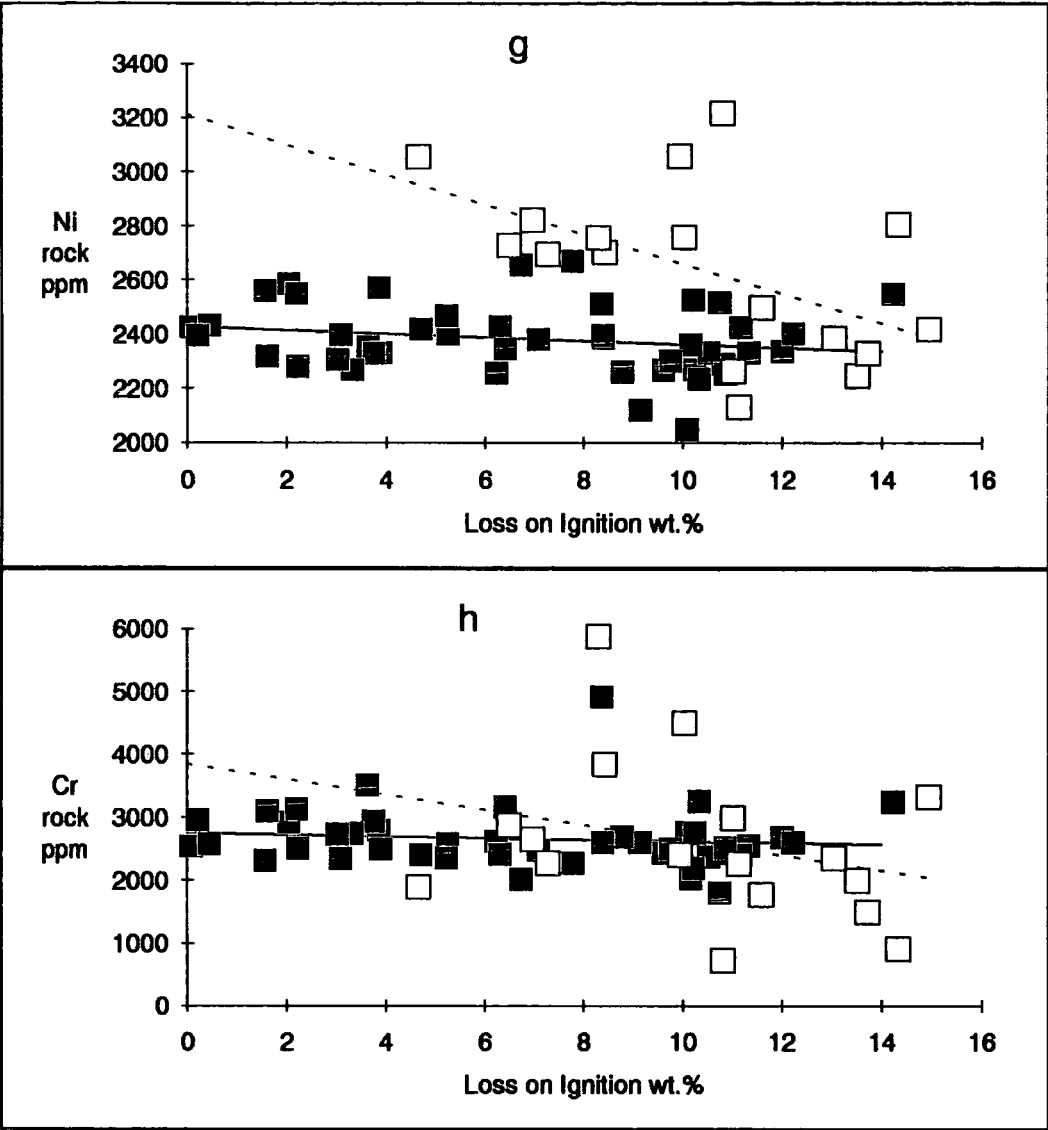
Figure (2.3) Plots of SiO_2, Al_2O_3, total Fe_2O_3, MgO, and CaO wt.% (recalculated volatile-free) and Ni and Cr in ppm against loss on ignition. Filled squares are harzburgites and open squares are dunites. Ol, opx and serp are the approximate compositions of olivine, orthopyroxene and serpentine respectively. The solid lines are the best-fit lines for the harzburgites and the dotted lines for the dunites.

The SiO_2 content of harzburgites shows a small increase (less than 1%) with increasing degree of serpentinization. This trend is expected, since serpentine is more SiO_2-rich (on an anhydrous basis) than olivine. However, dunites show remarkably uniform SiO_2 abundances with no apparent dependence on alteration.

The Al_2O_3 content of harzburgites and dunites shows an almost horizontal trend, suggesting that serpentinization does not affect this element.

The trend for Fe_2O_3(tot) is horizontal for harzburgites, but shows an addition trend for dunites. It will be shown later that this difference stems from the fact that dunites are cumulates of different degrees of fractionation and not the result of serpentinization.

MgO shows a decrease with increasing serpentinization both in harzburgites and dunites, suggesting that MgO is mobilized and removed during serpentinization. The maximum MgO loss of totally serpentinized harzburgite is ~6% relative and of dunites slightly less at ~4% relative.

The CaO abundance of harzburgites is very variable, due to the different modal proportions of ortho- and clinopyroxene in the rocks, but it does not show any obvious addition or depletion trend. Dunites show a much more restricted compositional range and a horizontal trend.

The Mg# of the harzburgites shows a decreasing trend with increased serpentinization. This is the result of the observed MgO loss while Fe_2O_3(tot) remains constant. A decreasing trend is also shown by the dunites, but this has a steeper negative slope, since dunites show an addition trend for Fe_2O_3(tot) as well.

The Ni and Cr contents of harzburgites show horizontal trends. In dunites, however, the overall trends suggest a removal of Ni and Cr with increasing serpentinization. These differences between dunites and harzburgites will be discussed next.

Figure 2.4 is a plot of the Mg# olivine against the Mg# of the whole rock for some dunites. Since dunites consist almost solely of olivine, the close agreement between the whole rock and olivine Mg# strongly suggests that dunites are unaffected by serpentinization. This is also supported by Figure 2.5, which shows that the molecular ratio (MgO+FeO)/SiO_2 of dunites is close to stoichiometric olivine.
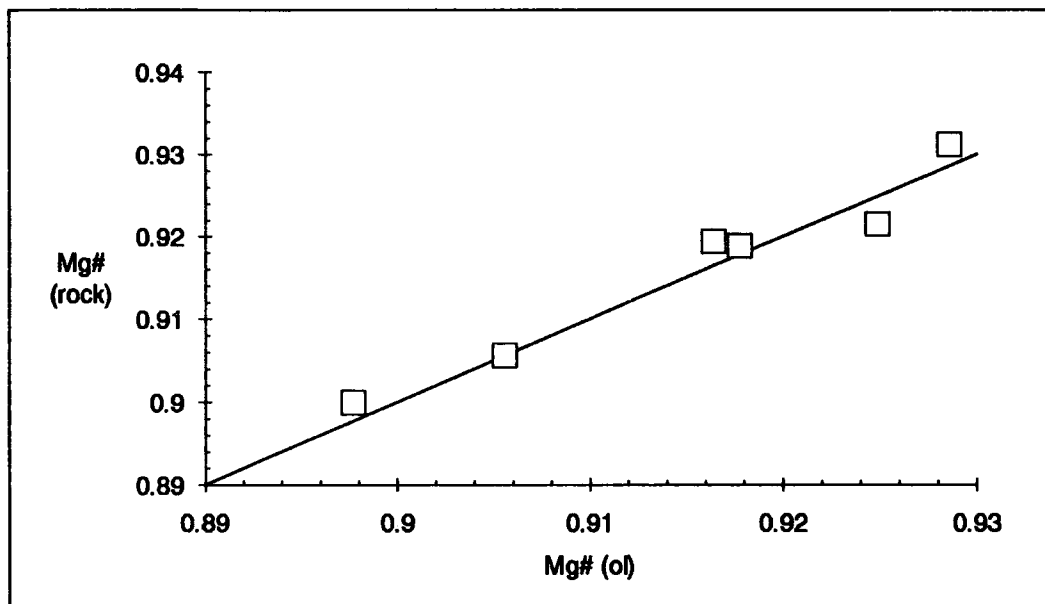
Figure (2.4) Plot of the Mg# of olivine vs. the whole rock Mg# in some dunites. The good agreement with the 1:1 line suggests that the Mg# of the whole rock has remained unchanged by serpentinization.

It will be noted that the elements that show a different behaviour between harzburgites and dunites (Fe_2O_3(tot), Ni, Cr) are also those which are the most affected by fractionation. Since there is no reasonable explanation for these discrepancies, and in view of the evidence in Figures 2.4 and 2.5, it appears that the dunite trends in Figures 2.3c,f,g,h are actually fortuitous, with the more evolved dunites being also the most serpentinized. This assumption is consistent with the apparent behaviour of all elements. The harzburgites, however, show a more restricted compositional range and conclusions can be more confidently drawn.

The only significant change of the harzburgite chemistry has been an increase of SiO_2 and a depletion of MgO that led to a concomitant decrease of the Mg#. The MgO depletion is the result of the hydration reaction of olivine to serpentine:

$$2Mg_2SiO_4 + 3H_2O = Mg_3Si_2O_5(OH)_4 + Mg(OH)_2 \quad\quad (2.6)$$
$$\text{olivine} \quad\quad\quad \text{serpentine} \quad\quad \text{brucite}$$

suggesting that a fraction of the brucite formed was removed by the fluid.

The same reaction also explains the apparent increase of SiO_2 with serpentinization. If MgO is removed from the products of equilibrium 2.6 the system increases its SiO_2 content. Thus, SiO_2 shows an increasing trend with serpentinization not as a result of addition but because it remains immobile.

The stability of Al_2O_3, Fe_2O_3, Cr, and Ni are in agreement with other studies of serpentinized ultramafics that concluded that the main change of the ultramafic chemistry has been the addition of water (Coleman and Keith, 1971). Engin and Hirst (1970) noted a Al_2O_3 depletion and Ni addition in peridotites with H_2O^+ wt.% content higher than ~10%, but this is not evident in Pindos peridotites. Although CaO is generally considered mobile (Loughnan, 1969; Moody, 1976b), there is no evidence of its removal in the Pindos harzburgites. This discrepancy is probably caused by the fact that clinopyroxene, which is the major Ca-bearing phase of these rocks, is very resistant to serpentinization.
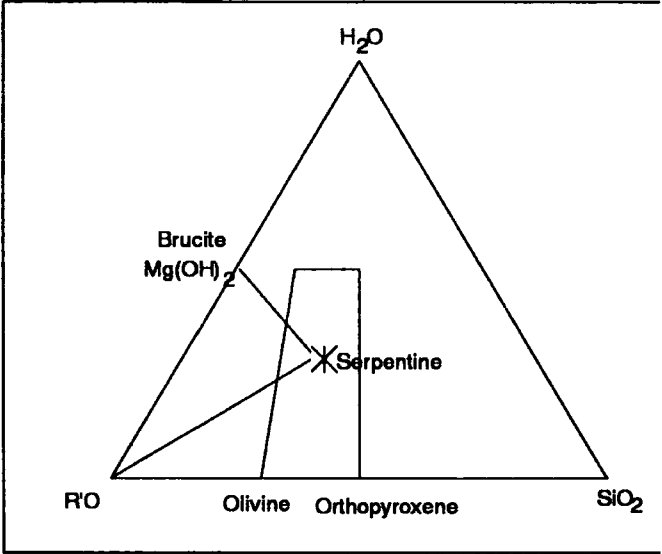
Figure (2.5a) Ternary plot of SiO_2-R'O-H_2O of harzburgites and dunites. R'O=(MgO+MnO+FeO(tot)+ CaO+NiO-Cr_2O_3-Al_2O_3) molecular fractions. Method of projection from Coleman and Keith, 1971)
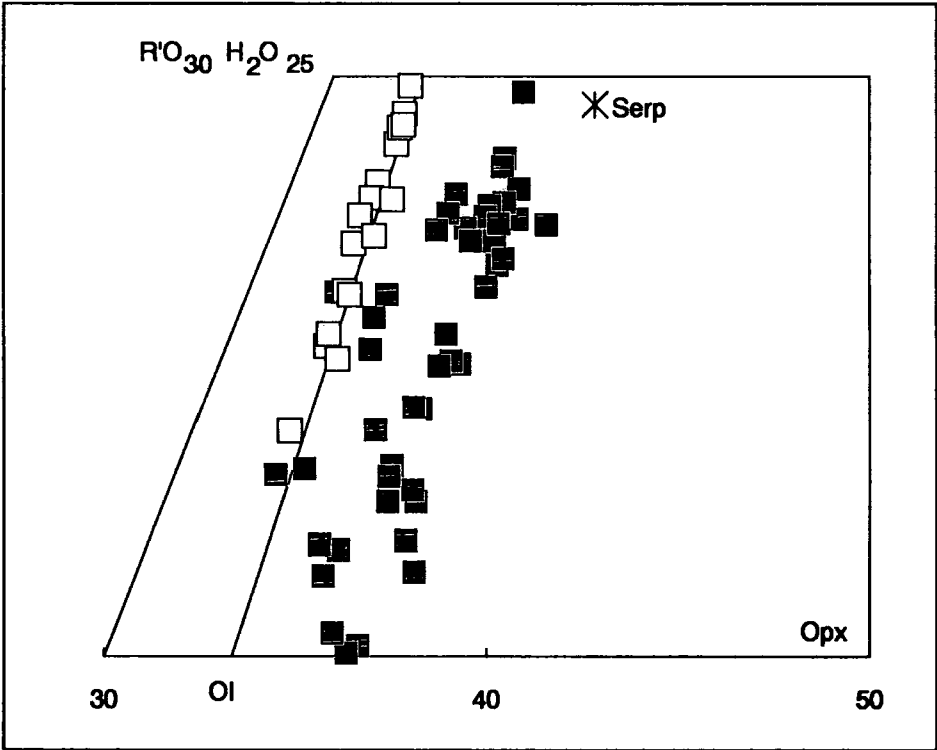
Figure (2.5b) A section of Figure 2.5a in detail. The line marked Ol represents compositions with R'O/SiO_2=2:1, i.e. stoichiometric olivine. The vertical line marked Opx represents orthopyroxene. The star is ideal serpentine composition. The dunites plot close to the Ol line, suggesting that their composition is unaffected by serpentinization.

2.7. The effect of serpentinization on sulphides.

Nickel-iron sulphides and alloys have been observed in most of the harzburgites and cumulate dunites, but they have three modes of occurrence:

i) Sulphides in clinopyroxene-bearing harzburgites from Vovousa, transition zone harzburgites, and cumulate dunites occur mainly interstitially to olivine but also frequently in contact with spinel grains. They consist of pentlandite ± pyrrhotite and their alteration products (magnetite and an unidentified alloy, possibly awaruite). The amount of sulphides present is very small (typically less than 1% but more in some dunites) and their size shows a wide range from ~0.5 mm to less than 0.1 mm.

ii) In addition to these samples, virtually every rock bears minute (a few tens of microns but very variable) sulphides found in the network of serpentine veins produced during serpentinization. Note that the reference to serpentine veins here does not signify the morphologies described in the early part of this Chapter but rather the network of serpentine that develops even in the least altered rocks around the silicate minerals. This is also the location where magnetite formed during serpentinization is concentrated (see Plate 2.2)

iii) Finally, sulphides are frequently found as inclusions in olivine and orthopyroxene, and porphyroclasts of these minerals frequently have abundant fluid inclusions with which euhedral crystals of sulphides are associated. The size of these sulphides is the same as that of type ii.

Eckstrand (1975) examined in detail the minor and trace opaque minerals that occur in serpentinized rocks. In this study he derived a general model for the occurrence of these minerals in terms of oxygen and sulphur fugacity as they are controlled by the large scale silicate reactions (Table 2.6, Figure 2.6). Eckstrand (op. cit.) described two modes of occurrence for the nickeliferous opaque minerals. The first is as disseminated intercumulous blebs with size of 1 mm and the second as smaller, finely disseminated grains dispersed throughout the serpentinized peridotite. His interpretation of the latter was that they represented nickel that was released after the breakdown of magmatic silicates. The general

equation that Eckstrand (1977) derived to describe the loss of sulphur during serpentinization is:

$$8FeS + Fe_{4.5}Ni_{4.5}S_8 + 8O_2 = 2.22\, Fe_3O_4 + Fe_{5.5}Ni_{3.5}S_8 + 1/3\, FeNi_3 + 4\, S_2 \qquad (2.7)$$
$$\text{po} \qquad \text{pn} \qquad\qquad \text{mg} \qquad \text{pn} \qquad\quad \text{aw}$$
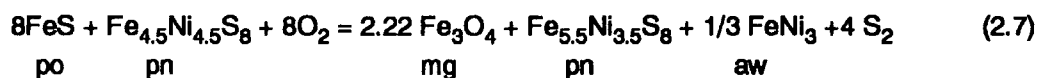
which best approximated the observed proportions of the products. As mentioned earlier, serpentinization in Fe-bearing assemblages is a redox reaction. The oxidation of the iron in silicates to magnetite produces a reducing H_2 front that controls the redox state of the small-sized sulphide assemblages. It will be noted that his is the redox state of the fluid-rock system and is distinct from the magmatic redox state of the rock (Chapter 3, oxygen geobarometry). As the nature of the fluid changes (e.g. by introduction of CO_2 from country rocks) the sulphide-oxide assemblage changes to that stable at the new conditions.

Zone	Silicate assemblage	Opaque assemblage	f_{O_2}	f_{S_2}
1	serpentine + relict olivine (0-75%) [H_2O front producing H_2]	mt + pn + aw	low	low
2	serpentine	a. mt + aw + hz b. mt + hz c. mt +-pn+-hz	intermediate	intermediate
3	talc + magnesite [CO_2 front producing O_2]	mt +pn+-hz+-ml	high	high
4	talc + magnesite	mt +hz+-pn	intermediate	intermediate
5	country rock	po+sp+cp+-py	low	low

Table (2.6) The opaque mineral assemblages and their relation to the serpentinite host. (Eckstrand, 1975). mt=magnetite, aw=awaruite, pn=pentlandite, po=pyrrhotite, hz=heazlewoodite, ml=millerite, cp=chalcopyrite, py=pyrite

-
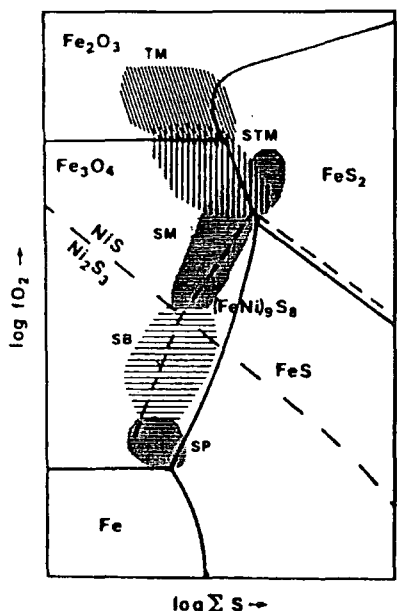
Figure (2.6) Log f_{O_2} - log ΣS diagram showing the stability fields of Fe-Ni sulphides and oxides and associated silicate or carbonate rocks. The shaded regions represent partially serpentinized peridotite (SP), serpentinite ± brucite (SB), serpentinite-magnesite (SM), serpentinite-magnesite-talc (STM, and talc-magnesite (TM). From after Eckstrand (1975).

The mode of occurrence of the sulphides in Pindos is consistent with this model. Type (i) sulphides are magmatic although of different origins. The sulphides in the clinopyroxene-bearing harzburgites are residual mantle sulphides after extraction of S-saturated magma (see Chapter 4, sulphur in the mantle). The sulphides in the transition-zone harzburgites and dunites represent droplets of immiscible sulphide melt that impregnated the harzburgites or were trapped in the intercumulous melt fraction of settling olivine crystals.

Type (ii) sulphides are the products of the alteration and redistribution of type (i) sulphides during interaction with the serpentinizing fluids. At least some of the Ni and/or Fe of these sulphides was probably supplied by the breakdown of olivine. The silicate and sulphide assemblage correspond to Zones 1 and 2 of Table 2.6, suggesting low to moderate oxygen fugacities and low sulphur fugacities.

The mode of occurrence of type (iii) sulphides suggests that they have a different history than that of types (i) and (ii). They were probably included in the porphyroclasts during recrystallization of the peridotites (see Chapter 3, rock textures), but their origin is uncertain. Their association with fluid inclusions suggests that they were distributed by a fluid phase, but whether this phase just promoted the redistribution of residual sulphides or was itself a S-rich fluid cannot be ascertained.

2.8. Summary

The textural evidence and the scarcity of high-temperature hydrothermal minerals suggest an environment of rapidly decreasing temperature for the serpentinization of the Pindos ophiolite. Interaction with fluid may have started at a temperature as high as 640°C and seawater was probably involved at that stage. Serpentine formation may have started at 300 to 350°C, depending on pressure, and continued until emplacement. The most common alteration assemblage is serpentine + magnetite ± brucite. In common with most ophiolites the dominant serpentine polymorph is lizardite. The presence of sheared serpentine indicates that at least some of the serpentinization was syntectonic and, by analogy with other ophiolites, may have included meteoric water.

For the majority of the rocks serpentinization was not complete and different minerals were variably affected, olivine being the most susceptible to alteration, followed in this respect by orthopyroxene, clinopyroxene and spinel. Except for the introduction of water and the removal of MgO the major element chemistry of the ultramafics has remained unchanged. In contrast to evidence of other studies, CaO loss was prevented by the resistance of clinopyroxene to alteration.

The serpentinizing fluids have affected the original Fe-Ni sulphide assemblages present in some rocks. Sulphur loss and oxidization has produced sulphur-poor and oxide assemblages while redistribution of the Ni and Fe of the silicates was taking place.

Chapter 3. Peridotite chemistry

3.1. Mineral habit

The predominant lithology of the Pindos mantle sequence is harzburgite. It consists mainly of forsterite olivine with variable amounts of enstatite pyroxene (see Table 3.1) and accessory but ubiquitous spinel (~1-2%). Clinopyroxene is sometimes present as distinct grains but the majority of the harzburgites lack free clinopyroxene except as exsolution in orthopyroxene grains. Recrystallization and tectonic fabrics are the norm in the harzburgites but the majority of the rocks have suffered serpentinization, which has obliterated most of their primary characteristics. The mode of occurrence and characteristic of the minerals will be described below. The terminology follows that of Mercier and Nicolas (1975).

3.1.1. Olivine

Olivine forms the groundmass in harzburgite, constituting 72-94% of the peridotite mode (Table 3.1), and occurs as two types of grain: i) porphyroclasts and, ii) neoblasts. The former are large (2-4 mm) grains, irregularly shaped, with curved or serrated boundaries that are often elongated as a result of stresses (Plate 3.1). They exhibit undulose extinction, indicating that lattice strain has taken place. Subgrains or deformation lamellae parallel to (100) are often formed and they give the grains a patchy or striped appearance under cross polarised light. Neoblasts are small (<0.5 mm) grains that are developed during recrystallization. They have straight to curvilinear margins and definite triple points between grains with 120° grain boundaries. Subgrains and deformation lamellae do not form in neoblasts, which have normal extinction (Plate 3.2). Sometimes neoblasts form sub-parallel bands that traverse the thin section or define a network around olivine and pyroxene porphyroclasts (Plate 3.12). Both types are usually found in a single thin section at varying proportions. Complete recrystallization of olivine to neoblasts is not rare, but there are usually some relict olivine or orthopyroxene porphyroclasts.

Sample	Olivine	Orthopyroxene	Clinopyroxene	Spinel
dr34	83.1%	11.3%	3.9%	1.7%
kk8812*	91.2%	3.4%	3.7%	1.8%
dr3*	89.7%	5.0%	3.6%	1.7%
dr9*	92.1%	2.8%	3.3%	1.8%
kk8820*	91.6%	4.2%	2.8%	1.3%
si43	77.9%	17.9%	2.8%	1.4%
dr23	91.1%	5.9%	1.7%	1.3%
ag2	79.6%	19.4%		1.0%
ag3	84.0%	14.6%		1.4%
bak1	84.5%	13.9%		1.5%
bo13	72.2%	26.3%		1.5%
dr42	89.6%	8.9%		1.5%
li8811	94.1%	4.4%		1.5%
li8816	66.7%	32.5%		0.8%
li8821	93.5%	5.3%		1.2%
li8826	89.7%	8.4%		2.0%

Table (3.1) Modal compositions of selected Pindos ultramafics. The compositions were calculated by least-squares fitting (minimisation of residuals) of whole-rock and mineral analyses. Samples marked with asterisk are transition zone harzburgites that have probably been affected by melt impregnation.

3.1.2. Orthopyroxene

All orthopyroxene in Pindos mantle rocks is enstatite and it constitutes 5-30% of the peridotite mode (Table 3.1). In thin section it is colourless, with straight extinction, low interference colours and high relief, which gives it the appearance of "floating" in a groundmass of olivine. It exhibits a good cleavage parallel to (110) and a less well developed one at right angles (010). It also frequently exhibits clinopyroxene exsolution lamellae parallel to (110) or, less frequently, exsolved clinopyroxene blebs. In common with olivine, orthopyroxene also occurs as porphyroclasts, or neoblasts. Orthopyroxene porphyroclasts are large (2-5 mm) grains that occur as isolated grains (Plate 3.3) or in clusters (Plate 3.4). If a rock has a well defined foliation, this is evident in thin section by the rough alignment of the orthopyroxene in bands that traverse the thin section.
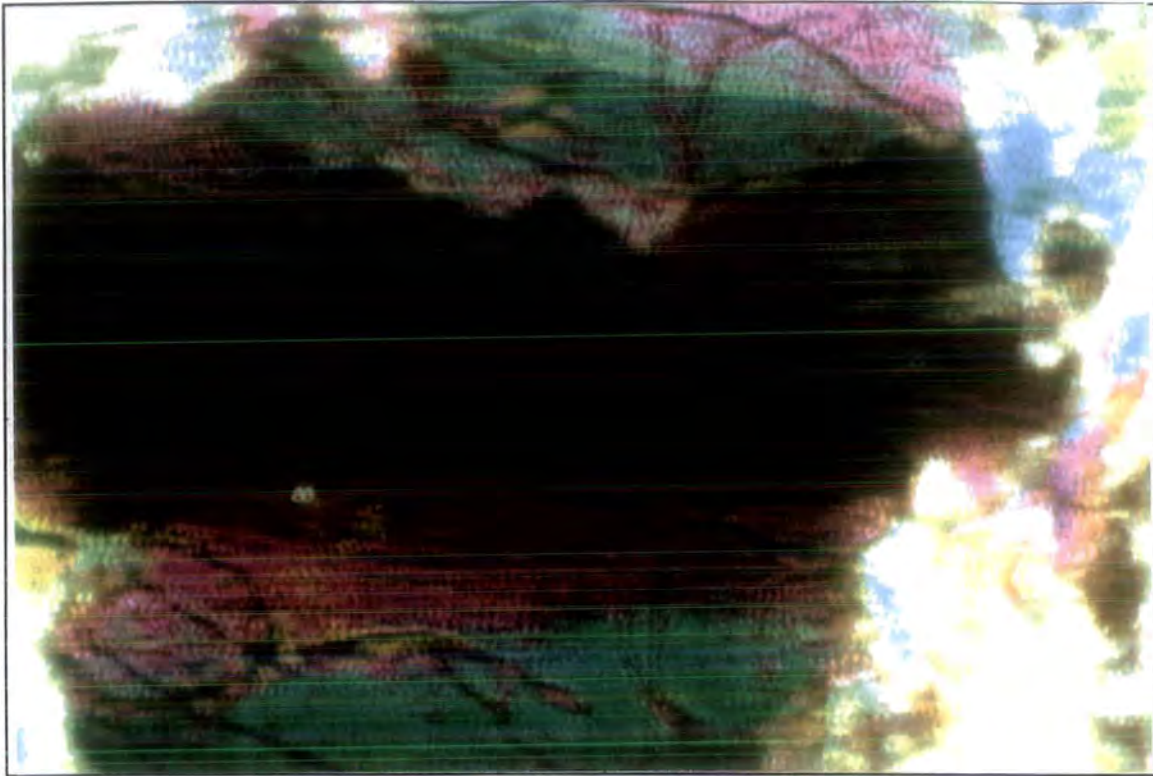
Plate (3.1) Olivine porphyroclast with deformation lamellae. Crossed nicols, field of view 1.3 mm.
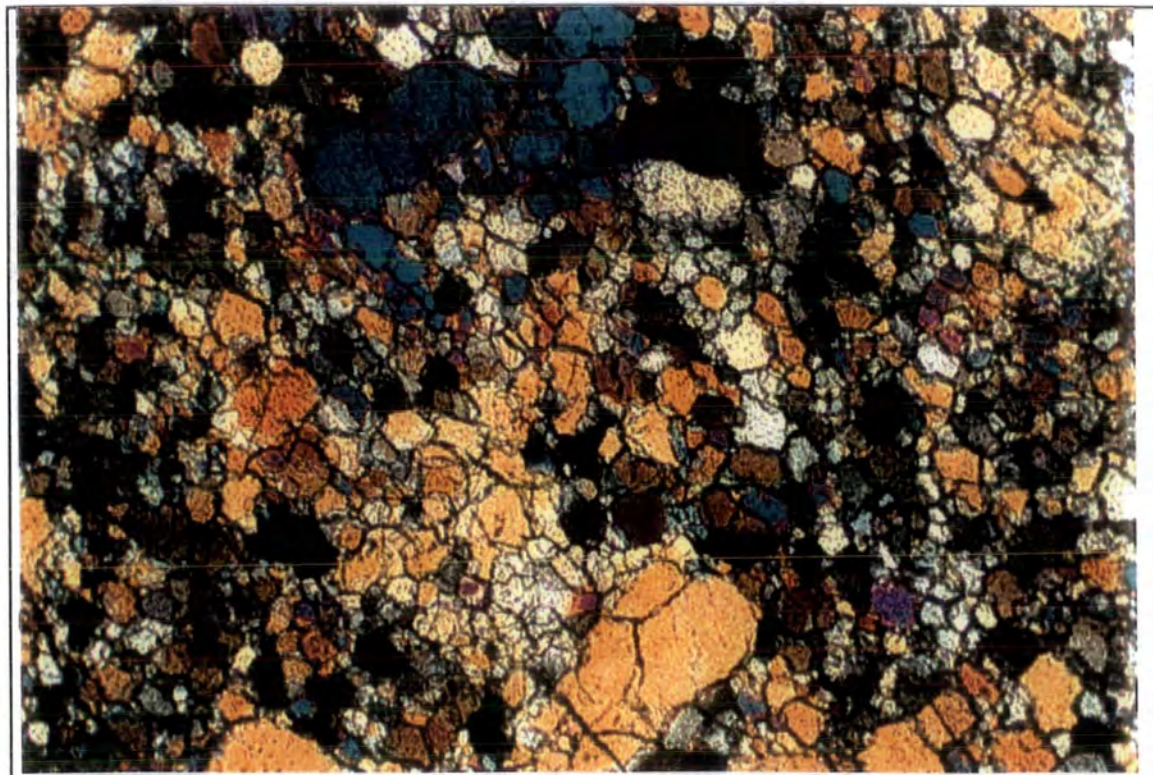
Plate (3.2) Recrystallized olivine neoblasts, lacking evidence of strain, and interstitial chromite. Note remnant olivine porphyroclasts in the upper and lower parts of the picture. Crossed nicols, field of view 1.3 mm.

Plate (3.3) Retort-shaped orthopyroxene porphyroclast with kinked cleavage and clinopyroxene exsolution lamellae. The lower right part of the crystal has slid and enclosed part of an olivine porphyroclast. Crossed nicols, field of view 3 mm.
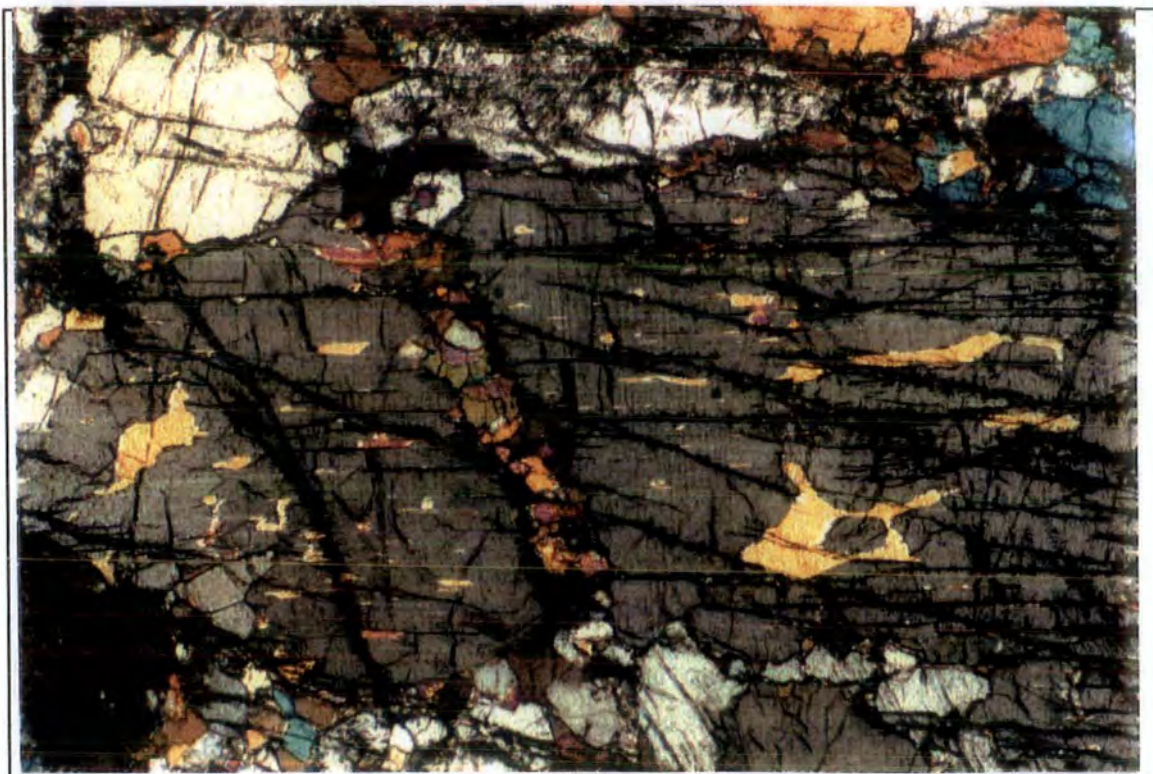
Plate (3.4) Part of a cluster of orthopyroxene porphyroclasts shown in Plate 3.7. Note clinopyroxene in exsolved blebs and recrystallized band. Crossed nicols, field of view 3 mm.
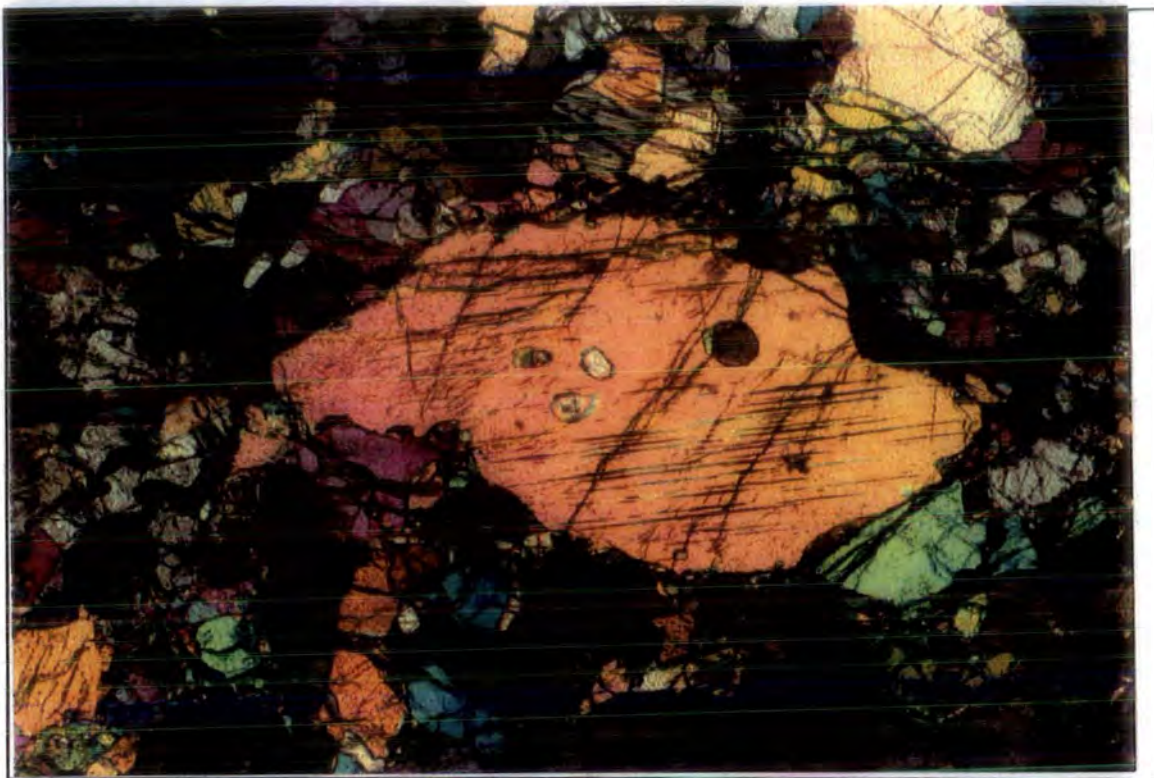
Plate (3.5) Clinopyroxene porphyroclast with orthopyroxene exsolution lamellae and round olivine inclusions. Crossed nicols, field of view 3 mm.
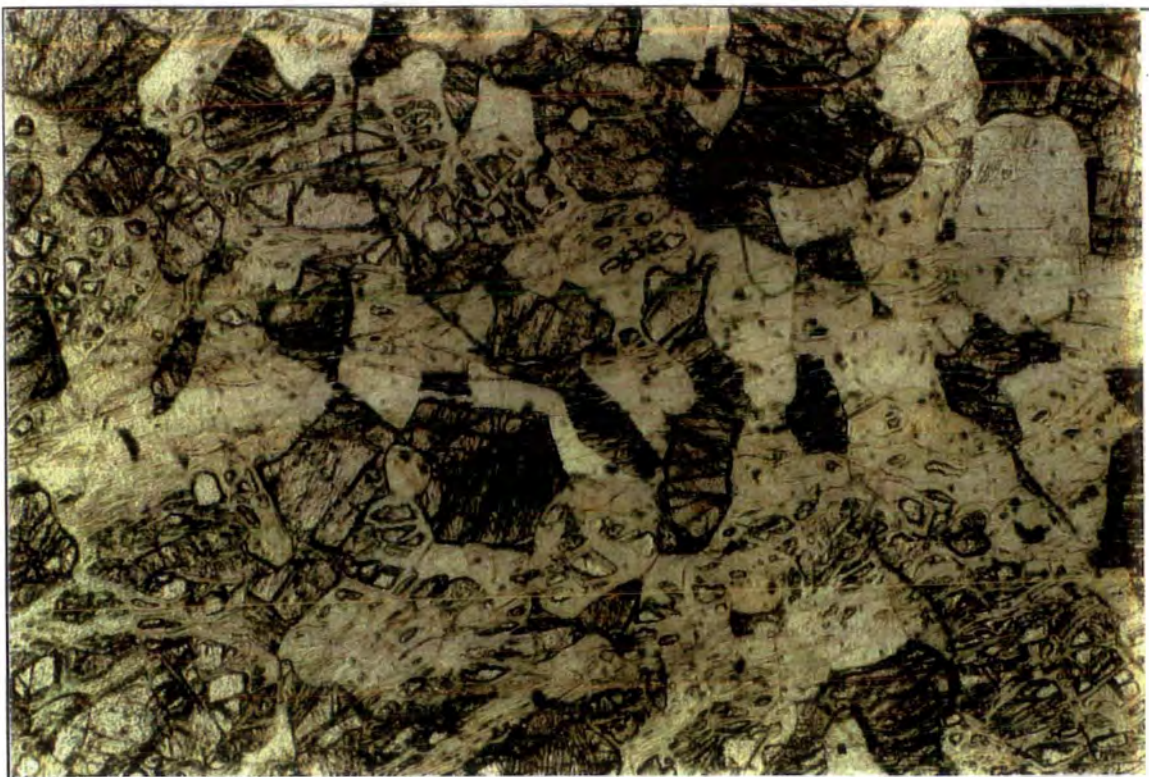
Plate (3.6) Interstitial clinopyroxene (high relief) and plagioclase between olivine grains (now serpentinized) in dunite. Plain polarized light, field of view 3 mm.
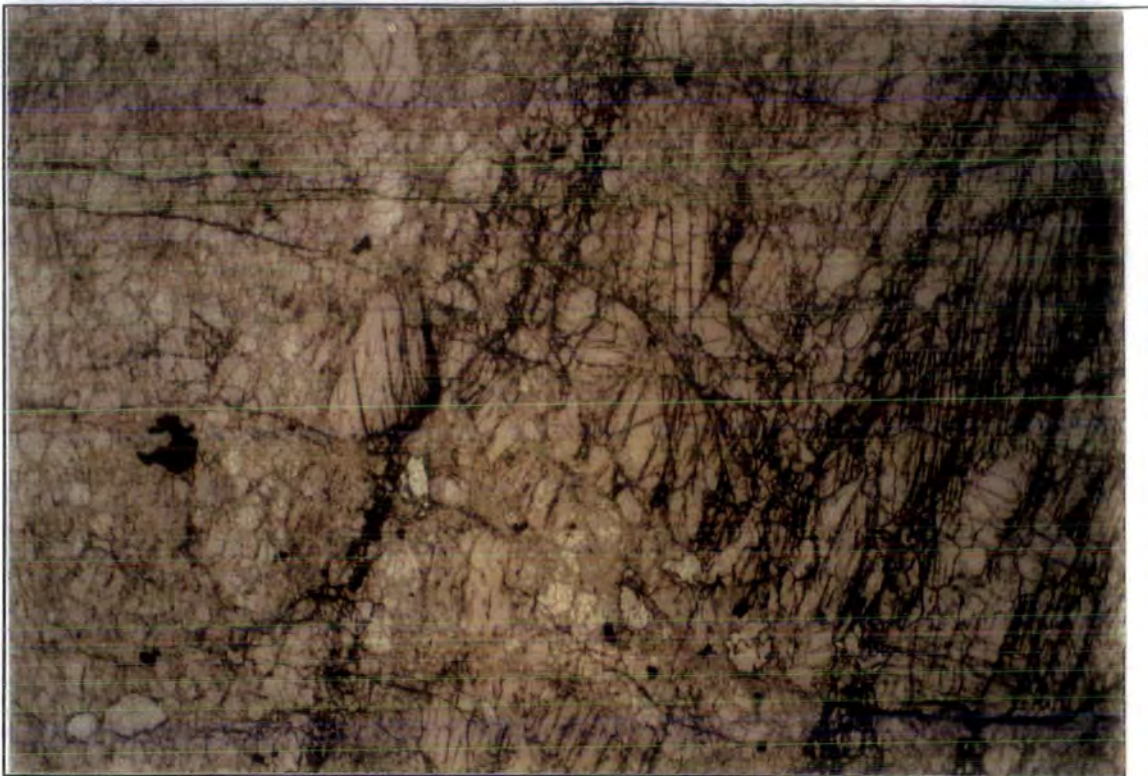
Plate (3.7) Wide range of spinel shapes and sizes down to less than 0.1 mm. The central part of the picture is occupied by a cluster of orthopyroxene porphyroclasts (high relief). Plain polarized light, field of view 13 mm.
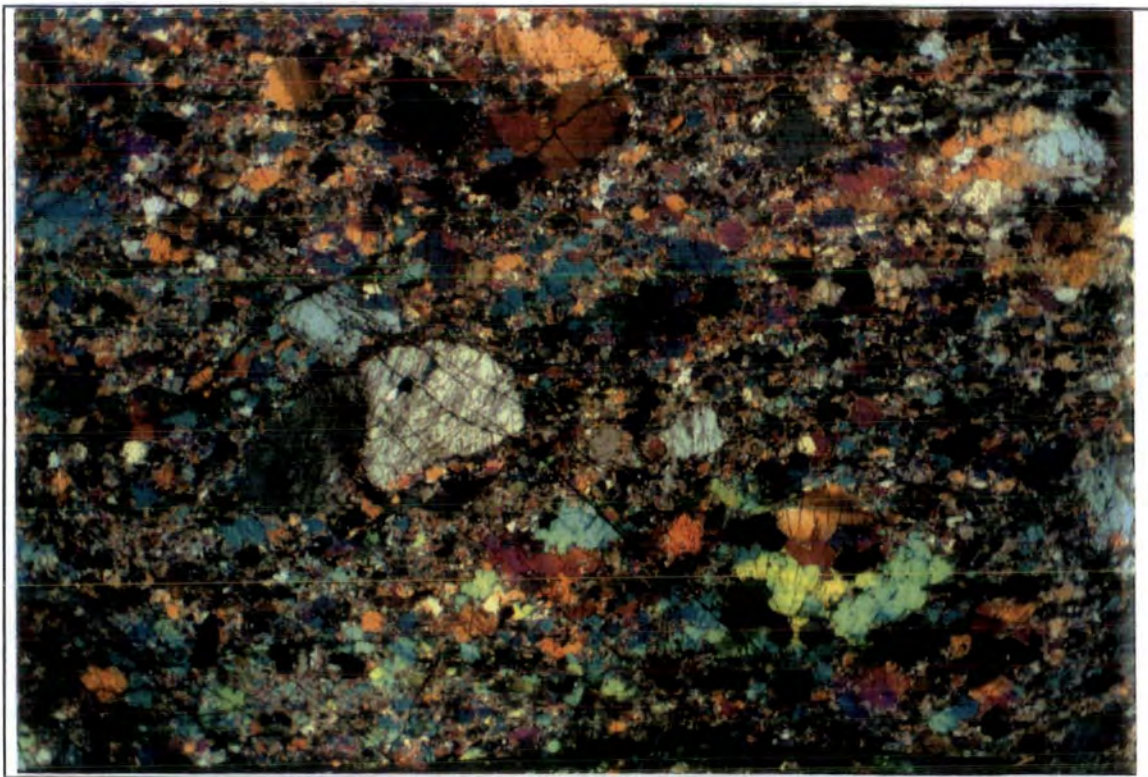
Plate (3.8) Alignment of spinels (black) parallel to the foliation. Crossed nicols, length of view 13 mm.
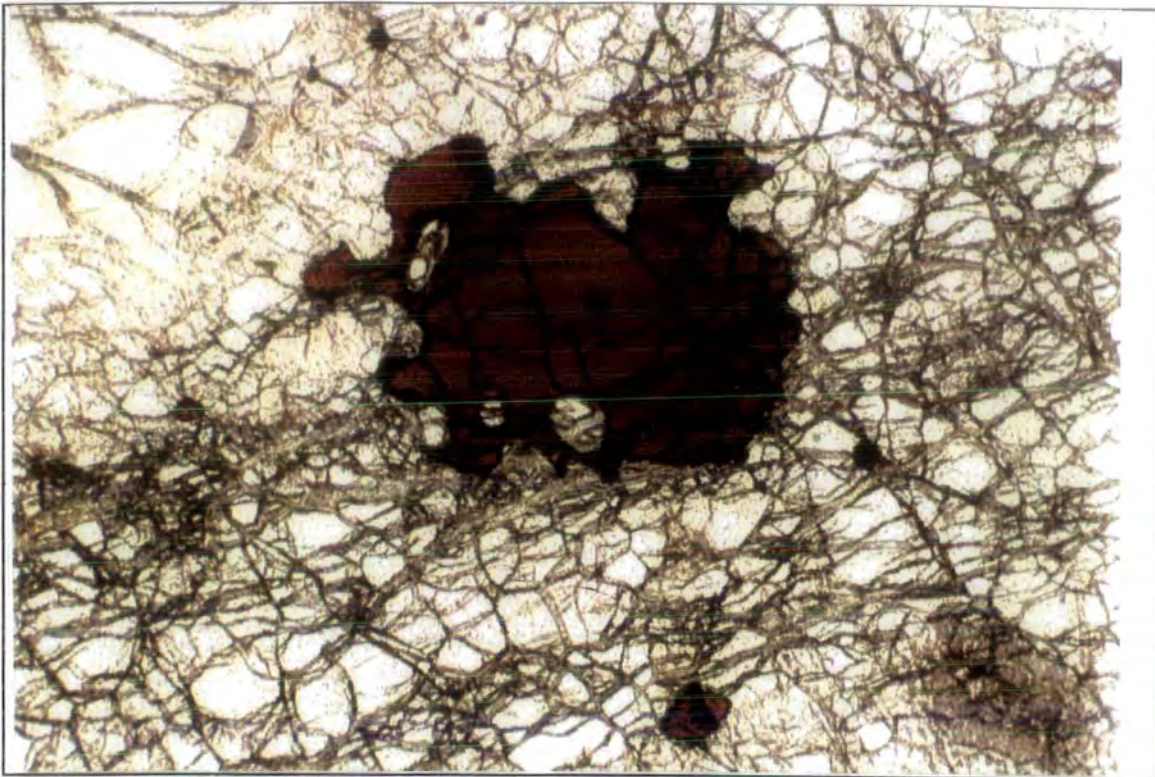
Plate (3.9) Large spinel grain with lobate margins. Plain polarized light, field of view 3 mm.
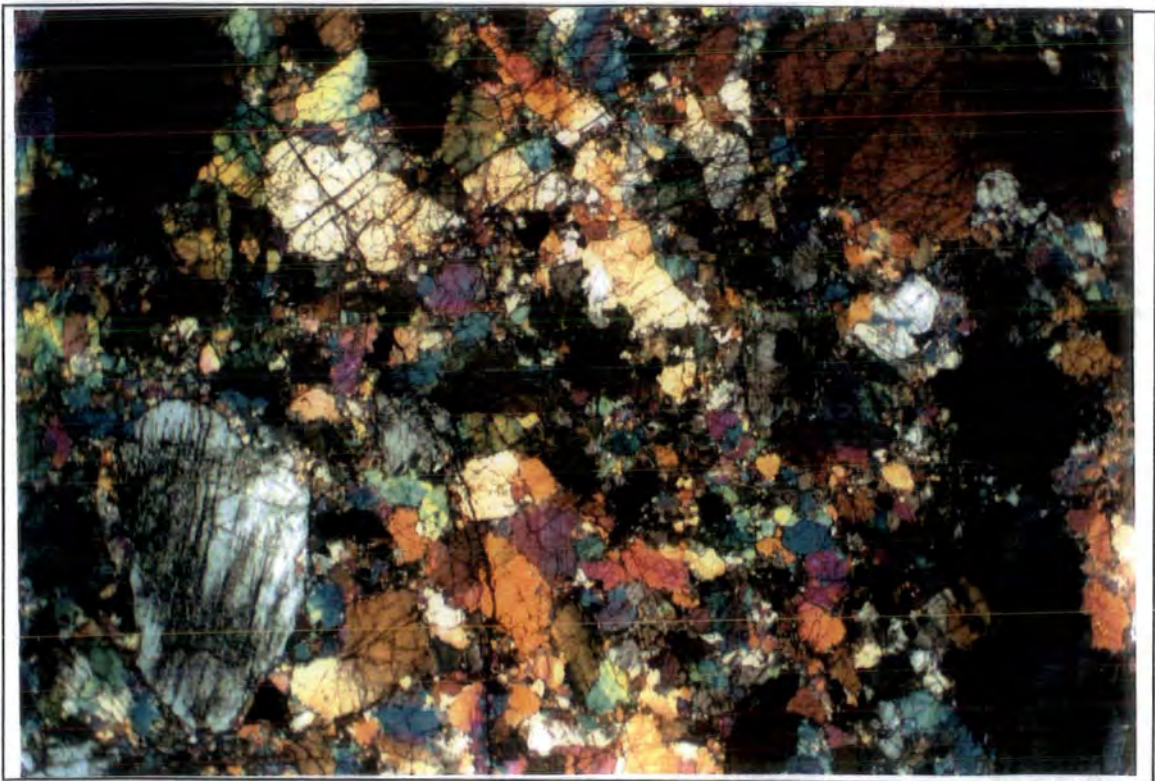
Plate (3.10) Coarse porphyroclastic texture. Crossed nicols, field of view 13 mm.
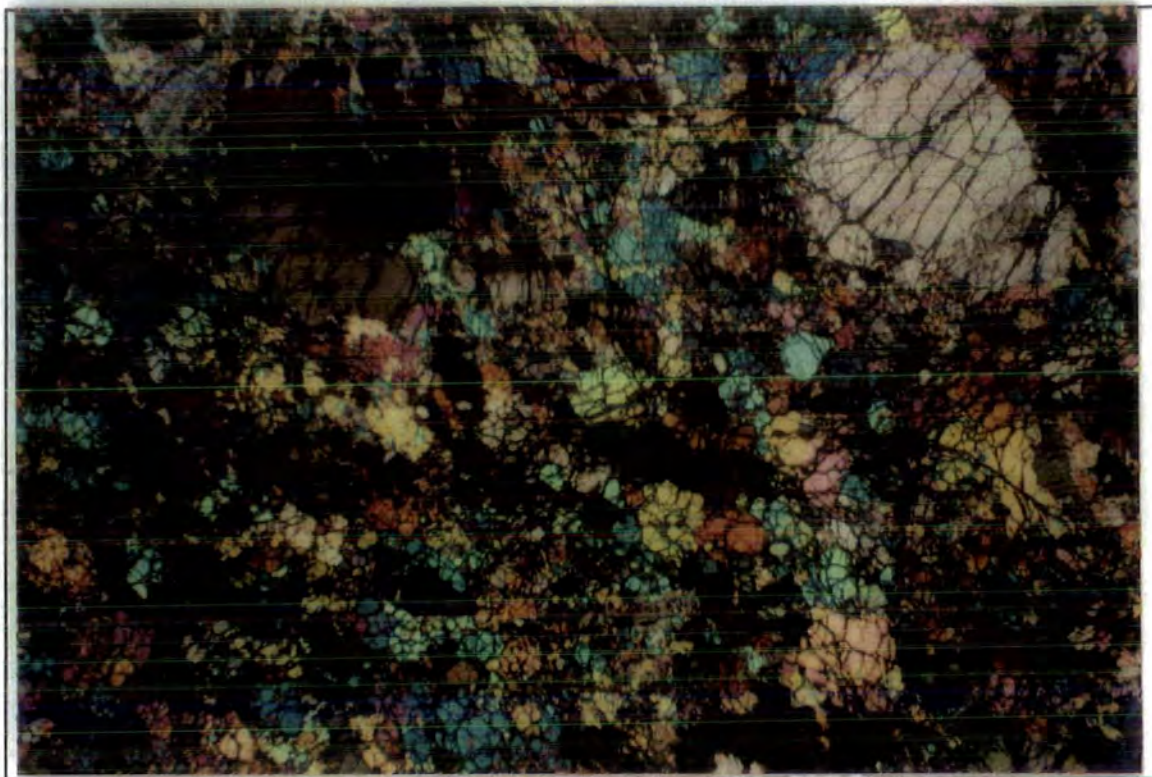
Plate (3.11) Equigranular mosaic texture with relict olivine and orthopyroxene porphyroclasts. Crossed nicols, field of view 13 mm.
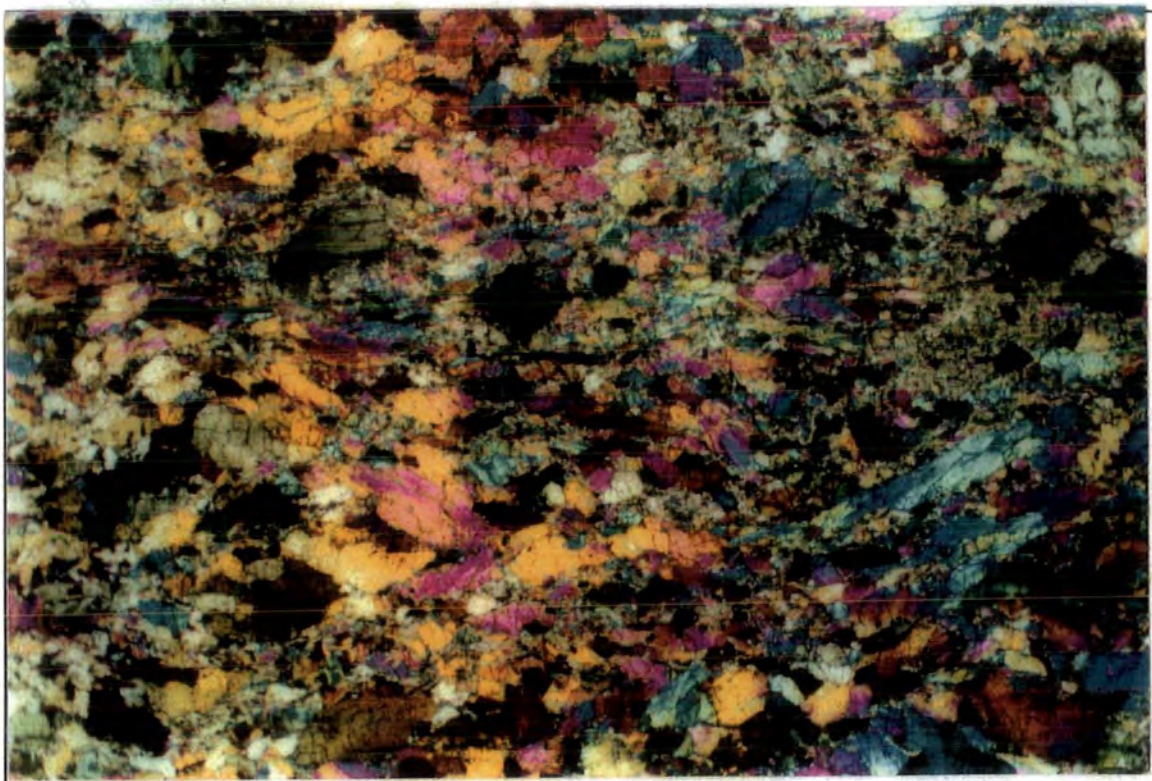
Plate (3.12) Tabular equigranular texture. Crossed nicols, field of view 13 mm.

The porphyroclasts can be tabular, irregular, retort shaped (Basu, 1977) or variably elongated, reflecting the amount of stress a rock has experienced. Lattice strain is evident in almost every sample, manifested in curved cleavage, undulose extinction, kink bands and the formation of subgrains. Clinopyroxene exsolution lamellae, when present, are always affected, indicating that exsolution was pre-deformation. Neoblasts are again smaller (<1mm) than porphyroclasts with normal extinction and no clinopyroxene exsolution. They frequently form the margin of porphyroclasts. Unlike olivine, neoblasts of orthopyroxene are seldom the only type of grain present in a thin section since, even in the most tectonized rocks, some relict orthopyroxene porphyroclasts remain.

3.1.3. Clinopyroxene

Clinopyroxene, as already mentioned, occurs chiefly as exsolution in orthopyroxene. Free clinopyroxene grains are present only in samples from Vovousa. In these rocks they form tabular, sub- to anhedral grains (up to 2 mm) that, sometimes, have exsolved orthopyroxene lamellae and evidence of strain (Plate 3.5).

Clinopyroxene is also present in the rocks from the transition zone, but it has a distinctly different appearance. It occurs as irregular grains, interstitial to olivine and is frequently associated with plagioclase (Plate 3.6). It does not exhibit evidence of strain or exsolution and it bears a distinct resemblance to the cumulus poikilitic clinopyroxene.

As mentioned earlier, (see Chapter 1, transition zone) this kind of clinopyroxene represents "frozen" droplets of a melt that impregnated and re-fertilized already depleted peridotite. Additional evidence is provided by the modal composition of the transition zone harzburgites (Table 3.1). The high olivine and low orthopyroxene modal contents of these samples suggest a depleted composition, which is at odds with the relatively high modal proportion of clinopyroxene, especially since harzburgites from other areas have lower olivine and higher orthopyroxene contents (i.e. more fertile), yet have no free clinopyroxene.

3.1.4. Spinel

Spinel is found as small (<2 mm) grains in the Pindos harzburgite. It may be translucent, orange-brown to deep red-brown, or opaque. It mainly occurs as round sub- to anhedral grains, in a wide range of sizes (Plate 3.7), and is mostly located at grain boundaries, not showing any preferred association with olivine or orthopyroxene. Spinels tend to form stringers aligned parallel to the foliation of the rock (Plate 3.8). Large spinels tend to occur as single grains, often with very irregular boundaries (Plates 3.7, 3.9). Smaller spinels tend to occur in clusters of 2-3 grains and have better developed habits, suggesting that these may derive from the recrystallization of large grains. It will be noted that vermicular intergrowths (Mercier and Nicolas, 1975) of orthopyroxene and spinel have not yet been observed in Pindos and that the characteristic "holly leaf" shaped spinels (Mercier and Nicolas, op. cit.) are rather rare.

Mantle tectonite classification		
Mercier and Nicolas (1975)	Basu (1977)	Pike and Schwarzman (1977)
Protogranular	Coarse granular	Allotriomorphic
Porphyroclastic	Porphyroclastic	Porphyroclastic
Equigranular	Equigranular or tabular mosaic	Equigranular mosaic

Table (3.2) Correlation of peridotite textural type and classification between different studies.

3.2. Rock textures

There are various systems of nomenclature for mantle metamorphic rocks (Mercier and Nicolas, 1975; Basu, 1977; Pike and Schwarzman, 1977) based on studies of ultramafic upper mantle xenoliths. Table 3.2 lists the most common textures encountered in these xenoliths and how they correspond between different classifications. The different categories reflect the slightly different interpretations for the origin of the textures, it will be noted,

however, that the xenolith suites used in these studies are from different locations and may correspond to dissimilar processes in the upper mantle.

The main textural elements of the Pindos harzburgites are:

A small number of samples preserve coarse grains (of all minerals) with lobate and cuspate boundaries (Plate 3.9). These samples have been observed mostly in peridotites from Vovousa. This texture is attributed to resorption or dissolution-reprecipitation creep (Spry, 1969), which may be promoted by the presence of melt during deformation acting as an medium for dissolution at pressure points and for re-precipitation in areas of reduced stress (Dick, 1979). This texture is, therefore, interpreted as partial melting texture and corresponds to the protogranular texture of Mercier and Nicolas (1975).

The majority of the samples (>90%) are characterized by deformation and recrystallization of the minerals. Coarse porphyroclastic textures are the first to be developed (Plate 3.10, Mercier and Nicolas, 1975). These are replaced by recrystallization with fine-grained textures that, almost always, preserve remnants of porphyroclasts (Plate 3.11, equigranular mosaic texture of Mercier and Nicolas, 1975). Frequently such rocks show elongation and sub-parallel orientation of the minerals (tabular mosaic texture of Basu, 1977).

The textures described above correlate with the rock fabrics in the field (see Chapter 1, Mantle sequence). Thus, peridotites with no or very weak foliation in the field have coarse-grained, weakly strained textures that indicate high temperature flow (1200°C Mercier and Nicolas, 1975). As deformation increases in intensity, strongly foliated rocks with decreasing porphyroclast size are formed. At the end remains a completely recrystallized rock wholly composed of fine-grain neoblasts.

3.3. Mineral chemistry

The silicate minerals of the Pindos ultramafic rocks (olivine, orthopyroxene, clinopyroxene) are highly magnesian and depleted in magmaphile elements, they show, however, compositional variations that are significant to the melting history of the peridotite. Their characteristics will be described below and will be compared to those of other ultramafic rocks from known geotectonic settings.

3.3.1. Olivine

The forsterite content of olivine in the harzburgites varies from 89.4 to 91.6 with an average of 90.8. The dunites have a higher average of 91.3 and show a larger variation from 89.8 to 92.9. In Table 3.3 this compositional range is compared with olivine from other Alpine peridotites. It can be seen that Pindos olivines are amongst the most magnesian, with Papuan olivines being the most refractory of all peridotites. It also displays a relatively wide range of compositions, compared to Lizard, Troodos, and Burro Mountain, as do olivines from Josephine, Oman, and Papua. The Bay of Islands ophiolite shows the most wide range of olivine compositions, because it includes fertile spinel lherzolites (Roberts, 1986).

The Cr_2O_3 and MnO wt.% contents of olivine vary from below the detection limit to maxima of 0.22 wt.% and 0.31 wt.% respectively, while NiO varies from 0.15 to 0.55 wt.% and shows a systematic relation with the forsterite fraction of olivine. In Figure 3.1 the Mg/(Mg+Fe) ratio (Mg#) in olivine is plotted against its Ni ppm content. The olivines from harzburgites show some scatter, which is probably due to analytical error, but show a relatively restricted range of Ni contents which consistent with a partial melting trend shown in the diagram. The Ni content of olivines from dunites shows a wider variation as well as much smaller values. Because of the high distribution coefficient of Ni in olivine (e.g. Hart and Davis, 1978) even a small amount of olivine crystallization will quickly deplete the melt in Ni. For example, Sato (1977) calculated that a primitive mantle-derived melt that crystallizes 10% olivine will reduce its Ni content by 50%. Thus the Ni content of dunites is consistent with their being cumulates of various degrees of fractionation precipitated from primitive melts.

Peridotite	Location	Forsterite range	Source
Lizard	Cornwall	89.1 - 91.0	Kirby (1979)
Burro Mountain	California	91.1 - 91.4	Loney et al. (1971)
Troodos	Cyprus	90.7 - 91.2	Greenbaum (1972)
Bay of Islands	Newfoundland	87.8 - 92.2	Roberts (1986)
Papua	Papua, New Guinea	91.6 - 93.6	England and Davies (1973)
Josephine	Oregon	89.5 - 91.2	Dick (1977)
Semail	Oman	89.2 - 91.7	Brown (1982)
Pindos	NW Greece	89.4 - 91.6	This study

Table (3.3) Range of olivine compositions for some Alpine peridotites.
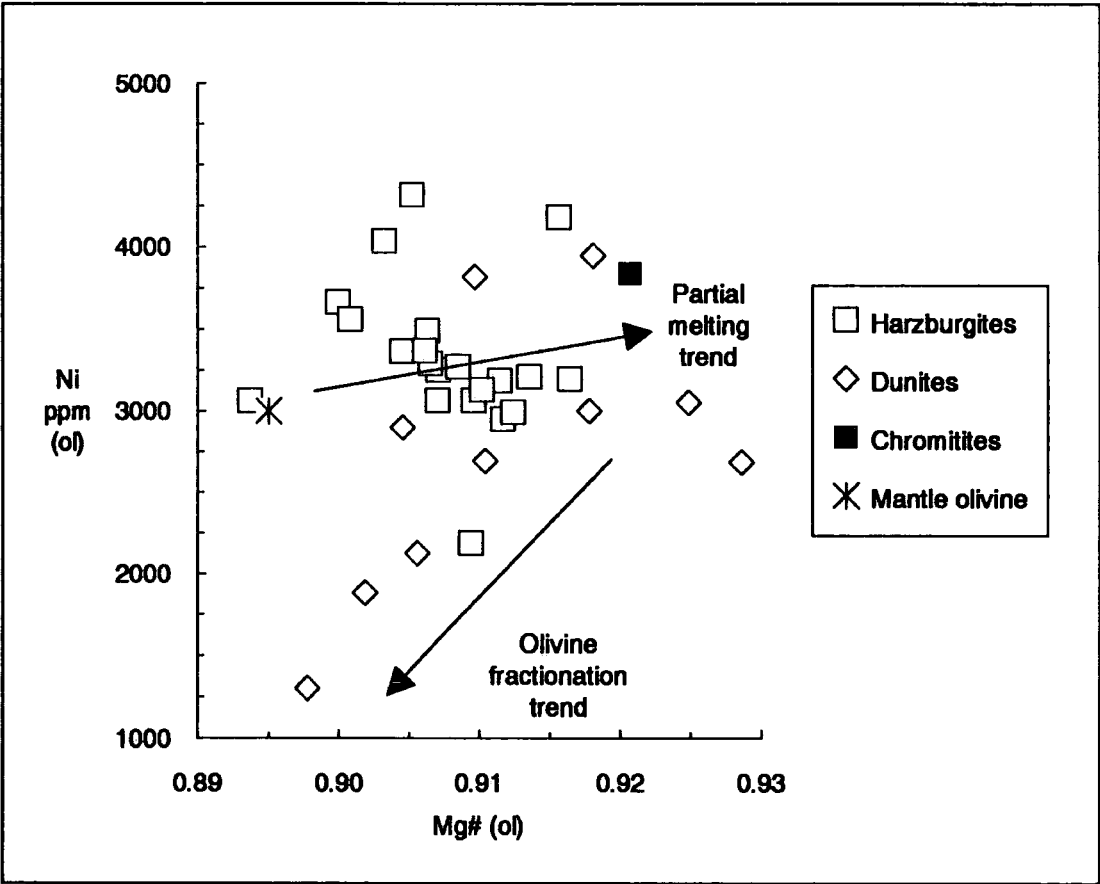
Figure (3.1) Ni (ppm) vs. Mg# in olivine. Mantle olivine composition from Sato (1977).

3.3.2. Orthopyroxene

Orthopyroxene in the Pindos harzburgite ranges in composition from $Wo_{0.8}En_{91.3}Fs_{7.9}$ to $Wo_{3.4}En_{86.6}Fs_{10.0}$ with an average of $Wo_{2.2}En_{89.1}Fs_{8.7}$. It has slightly higher Mg# than olivine, ranging from 0.897 to 0.922 with an average of 0.911. The Al_2O_3 and CaO contents are relatively low, ranging from 0.45 to 2.85 wt.% and 0.43 to 1.90 wt.%

respectively. Na_2O, K_2O and NiO are all below detection limits. TiO_2 and MnO are frequently also below detection limit, but may reach 0.08 and 0.32 wt.% respectively. Cr_2O_3 varies between 0.13 and 0.78 wt.%.

Figure 3.2 is a plot of enstatites from Pindos and other peridotites in the pyroxene quadrilateral and Figure 3.3 shows the relative positions of the different peridotite fields. Pindos enstatites plot at the Mg-rich, Ca-poor end of the abyssal peridotites field and show a large overlap with orthopyroxenes from the Oman ophiolite. Vourinos orthopyroxenes are slightly more magnesian, whereas the Papuan enstatites represent the most refractory compositions and show very limited overlap with Pindos.

Figure 3.4 shows a good linear correlation of the Al_2O_3 wt.% content of orthopyroxene with that of the whole rock. Bonatti and Michael (1989) showed that the Al_2O_3 abundance of peridotites is related to their geotectonic setting, decreasing from pre-oceanic rifts to mid-ocean ridges to subduction zones, suggesting an increase in the amount of partial melting. Figure 3.4 indicates that the decreasing Al_2O_3 wt.% content of the rock is reflected in the composition of the minerals (see also Figures 3.11 and 3.17).

The Cr content of orthopyroxenes is shown in relation to the spinel Cr# in Figure 3.5. It can be seen that the most Cr-rich enstatite does not co-exist with the most Cr-rich chromite. The enstatite Cr content reaches a maximum for a spinel Cr# of around 0.5 and then decreases, producing a parabolic trend. Nagata et al. (1983) examined this trend in a large number of peridotites and showed that it is best explained in relation to exchange equilibria between orthopyroxene and spinel spinel end-member components. Nagata et al. (1983) also found that the same relation applies to clinopyroxene-spinel equilibria. Figure 3.5 shows that, according to the conclusions of Nagata et al. (op.cit.), orthopyroxene and spinel in the Pindos peridotites are in thermal equilibrium with respect to Cr.

Figure 3.6 shows that the Mg# of olivine and orthopyroxene vary in a linear fashion, suggesting that the Fe-Mg exchange with olivine controls the orthopyroxene chemistry. This variation also represents variation in whole-rock Mg#, since olivine and orthopyroxene make up 95-99% of the rock. Note that, although a wide range of compositions is shown, peridotites from the same area show a more restricted range, suggesting that they experienced broadly similar degrees of partial melting.
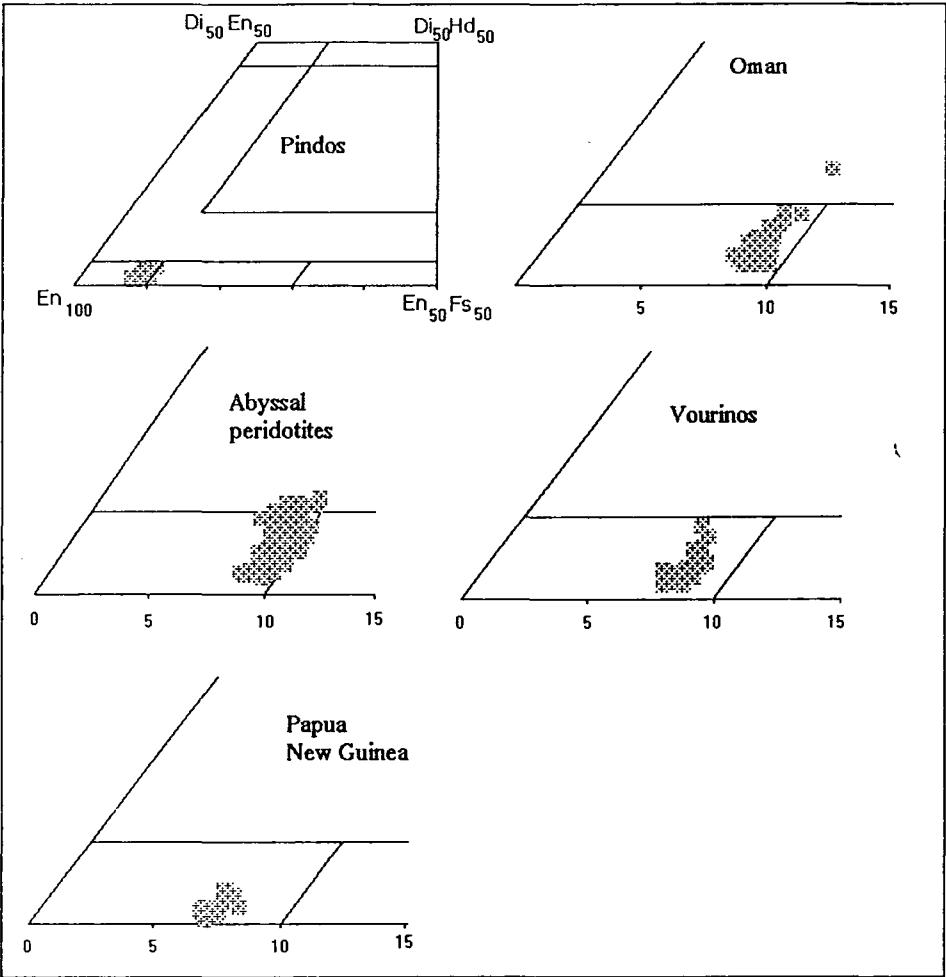
Figure (3.2) Part of the pyroxene quadrilateral showing enstatite compositions from the Pindos harzburgite.   Sources for the abyssal peridotites field are: Arai and Fujii (1978), Sinton (1978), Hamlyn and Bonatti (1980), Nicholls et al. (1981), Michael and Bonatti (1985), Dick (1989), Fujii (1990), Juteau et al. (1990) and Komor et al. (1990). Data from Oman: Brown (1982) and Roberts (1986); Vourinos: Mercier (1980); Papua, New Guinea: England and Davies (1971).
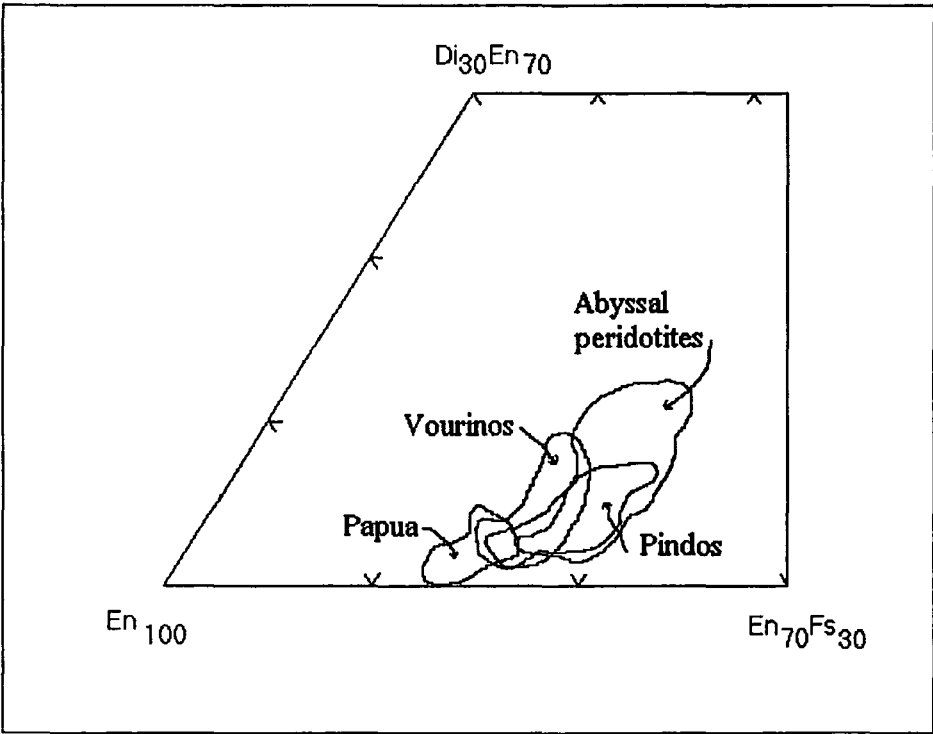
Figure (3.3) Comparison of the range of enstatite compositions in the Pindos harzburgites with the Peridotites in Figure 3.2. Oman is omitted for clarity.
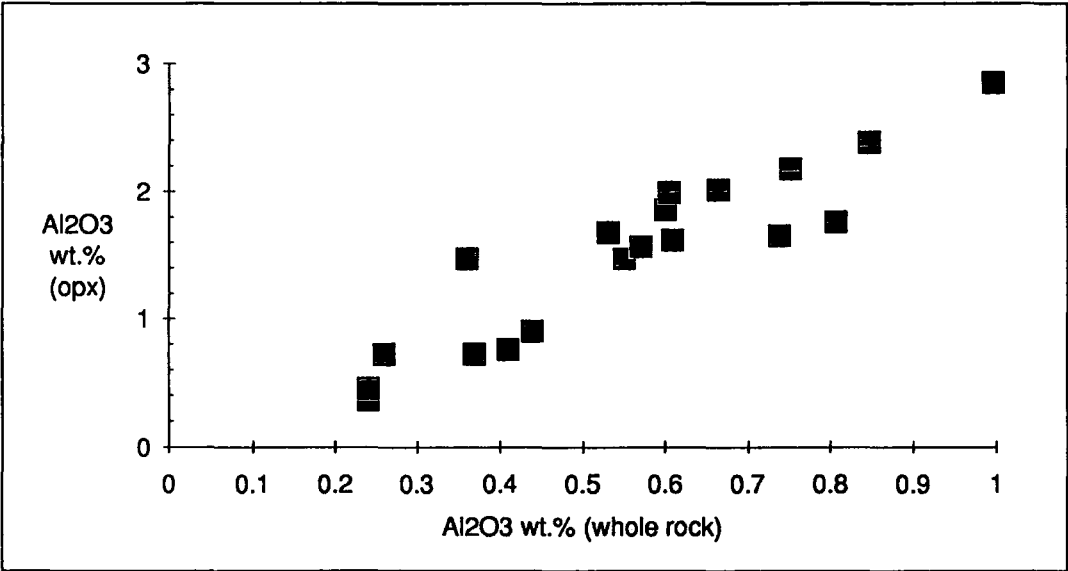
Figure (3.4) Linear correlation of the Al_2O_3 wt.% content of orthopyroxene with Al_2O_3 wt.% whole rock abundance.
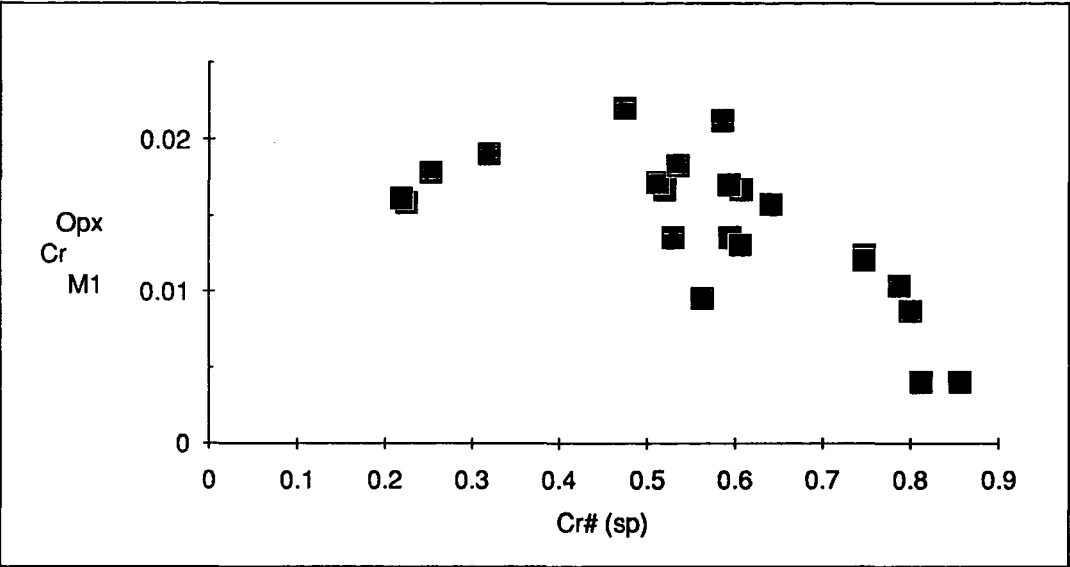
Figure (3.5) Plot of the Cr# of spinel vs. the Cr_{M1}^{opx} fraction. Note the change from an increasing to a decreasing trend at a Cr# around 0.5 that produces a parabolic pattern.
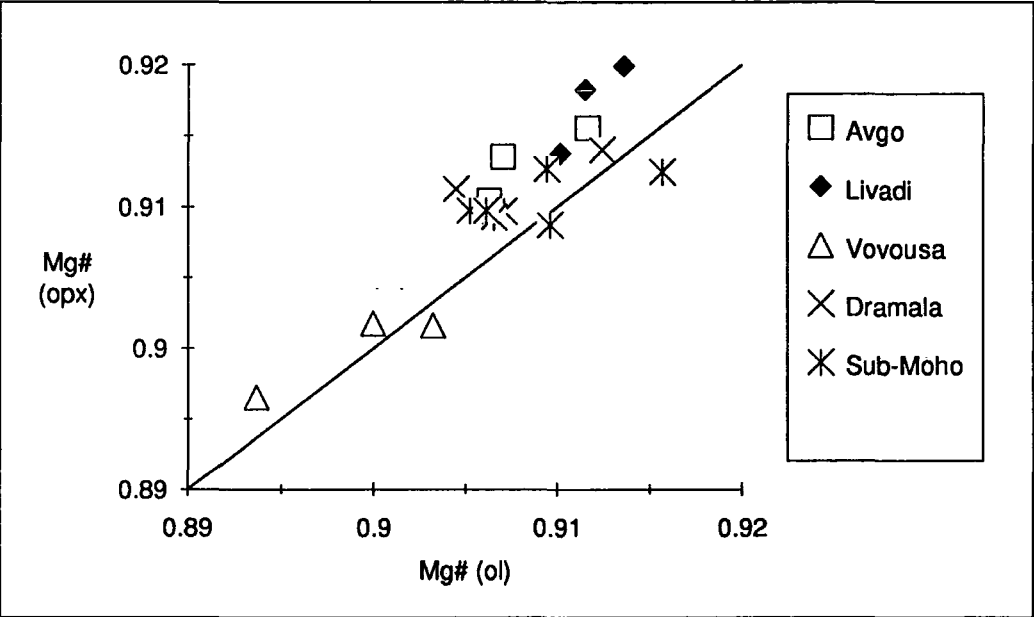
Figure (3.6) Mg/(Mg+Fe) in olivine vs. Mg/(Mg+Fe) in orthopyroxene. Peridotites from different localities are indicated. Samples marked "Sub-Moho" are transition-zone harzburgites (Table 3.1).
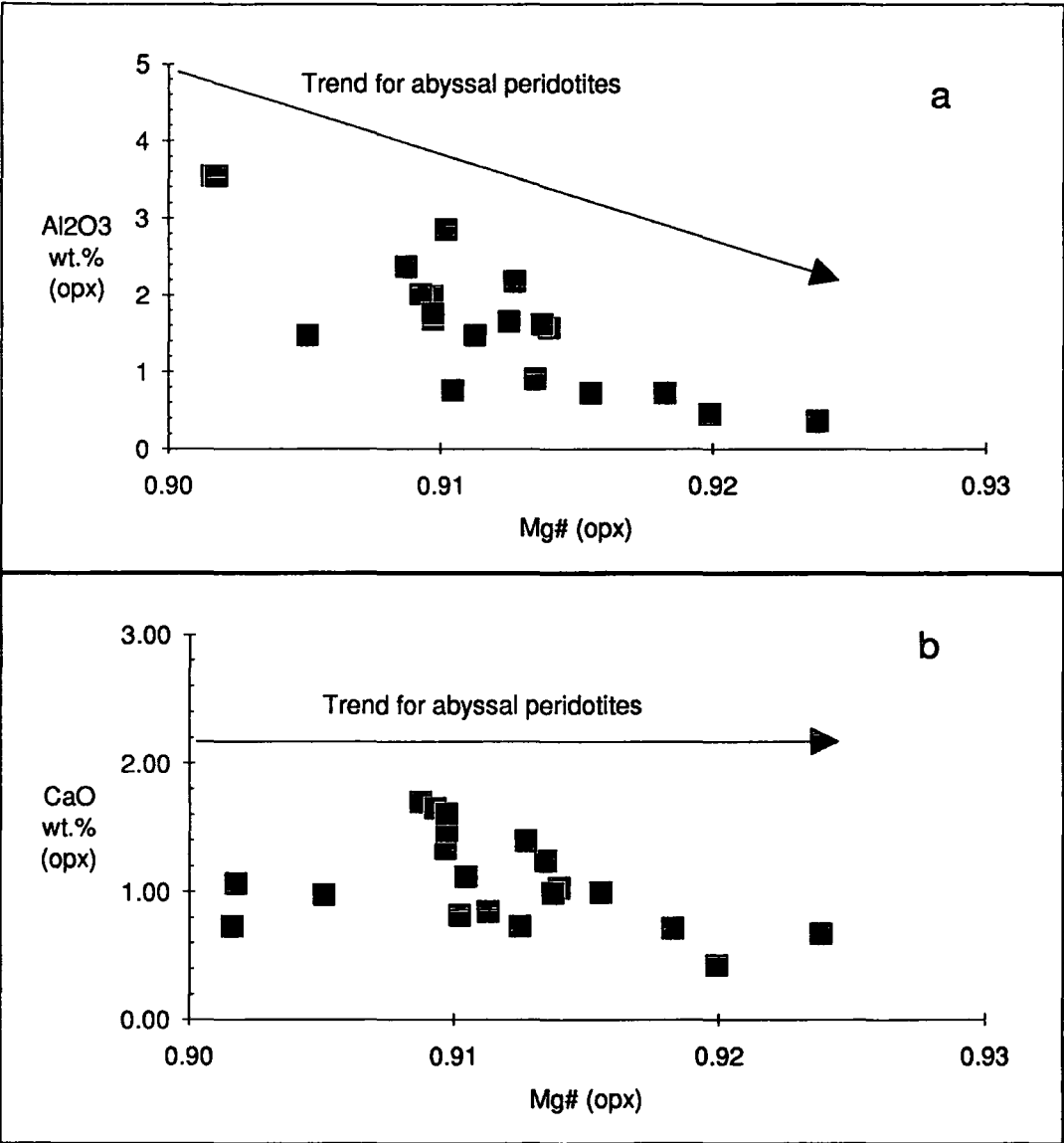
Figure (3.7) Enstatite Mg# vs. Al_2O_3 and CaO wt.%. CaO is more uniform than Al_2O_3 but still more variable than in abyssal peridotites. Abyssal peridotite field from Dick and Fisher (1984).
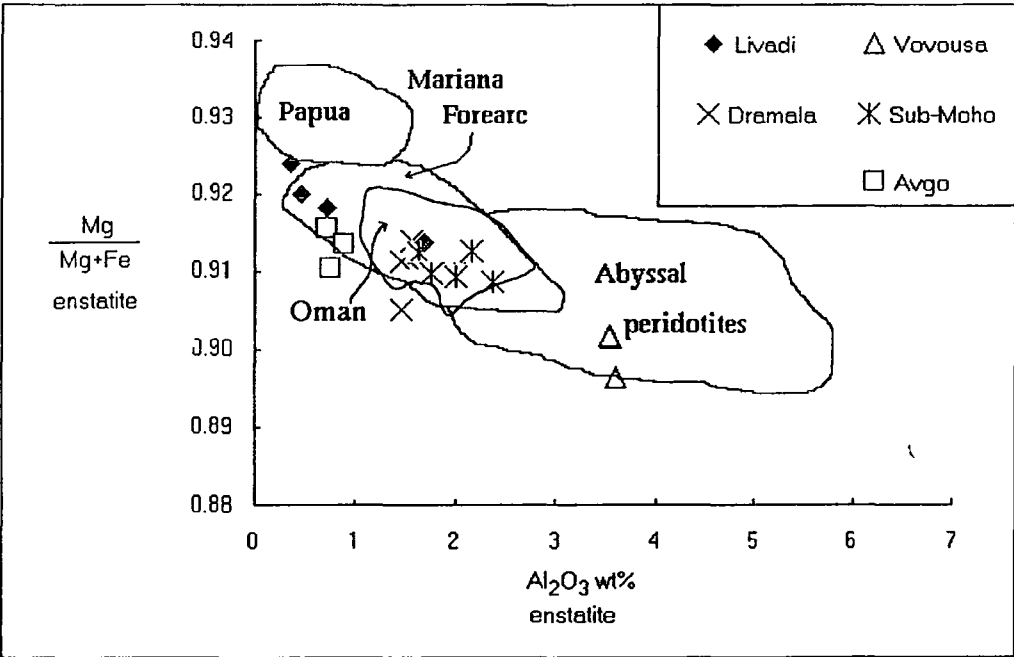
Figure (3.8) Enstatite Mg# vs. Al_2O_3 wt.%. Pindos follows the general enstatite trend of decreasing Al_2O_3 with increase in the Mg/(Mg+Fe) ratio. Sources for abyssal peridotites, see Figure 3.2.

Figure 3.7a,b is a plot of Mg# against Al_2O_3 wt.% and CaO wt.% in orthopyroxene. Also shown are the trends for abyssal peridotites of Dick and Fisher (1984). These authors examined the process of melting beneath mid-ocean ridges and showed that the Al_2O_3 content of orthopyroxene decreases steadily with partial melting. The CaO content of orthopyroxene from abyssal peridotites is fairly constant, suggesting a melting history where clinopyroxene was involved, buffering the CaO content of orthopyroxene. This contrasted the trends shown by ophiolites where CaO in orthopyroxene decreases with partial melting (Dick and Fisher, op. cit.). The Al_2O_3 and CaO contents of Pindos enstatites are both lower than those of abyssal peridotites. Al_2O_3 has a decreasing trend that is subparallel to the trend of abyssal peridotites. The data for CaO are more scattered and show less variation than Al_2O_3, but there is a clear decrease for the most MgO-rich enstatites. It can be noted, however, that the CaO content of orthopyroxene also depends on temperature (see later, geothermometry) and comparisons are not always simple.

The simpler behaviour of Al_2O_3 allows the uncomplicated comparison of peridotites from different settings. Figure 3.8 is a plot of Al_2O_3 wt.% against Mg# in for Pindos enstatites, showing fields for abyssal, Oman, and Papuan peridotites. There is a general decreasing

trend of Al_2O_3 with increasing Mg#, which reflects the increasingly depleted nature of the peridotites considered. In this plot is also evident the difference in composition of peridotites from different areas. Peridotites from Vovousa, being the less depleted, plot in the field of abyssal peridotites. There is some overlap of the rest of the data with this field, but the good agreement with the fields for Oman and Papua suggest that they represent the fertile end of the spectrum for subduction zone-related peridotites rather than the depleted end of abyssal peridotites. Samples from or immediately below the Moho (marked Sub-Moho, Figure 3.8) are very similar to Dramala peridotites. Field evidence suggested that the stratigraphic position of Dramala is near the Moho and the chemistry of the Dramala peridotite supports this conclusion. It will be noted, however, that sub-Moho peridotites inevitably include some depleted harzburgites that were re-fertilized by melt impregnation, although it is not easy to establish how severely this impregnation changed the original composition. These peridotites plot almost, entirely, within the field for Oman. Harzburgites from Livadi and Avgo, however, show more depleted compositions, but not as depleted as Papuan harzburgites. Viewed together, the variation of the composition of the peridotites from the southern part of Pindos show remarkable similarity, both in composition and compositional range, with peridotites dredged from the Mariana forearc. The peridotite from Vovousa has a distinct composition and is clearly less depleted than the rest of the complex.

3.3.3. Clinopyroxene

The clinopyroxene of the Pindos harzburgite is diopside, ranging from $Wo_{50.0}En_{45.4}Fs_{4.6}$ to $Wo_{42.7}En_{53.4}Fs_{3.9}$ with an average of $Wo_{47.0}En_{48.8}Fs_{4.2}$. It also has the highest Mg/(Mg+Fe) ratios, ranging from 0.898 to 0.935 with an average of 0.928, but does not show a correlation with the Mg# of orthopyroxene (Figure 3.10). Its Al_2O_3 is higher than that of the orthopyroxene, ranging from 1.51 to 2.90 wt.%. TiO_2, MnO, and Na_2O reach maxima of 0.29, 0.14, and 0.61 wt.% respectively, whereas Cr_2O_3 varies from 0.55 to 1.15 wt.%.

Figure 3.9 shows a plot of clinopyroxenes and co-existing orthopyroxenes from Pindos peridotites in the pyroxene quadrilateral. The clinopyroxenes plot at the

low_temperature end of the abyssal peridotites field and show a wider compositional range than the orthopyroxenes. This is mainly caused by the greater sensitivity of the Wo component of clinopyroxene to temperature compared to that of orthopyroxene. The wide range of compositions in Figure 3.9 indicates that the peridotites were equilibrated in a relatively wide temperature interval.

The variation of the Mg# of clinopyroxene with that of orthopyroxene is shown in Figure 3.10. In contrast to the same plot of olivine against orthopyroxene, the data do not show any apparent trend. This is probably the result of the more complex ortho-clinopyroxene equilibria imposed by the two-pyroxene solvus on mineral pairs, although the possibility that some compositions are not in equilibrium cannot be excluded.

In contrast to FeO and MgO, the clinopyroxene Al_2O_3 wt.% abundance shows a good linear correlation with that of orthopyroxene (Figure 3.11), suggesting that a state of equilibrium between the two minerals exists for this element. It will be noted that the trend of the Pindos peridotites in Figure (3.11) shows a clockwise rotation, compared to the trend that Johan and Augé (1986) suggest. These authors considered mineral compositions from a variety of peridotites, including a large number of data from fertile spinel lherzolite xenoliths. The observed angular relation of the Pindos pyroxene trend to that of Johan and Augé (1986) is consistent with the unmixing of aluminous orthopyroxene from clinopyroxene (Duncan and Green, 1987).

Unlike Al_2O_3, the Cr# of co-existing pyroxenes does not show a simple linear trend (Figure 3.12). As mentioned earlier, this is the result of the spinel exchange reactions with pyroxenes on the Cr intermineral partitioning. Still, a positive correlation is displayed in Figure 3.12 and it is obvious that clinopyroxene is more Cr-rich than orthopyroxene.
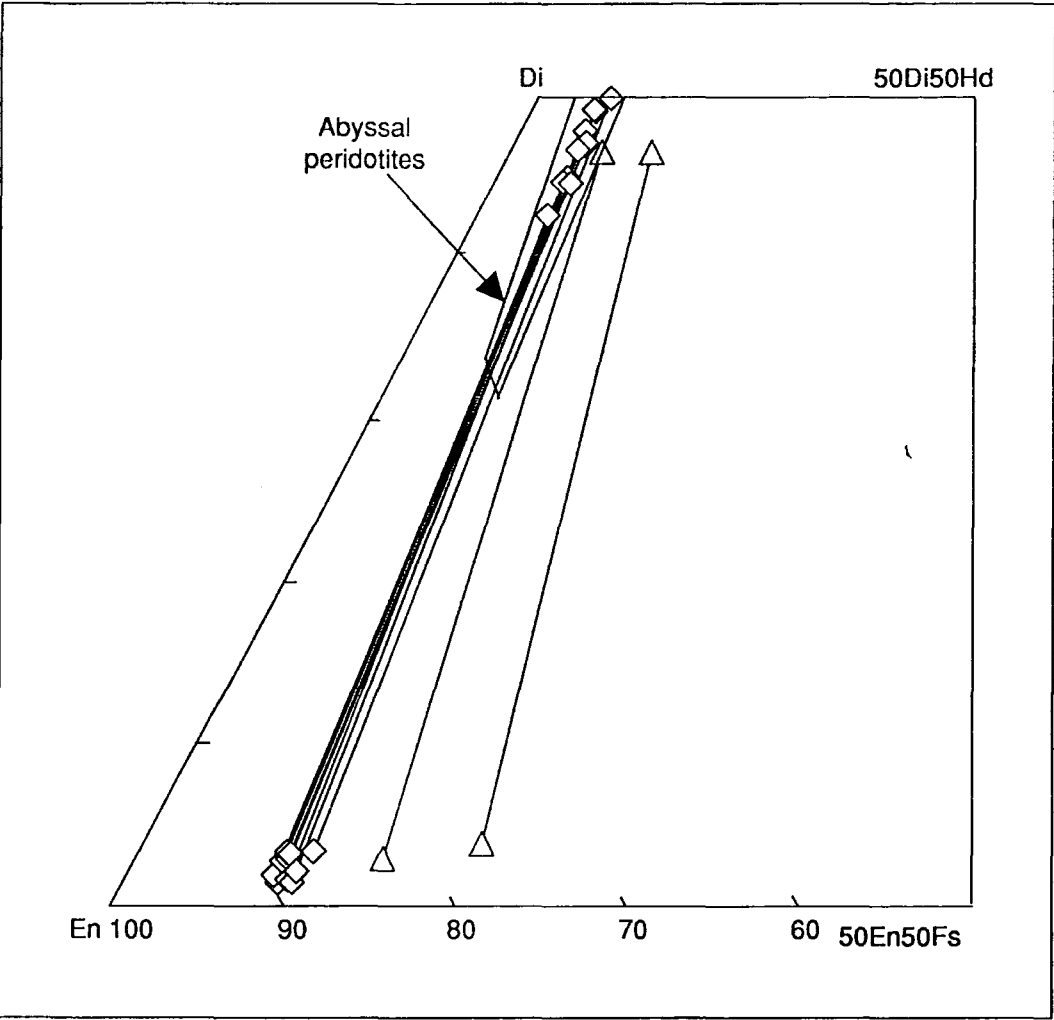
Figure (3.9) Plot of orthopyroxene-clinopyroxene pairs in the pyroxene quadrilateral. Tie lines connect coexisting minerals. The triangles are represent two websterite samples (Table 3.1). Sources for the field for abyssal peridotites as in Figure 3.2.
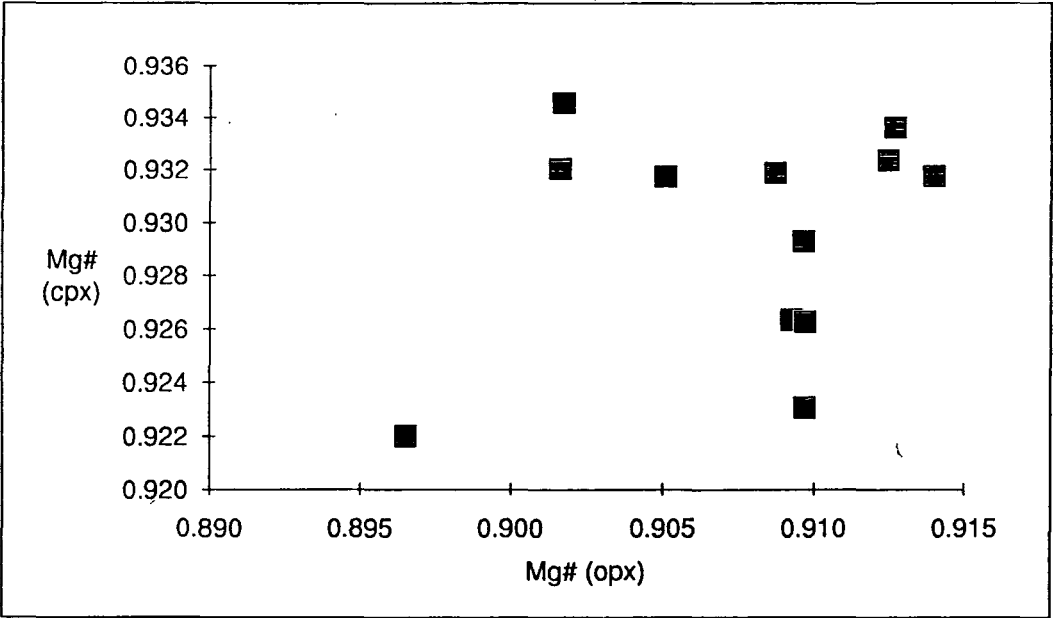
Figure (3.10) Plot of the Mg# of orthopyroxene vs. that of clinopyroxene for Pindos peridotites, showing a lack of correlation.
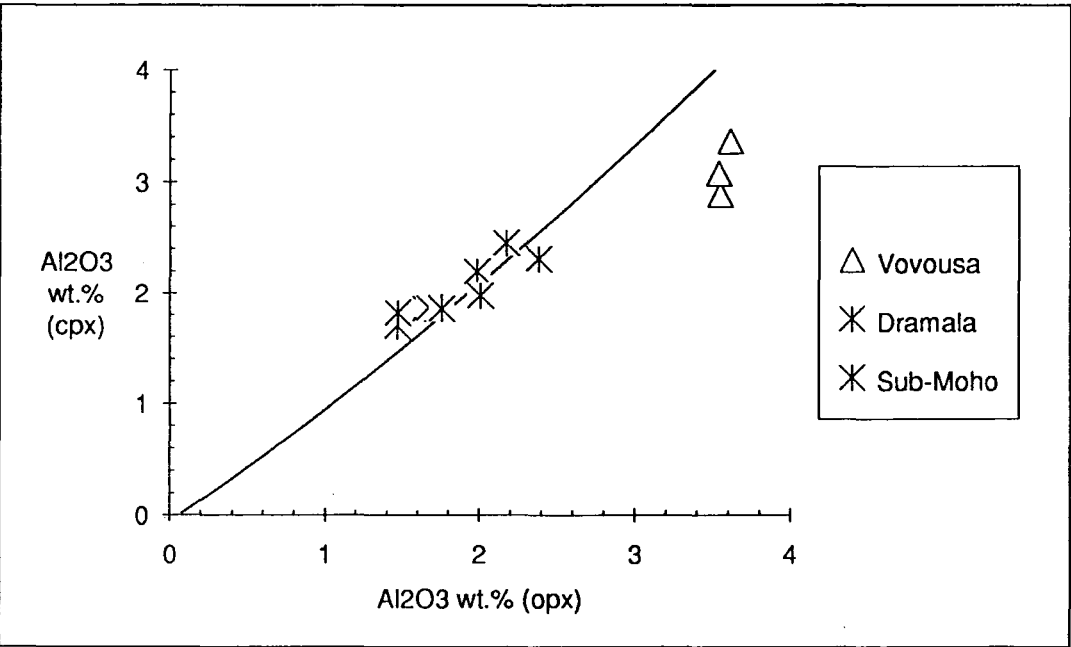
Figure (3.11) Al_2O_3 wt.% in orthopyroxene vs. Al_2O_3 wt.% in clinopyroxene. A positive correlation is displayed. The line is using the equations that Johan and Augé (1986) derived for the Al_2O_3 distribution between orthopyroxene, clinopyroxene, and spinel in spinel lherzolites xenoliths and ophiolites.
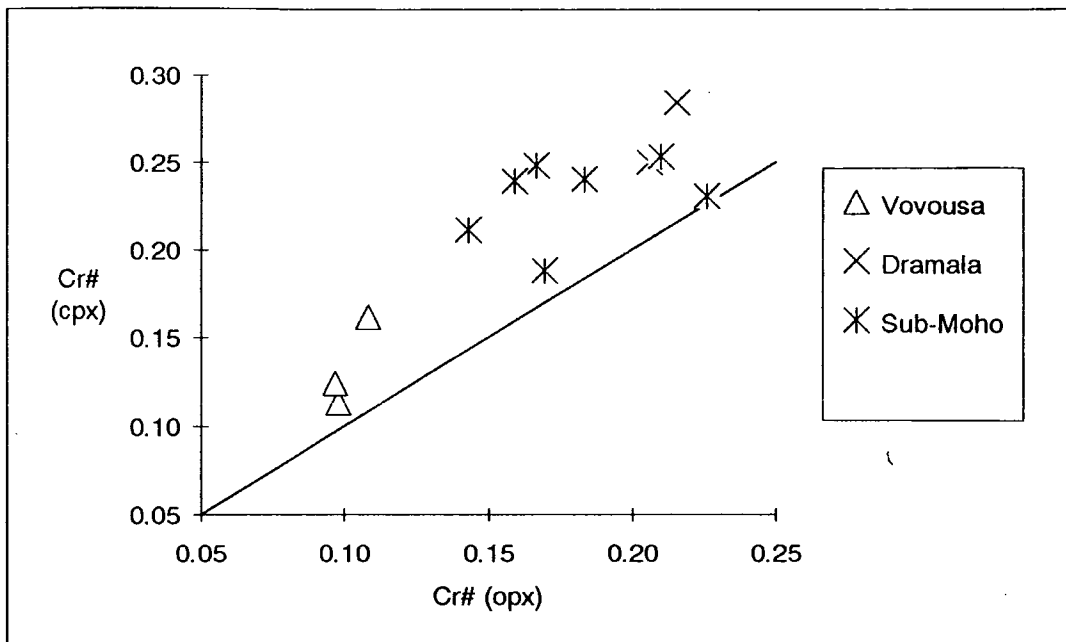
Figure (3.12) Plot of the Cr# of orthopyroxene vs. the Cr# of clinopyroxene. A good correlation is displayed. 1:1 line shown for reference.

3.3.4. Spinel

Spinel in harzburgites shows a wide variation of the Cr/(Cr+Al) ratio (Cr#) from 0.220 to 0.857 over a more limited range of Mg/(Mg+Fe) ratio (Mg#) from 0.421 to 0.694. Spinel in dunites shows more limited variation for both ratios with Cr# from 0.439 to 0.827 and Mg# in the lower range of 0.361 to 0.621. These ratios also vary to a limited extent in single grains. Figure 3.13 is a plot of Mg# against Cr# for core and rim spinel compositions in 6 samples that span almost the whole spinel compositional range. It can be seen that the Cr# of rims is always slightly lower than the core, the Mg#, however, does not show a consistent pattern. This type of Cr# zoning in spinel is well documented in virtually every study of peridotites and is the result of the re-equilibration of spinel (Henderson and Wood, 1981) and is referred to as normal zoning. Note that reverse zoning, which is the result of hydrothermal alteration of spinel (Kimball, 1988, 1990; see also Chapter 2, serpentinization), is accompanied by very low Mg# of the rims, due to Al and Mg mobilization, and has not been encountered in Pindos.
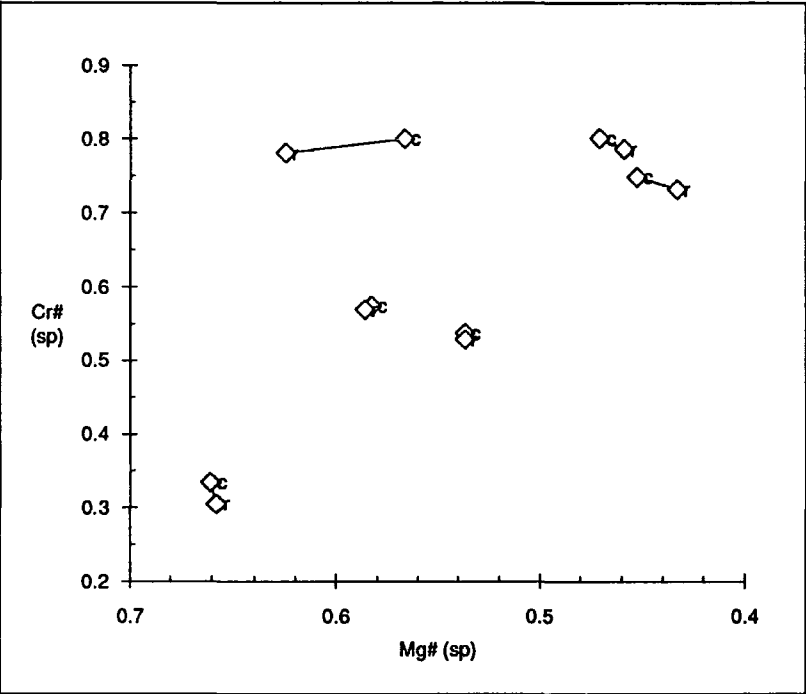
Figure (3.13) Plot of Mg# vs Cr# in spinel for core-rim pairs. The points are average compositions for the thin section. Lines connect the rim (r) and core (c) compositions. Note that the Cr# of rims is always lower than the Cr# of the cores, while the Mg# does not show a consistent pattern.
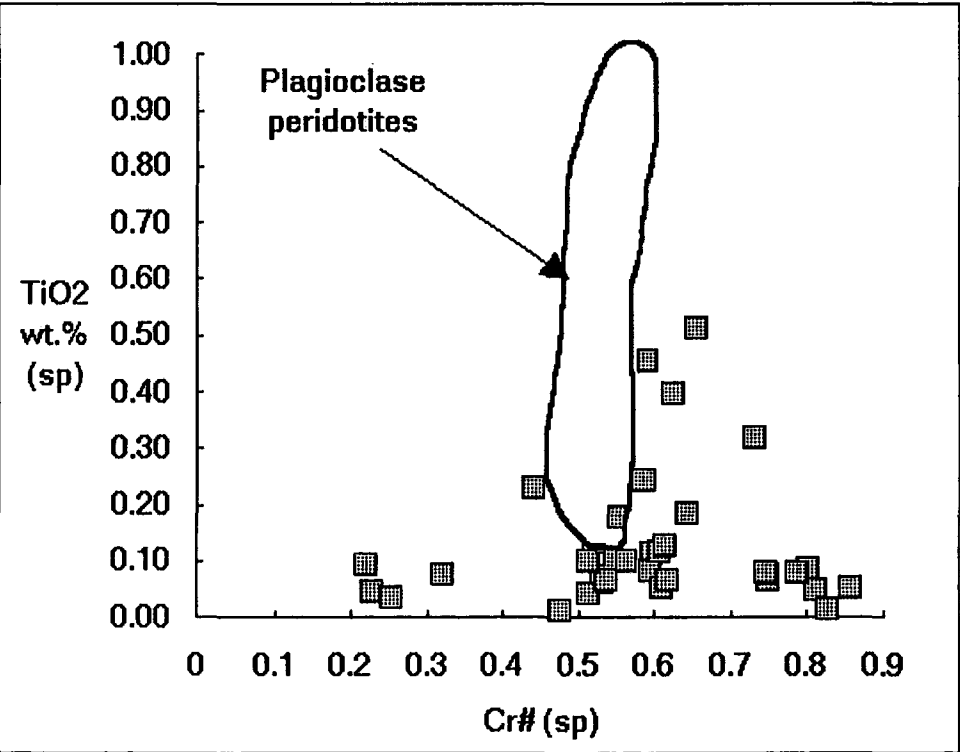
Figure (3.14) TiO2 wt.% against Cr# in spinel. Field for abyssal plagioclase peridotites from Dick and Bullen (1984)

The TiO_2 content of the spinels is usually below detection limit but is higher in some dunites and melt-impregnated harzburgites and may reach 0.51 wt.%. In Figure 3.14, TiO_2 is plotted against Cr# in spinel. The samples with higher TiO_2 plot very near the abyssal plagioclase peridotite field of Dick and Bullen (1984), suggesting that equilibration with a percolating melt has affected these spinels.

In Figure 3.15 Mg/(Mg+Fe) is plotted against Cr/(Cr+Al) in spinel. The Pindos spinels fall largely outside the field for abyssal peridotites of Dick and Bullen (1984), although some overlap does occur. Dick and Bullen (op. cit.) classified peridotites according to the Cr# of their spinels: spinels from type I peridotites have spinels that plot within the abyssal peridotite field; spinels from type III peridotites plot outside the abyssal peridotite field, and spinels from type II peridotites the spinels span the full range of compositions in type I and III peridotites. Although Pindos would appear to belong to type II peridotites, samples with Cr# less than 0.45 come from Vovousa. It has already been mentioned that harzburgite from Vovousa contains free clinopyroxene and was generally more fertile than the rest of the complex. The observed variation in spinel composition is consistent with the variation of the co-existing phases and further supports a mid-ocean ridge-related environment for the north part of the complex. So, considered alone, the south part of the Pindos complex belongs to type III ophiolites (subduction-related, such as Vourinos, Samail, Troodos and New Caledonia (Dick and Bullen, 1984).
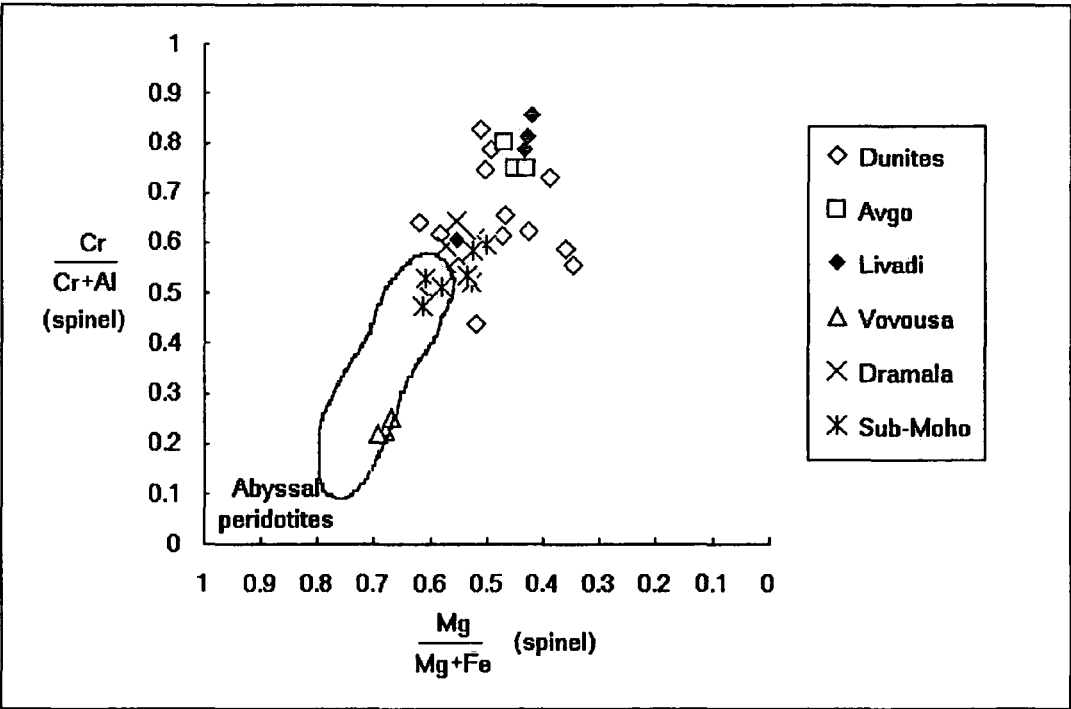
Figure (3.15) Negative correlation of the Mg/(Mg+Fe) vs. Cr/(Cr+Al) ratios in spinel. Field for abyssal peridotites is from Dick and Bullen (1984).

It has been shown (Dick, 1977; Henry and Medaris, 1980, Lehman, 1983) that spinel is affected by low temperature re-equilibration. In particular, the K_D of the reaction:

$$MgSi_{0.5}O_2 \quad + \quad Fe(Cr,Al)_2O_4 \quad = \quad FeSi_{0.5}O_2 \quad + \quad Mg(Cr,Al)_2O_4$$
$$\text{olivine} \qquad\qquad \text{spinel} \qquad\qquad \text{olivine} \qquad\qquad \text{spinel}$$
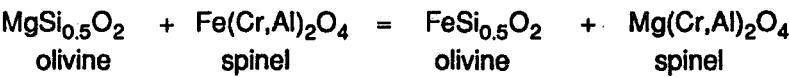
varies with temperature and spinel composition (see next, olivine-spinel thermometry). Because the olivine-spinel Fe-Mg exchange continues to low temperatures (as low as 500°C) the spinel composition, and especially the Mg#, often deviates from the original magmatic composition. This is evident in Figure 3.15 by the great range of Mg# in dunite spinels. Dick (1977) showed that the Mg# of spinels from rocks with varying proportions of spinels decreases with increasing modal amount of olivine. Olivine acts as a sink for MgO while its own composition is buffered by its larger modal proportion.

This change of spinel composition can be corrected using any of the thermometric expressions for olivine-spinel Fe-Mg exchange presented in the following section. By making simple assumptions about the original magmatic system conditions such an expression can be reversed and solved for the spinel composition using mass balance. The assumptions

used in the calculations were that the magmatic temperature of spinel crystallisation was 1150°C (an arbitrary choice), at oxygen fugacity conditions controlled by the QFM buffer (see later, oxygen geobarometry) and a pressure of 5 kb (see geobarometry). The ferric iron fraction of spinel $Y_{Fe^{3+}}^{sp}$ of 0.02 was used, being the average value of Pindos spinels. The spinel/olivine modal ratio was taken to be 0.015, which is appropriate for the harzburgites considered.

The results of this calculation are presented in Figure 3.16. The thermometric expression used for the calculations is that of Engi (1983) (Equation 3.6). The Mg#-Cr# diagram (Figure 3.16) has been contoured with the Fo content of co-existing olivine. This was calculated with the same assumptions using Equation 3.35 of Ballhaus et al. (1990) that relates olivine and spinel compositions to temperature and oxygen fugacity. The result of the recalculation of the spinel composition is that the wide range of spinel Mg# shown in Figure 3.15 is now much more restricted and is much closer to the theoretical magmatic trend. It will be noted that the predicted equilibrium olivines at 1 atmosphere pressure range from $Fo_{89.5}$ to $Fo_{92.5}$, a very good agreement with the observed compositions. In addition, the more Cr-rich spinels are in equilibrium with the more Fo-rich olivine, as is expected for a partial melting trend. In contrast, the equilibrium olivine at 10 kb is more forsteritic than any olivine analysed in this study. This is consistent with the suggested low pressures of formation for Pindos presented later (see geobarometry).

Figure 3.17 shows that the Al_2O_3 wt.% content of spinel correlates linearly with that of orthopyroxene and it is in good agreement with the calculations of Johan and Augé (1986). The covariance of the aluminium abundance of orthopyroxene with that of clinopyroxene and spinel reflect the Al_2O_3 depletion of the whole rock with increasing degree of partial melting that was mentioned earlier.

Despite the linear trend of Al_2O_3 between spinel and orthopyroxene, the parabolic trend of Cr partitioning between these minerals results in a poorer correlation of their Cr# (Figure 3.18). Still a positive correlation is displayed, with high spinel Cr# corresponding to high orthopyroxene Cr#.
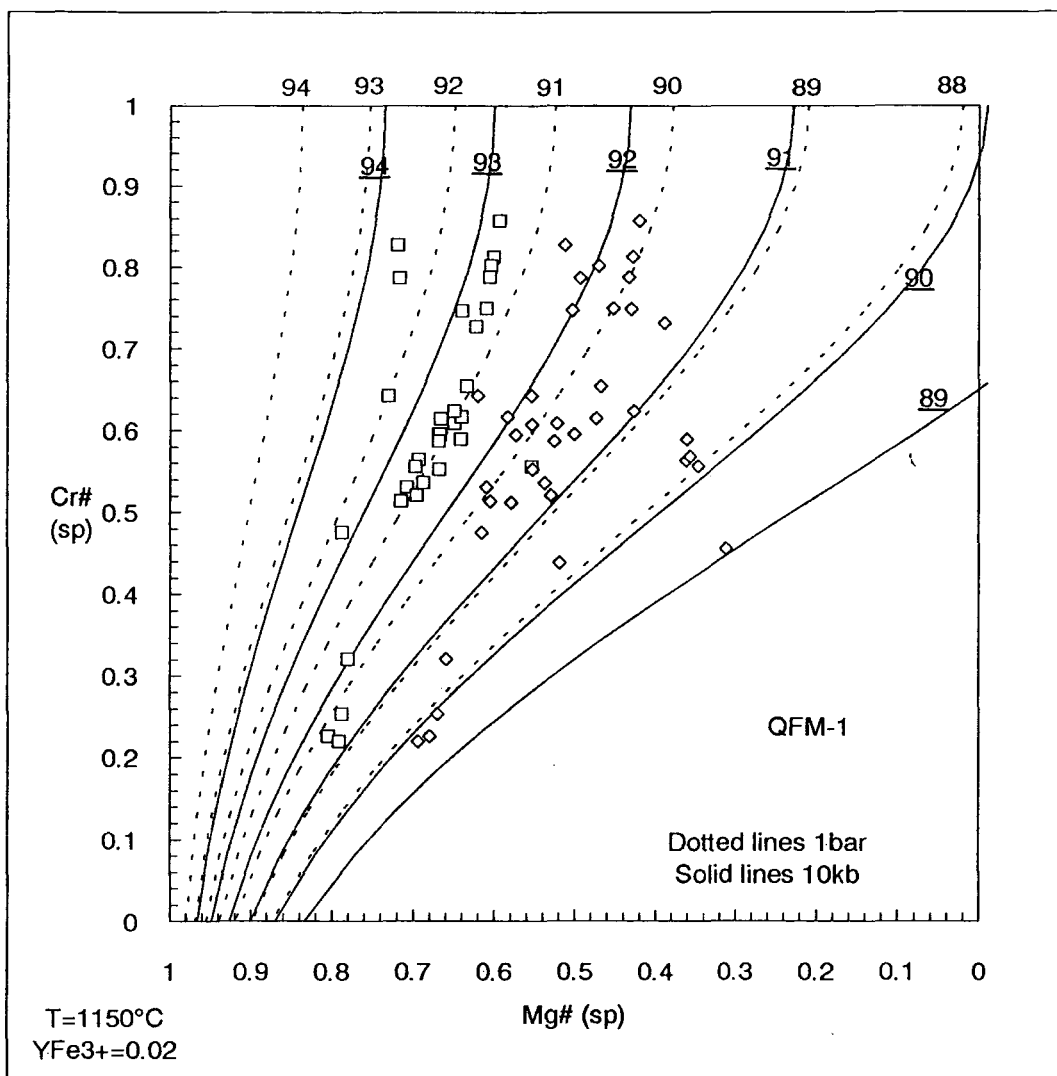
Figure (3.16) Plot of Mg/(Mg+Al) vs. Cr/(Cr+Al) for spinels recalculated at magmatic conditions. The contours were calculated using thermobarobetric equations for the olivine-spinel Mg-Fe exchange equilibrium (see text). Rhombs are observed compositions. Squares are recalculated. Numbers refer to the forsterite content of olivine in equilibrium with spinel. Underlined numbers refer to the contours for 10 kb pressure. Temperature is 1150°C and oxygen fugacity 1 log unit below the QFM buffer.

.·′
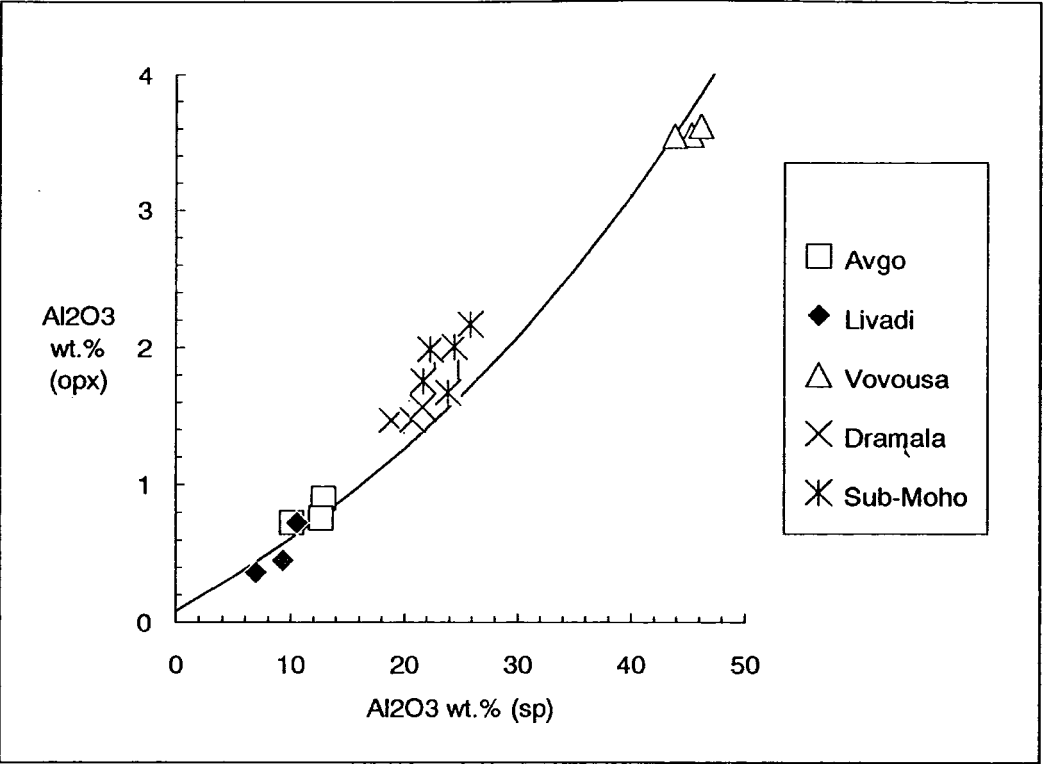
Figure (3.17) Al_2O_3 wt.% in spinel vs. Al_2O_3 wt.% in orthopyroxene. The line is from the empirical equation of Johan and Augé (1986) (see also Figure 3.11).
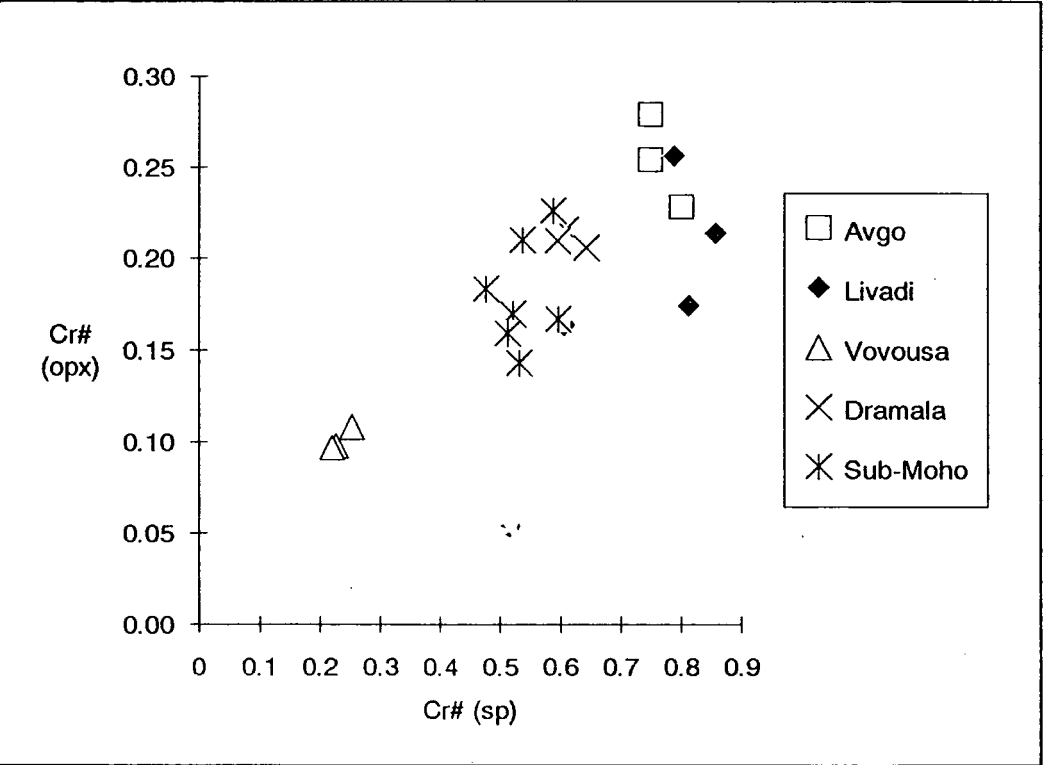
Figure (3.18) Cr/(Cr+Al) in spinel vs. Cr/(Cr+Al) in orthopyroxene. A positive correlation is displayed.
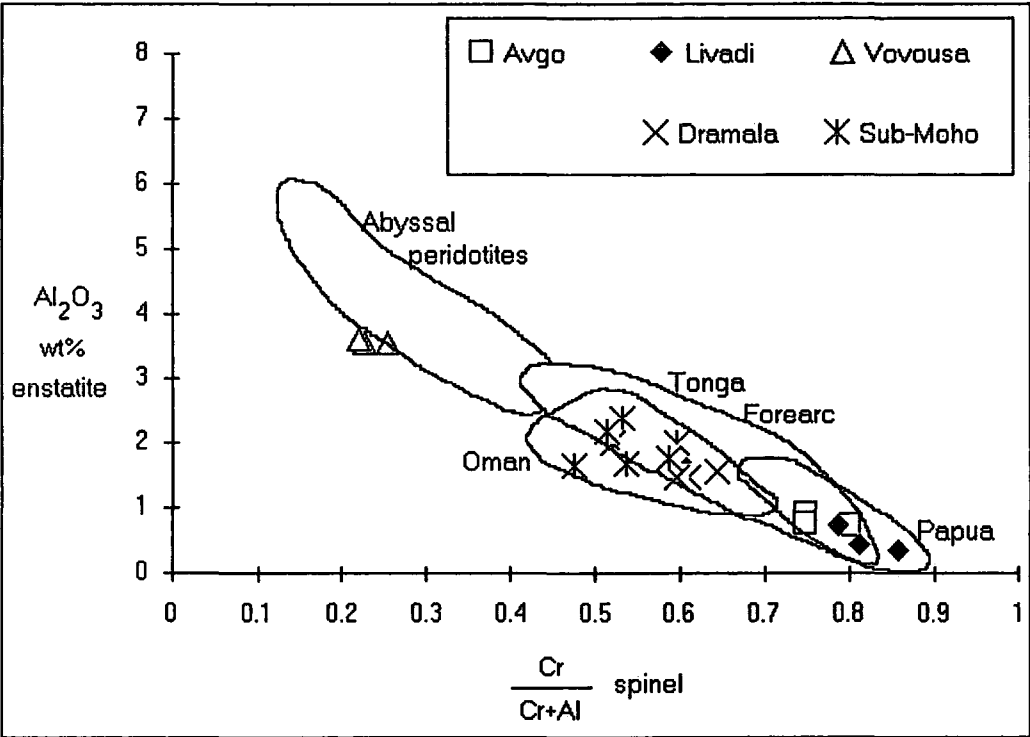
Figure (3.19) Cr/(Cr+Al) in spinel vs. Al_2O_3 wt.% in orthopyroxene. A negative correlation is displayed in all peridotites considered. Sources of data in Figure 3.2.

The Al_2O_3 wt.% content of orthopyroxene is plotted against the Cr# of spinel in Figure 3.19. Since both parameters are sensitive to partial melting they show a good linear correlation for all the peridotites considered. The field for abyssal peridotites is clearly separated from the fields of subduction-related peridotites. As in Figure 3.8, the Vovousa peridotites plot entirely in the field for abyssal peridotites. In this plot there is some overlap with the field for Papuan harzburgites, and the rocks from Livadi and Avgo plot within this field. This is because the characteristic that separated the Papuan rocks from the rest is their MgO-rich nature, which cannot be represented in this plot. The relation of the sub-Moho and Dramala peridotites to the Oman field is the same as in Figure 3.8 (i.e. overlapping), but if all the localities are considered the peridotites that Pindos most resembles are the dredged samples from the Tongan forearc.

3.4. Geothermometry

Knowledge of the pressure, temperature and oxygen fugacity conditions in which a rock was formed is obviously valuable in petrogenesis. Towards this end many researchers have studied exchange reactions of elements that are susceptible to changing conditions in ultramafic assemblages. Several thermobarometric expressions are available that can be applied to the minerals present in the Pindos ultramafic rocks (i.e. olivine + spinel ± orthopyroxene ± clinopyroxene). It should be always borne in mind, however, that these expressions only give reliable results if the following of requirements are met:

a) a state of equilibrium exists between the minerals involved;

b) the minerals lie within the compositional range for which the expression was formulated (or to which it can safely be extrapolated);

c) the results will reflect the conditions in which the last equilibration occurred.

Regarding the application of any thermometer to a mineral assemblage, there are two kinds of equilibria to be considered. One kind is rim-rim equilibrium, which may continue until the blocking temperature of the reaction is reached. Such equilibria are of little use because, apart from the difficulties in obtaining true rim compositions (microprobe beam problems, alteration), the calculated temperature should be the final blocking temperature of the exchange reaction, assuming that equilibrium is always maintained.

The second type of equilibrium is that which exists between mineral cores. Because of the sluggishness of some exchange reactions core-core equilibria may have preserved the compositions at a previous isothermal stage, if any. In the following sections temperature, pressure, and oxygen fugacities will be calculated from mineral core compositions.

3.4.1. Olivine-spinel Mg-Fe^{2+} exchange

The exchange of Fe^{2+} and Mg between olivine and spinel was first suggested as a potential geothermometer by Irvine (1965). He established that the empirical distribution coefficient of reaction (3.1) varies mainly with temperature and spinel composition. The K_D of this reaction is defined in Equation 3.2.

$$MgSi_{0.5}O_2 \quad + \quad Fe(Cr,Al)_2O_4 \quad = \quad FeSi_{0.5}O_2 \quad + \quad Mg(Cr,Al)_2O_4 \qquad (3.1)$$

$$\text{olivine} \qquad\qquad \text{spinel} \qquad\qquad\quad \text{olivine} \qquad\qquad\quad \text{spinel}$$
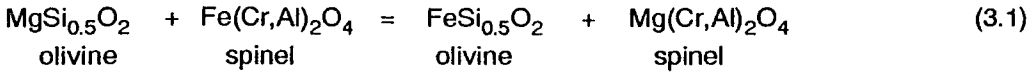
$$K_D = \frac{X_{Mg}^{ol}X_{Fe^{2+}}^{sp}}{X_{Fe^{2+}}^{ol}X_{Mg}^{sp}} \qquad\qquad\qquad (3.2)$$

X_i^a is the mole fraction of component i in phase a, for reaction (3.1). K_D varies mainly with temperature, but also with the mole fraction of trivalent cation i, $Y_{sp}^i = \frac{i}{Cr+Al+Fe^{3+}}$, in the octahedral site of the spinel structure, especially Y_{sp}^{Cr}.

The first calibration of this thermometer was by Jackson (1969) and several more have been proposed since then. They are based on thermochemical data (Jackson, 1969, Roeder et al., 1979, Engi, 1983, Ono, 1983, O'Neill and Wall, 1987) or natural assemblages (Evans and Frost, 1975, Fabriès, 1979) or a combination of the two (Fujii, 1977). Four of these calibrations (Fabriès, 1979, Engi, 1983, Ono, 1983, O'Neill and Wall, 1987) have been used in this study and are presented and compared below.

3.4.1.1. Fabriès (1979)

The calibration of Fabriès (1979) was an improvement of the original calibration of Jackson (1969) using mineral data on igneous and metamorphic rocks of known formation or re-equilibration temperatures. He arrived at the widely used expression:

$$T(^{\circ}K) = \frac{4250Y_{sp}^{Cr}+1343}{lnK_D^o+1.825Y_{sp}^{Cr}+0.571} \qquad\qquad (3.3)$$

where lnK_D^o is the constant of Equation 3.1 normalized to a ferric-free basis:

$$lnK_D^o = lnK_D - 2Y_{sp}^{Fe^{3+}} \qquad\qquad\qquad (3.4)$$

The calibration range is $0.1 < Y_{sp}^{Cr} < 0.7$ and $Y_{sp}^{Fe^{3+}} < 0.12$. Although no pressure correction was applied, the rocks used for calibration were taken from a wide variety of tectonic settings (extrusives, layered intrusions, lunar basalts, mantle and metamorphic rocks), which implies that pressure has no significant effect on the olivine-spinel equilibrium.

3.4.1.2. Ono (1983)

Ono (1983) conducted two sets of diffusion experiments between olivine and spinel in the Al-free and Cr-free systems. the former between 650°C, 2 kb and 1530°C, 10.5 kb and the latter between 650°C, 2 kb and 1483°C, 10.5 kb. He arrived at the expression:

$$T(°K) = \frac{(0.057+0.34X)10^4}{\ln K_D + 0.934 - 0.102}$$

(3.5)

where X=Cr/(Cr+Al) in spinel. Ono (op. cit.) states an uncertainty of 70°C at 10.5 kb pressure, for spinel of 0-6% Fe_3O_4 coexisting with olivine of Fo_{80} to Fo_{90}. Although he makes no correction for ferric iron in spinel, he makes use of the Cr/(Cr+Al) ratio rather than the Y_{sp}^{Cr} of Fabriès (1979).

3.4.1.3. Engi (1983)

Engi (1983) used a different approach by rigorously modelling reciprocal spinel $(MgAl_2O_4\text{-}FeAl_2O_4\text{-}FeCr_2O_4\text{-}FeAl_2O_4)$ using speciation formation rather than the classical reciprocal solution model. He derived thermodynamic data by conducting a set of experiments between 600°C and 900°C, at 300 to 1000 bars, which, in combination with data from the literature, he used to constrain his model. He arrived at the following thermometric expression:

$$T(°C) = \sum_{j=0}^{3} \sum_{i=0}^{3} A_{ji} (\ln K_D)^i (Y_{sp}^{Cr})^j$$

(3.6)

where Y_{sp}^{Cr}=Cr/(Cr+Al) in spinel. The term A_{ji} is a set of regression coefficients that depend on X_{Mg}^{bulk} and r_{modal}. These parameters depend on the relative abundance of olivine and spinel. X_{Mg}^{bulk} is the abundance weighted average, of X_{Mg}^{Ol} and X_{Mg}^{sp} and r_{modal} is the modal ratio of olivine/spinel. The introduction of these terms is an attempt to correct K_D for the effects of composition. Three sets of coefficients are given:

AT, for Alpine-type peridotites with X_{Mg}^{bulk} = 0.88 and r_{modal} = 20

LI, for layered intrusion-type peridotites with X_{Mg}^{bulk} = 0.80 and r_{modal} = 15

CO, for chromite-olivine cumulate-type peridotites with X_{Mg}^{bulk} = 0.64 and r_{modal} = 1

It will be noted that this is the only calibration to take into account the chemical and modal composition of the rock.

Corrections in lnK_D for ferric iron in spinel and pressure can be applied to Equation 3.6:

$$lnK_D cor = lnK_D - plnK_D - \Delta_{Fe3+}lnK_D \qquad (3.7)$$

where

$$\Delta plnK_D = P(C1T^{C2} + C3Y_{sp}^{Cr} + C4(1 - \frac{T+273.15}{1420})(Y_{sp}^{Cr} - 0.35)^2) \qquad (3.8)$$

Pressure P is in kb, temperature T in °C,

C1=0.017904
C2=-0.292880
C3=0.004668
C4=0.018530

and

$$\Delta_{Fe3+}lnK_D = 2.2Y_{sp}^{Fe^{3+}} \qquad (3.9)$$

The useful range of the thermometer is considered to be 600°C ≤ T ≤ 1400°C and $Y_{sp}^{Fe^{3+}}$ ≤0.15 (Engi, 1983).

3.4.1.4.O'Neill and Wall (1987)

O'Neill and Wall (1987) obtained a new calibration of the same olivine-spinel geothermometer as a by-product of their formulation of the olivine-orthopyroxene-spinel oxygen geobarometer using thermodynamic arguments. Their thermometric expression is:

$$T(°K) = \frac{6530 + (5000 + 10.8P)(X_{ol}^{Mg} - X_{ol}^{Fe}) - 1960(1 + X_{sp}^{Ti})(X_{sp}^{Mg} - X_{sp}^{Fe^{2+}} + 18620X_{sp}^{Cr} + 25150(X_{sp}^{Fe^{3+}} + X_{Ti}^{sp}))}{RlnK_D + 4.705}$$

$$(3.10)$$

where R=8.31441 ($JK^{-1}mol^{-1}$) and pressure P in kb.

This is the first formulation of the olivine-spinel geothermometer to specifically take the effect of Ti into account, although the very low Ti abundance in the rocks of this study means that its effect on calculated temperatures will be minimal.

3.4.1.5. Application

In Fig 3.20 the results of the four olivine-spinel geothermometers are presented. All four thermometers give similar results that peak between 700°C and 800°C. One exception is the thermometer of Engi (1983) that has a small peak between 800°C and 900°C although all temperatures from 700°C to 900°C are reported with almost the same frequency. One possible explanation for this is that, because his model takes into account the modal composition of the rock, it may compensate to some extent for subsolidus re-equilibration and the temperatures reported may be closer to the true magmatic temperature of crystallization.
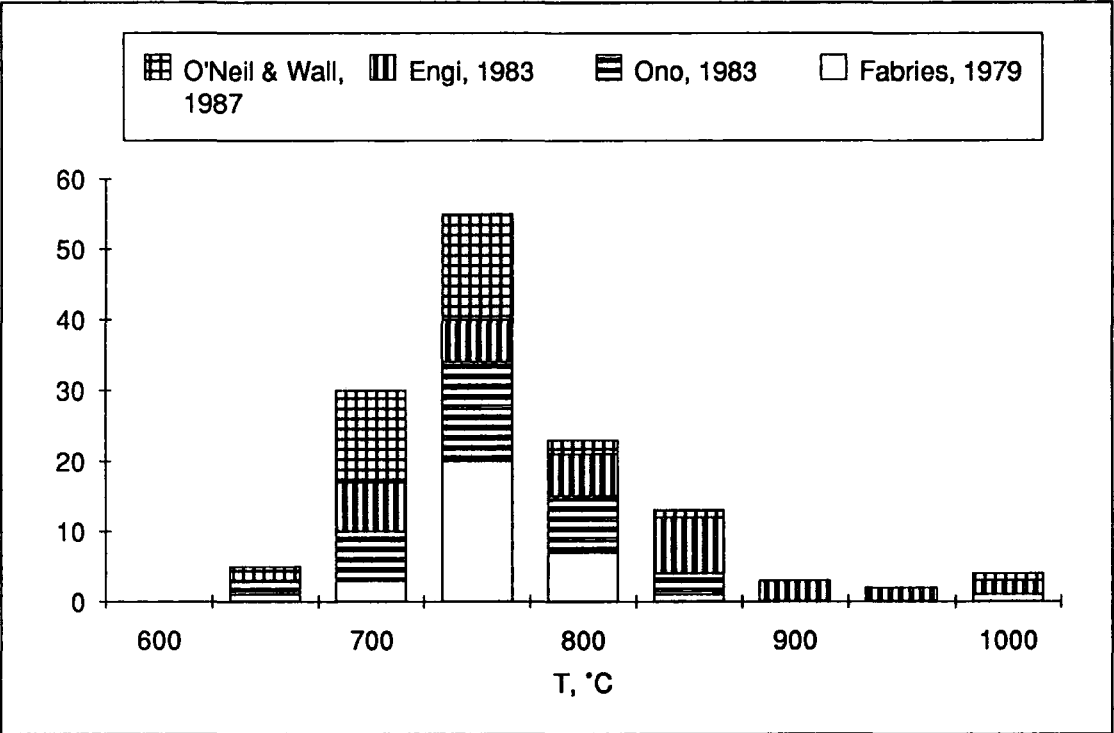
Figure (3.20) Frequency diagram of temperature for the four olivine-spinel geothermometers. A total of 33 dunites and harzburgites are shown.

3.4.2. Aluminium solubility in orthopyroxene

The thermodynamic calculations of Obata (1976) and experimental studies in the system MgO-Al_2O_3-SiO_2 (Fujii, 1976, Dunckwerth and Newton, 1978) have shown that the solubility of Al in orthopyroxene coexisting with olivine and spinel is mainly a function of temperature with a negligible effect from pressure. The solubility of alumina in orthopyroxene is controlled by the reaction:

$$MgAl_2O_4 + Mg_2Si_2O_6 = Mg_2SiO_4 + MgAl_2SiO_6 \qquad (3.11)$$

$$\text{spinel} \quad + \quad \text{enstatite} \quad \rightleftharpoons \quad \text{olivine} \quad + \quad \text{Al-enstatite}$$
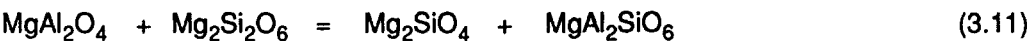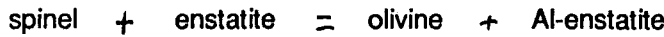
with a temperature dependent K_D defined as:

$$K_D = \frac{(X_{Mg})_{ol}^2 (X_{Al}^{M1})_{opx}}{(X_{Mg}^{M1})_{opx}(X_{Mg})_{sp}(X_{Al})_{sp}^2} \tag{3.12}$$

where $(X_i^m)_a$ is the cation fraction of element i in site m of phase a, and with olivine and spinel calculated on a 4-oxygen basis and orthopyroxene on a 6-oxygen basis.

3.4.2.1. Sachtleben and Seck (1981)

The first calibration of this geothermometer was attempted by Sachtleben and Seck (1981) on continental spinel lherzolites. They found that Cr had a considerable effect on Al partitioning and made an empirical correction. The expression they arrived at was:

$$T(^{o}C) = \frac{4.59 + \ln K_D - 1.552 Y_{Cr}^{sp}}{0.0025} \tag{3.13}$$

The authors did not state the compositional range within which their thermometer is accurate, but the rocks that were used for the calibration had Cr/(Cr+Al) ratios in spinel between 10 and 60 and were considered to have re-equilibrated at temperatures between 950°C and 1150°C.

3.4.2.2. Witt-Eickschen and Seck (1991)

The thermometer of Sachtleben and Seck (1981) was re-calibrated by Witt-Eickschen and Seck (1991) using an extended data set of continental spinel lherzolites.

$$T(^{o}C) = 2248.25 + 991.58 \ln K_D + 153.32 \ln K_D^2 + 539.05 Y_{Cr}^{sp} - 2005.74 Y_{Cr}^{sp2} \tag{3.14}$$

They also formulated another expression based on the same reaction (3.11):

$$T(^{o}C) = 636.54 + 14527.32 (X_{Cr}^{M1})_{opx} + 2088.21 (X_{Al}^{M1})_{opx} \tag{3.15}$$

which is less susceptible to late chemical changes, as opposed to the Mg content of spinel, but, because of the non-ideal solution behaviour of orthopyroxene with spinel, is applicable only to orthopyroxenes with X_{Al}^{M1} in the range 0.05 to 0.11. The conditions of equilibration and

characteristics of spinel in this re-calibration are similar to those of Sachtleben and Seck (1981).

3.4.2.3. Webb and Wood (1986)

Webb and Wood (1986) also formulated a thermometric expression based on reaction (3.11), after performing experiments on synthetic mixtures of spinel ($Mg(Cr,Al)_2O_4$) and clinopyroxene (ureyite and jadeite) at 1000°C and 1100°C and 25 kb pressure. From these experiments they derived thermodynamic data that enabled them to formulate a simplified version of the thermometer of Gasparic and Newton (1984):

$$T(^{o}K) = 3857\,K_D\,exp\left[\frac{-X_{Cr}^{sp}(5400X_{Cr}^{sp}+4500X_{Fe}^{sp})}{1.987T}\right] + 716 + P \qquad (3.16)$$

with K_D as in Equation 3.12 and $(X_i^m)_a$ as previously defined. Temperature is calculated by iteration.

3.4.2.4. Application

Figure 3.21 is a frequency diagram of the temperatures reported by the three described geothermometers. As was expected, since the Sachtleben and Seck (1981) and the Witt-Eickschen and Seck (1991) versions are based on the same model, they give similar temperatures for the same assemblages and this tends to create two artificial peaks in the diagram. The Webb and Wood (1986) version reports temperatures that are 150°C to 200°C lower than the two other versions. In view of the fact that the thermometers of Sachtleben and Seck (1981) and Witt-Eickschen and Seck (1991) are based on fertile spinel lherzolites, the version of Webb and Wood (1986) is considered more appropriate for Pindos rocks. This is because the two first thermometers are calibrated only in the low-Cr limb of the parabolic trend in Figure 3.5. In contrast, Webb and Wood (1986) included spinel with high Cr/Al ratios, thus correcting for the non-ideality of orthopyroxene-spinel equilibria. This thermometer also shows a twin distribution of temperatures, a low-temperature peak at ~800°C, that is the

same, within uncertainty, to the olivine-spinel thermometers, and a high-temperature peak at 950-1000°C.
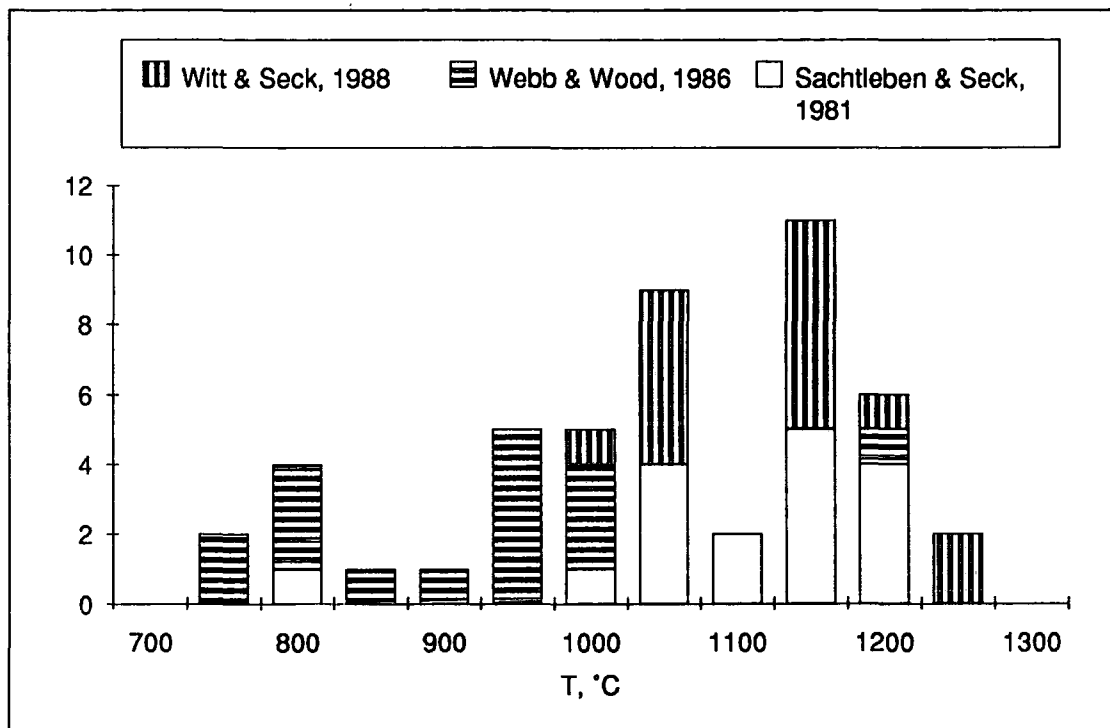
Figure (3.21) Frequency diagram of temperature for the three geothermometers based on the Al-solubility in orthopyroxene. A total of 17 harzburgites is shown.

3.4.3. Co-existing pyroxenes

The potential of coexisting high-Ca and low-Ca pyroxenes to provide thermometric information has long been recognized. In particular, the expansion of the solvus in the pyroxene quadrilateral dictates that the Ca content of the high-Ca pyroxene increases with decreasing temperature, while that of the low-Ca phase decreases (e.g. Lindsley and Anderson, 1983). Numerous geothermometers based on this property have appeared in the literature. All methods involve an initial projection of natural compositions onto the simple Ca-Mg-Fe pyroxene plane. After this projection, some models further project the quadrilateral compositions onto the En-Di (Fe-free) join and use a solution model (e.g. Wells, 1977), or use phase equilibria within the quadrilateral (e.g. Lindsley and Anderson, 1983), or a combination of phase equilibria and natural occurrences (e.g. Mercier, 1976) to determine temperatures.

The thermometers of Wells (1977), Davidson and Lindsley (1985), Sen and Jones (1989), and Brey and Köhler (1990) have been applied to pyroxene pairs from the Pindos harzburgites.

3.4.3.1. Wells (1977)

Wells (1977) applied a simple mixing model to the ortho- and clinopyroxene solid solution for compositions in the CMS system using an empirical correction for the effect of iron. His model is based on the well known reaction (17) between coexisting ortho- and clinopyroxene:

$$Mg_2Si_2O_6 \quad = \quad Mg_2Si_2O_6 \qquad (3.17)$$
$$\text{orthopyroxene} \quad \text{clinopyroxene}$$

The K_D of reaction (3.17) is defined as :

$$K_D = \frac{a^{cpx}_{Mg_2Si_2O_6}}{a^{opx}_{Mg_2Si_2O_6}} \qquad (3.18)$$

Wells (1977) applied the ideal two-site solution model of Wood and Banno (1973) to calculate the activities of end-member pyroxenes, and used available experiments in the CMAS system to evaluate the temperature dependence of K_D. He then used experiments in Fe-bearing systems to apply an empirical correction for Fe and arrived at the simple expression:

$$T(^oK) = \frac{7341}{3.355 + 2.44X^{opx}_{Fe} - \ln K_D} \qquad (3.19)$$

3.4.3.2. Davidson and Lindsley (1985)

Davidson and Lindsley (1985) developed a non-convergent site-disorder model for quadrilateral pyroxenes using experimentally determined equilibria to determine the solution parameters. Application of their model to natural assemblages requires the determination of pyroxene components (e.g. enstatite, acmite, jadeite etc.) in the minerals according to the method of Lindsley and Andersen (1983). The model provides thermometric information by

estimating the best tie-lines of coexisting low-Ca and high-Ca pyroxenes in the pyroxene quadrilateral. This is achieved by sequential non-linear least-squares fitting between the calculated and natural equilibria and minimisation of the sum of the residuals. The calculations were performed using a computer program supplied by the authors.

3.4.3.3. Sen and Jones (1989)

Sen and Jones (1989) used the approach of Wells (1977) to the pyroxenes exchange reaction (Equation 3.17) and use the partitioning coefficients K_{D1} and K_{D2} to empirically formulate two thermometric expressions:

$$T(^{\circ}K) = 4900/(1.807\text{-}lnK_{D1}) \tag{3.20}$$

and

$$T(^{\circ}K) = 7045/(2.47\text{-}lnK_{D2}) \tag{3.21}$$

where $K_{D1}=[X_{En}]^{cpx}/[X_{En}]^{opx}$ and $K_{D2}=[X_{Di}]^{opx}/[X_{Di}]^{cpx}$ and the En and Di mole fractions calculated using the method of Wood and Banno (1973). The estimated accuracy of this thermometer when applied to natural spinel lherzolites is $\pm50^{\circ}C$.

3.4.3.4. Brey and Köhler (1990)

Brey and Köhler (1990) performed experiments on natural peridotitic systems at temperatures ranging from 900-1400°C and pressures from 2-60 kb. They used the results to formulate a semi-empirical pyroxene thermometer arrived at the pressure dependent expression (3.22):

$$T(^{\circ}K)=\frac{23664+(24.9+126.3X_{Fe}^{cpx})P}{13.38+(ln\overset{\bullet}{K}_{D})^{2}+11.59X_{Fe}^{opx}} \tag{3.22}$$

where

$$\overset{\bullet}{K}_{D}=(1\text{-}Ca^{*})^{cpx}/(1\text{-}Ca^{*})^{opx}$$

$$Ca^{*}=Ca^{M2}/(1\text{-}Na^{M2})$$

$$X_{Fe}^{opx}=Fe/(Fe+Mg)$$

3.4.3.5. Application

Figure 3.22 is a frequency diagram of temperature for the coexisting pyroxenes thermometers that were described previously. It can be seen that there is a broad peak between 850°C and 950°C although if every thermometer is examined separately, it is only the Wells (1977) version that peaks in the same interval. Two-pyroxene thermometers are considered very accurate although they have limitations. One such limitation is their sensitivity to components that have not been allowed for in the calibration. Interestingly, the more consistent results are obtained from a CMS system calibrated thermometer, that of Wells (1977). A possible explanation for the wide variation of results from the thermometers is that orthopyroxene and clinopyroxene are not in equilibrium. This may be true for the peridotites that suffered melt impregnation. In view of this possibility, the thermometer that probably gives the most accurate results is that of Davidson and Lindsley (1985), because it calculates the temperature using only the clinopyroxene composition. This thermometer also shows two peaks, one at ~850°C and a higher one at ~950°C. The agreement between the Davidson and Lindsley (1985) and the Webb and Wood (1986) thermometers is reasonably good, considering the different types of equilibria used.
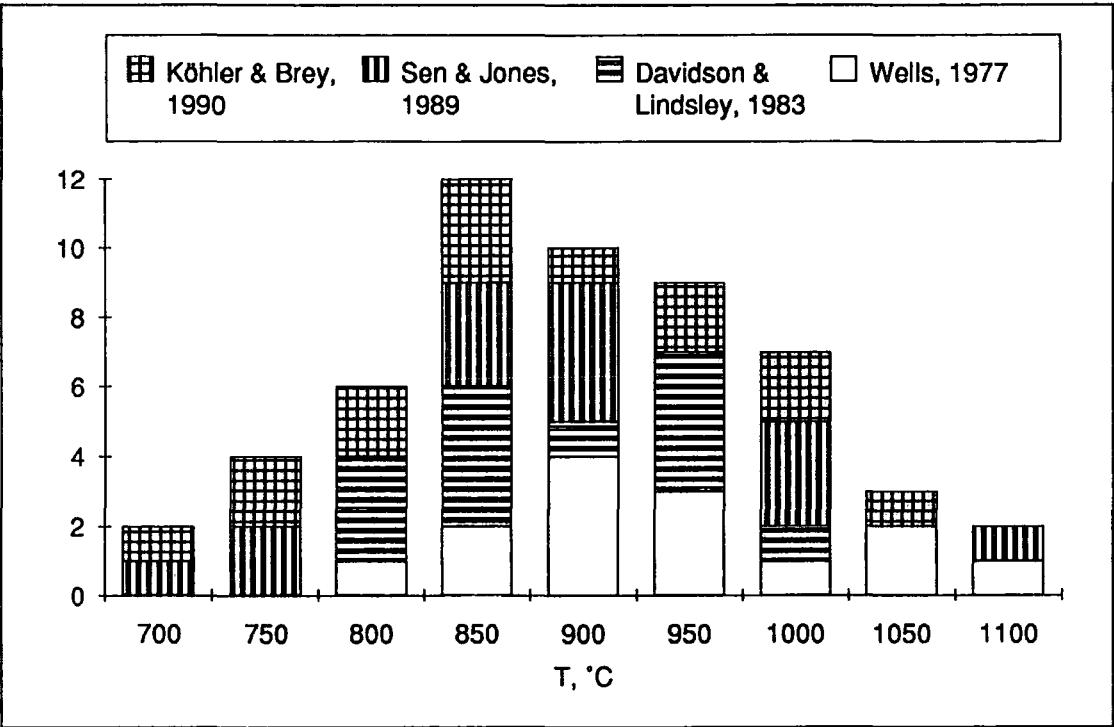
Figure (3.22) Frequency diagram of temperature for the coexisting pyroxenes thermometers. A total of 14 harzburgites is shown.

3.5. Geobarometry

Unfortunately, an accurate and easy to use geobarometer for spinel-facies peridotites is not available. The Al exchange between orthopyroxene and a co-existing Al-rich phase is pressure-dependent (MacGregor, 1974; Stroh, 1976), but the application to natural assemblages requires Al-saturation of the peridotite. In practice this restricts the application to garnet peridotites (Nickel and Green, 1985) and, possibly, to fertile spinel lherzolites. Pindos peridotites, however, in common with other ophiolite peridotites (e.g. Dick, 1977), are Al-undersaturated (see earlier, orthopyroxene chemistry) and application of the geobarometer is not meaningful.

Mercier et al. (1984) formulated an empirical barometric relation based on the ratio

$$K_f = [Ca^*]_{opx}/(1-[Ca^*]_{cpx})$$ (3.23)

where

$$Ca^* = Ca/(1-Na)_{opx}(1-Na)_{cpx}$$ (3.24)

Mercier et al. (op. cit.) used available experiments in the CMS and CMAS systems to calibrate two simple equations:

$$P(Gpa) = 1.279/(K_f + 0.006) - 2.29 \qquad (3.25)$$

$$P(Gpa) = 1.073/(K_f + 0.028) - 1.65 \qquad (3.26)$$

Equation 3.25 was determined using all available data, while Equation 3.26 was determined using only experiments at pressures higher than 0.5 Gpa.

Application of either of Equations 3.25 or 3.26 to Pindos peridotites yielded widely varying and geologically unreasonable pressures in the range of minus 20 to plus 40 kb. Although the reason for this may be that the minerals that were used were in disequilibrium, it seems more likely that there are inherent deficiencies to the model. Firstly, it was formulated using CMS and CMAS data with no attempt to correct for the effect of Fe or Cr. The latter has been shown to have a drastic effect on pyroxene equilibria (Wells, 1977; Sachtleben and Seck, 1981) and this is especially true for the Pindos ultramafics due to their refractory nature. Secondly, Mercier et al. (1984) assumed that K_f is not temperature dependent, hence no temperature correction was used in Equations 3.25 or 3.26. Brey and Köhler (1990), however, use an almost identical parameter to K_f (Equation 3.22) in their thermometer, thus invalidating the assumption of Mercier et al. (1984). Notably, Mercier et al. (op. cit.) tested their geobarometer on Al-rich lherzolites (Newfoundland and Tibet) for which they obtained reasonable results.

Recently Köhler and Brey (1990) formulated a new geobarometer that is applicable to spinel and plagioclase lherzolites. This is based on the exchange of Ca in olivine coexisting with clinopyroxene according to reaction:

$$Mg_2SiO_4 + CaMgSi_2O_6 = CaMgSi_2O_6 + Mg_2SiO_4 \qquad (3.27)$$
olivine   clinopyroxene   olivine   clinopyroxene
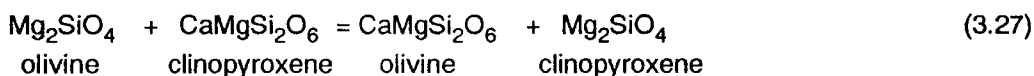
Although this barometer is considered very accurate (±1.7 kb) it requires the extremely accurate determination of Ca in olivine. Köhler and Brey (1990) used olivine

standards analysed by isotope dilution and analysed unknowns either with an ion probe or with a wavelength dispersive electron probe with three spectrometers simultaneously on Ca!

Despite the absence of a suitable geobarometer, some constraints can be placed in the depth of formation of the mantle sequence. The presence of spinel in the mantle signifies that the pressure was less than 20 kb (spinel lherzolite stability field) and less than 5 kb near the Moho, where plagioclase is found in the transition zone (plagioclase lherzolite stability field).

Additional information on the pressure of equilibration of the Pindos peridotites can be obtained from consideration of experimental melting studies on natural peridotites. The similarity in composition of the experimental charges with the natural assemblages permits a direct comparison of the two, whereas experiments in simple systems require rigorous thermodynamic modelling before they can be extended to complex systems. The experiments of Jaques (1980) on Hawaian pyrolite and Tinaquillo lherzolite have been selected for comparison, because they were performed in a wide range of temperatures and pressures.

Figure 3.23 shows that the Al_2O_3 wt.% content of orthopyroxene is pressure- as well as temperature dependent. However, the aluminium abundance of natural orthopyroxenes cannot be directly compared with that of the experimental orthopyroxenes before the effects of temperature and partial melting are minimized. This can be done if the Al_2O_3 content of orthopyroxene is normalized against that of spinel, since they show sympathetic variation, independent of temperature (see Figure 3.17). The effect of Cr partitioning between orthopyroxene and spinel is taken into account by using the Cr/Al ratio of each mineral instead of just their Al abundances. If then the ratio $\frac{(Cr/Al_{M1}^{opx})}{(Cr/Al)_{sp}}$ is plotted against Al_{opx}, a good separation of the experiments at different pressures should result. In practice, instead of Al_{opx}, the ratio (Ca^{opx}/Al_{M1}^{opx}) gives much clearer separation because, by including the Ca in orthopyroxene, the effects of coexisting clinopyroxene are taken into account.

Figure 3.25 is a plot of the ratio $\dfrac{(Cr/Al_{M1}^{opx})}{(Cr/Al)_{sp}}$ against (Ca^{opx}/Al_{M1}^{opx}) for the Pindos

peridotites. The fields for different pressures have been derived from the experiments of

Jaques (1980) (Figure 3.23). This plot confirms the suggestion that Pindos harzburgites have

equilibrated at relatively low pressures. The majority of the peridotites plot in the fields of 5-10

kb, while only one sample plots in the 2 kb field. Notably, the peridotites from Vovousa

(marked BO in Figure 3.25) plot at high pressures (10-15 kb). This is consistent with the

higher Al_2O_3 wt.% content of orthopyroxene in these samples, since the Al-solubility of

orthopyroxene increases with pressure at constant temperature.

A more rigorous parameterization of the experimental results that would yield

quantitative results is possible, however, it is questionable whether equilibrium melting

experiments can adequately reproduce the melting of natural peridotites and further

refinement is unwarranted.
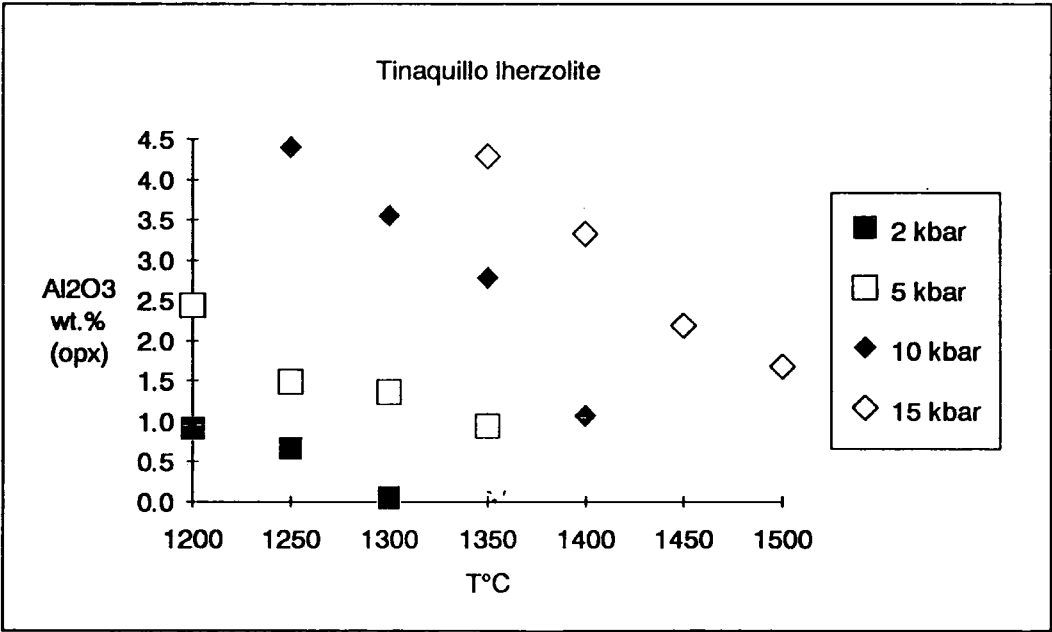
Figure (3.23) Variation of the Al_2O_3 wt.% content of orthopyroxene with pressure and
temperature for the experiments of Jaques (1980) on the Tinaquillo lherzolite.
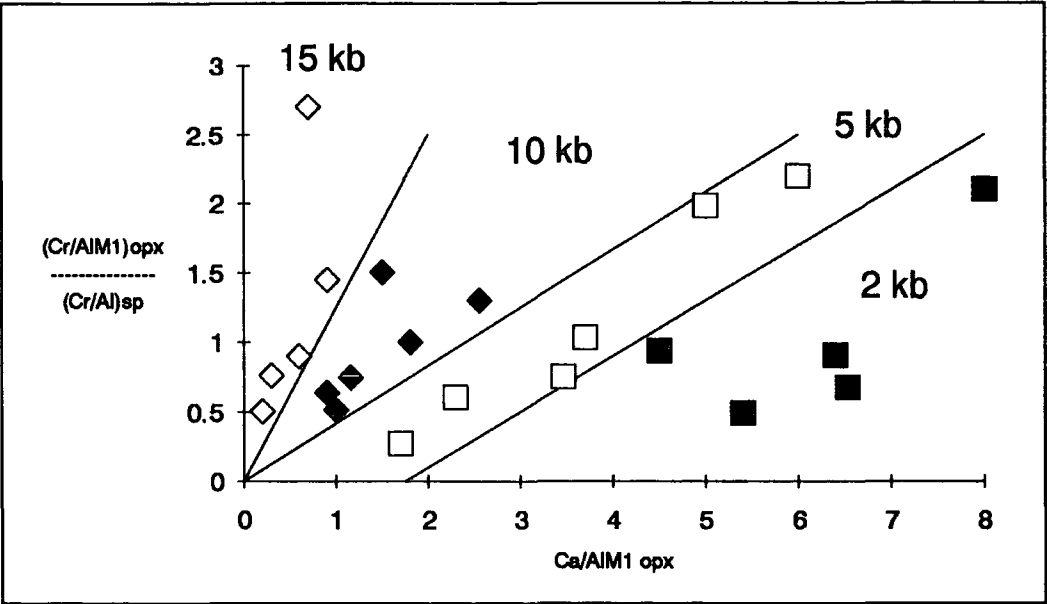
Figure (3.24) Plot of $\dfrac{(Cr/Al)_{opx}}{(Cr/Al)_{sp}}$ vs. (Ca^{opx}/Al_{M1}^{opx}) for the experiments of Jaques (1980) on

Hawaian pyrolite and Tinaquillo lherzolite. The plot achieves good separation of the experiments at the same pressure regardless of temperature or composition. Symbols as in Figure 3.23.
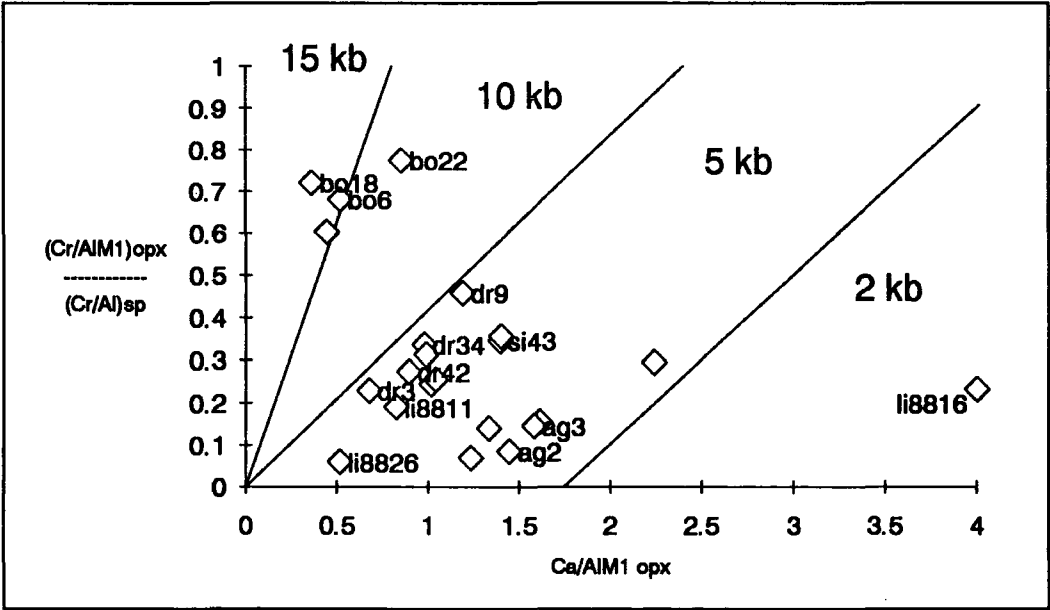
Figure (3.25) Estimated pressures of equilibration for the Pindos harzburgites. Pressure fields from Figure 24.

3.6. Oxygen fugacity

Mineral equilibria involving phases of variable Fe^{2+}/Fe^{3+} ratios have the potential to provide information about the redox state of the system where they were formed. For example, the Fe^{2+}/Fe^{3+} ratio has been used to calculate the oxygen fugacity of mantle derived basalts (Haggerty, 1978). For solid assemblages, equilibria between olivine-orthopyroxene-ilmenite and spinel-ilmenite have been used (Eggler, 1983, Haggerty and Tompkins, 1983) to obtain estimates of the equilibrium oxygen fugacities in mantle derived xenoliths and megacrysts. The scarcity, however, of ilmenite in all but a small percentage of mantle-derived rocks limits the value of this method. In contrast, the assemblage olivine-orthopyroxene-spinel is present in a wide range of rock compositions and mantle conditions and can be used to extract information about the redox state of the mantle. At least three independent calibrations of oxygen geobarometers, that are based on the olivine-orthopyroxene-spinel assemblage, have appeared recently in the literature (O'Neill and Wall, 1987, Ballhaus et al., 1990, Wood, 1990). The reaction that forms the basis of the olivine-orthopyroxene-spinel oxygen geobarometer is the quartz-fayalite-magnetite (QFM) equilibrium (Equation 3.28). Simple thermodynamics can be used to describe the state of the system at equilibrium (Equation 3.29).

$$3\ Fe_2SiO_4 + O_2 = 2\ Fe_3O_4 + 3\ SiO_2 \tag{3.28}$$
olivine   spinel   quartz
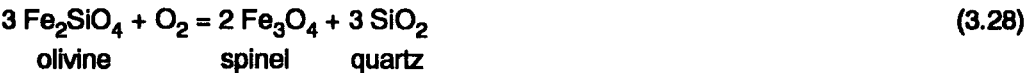
$$\log(f_{O_2}) = \frac{\Delta G}{2.303RT} + 2\log(a^{sp}_{Fe_3O_4}) + 3\log(a_{SiO_2}) - 3\log(a^{ol}_{Fe_2SiO_4}) \tag{3.29}$$

The different versions of the geobarometer will be presented and compared below.

3.6.1. O'Neill and Wall (1987)

Since peridotites are SiO_2 undersaturated, O'Neill and Wall (1987) calculated the silica activity from reaction 3.30.

$$Mg_2SiO_4 + SiO_2 = Mg_2Si_2O_6 \tag{3.30}$$

olivine   quartz   enstatite

They used available thermodynamic data and adopted an ideal two site mixing model for orthopyroxene and a two-site regular model for olivine to calculate the activities of forsterite, fayalite and enstatite. O'Neill and Wall's (1987) expression for the activity of SiO_2 in the mantle assemblage is:

$$\log\,(a_{SiO_2}) = -\frac{350}{T} - \frac{0.020P}{T} + \log\,(a_{Mg_2Si_2O_6}^{opx}) - \log\,(a_{Mg_2SiO_4}^{ol}) \tag{3.31}$$

In order to calculate the activity of magnetite in spinel O'Neill and Wall (1987) used the complex model for multicomponent spinel of O'Neil and Navrotsky (1984) and calculated the oxygen fugacity from Equation 3.29. A by-product of their work was the formulation of the olivine-spinel thermometer that was presented earlier. The uncertainty of the thermodynamic data that O'Neill and Wall (1987) used results in an accumulated error for the calculated f_{O_2} of ~0.5 log units (O'Neil and Wall, 1987).

3.6.2. Wood (1990)

Wood (1990) used equilibrium 3.32 to formulate his version of the olivine-orthopyroxene-spinel oxygen geobarometer. This reaction is essentially identical to Equation 3.28 but it leads to the use of a different set of components for the calculation of oxygen fugacity.

$$6Fe_2SiO_4 + O_2 = 3Fe_2Si_2O_6 + 2Fe_3O_4 \tag{3.32}$$
$$\text{olivine} \qquad\qquad \text{orthopyroxene} \quad \text{spinel}$$
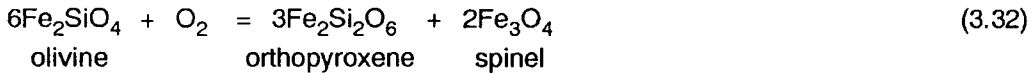
Olivine and orthopyroxene activities were treated in the same way as in the O'Neill and Wall (1987) version, but magnetite activity in spinel was calculated by measuring the Fe_3O_4 content of experimental spinels and using the spinel model of Nell and Wood (1989). He then used the Mattioli and Wood (1988) model for Equation 3.29 and arrived at Equation 3.33:

$$\log(f_{O_2})_{PT} = \frac{220}{T} + 0.35 - \frac{0.0369P}{T} - 12\log X_{Fe}^{ol} - \frac{2620}{T}(X_{Mg}^{ol})^2 + 3\log(X_{Fe}^{M1}X_{Fe}^{M2})_{opx} + 2\log a_{Fe_3O_4}^{sp} \tag{3.33}$$

where X_{Fe}^{ol} and X_{Mg}^{ol} refer to mole fractions of Fe and Mg end-members in olivine, P is in bars, T is temperature in Kelvin, $X_{Fe}^{M1}X_{Fe}^{M2}$ in orthopyroxene refer to atomic fractions of Fe in the two orthopyroxene sites.

The $a_{Fe_3O_4}^{sp}$ is given by:

$$\log a^{sp}_{Fe_3O_4} = \log\left[\frac{(Fe^{2+})(Fe^{3+})^2}{4}\right] + \frac{1}{T}\left(406(Al)^2 + 653(Mg)(Al) + 299(Cr)^2 + 199(Al)(Cr) + 346(Mg)(Cr)\right)$$

$$(3.34)$$

where the terms in parentheses (Al), (Cr) etc. refer to total Al, Cr, Mg, Fe^{2+} and Fe^{3+} cations in the spinel structure on a four oxygen basis.

3.6.3. Ballhaus et al. (1990)

Ballhaus et al. (1990) used a semi-empirical approach in formulating their version of the olivine-orthopyroxene-spinel oxygen barometer. They performed experiments on spinel lherzolites over a range of pressures from 1 to 2.5 GPa, temperatures from 1313 to 1573°K, f_{O_2} from iron-wüstite to magnetite-haematite and mole fraction of Cr in spinel from 0.19 to 0.85. They determined the numerical parameters by multiple linear regression to arrive at an equation that gives the difference in oxygen fugacity relative to the QFM buffer (Equation 3.35).

$$\Delta\log(f_{O_2}) = 0.27 - \frac{2505 - 400P - 3200(1 - X^{Ol}_{Fe})^2 + 2630(X^{sp}_{Al})^2}{T} - 6\log(X^{Ol}_{Fe}) + 2\log(X^{sp}_{Fe^{2+}}) + 4\log(X^{sp}_{Fe^{3+}})$$

$$(3.35)$$

where T is in °K, pressure P in GPa, X^{Ol}_{Fe} and $X^{sp}_{Fe^{2+}}$ are the $Fe^{2+}/(Mg+Fe^{2+})$ cation ratios in olivine and spinel, and $X^{sp}_{Fe^{3+}}$ and X^{sp}_{Al} are the $Fe^{3+}/\sum R^{3+}$ and $Al/\sum R^{3+}$ cation ratios in spinel.

It will be noted that the orthopyroxene composition does not appears in this formulation. This is because since its composition can be calculated from the composition of the equilibrium olivine (e.g. Sack and Ghiorso, 1989) and is, thus, implicitly accommodated in the parameterization. An advantage of this formulation is that it permits the calculation of oxygen fugacity in dunites, assuming that they are close to equilibrium with orthopyroxene. Ballhaus et al. (1990) suggested that the uncertainty of the calculated f_{O_2} is ~0.5 log units.

3.6.4. Application and comparison

In order to facilitate comparison, the oxygen fugacities have been calculated relative to the QFM buffer (O'Neil, 1987). The temperature used in the calculations is the average of the four olivine-spinel geothermometers. The reason for this choice is that they are more

consistent than the olivine-orthopyroxene-spinel thermometers and can be applied to assemblages that lack clinopyroxene. Since oxygen fugacity is calculated at the same temperature for every version of the oxygen geobarometer, the low temperatures calculated using these thermometers do not affect the results. In Figures 3.26 to 3.28 ΔlogQFM, calculated with the three different calibrations presented above, is plotted against Cr/(Cr+Al) in spinel as reference.

Comparison of Figures 3.26-3.28 shows that the f_{O_2} calculated using the method of O'Neil and Wall (1987) is as low as 5 log units below QFM, considerably lower that the results from either the Wood (1990) (Figure 3.27) or Ballhaus et al. (1990) methods Figure 3.28) . In fact, comparisons of this barometer with the newer calibrations (Wood, 1990; Ballhaus et al., 1990, 1991) has shown that it consistently reports lower f_{O_2}'s by 0.5-1.5 log units. In addition, Ballhaus et al. (1991) showed that the thermometric and barometric expression of O'Neil and Wall (1987) is dependent on spinel composition, particularly Cr#. This composition dependence, and the fact that the other two expressions agree whithin ~0.5 log units with each other, suggests that the barometer of O'Neil and Wall (1987) is not suitable for the Cr-rich Pindos peridotites and it will not be further considered.

Figures 3.29 and 3.30 show the calculated f_{O_2} using the two more recent calibrations in relation to other peridotites. There is a systematic tendency of the Wood (1990) expression to report f_{O_2}'s slightly higher than the Ballhaus et. al. (1990) method. This has been noted in other studies as well (Ballhaus et al., 1990, 1991), but this difference is within the uncertainty of either method and neither formulation will be favoured. Before discussing, however the fields shown in Figures 3.29 and 3.30, the validity of an important assumption in calculating f_{O_2} must be considered.
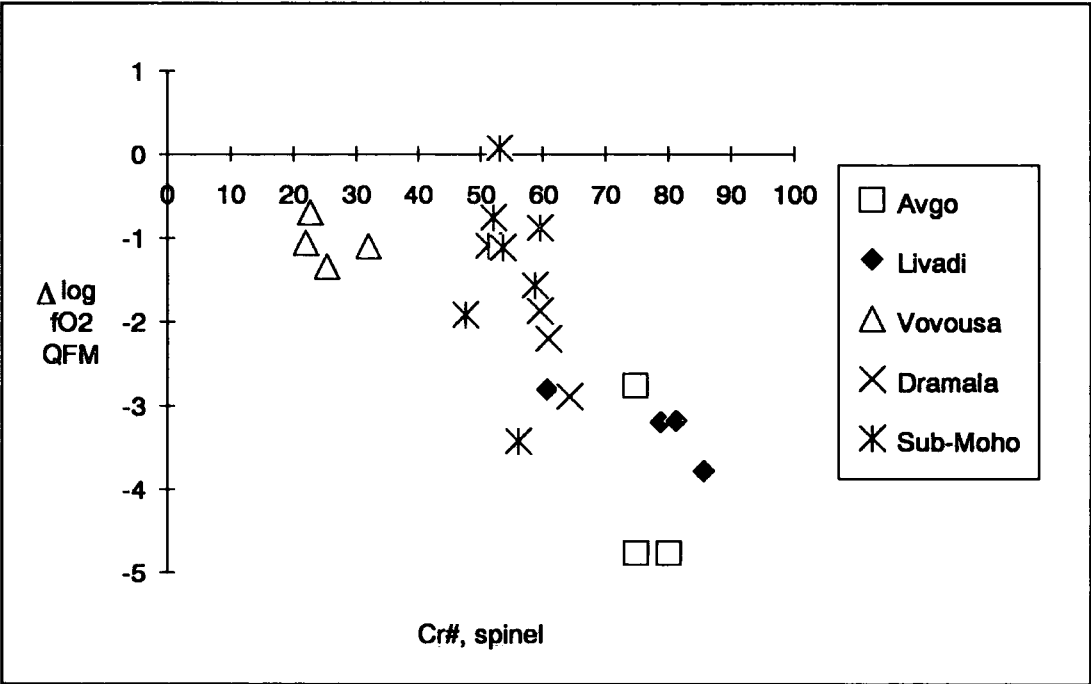
Figure (3.26) ΔlogQFM vs. Cr# in spinel for Pindos harzburgites from various localities. Calculated with the oxygen geobarometer of O'Neil and Wall (1987).
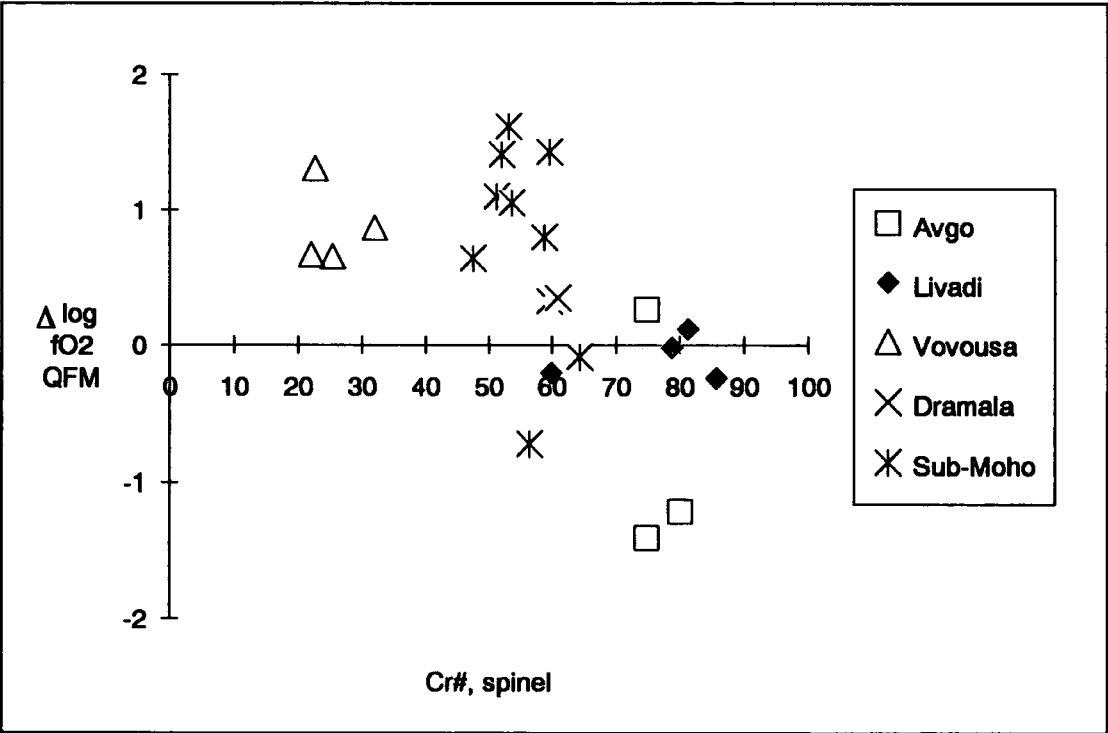
Figure (3.27) ΔlogQFM vs. Cr# in spinel for Pindos harzburgites from various localities. Calculated with the oxygen geobarometer of Wood (1990).
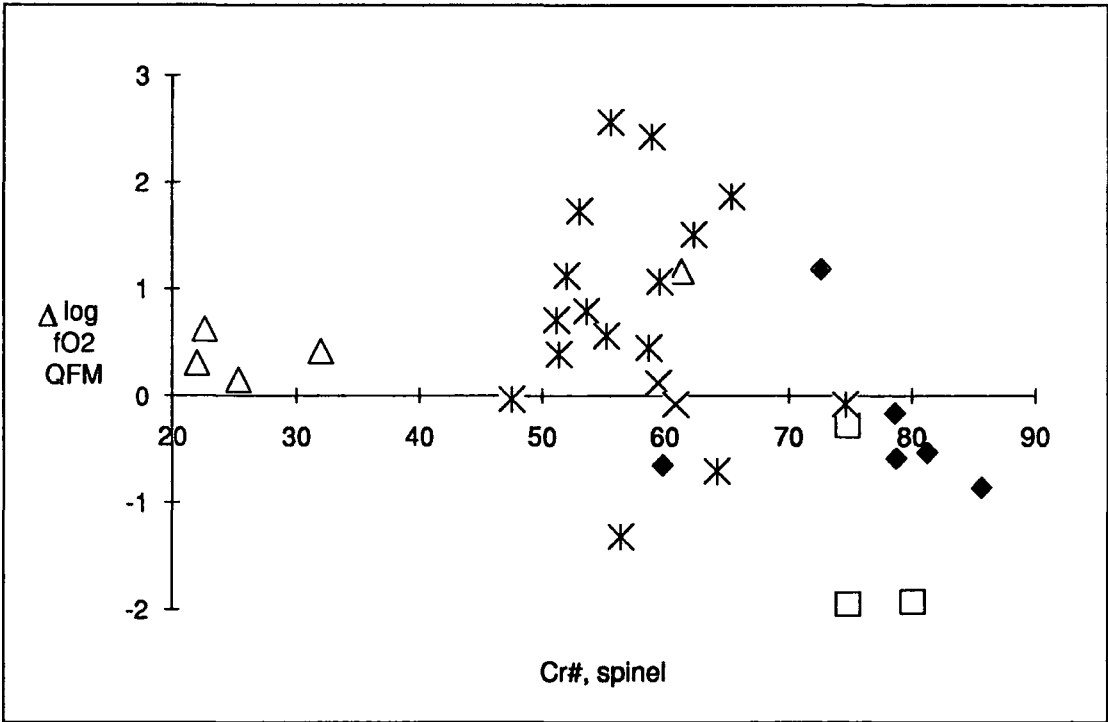
Figure (3.28) ∆logQFM vs. Cr# in spinel, calculated with the oxygen geobarometer of Ballhaus et al. (1990). Symbols as in Figure 3.27.
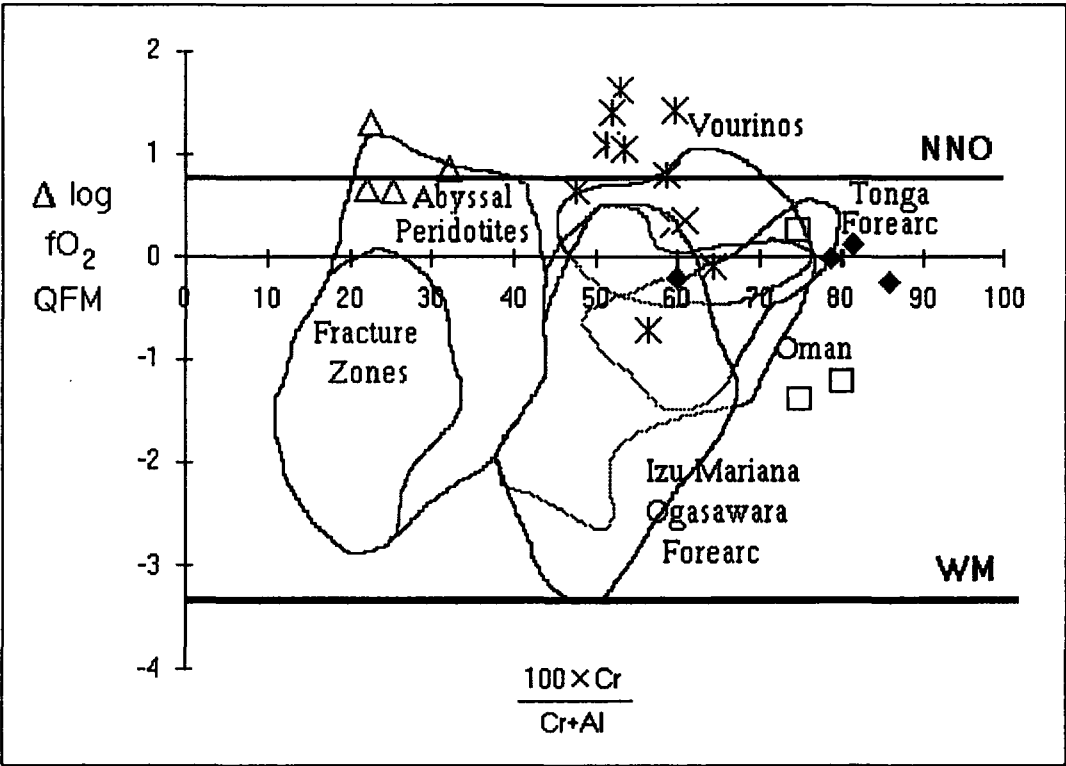
Figure (3.29) ∆logQFM vs. Cr# in spinel, calculated with the oxygen geobarometer of Wood (1990). Symbols as in Figures 3.26 to 3.28. The fields for various peridotites were calculated from published analyses. Sources for abyssal peridotites, Vourinos, and Oman are listed in Figure 3.2. Fracture zones: Dick (1989). Tonga forearc: Bloomer and Fisher (1987). Izu-Mariana-Ogasawara Forearc: Ishii et al. (in press). The positions of the nickel-nickel oxide and wüstite-magnetite buffers relative to QFM are calculated at 1200°C.
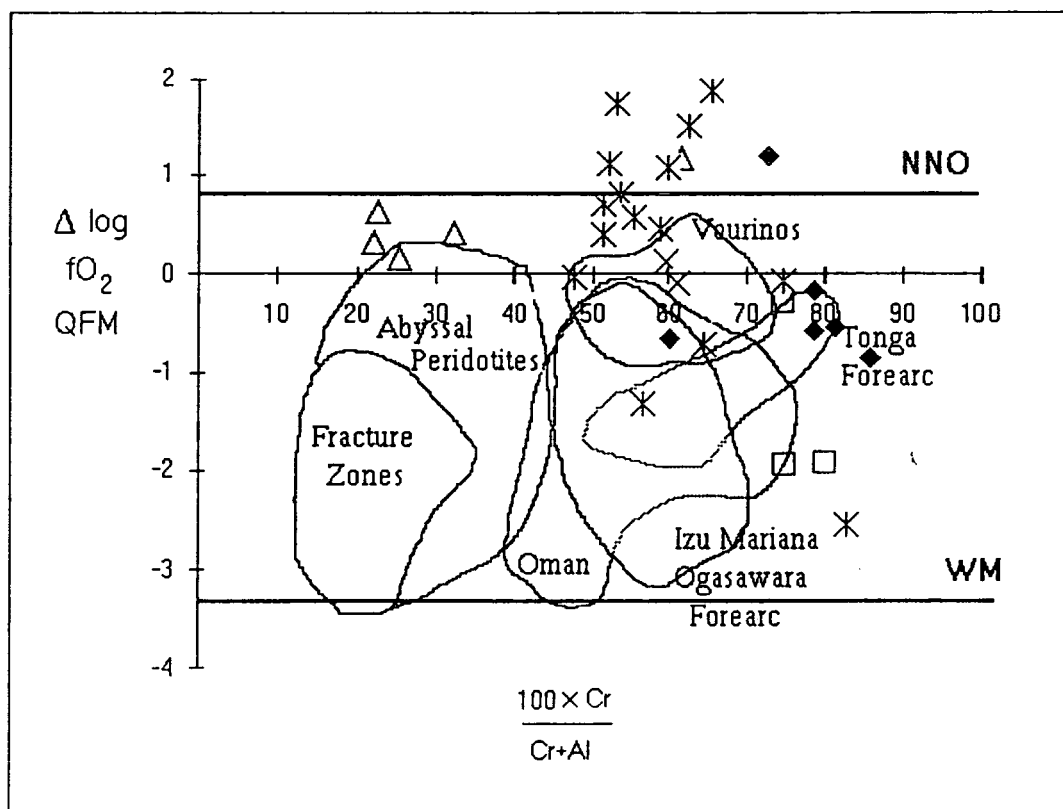
Figure (3.30) ΔlogQFM vs. Cr# in spinel, calculated with the oxygen geobarometer of Ballhaus et al. (1990). Symbols and fields as in Figure 3.29.

3.6.5. Determination of the magnetite fraction in spinel

With the development of the olivine-orthopyroxene-spinel oxygen geobarometer the validity of determining the Fe^{3+} fraction of spinel by stoichiometry[2] has been questioned (Wood and Virgo, 1989; Wood, 1991, pers. comm.). The argument presented by these authors is that, in calculating the Fe^{3+} fraction of spinel by stoichiometry, a very small quantity is determined by the difference of the sum of two large quantities (Cr+Al in spinel) from ideal site ocuppancy. It follows that even relatively small errors in the determination of Al and Cr, which would be acceptable for any other purpose, result in large errors for Fe^{3+}. In addition, empirical correction factors for Al in microprobe correction procedures are poorly constrained (Wood and Virgo, 1989) and introduce additional systematic errors. Wood and Virgo (op. cit.) presented a compelling

---

[2] In stoichiometric spinels the ratio of the trivalent to divalent atoms is 2. This permits the determination of the Fe^{3+} fraction of spinel when this ratio deviates from the ideal.

argument, showing that in microprobe analyses of the same spinel at different laboratories using different correction procedures (ZAF, Bence & Albee, PAP) the magnetite fraction of spinel ($X_{Fe_3O_4}$) varied by a factor of up to 5. This variation of $X_{Fe_3O_4}$ is equivalent to ~3.5 log units of f_{O_2} or a variation from below QFM to iron-wüstite, thus rendering any calibration of the barometer useless.

Wood and Virgo (1989) showed that, with careful calibration, microprobe analyses can be precise enough to be of use in determining $X_{Fe_3O_4}$, but is very inaccurate, i.e. $X_{Fe_3O_4}$ calculated by stoichiometry has a low standard error and good reproducibility but this value is different from the $X_{Fe_3O_4}$ as determined by Mössbauer spectroscopy. In order to improve this inaccuracy they suggested a procedure, whereby the $X_{Fe_3O_4}$ of spinel as determined by stoichiometry is re-calculated using secondary spinel standards of known $Fe^{2+}/\Sigma Fe$ ratio.

Despite the apparent superiority of Mössbauer spectroscopy as an analytical method of determination of $X_{Fe_3O_4}$, Ballhaus et al. (1991) suggested that this is not necessarily true. They noted that Mössbauer spectroscopy requires relatively large samples (~200 mg for typical mantle spinels) and single grains, later selected as secondary standards, may not be representative of the bulk $Fe^{2+}/\Sigma Fe$ ratio. They also pointed out that the interpretation of Mössbauer spectra for spinel is disputed and errors are potentially large (see also Dyar et al., 1989; Canil et al, 1990). Ballhaus et al. (1991) suggested that continuous checking of the microprobe calibration against a well-defined spinel standard, that is not included in the calibration, yields sufficiently accurate $X_{Fe_3O_4}$, as long as spinel is stoichiometric. The fact that Ballhaus et al. (1990) calibrated their version of the oxygen geobarometer using this method strongly supports the conclusion of Ballhaus et al. (1991).

Additional evidence in favour of the determination of $X_{Fe_3O_4}$ by stoichiometry comes from the determination of f_{O_2} in abyssal peridotites (Figures 3.29 and 3.30). The range and average of f_{O_2} is indistinguishable from the f_{O_2} as deduced from MORB (Christie et al., 1986) and as determined directly from spinel separates (Bryndzia et al., 1989; Bryndzia and Wood, 1990) using Mössbauer spectroscopy. Notably, Bryndzia and Wood (1990) report that they found no significant difference to the $X_{Fe_3O_4}$ as determined by Mössbauer spectroscopy and stoichiometry.

3.6.6. Oxygen fugacity calculated using secondary spinel standards

In an attempt to ascertain whether determination of $X_{Fe_3O_4}$ is accurate and verify the results of this study, the method of Wood and Virgo (1989) was used to determine the $Fe^{2+}/\Sigma Fe$ ratio of spinels in the Pindos peridotites. This method involves the empirical correction of the $Fe^{2+}/\Sigma Fe$ ratio using spinels of known $Fe^{2+}/\Sigma Fe$ ratio (determined by Mössbauer spectroscopy). The secondary spinel standards used were separates from continental spinel lherzolites (KLB8305, KLB8311, KLB8316, and MHP79-1, Wood and Virgo, 1989) supplied by Professor Wood.

After the usual calibration of the microprobe, the secondary spinel standards were ana-lysed 10-15 times before and after analysis of the unknowns and a calibration curve of the type:

$$\frac{Fe^{2+}}{\Sigma Fe}\text{Mössbauer} - \frac{Fe^{2+}}{\Sigma Fe}\text{calculated} = A + B * Cr\# \tag{3.36}$$

was constructed. The coefficients A and B change from day to day, depending on the analytical conditions and calibration of the microprobe, but this change was found to be small and, subsequently, an average correction curve was constructed and used to correct previously obtained analyses (Figure 3.31).
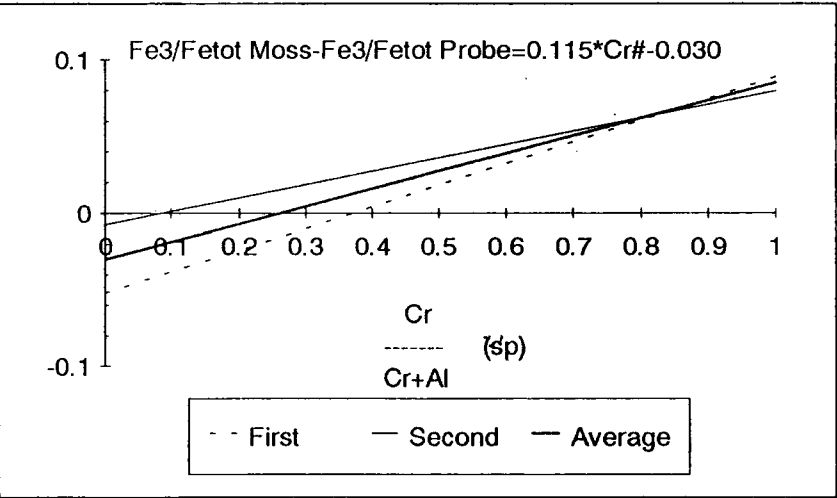
Figure (3.31) Empirical correction of the $Fe^{2+}/\Sigma Fe$ ratio of spinels using secondary spinel standards.
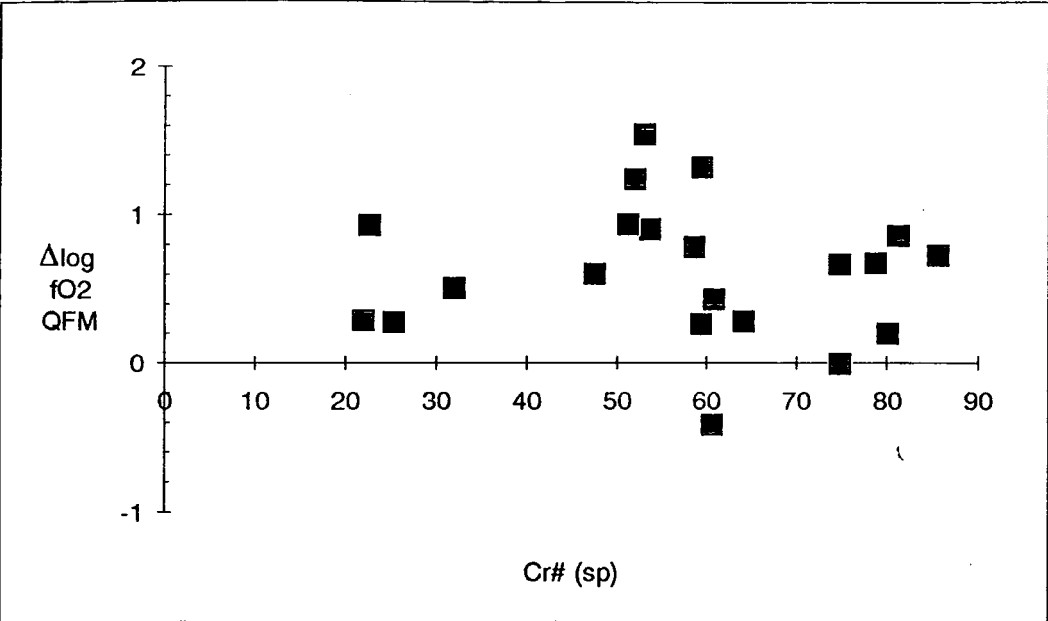
Figure (3.32) ΔlogQFM vs. Cr# in spinel for Pindos harzburgites. $X_{Fe_3O_4}$ in spinel was corrected using the method of Wood and Virgo (1989). ΔlogQFM was calculated with the oxygen geobarometer of Wood (1990).
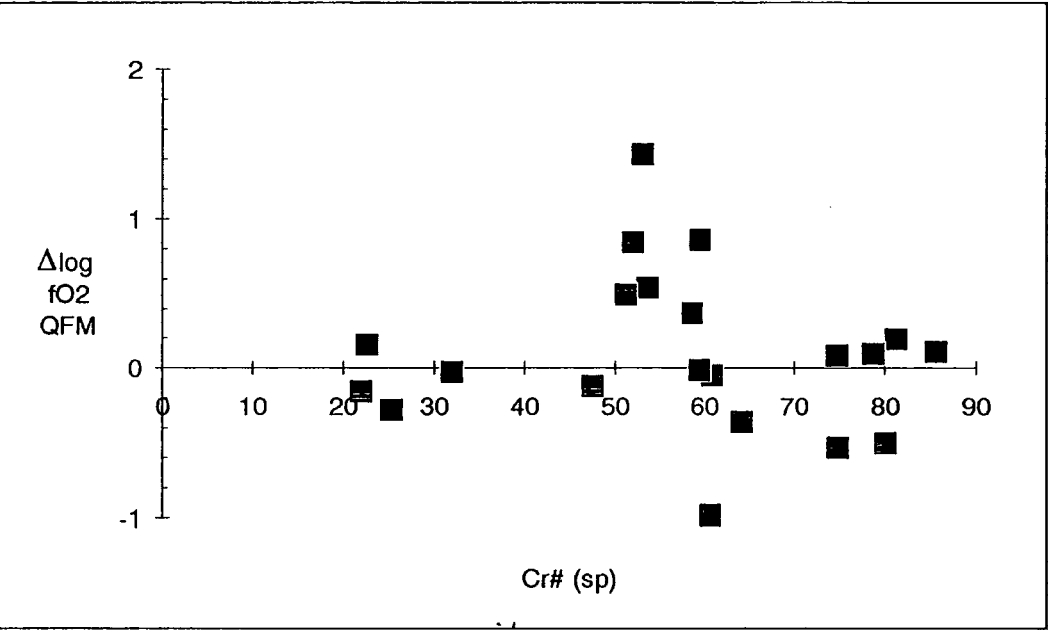
Figure (3.33) ΔlogQFM vs. Cr# in spinel. $X_{Fe_3O_4}$ in spinel was corrected using the method of Wood and Virgo (1989). ΔlogQFM was calculated with the oxygen geobarometer of Ballhaus et al. (1990).

The f_{O_2} values calculated with the calibrations of Wood (1990) and Ballhaus et al. (1990) using the corrected spinel analyses are shown in Figures 3.32 and 3.33. It will be noted that, whereas in Figures 3.26 to 3.28 a range of f_{O_2} of almost 4 log units was displayed,

the range of f_{O_2} calculated using the corrected spinel compositions is considerably smaller. Furthermore, those peridotites that showed very reduced f_{O_2} (as much as 3 log units below QFM) are now indistinguishable from the rest.

As described earlier, the oxygen fugacities calculated with the Wood (1990) version of the oxygen geobarometer are slightly higher than those calculated with the Ballhaus et al. (1990) version. The average f_{O_2} for the Wood (1990) expression is 0.6 log units above the QFM buffer and that the Ballhaus et al. (1990) formulation is 0.1 log units above the QFM buffer. It will be noted that the peridotites with the lowest Cr# (Vovousa samples) show essentially the same f_{O_2} as the other peridotites. Since a mid-ocean ridge origin was inferred for these samples, the similarity of their redox state with the more depleted peridotites suggests that the whole complex equilibrated at the same f_{O_2} conditions. Assuming that the elevated f_{O_2} of subduction-related peridotites results from the introduction of water from the subducting slab, it appears that water was also introduced to the Vovousa peridotites.

This change in the calculated oxygen fugacities has significant consequences regarding the redox conditions of the Pindos peridotites. Island-arc magmas are generally more oxidized than MORB (Arculus, 1985; Ballhaus et al., 1991) and, since the redox condition of a melt is imposed on it in its source region (Carmichael, 1991), MORB mantle is expected to be more reduced than SSZ-related peridotites. Figures 3.29 and 3.30, however, suggest that there is no difference between the oxidation state of abyssal and SSZ-related peridotites. Unfortunately the fields in these figures were calculated by stoichiometry using published analyses and there is no way to check the accuracy of these calculations. In view of the drastic effect of the Mössbauer correction on Pindos spinels, it must be concluded that the calculations are meaningless.

Thus, the results from the corrected calculations for Pindos are in good agreement with the generally accepted suggestion that SSZ-related magmatism involves relatively oxidized source regions. It will be noted that in all the calculated f_{O_2}'s presented in Figures 3.26 to 3.33, the sub-Moho peridotites show consistently higher f_{O_2} than the rest of the samples. This suggests that the melt that impregnated these samples had a high oxidation state that reset the redox state of the spinels.

3.7. Summary

The Pindos peridotites have experienced extensive deformation and recrystallization, probably in two stages. A high temperature event (~1000°C) recorded in the majority of the samples that resulted in porphyroclastic textures (Mercier and Nicolas, 1975). The lattice of minerals forming porphyroclasts is displaced and sub-grains or kink bands are formed. Pyroxenes have bent cleavage and exsolution lamellae. Spinels, originally as large grains, have been recrystallized and re-distributed as small grains interstitial to the silicates. Foliation is often developed by the alignment of porphyroclasts in preferred orientation. A low temperature event (?800°C) resulted in extensive recrystallization. Neoblasts are formed, in varying proportions to the porphyroclasts. The original coarse porphyroclastic textures are replaced to varying degrees by fine-grained mosaic textures (Mercier and Nicolas, 1975), where relict porphyroclasts, usually of orthopyroxene, persist.

The chemistry of the minerals shows a wide range of compositions that are interpreted as residua after partial melting of a fertile mantle, having experienced at least one episode of melt extraction. The peridotite mineral chemistry ranges from the relatively undepleted Vovousa peridotites to the refractory Avgo and Livadi harzburgites. Individual areas, however, show a more restricted range of compositions and more uniform degrees of partial melting. Comparison with peridotites from different geotectonic settings shows that there are systematic similarities. Thus, the Vovousa ultramafics show affinities to MORB-related peridotites, whereas the rest of the complex compares favourably with subduction-related peridotites. Given the distinction between melting in dry conditions of the Vovousa mantle, as opposed to the wet melting probably experienced by the rest of the complex, the composition and compositional range of the south part of Pindos are strikingly similar to peridotites dredged from present-day subduction zones. The process that produced this heterogeneity was probably the introduction of fluids from the subducting slab to parts of the overlying mantle wedge that responded in different ways. Thus, the Vovousa mantle bears evidence of fluid interaction (relatively high redox state) but did not experience second-stage melting, being probably too cold or, more likely, too deep. In contrast, peridotites from Livadi

and Avgo experienced large amounts of melting, exceeded only by those experienced by the harzburgite of the Papua ophiolite.

The Pindos ophiolite has experienced two stages of re-equilibration at low pressures (<10 kb). The first stage occurred over a relatively broad range of temperature, between 850-950°C, recorded by mineral equilibria with high-blocking temperatures, and the second at ~750°C, recorded by olivine-spinel pairs.

The oxygen fugacity of the peridotites, as recorded in the olivine-orthopyroxene-spinel equilibrium, is slightly oxidized, compared to mid-ocean ridge-related mantle, ranging from the QFM buffer to 1.5 log units above this buffer. Thus, the redox state of the Pindos mantle is appropriate for a source of subduction zone magmatism.

Chapter 4. Platinum-group elements (PGE)

4.1. Properties of the PGE

The PGE belong to group VII of the 5th and 6th transition periods of the periodic table. They exhibit strong siderophilic and chalcophilic affinities. The former is exemplified by their high concentration in iron meteorites, preferential partitioning in the Ni-Fe phase of chondrites and in the metallic phase in the presence of sulphides in iron meteorites, the tendency to form alloys between themselves and other metals and the high proportion of metallic bonding characteristics of many platinum-group minerals (PGM). Their chalcophilic affinities are indicated by their preference for the sulphide over the silicate phase, their high concentration in Ni-Cu ores and the existence of many platinum-group mineral sulphides. Keays and Crocket (1970) found that, in the absence of chalcogens, Pt is strongly siderophilic followed in this respect by Ir and Os .

Table 4.1 shows some of the properties of the PGE. Their metallic properties suggest a classification in pairs (Ru-Os, Rh-Ir, Pd-Pt), i.e. elements located on the same column of the periodic system (Westland, 1981). Os and Ru crystallize in an hexagonal close-packed lattice, as opposed to the cubic close-packed lattice of the rest of the PGEs. Thus Os and Ru form complete solid solutions between themselves but have restricted solubilities in the rest of the PGEs. Other elements with which PGEs form complete, temperature restricted or limited solid solution are As, Bi, Cu, Fe, Hg, In, Ni, Pb, Se, Sn and Te, although not all of the experimentally documented compounds exist in nature (see Berlincourt, 1981, for a compilation).

Being transitional elements the PGE have a wide range of oxidation states, the highest possible, as well as the most characteristic of which, increase with atomic number and decrease along a row from left to right. Only a fraction of the number of possible oxidation states of the PGE are found under geologically reasonable conditions. Only the low sulphides of Pt, Pd and Ir have been observed as minerals (see Table 4.2).

Naldrett et al. (1979) first used chondrite normalized spidergrams of the PGE in a manner analogous to chondrite normalized patterns of the REE. In contrast to the latter, the order of the PGE is not of increasing atomic number or atomic radius but of decreasing melting point, i.e. Os, Ir, Ru, Rh, Pt, Pd. This demonstrates the limited control of silicate phases over the PGEs, but it has yet to be proven experimentally that the PGE partition into any phase in that order (see later). Still, it is generally accepted that during partial melting and fractionation Os, Ir and Ru behave compatibly, whereas Rh, Pt and Pd behave incompatibly (e.g. Barnes et al., 1985). The two groups are referred to as IPGE and PPGE respectively. Because of the overwhelming abundance of Ir and Pd analyses in the literature, compared to those of the rest of the PGE (Cabri, 1981), they are often used as representative of their respective groups, and the Pd/Ir ratio as indicator of the degree of their fractionation, in much the same way that the La/Lu ratio is used to characterize the REE.

	Ru	Rh	Pd	Os	Ir	Pt
Atomic number	44	45	46	76	77	78
Atomic weight+	101.07	102.91	106.40	190.20	192.20	195.09
Lattice structure+	h.c.p.	f.c.c.	f.c.c.	h.c.p.	f.c.c.	f.c.c.
Lattice constant,a , Å *	2.7058	3.8031	3.8898	2.7341	3.8394	3.9231
c/a ratio*	1.5825			1.5799		
Density at 20°C, kg/m^{-3}X10^{-3}*	12.2	12.4	12.0	22.5	22.4	21.45
Melting point, °C*	2334	1967	1555	3050	2454	1768.4
Boiling point, °C*	3900	3727	3140	5027	4130	3827
Atom radius, cm^{-8} (12-fold coordination)*	1.336	1.342	1.373	1.350	1.355	1.385
radius, cm^{-8}*	1.241	1.247	1.278	1.255	1.260	1.290
Possible oxidation states +	0,(I),II, III,IV, (V),VI	0,I,II, III,IV,V, VI,VII,VIII	0,I,II, IV	0,(I),II, III,IV, (V),VI	0,(I),II,II I,IV, VI,VII,V III	0,II,III, IV,VI
Characteristic oxidation states +	III,IV,VI ,VII,VIII	III	II	VI,VII, VII	III,VI	II,IV

Table (4.1) Properties of the platinum-group metals. f.c.c. = face-centred cubic, h.c.p. = hexagonal close-packed. *Westland (1981), +Ginzburg et al. (1975)

Name	Composition	Symmetry
Anduoite ($RuAs_2$)	$(Ru,Os,Ir)As_2$	orthorhombic
Arsenopalladinite Pd(AsSb)	$(Pd_{7.99}Cu_{0.01})(As_{2.5}Sb_{0.5})$	triclinic
Braggite (PdS)	$Pt_{0.63}Pd_{0.24}Ni_{0.12}S_{1.01}$	tetragonal
Cooperite (PtS)	$Pt_{0.96}Pd_{0.03}Ni_{0.03}S_{0.99}$	tetragonal
Erlichmanite (OsS_2)	$(Os,Ru,Ir)S_2$	cubic
Froodite (a-$PdBi_2$)	$(Pd,Pt)(Bi,Te)_2$	monoclinic
Hollingworthite (RhAsS)	$(Rh,Pt,Ru)AsS$	cubic
Irarsite (IrAsS)	$(Ir,Ru,Rh,Pt)AsS$	cubic
Iridarsenite ($IrAs_2$)	$(Ir,Ru,Pt,Os)As_2$	monoclinic
Iridium (Ir>80 at.%)	$Ir,Pt,Os,...$	cubic
Iridosmine Ir>Os	$Os_{0.53}Ir_{0.41}Ru_{0.04}Fe_{0.01}Pt_{<0.01}Rh_{<0.01}$	hexagonal
Isoferroplatinum (Pt3Fe)	$Pt_{2.93}Fe_{1.01}Sb_{0.03}Cu_{0.02}Ni_{0.01}$	cubic
Laurite (RuS_2)	$(Ru,Os,Ir)S_2$	cubic
Moncheite ($PtTe_2$)	$Pt_{1.01}(Te_{1.96}Bi_{0.03})$	hexagonal
Nigliite (PtSn)	$Pt(Sn,Bi,Sb)$	hexagonal
Omeiite ($OsAs_2$)	$(Os,Ru,Ir)As_2$	orthorhombic
Osarsite (OsAsS)	$(Os_{0.48}Ru_{0.46}Ni_{0.04}Ir_{0.02}Pd_{0.02}Pt_{0.005}Rh_{0.005})$ $As_{1.05}S_{0.92}$	monoclinic
Osmiridium (Os>Ir)	$Ir_{0.57}Os_{0.35}Pt_{0.03}Ru_{0.03}Rh_{0.01}Fe_{0.01}Cu_{<0.01}$	cubic
Osmium (Os>80 at.%)	$Os, Ir, Ru, Pt, Pd, Rh, Fe, Cu, Ni...$	hexagonal
Palladium (Pd)	$Pd, Pb, Rh, Pt, Os, Ir...$	cubic
Platarsite ($Pt(AsS)_2$)	$Pt_{0.34}Rh_{0.30}Ru_{0.28}Ir_{0.05}Os_{0.01}As_{1.03}S_{0.99}$	cubic
Platinum (Pt>80 at.%)	$Pt_{0.80}Fe_{0.16}Cu_{0.03}Pd_{0.01}$	cubic
Prassoite (RhS)	$(Rh_{2.25}Cu_{0.35}Ru_{0.26}Ni_{0.09}Pt_{0.01})_3S_4$	cubic
Rhodium (Rh>Pt)	$Rh_{0.57}Pt_{0.43}$	cubic
Ruthenium (Ru>80 at.%)	$Ru,Pt,Ir,Rh,...$	hexagonal
Sperrylite ($PtAs_2$)	$Pt_{1.00}As_{1.99}Sb_{0.01}$	cubic
Stillwaterite (Pd_8As_3)	$Pd_{7.97}As_{3.03}$	hexagonal
Sudburyite (PdSb)	$(Pd_{0.97}Ni_{0.03})(Sb_{0.85}Te_{0.10}Bi_{0.05})$	hexagonal
Tetraferroplatinum (PtFe)	$(Pt_{1.03}Ir_{0.01})(Fe_{0.69}Cu_{0.24}Ni_{0.02}Sb_{0.01})$	tetragonal
Vysotskite (PdS)	$Pd_{0.89}Ni_{0.09}Pt_{0.01}S_{1.01}$	tetragonal
Xingzhongite (IrS?)	$Ir_{0.50}Cu_{0.35}Rh_{0.13}Pb_{0.07}S_{0.95}$	cubic

Table (4.2) Some platinum-group minerals. Where a specific composition is given it represents one for which crystallographic parameters have been measured, and it is not necessarily characteristic of the mineral. Cabri (1976, 1981)

4.2. PGE mineralogy

Table 4.2 lists some of the minerals in which PGE are major elements. Most of the information about PGM comes from mineralogical studies of layered intrusions, Ni-Cu sulphides and alluvial deposits. This reflects both the bias of the research towards economically important areas as well as the elusive nature of the PGM due to their minute size. In the last 10 years, however, an increasing amount of information has accumulated about the distribution of PGM in ophiolites (Constandinides et al., 1979; Stockman and Hlava, 1984; Legendre and Augé, 1985; Augé, 1988; Burgath, 1988; Cocherie et al., 1989; Prichard et al., 1989; Bacuta et al., 1990; Corrivaux and Laflamme, 1990) and especially PGE-enriched chromitites. There is not much information about the distribution of PGM in the mantle. Keays et al. (1981) first detected Pt-Pd-bearing sulphides in spinel lherzolite xenoliths and Stone and Fleet (1991) reported a Pd-bearing Pt-Fe alloy in olivine megacrysts from kimberlite, but no IPGE bearing phases have been yet identified in mantle-derived rocks.

The PGE also occur in solid solution in several sulphide, arsenide, telluride, selenide and sulpharsenide minerals. Of the base-metal sulphides, pentlandite and pyrrhotite have been reported to contain PGE (Chyi and Crocket, 1976; Cabri and Laflamme, 1981) and the latter has also been synthesized experimentally (Skinner et al., 1976). Ni and Co sulphides and alloys also can contain PGE (Cabri and Laflamme, 1981; Karup-Møller and Makovicky, 1986) and recently PGE-bearing awaruite (Ni_3Fe) has been found in chromitites from Thetford Mines (Corrivaux and Laflamme, 1990; Gauthier et al., 1990).

4.3. Pindos peridotites

Table 4.3 shows the PGE compositions for ten Pindos mantle peridotites together with the analyses of other mantle derived peridotites. The chondrite-normalized patterns for these peridotites are shown in Figure 4.1 and are compared with other peridotites in Figure 4.2. In common with the results of other studies, the peridotites have all relatively unfractionated PGE patterns, although some minor anomalies occur, e.g. a negative Pt anomaly for some of the Pindos samples, Troodos and Lewis Hill (but the opposite for

Thetford Mines) and a positive Rh anomaly for Pindos. These anomalies are difficult to explain, since there are many uncertainties about the behaviour of the PGE during partial melting. This, however, does not detract from the fact that the Pd/Ir ratios are essentially chondritic. The data of Page and Talkington (1984) for Ir and Ru in Newfoundland peridotites are maximum values and they may have similar true values with the rest of the peridotites.

	Rock Type	Os	Ir	Ru	Rh	Pt	Pd
BAK1	Harzburgite		1.9	3.5	1.0	2.8	4.2
AG1	Harzburgite		2.3	5.0	1.5	3.9	3.8
BO9	Harzburgite		2.3	4.3	0.9	2.6	1.0
DR42	Harzburgite		2.4	4.2	1.1	3.3	4.9
LI8821	Harzburgite		2.4	3.4	1.2	5.0	1.0
DR6	Harzburgite		2.5	5.0	2.0	18.0*	3.0
BO13	Harzburgite		2.6	6.0	1.8	5.2	3.4
DR34	Harzburgite		2.8	6.0	1.3	5.0	2.5
AG3	Harzburgite		2.9	6.2	1.2	7.0	2.6
BO6	Harzburgite		4.8	7.8	2.0	9.0	3.8
DR20	Dunite*		2.2	4.5	1.2	1.2	0.6
Harzburgite mean			2.7	5.1	1.4	4.5	3.0
Standard deviation			0.8	1.4	0.4	2.3	1.3
Range			4.8-	7.8-	2.0-	18.0-	4.9-
			1.9	3.4	0.9	2.6	1.0
Troodos	Harzburgite	4.0	3.0	6.5	1.0	3.5	6.0
Lewis Hill	Harzburgite	3.16	3.13	7.23	1.84	5.19	3.87
Newfoundland	Harzburgite		<25	<100	3.2	10.2	6.9
Thetford Mines	Harzburgite		3.2			10	3.8
Spinel lherzolite xenoliths[1]		3.4	3.7				3.6
Spinel lherzolite xenoliths[2]			2.95				4.1
Mantle estimate			5.2	7.7	1.4	10.7	6.0
Average C1 chondrite		515	540	687	196	1018	540

Table (4.3) PGE abundances of 10 harzburgites and one dunite from Pindos. Values are in ppb. Data from Troodos: Prichard and Lord (1990), Lewis Hill: Edwards (1990), Thetford Mines: Oshin and Crocket (1982), Newfoundland: Page and Talkington (1984), spinel lherzolites[1]: Morgan et al. (1981), spinel lherzolites[2]: Mitchell and Keays (1981), mantle estimate: Barnes et al. (1988), C1 chondrite average: Naldrett (1981b). *not included in mean and standard deviation calculation.
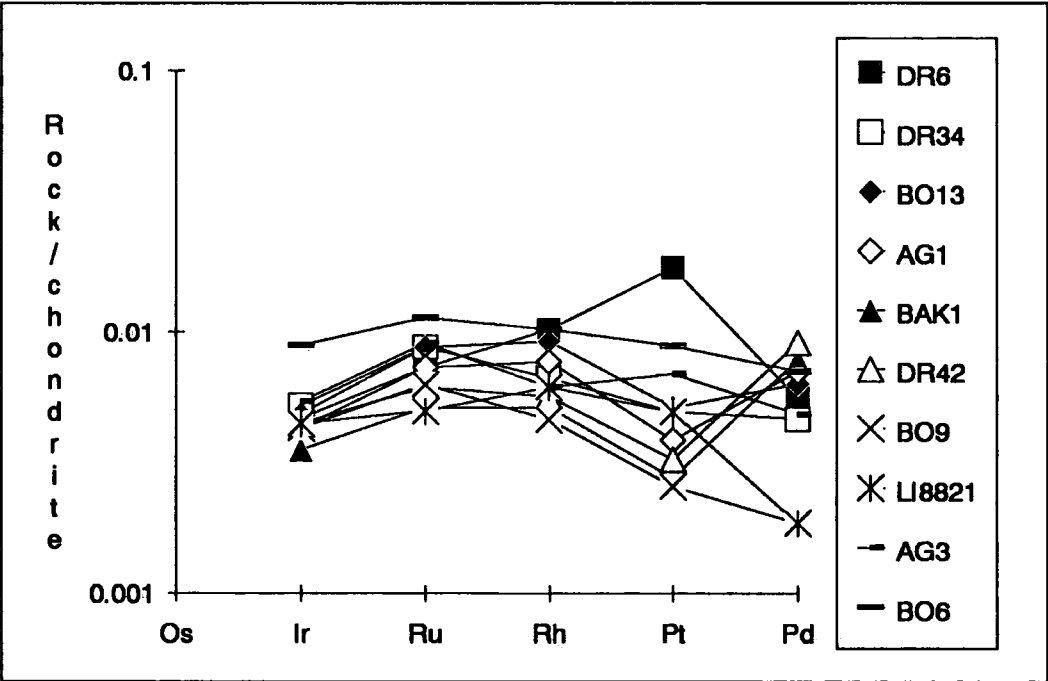
Figure (4.1) Chondrite-normalized patterns for the Pindos harzburgites in Table 4.3.
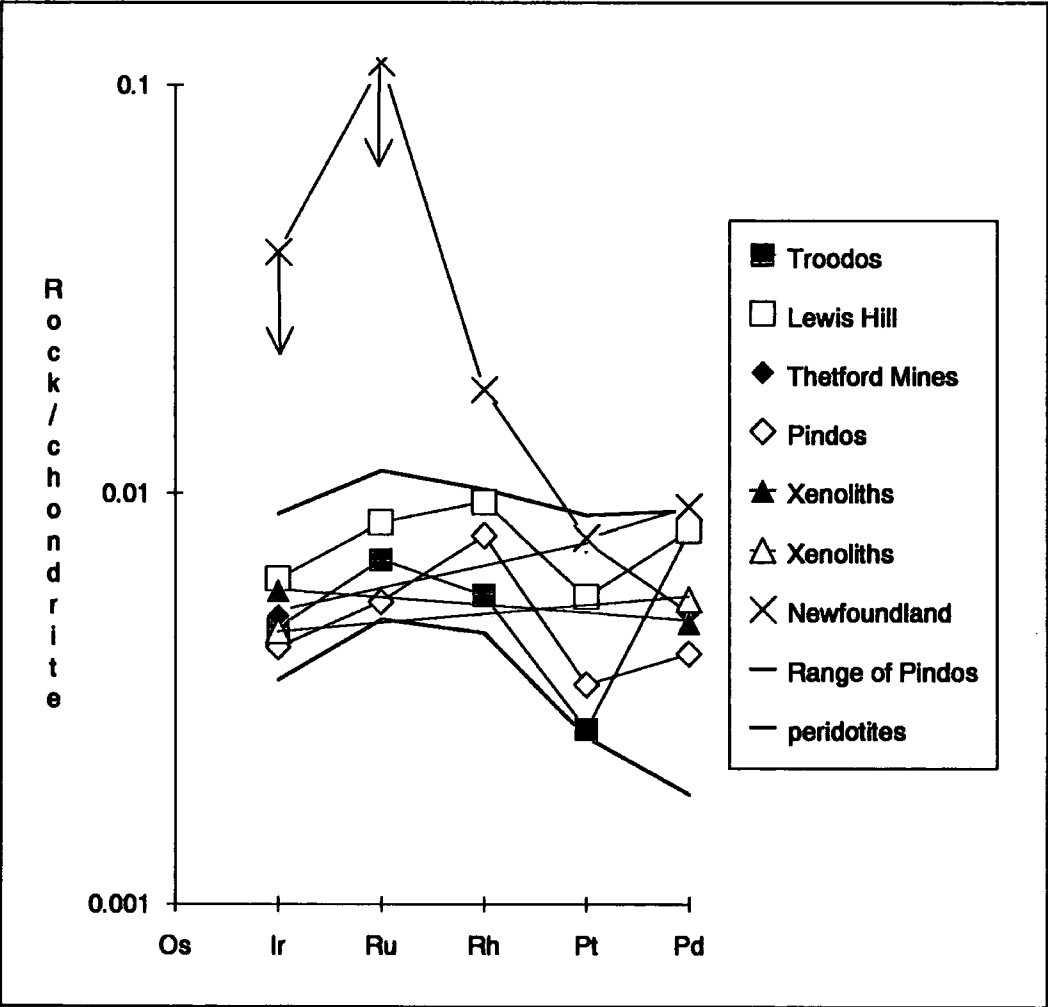
Figure (4.2) Chondrite-normalized patterns for the peridotites in Table 4.3.
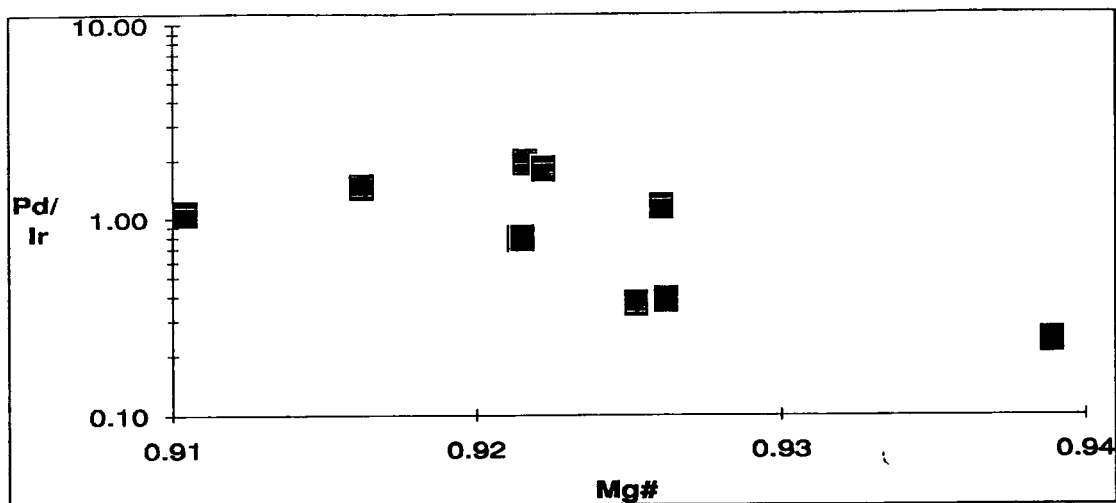
Figure (4.3) Plot of Pd/Ir vs. Mg# for the harzburgites of Table 4.3. There is a slight decrease of the Pd/Ir ratio with increasing Mg#.

Figure 4.3 shows that the Pd/Ir ratio varies with Mg#. There is a slight decrease of the Pd/Ir ratio with high Mg# but the trend is almost horizontal until an Mg# value 0.947. It appears that in the first stages of melting the two elements have similar distribution coefficients, whereas later Ir becomes more compatible than Pd.

One of the striking aspects of the PGE contents of the rocks of Table 4.3 is that, although they encompass the spectrum from fertile spinel lherzolites to depleted SSZ related harzburgites, they have relatively uniform PGE contents, especially taking into account the variability introduced by the different methods of analysis. This would suggest that the bulk partition coefficient during melting for each of the PGE is near 1.

4.4. Chromite-rich rocks

Table 4.4 shows the composition of four chromite-rich rocks from Pindos; the same compositions appear in Figure 4.4 along with compositions of other chromite-rich rocks from Alpine peridotite complexes and layered intrusions. It is apparent that the chromite-rich rocks are enriched in PGE relative to the peridotites of Table 4.3. Many other studies have confirmed the association of a high level of PGE with chromite relative to the spatially associated silicate rocks (i.e. dunites and harzburgites). Figure 4.5 shows the chondrite normalized patterns for chromitites from various ophiolite complexes that have a negatively sloping pattern. This feature of ophiolitic chromitites reflects their association with laurite and

Os-Ir alloys (Constandinides et al., 1979, Legendre and Augé, 1985, Stockman and Hlava, 1984, Augé, 1988, Burgath, 1988, Cocherie et al., 1989).

		Ir	Ru	Rh	Pt	Pd
742	chromitite	8.2	15.17	14.35	19.7	49.2
741	olivine chromitite	9.0	11.7	12.9	97.2	103.5
732	olivine chromitite	46.5	37.2	10.23	61.8	20.0
KK48	chromitiferous dunite	9.2	10.12	15.7	172	609

Table (4.4) PGE abundances of four chromite-rich rocks in Pindos. Values in ppb.

This relationship was contrasted with the positive pattern of chromitites from layered intrusions (Figure 4.4). Although this is true for the Bushveld complex, Talkington and Watkinson (1985) showed that, when examined in more detail, the Stillwater chromitite seams had more complex patterns (Figure 4.4). They argued that the pattern of a chromitite is inherited by its PGE mineralogy, the main difference being the presence of sulphides and arsenides that carry the PPGE. The mineralogic studies quoted all stressed the mode of occurrence of laurite and Os-Ir alloys, as primary euhedral inclusions in chromite and the association of PPGE-bearing minerals with the silicate matrix. They suggested that laurite and Os-Ir alloys precipitate early and are trapped by the nucleating chromite. Sulphides occur at a later stage, if sulphur saturation is attained. This conclusion has been upheld in subsequent studies of ophiolitic chromitites with positive patterns, where a high proportion of PPGE-bearing minerals has been identified (Prichard et al., 1989, Corrivaux and Laflamme, 1990).

Figure 4.4 shows that, with the exception of sample 732 that has has flat to negative pattern, Pindos chromitites have pronounced positive patterns. In particular, they have simlar Ir, Ru, and Rh abundances but varying Pt and Pd contents. Sample kk48 is particularly rich in Pd, reaching almost chondritic levels. This high Pd abundance is most likely due to the presence of a substantial fraction of Fe-Ni sulphides, constituting ~15% of the mode. Fe-Ni sulphides and alloys were detected in all other samples as well, but in smaller proportions, accounting for the different levels of Pt and Pd in these samples. In contrast, the Ir, Ru, and

Rh contents of these samples are fairly uniform, suggesting that they are not controlled by the sulphide.
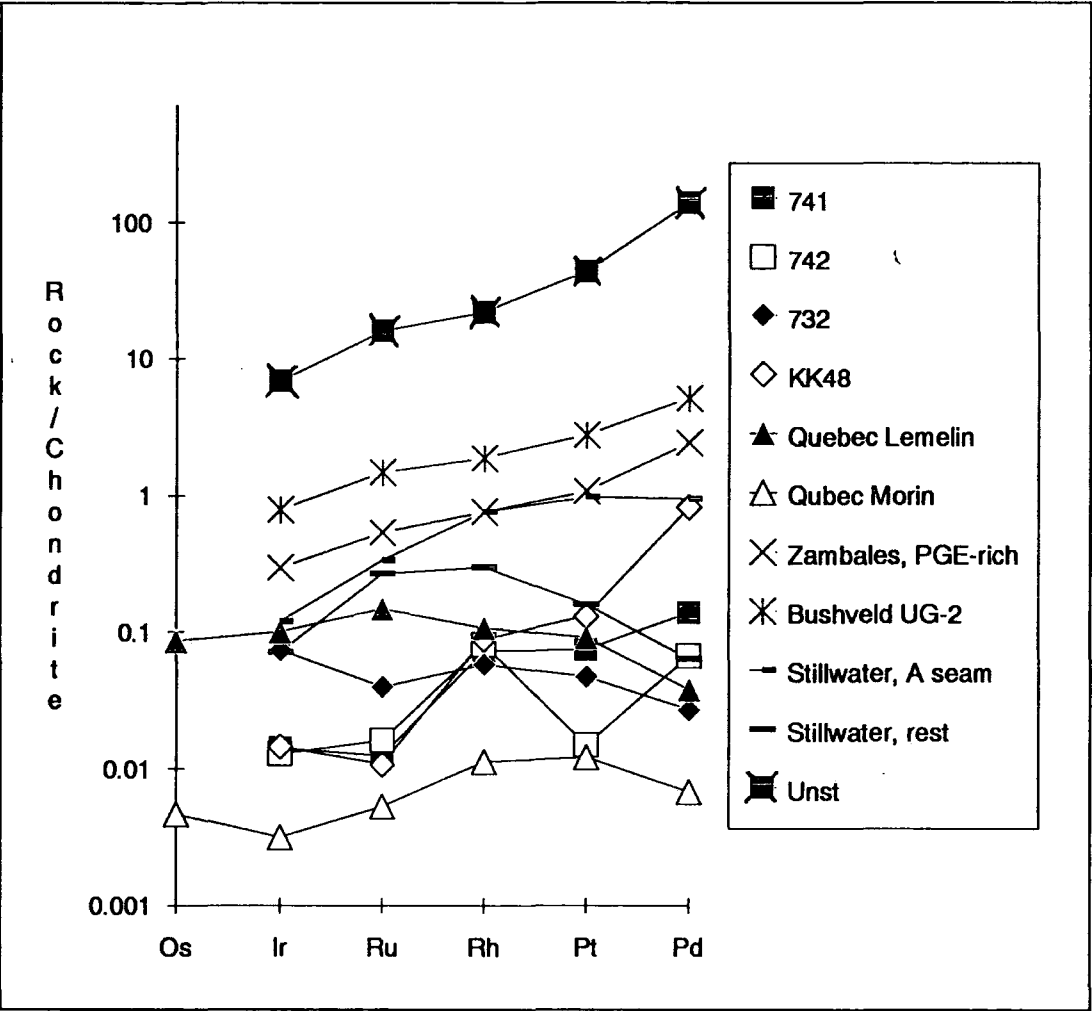
Figure (4.4) Chondrite-normalized patterns for chromitites from various ophiolites and layered intrusions. Data for Quebec: Gauthier et al. (1990), Zambales, Bacuta et al. (1990), Stillwater: Page et al. (1976), Unst, Shetlands: Prichard et al. (1985).
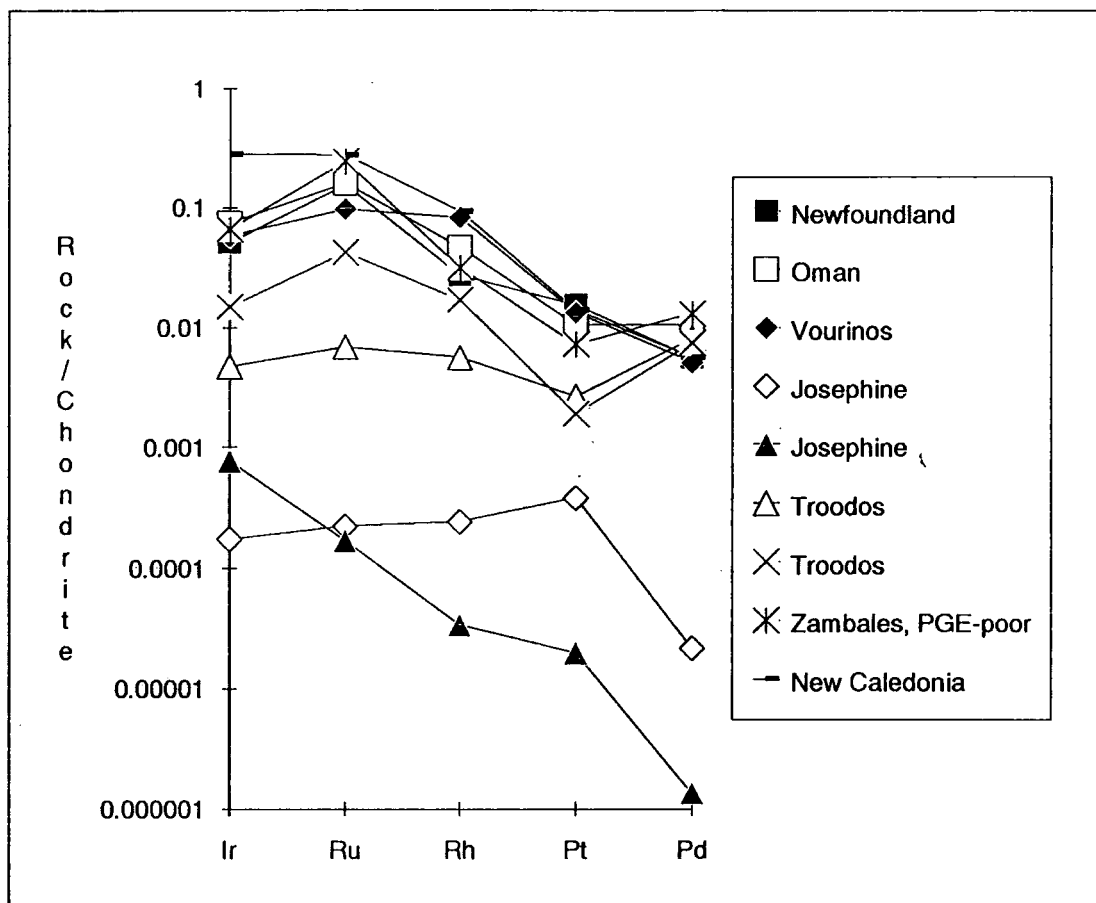
Figure (4.5) Chondrite normalized patterns for chromitites from various ophiolites. Data for Newfoundland: Page and Talkington (1984), Page et al. (1982a), Vourinos: Economou (1983), Josephine: Page et al. (1986), Troodos: Prichard and Lord (1990), Zambales, Bacuta et al. (1990), New Caledonia, Page et al. (1982b).

4.5. Causes of PGE fractionation

The two main petrogenetic processes that take place in an ophiolitic system are partial melting and crystal fractionation. The way that these affect the PGE content of any rock will depend on the phases that participate in these processes and the partitioning of the PGE in these phases. Mafic silicates, chromite and sulphides have been suggested as possible causes of PGE fractionation and all are present in the Pindos ophiolite; their affects on PGE will be discussed below.

4.5.1. Mafic silicates (Olivine, pyroxenes)

The association of olivine with elevated Ir contents (e.g. Gijbels et al., 1976) has led to the suggestion that it may act as a sink for the IPGE in the absence of another collector

(Crocket, 1979). If this is true, then partial melting, where olivine is an increasingly dominant phase, should enrich the restite in IPGE over PPGE, producing an increasingly negative pattern. It has already been mentioned that the Pd/Ir ratio increases with increasing Mg number in the Pindos harzburgites. The contribution of olivine, however, cannot be assessed, since other phases may play important roles. Mitchell and Keays (1981) analyzed mineral separates of spinel lherzolite xenoliths and found no enrichment of Ir over Pd in the olivine separates. In contrast Oshin and Crocket (1982), who also analyzed olivine separated from a harzburgite, found that Pd was enriched relative to Ir. Their analysis, however, reported a large value for Pt (7.8 ppb Pt compared to 0.75 ppb for Pd and 0.38 ppb for Ir) which makes it suspect. A problem that complicates interpretations of analyses of mineral separates is the problem of contamination from a PGE enriched phase (e.g. sulphides). Mitchell and Keays (op. cit.) considered the effects of a possible contamination and suggested that a real crystallographic control exists for the PGE between phases; their argument, however, is based on the implicit assumption that a single contaminating phase contributes both Pd and Ir. Although this is probably true for the spinel lherzolite xenoliths that they studied, the possibility exists that, whereas Pd is strongly partitioned in the sulphide, Ir will be preferentially enriched in any metallic phase present.

If, following the argument of Mitchell and Keays (op. cit.), the samples with the lowest PGE contents, being the least likely to be contaminated by a PGE-enriched phase, represent the true PGE content in a silicate phase, then pure olivine in the spinel lherzolites examined would contain 0.07 ppb Ir and 0.02 ppb Pd. This is identical to the estimated Ir of pure olivine of Gijbels et al. (1976) for olivines of the Rhum complex. Since this value is too low compared to the PGE abundances of the harzburgites in Table 4.3, it follows that the PGEs in these rocks are contributed by another PGE enriched phase that conceals the contribution of olivine. One analysis of a garnet harzburgite xenolith from Morgan et al. (1981) has sufficiently low values of PGEs to allow the assumption that they are controlled solely by the silicate (0.059 ppb Os, 0.052 ppb Ir and 0.09 ppb Pd). The Pd/Ir ratio is 1.7 which is only slightly higher than the chondritic ratio but clearly shows that Ir is not enriched over Pd.

Mitchell and Keays (1981) also analysed ortho- and clinopyroxene separates from the spinel lherzolites. Although they did not find any systematic enrichment of Ir over Pd, the absolute PGE levels were higher than in olivine, with clinopyroxene commonly containing more PGE than orthopyroxene. This is in conflict with the observation of Gijbels et al. (1976), that olivine from the Rhum complex has higher PGE contents than clinopyroxene, but they attributed this to chromite inclusions in olivine. Their estimation of the Ir content of pure clinopyroxene was 0.075 ppb, which is almost identical to their 0.07 ppb estimate for olivine.

If olivine can accept PGEs in solid solution then its contribution will only be significant in the absence of a PGE enriched phase and then it will not be capable of fractionating the PGE.

4.5.2. Chromite

The strongly negative chondrite normalized PGE patterns of chromitites from ophiolitic complexes has led to the suggestion that chromite accepts IPGE over PPGE in its lattice and so it can fractionate the PGE (e.g. Agiorgitis and Wolf, 1978, Economou, 1983). Recent experimental studies have shown that Ru and Rh are compatible with respect to chromite (see Table 4.5), whereas Pd is incompatible, but that the behaviour of the PGE in natural systems may be more complicated. It has been argued that the chondrite normalized pattern of chromitites reflects the PGE mineralogy of the rock, but that PGM are difficult to detect due to their minute size. Cocherie et al. (1989) examined the PGE and PGM in separated chromitites from the Vourinos complex; they confirmed that the PGE pattern of the chromites was due to inclusions of IPGE bearing minerals and did not observe any correlation of the chromite chemistry with its PGE content, as was reported by Economou (op. cit.).
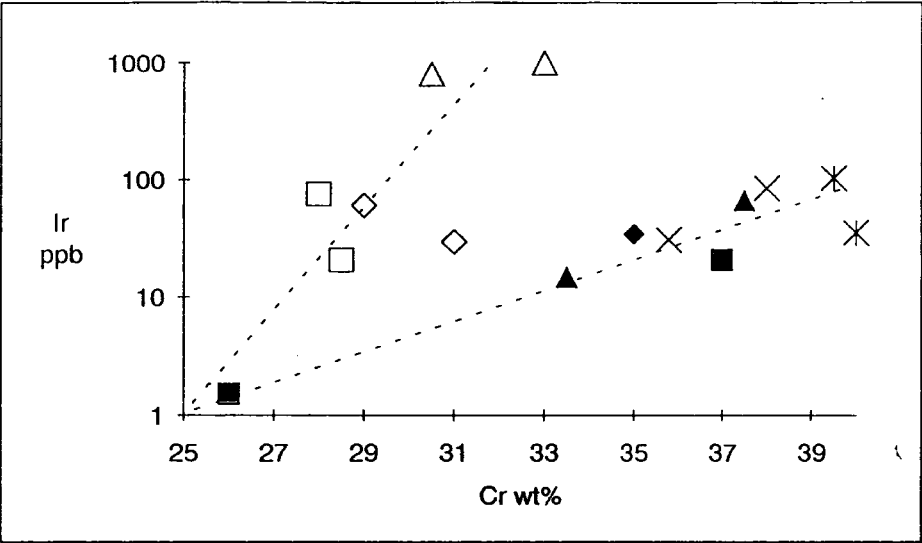
Figure (4.6) Ir vs. Cr wt.% for chromitites from various Greek locations. The symbols represent different locations. From Agiorgitis and Wolf (1978).
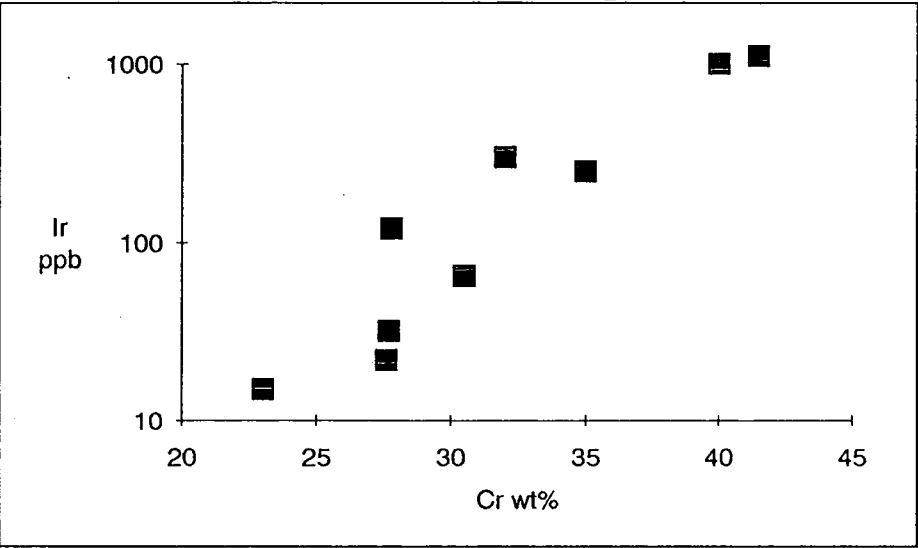
Figure (4.7) Ir vs. Cr wt.% for chromitites from the Josephine and Onion Mountain Alpine peridotite complexes, southwestern Oregon. From Stockman and Hlava (1984)

The correlations between chromite chemistry and PGE content (Figure 4.6) reported by Agiorgitis and Wolf (1978) were based on samples from different ophiolites and it is tempting to dismiss them as fortuitous. Stockman and Hlava (1984) studied the PGE mineralogy of chromitites from two Oregon complexes (Josephine and Onion Mountain) that are probably genetically related. Although they did not support the suggestion that chromite accepts PGE in its lattice, they presented a plot of Ir vs. Cr wt.%, which is reproduced in Figure 4.7, that shows a correlation and resembles that of Agiorgitis and Wolf (op. cit.). It will

be noted that the Cr wt.% varies by a factor of ~2, whereas the Ir content varies by a factor of 100. If we assume that the chromite precipitated from a melt by fractional crystallization, then we can calculate its composition using the equation of Shaw (1970):

$$\frac{Cr}{Cl} = (1-F)^{(\frac{1}{D}-1)} \tag{4.1}$$

where Cr is the composition of the phase being fractionated, Cl is the composition of the initial liquid, F is the degree of melting and D is the distribution coefficient. The ratio of compositions of the chromite at two different instances will be:

$$\frac{Cr_1}{Cr_2} = (\frac{1-F_1}{1-F_2})^{(\frac{1}{D}-1)} \tag{4.2}$$

where $F_1 > F_2$. Since the value of D is larger than 1, for compatible elements, the value of the exponent $(\frac{1}{D}-1)$ is always negative. This means that the value of Cr_1/Cr_2 can never exceed the value of $(1-F_1)/(1-F_2)$. Thus, a difference of three orders of magnitude in the Ir content of two chromitite samples requires that chromite be fractionated until the last drops of melt crystallize, clearly an unrealistic proposition. It will be noted that the range of the chromite Cr abundances support a magmatic origin, with 2-4% fractional crystallization of chromite being adequate to reproduces the observed abundances.

If the PGE content of cumulate chromite can be explained by the presence of PGM, studies of chromite separates from harzburgites have failed to reveal their presence (Cocherie et al., 1989). Figure 4.8 shows the PGE patterns for chromite separates from harzburgites from the Vourinos and Thetford Mines complexes, as well as spinel lherzolite xenoliths. The chromites from xenoliths and Vourinos have unfractionated patterns that mirror the patterns for whole rock PGE abundances, albeit at different absolute concentrations.
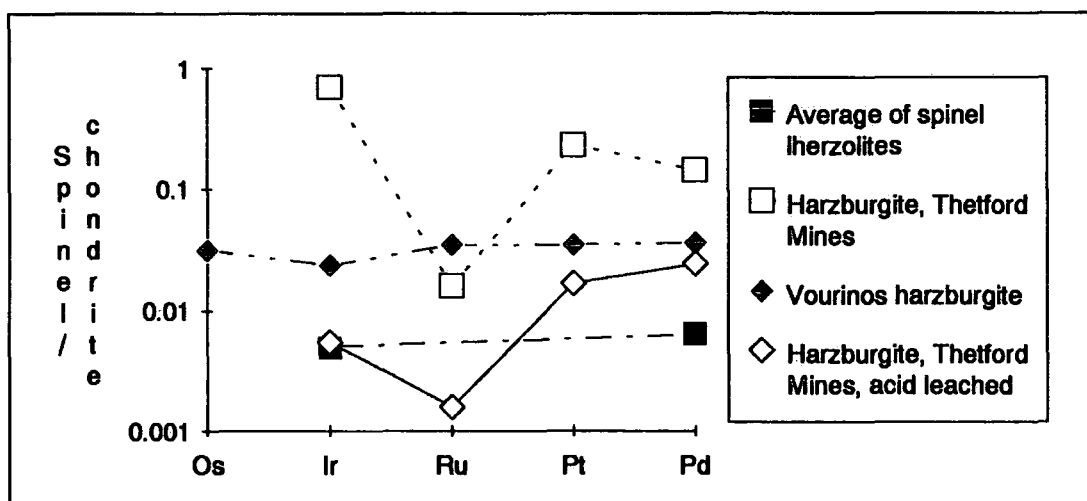
Figure (4.8) Chondrite-normalized patterns of spinel separates from spinel lherzolites (Mitchell and Keays, 1981), Thetford Mines (Oshin and Crocket, 1982), and Cocherie et al. (1989)

Since the Vourinos harzburgite has been subjected to a high degree of partial melting compared to the spinel lherzolite xenoliths, the higher PGE concentrations of the chromite suggest that the PGEs may partition in spinel. Even so, the distribution coefficients should be similar and still could not fractionate the PGE. The unleached separates from Thetford Mines are the most enriched in PGEs and show a Ru negative anomaly that is absent in Vourinos. The leached composition shows much reduced PGE levels (Ir more so than Pt and Pd) and retains the Ru anomaly. Oshin and Crocket (1982) suggested that chromite, in the high temperature conditions of the upper mantle, accepts PGEs in defect sites and vacancies and that these migrate towards grain boundaries during emplacement of the peridotite. However, the reason for the negative Ru anomaly is still not clear and it is in complete contrast to the Ru enrichment of cumulate chromites.

Capobianco et al. (1990a,b) have studied experimentally the partitioning of Ru, Rh, and Pd in spinel and arrived at spinel/silicate liquid distribution coefficients (Table 4.5). Their results show that Ru and Rh are compatible whereas Pd is incompatible. However, the absolute distribution coefficient values in the Fe-bearing system are much higher than in the CMAS. In addition, the effect of Cr on partitioning remains unknown. These uncertainties make application of the distribution coefficients of Capobianco et al. (1990a,b) to natural systems questionable. Assuming that Os and Ir will behave in a similar way to Ru, these

distribution coefficients are in agreement with observed PGE abundances from ophiolitic chromitites (Figure 4.5), even if Rh is never so abundant. If, however, their effect on the basaltic melt is considered, using Equation 4.2, it is obvious that even the smallest amount of chromite fractionation will totally deplete the melt of Ru and Rh. Figure 4.12 shows that oceanic basalts do not show such a drastic depletion, even though the PGE pattern has a positive slope. Furthermore, if these distribution coefficients were true, they would be of the same magnitude as those for sulphide/silicate melts. The chromite PGE levels should also be similar to sulphide globules from MORB, i.e. in the order of ten of thousands of ppb (Peach et al., 1990).

4.5.3. Sulphides

Sulphides are frequently associated with high PGE concentrations, e.g. in komatiitic Ni-Cu sulphides (Naldrett, 1981a), layered intrusions and sulphide globules from MORB (Peach et al., 1990). As mentioned earlier, sulphides are believed to be the main host of PGEs in the mantle (Keays et al., 1981; Mitchell and Keays, 1981; Garuti et al. 1984) and the very high distribution coefficients between sulphide melt and silicate melt for the PGE (Ross and Keays, 1979; Campbell and Barnes, 1984; Jones and Drake, 1986) makes imperative their consideration in any PGE melting model. Recently the distribution coefficients of Ir, Pt and Pd have been experimentally determined (Peach et al., 1990; Stone et al., 1990; Table 4.5). These studies confirmed the high estimates of sulphide/silicate melt distribution coefficients for the PGEs. The study of Peach et al. (1990) is based on Ir, Pt, and Pd determinations of MORB glass and coexisting sulphide globules. The value for Pd is an estimate, since Pd in the glass was below the detection limit. The value for Pt is not given by the above authors, because of the same problem as with Pd and the lack of any means of making an accurate guess, but it can be derived from the Ir data using mass balance of the sulphide and glass. A further complication is the question of whether the sulphide was in equilibrium with the glass; this was considered by the authors and they suggested that the coefficients are an accurate estimate. The values of Stone et al. (1990) vary considerably but the lowest values are in good agreement with those of Peach et al. (1990), especially

considering that Pt and Pd values in the glass had to be deduced. The estimated value for the Pt distribution coefficient is in good agreement with that of Stone et al. (1990), suggesting that the one order of magnitude difference with those of Ir and Pd is not an artefact of calculation. An important difference is the ratio of the coefficients of Ir/Pd. Peach et al. (1990) suggest that Pd is more compatible than Ir, but this is in contradiction of their observed behaviour during partial melting in the Pindos peridotites (Figure 4.2). The values of Stone et al. (1990) observe this relationship and are therefore preferred.

	Os	Ir	Ru	Rh	Pt	Pd	Conditions	
Sulphide melt /silicate melt		$1.21\text{-}1.64 \times 10^4$			$7.6\text{-}13.9 \times 10^{3*}$	3.5×10^4	MORB FAMOUS 526-1	Peach et al. (1990)
Sulphide melt /silicate melt		2.0×10^4						Jones and Drake (1986)
Sulphide melt /basalt melt		$5.5\text{-}20 \times 10^4$			$1.7\text{-}15 \times 103$	$3.9\text{-}20 \times 10^4$	1200 °C, fO_2 -9.2 (MW), fS_2-0.9	Stone et al. (1990)
Spinel/silicate melt			22 & 25	78 & 90		<0.02	Mg-Al spinel, Mg-Al-Ca-Si melt	Capobianco and Drake (1990a)
Spinel/silicate melt		·´	8000	300		0.8	Fe-Mg-Al spinel, Fe-Mg-Al-Ca-Si melt	Capobianco and Drake (1990b)
Fe-alloy/sulphide melt	>1000	>1000		30-110	>1000	1-2	Fe-Ni-S system, 1000 to 1400 °C	Fleet and Stone (1991)
unknown phase /silicate melt		1000	500	1220	950	1083	UG2 chromitite	Hiemstra (1985)

Table (4.5) Distribution coefficients of PGE in various systems. *calculated by mass balance from the data of Peach et al. (1990)

4.5.4. Alloys

Because of their siderophilic nature, the PGEs will partition into a metallic phase if one is present. Fleet and Stone (1991) experimentally determined distribution coefficients for the PGEs in the Fe-Ni-S system between a Fe-alloy and sulphide melt (Table 4.5). They pointed out that the distribution coefficients are bound to vary with temperature and phase compositions. The results show that Os, Ir, and Pt partition very strongly in the metallic phase, followed in this respect by Rh, whereas Pd is only slightly compatible. Although this shows that a metallic phase would be very effective in fractionating the PGEs, especially in fractionating Pd from the rest, the presence of a metallic phase in the evolution of the melt is questionable. A fractionating silicate melt is unlikely to reach the solubility limit of Fe or Ni and exsolve a metallic phase. This does not exclude the possibility of the presence of a metallic phase in an immiscible sulphide liquid, if one is formed, in which case the distribution coefficients will dictate the partitioning of the PGE in the sulphide-alloy phase.

4.5.5. Oxygen fugacity

The effect of the oxygen fugacity (f_{O_2}) on the solubility of Ir and Pt in a basaltic melt was recently investigated experimentally (Amossé et al., 1990). Figure 4.9 shows the solubility of Ir and Pt as a function of f_{O_2}. An increase of the f_{O_2} has a pronounced effect on the solubility of Ir, which decreases rapidly to sub-ppb levels. For the same change of f_{O_2}, Pt solubility changes less abruptly and remains much greater in the experimental charges than the Pt content of natural magmas. Amossé et al. (1990) conducted the experiments at a relatively high temperature (1430°C) in order to achieve the low viscosities necessary to obtain equilibrium conditions of the melt. They pointed out that the solubilities of Ir and Pt increase with increasing temperature, but maintained that the relative differences in their solubility would remain the same at lower temperatures.

As Amossé et al. (1990) pointed out, the different behaviour of Ir and Pt may explain the IPGE over PPGE enrichment that is observed in many Alpine chromitites. An increase in

the oxygen fugacity of a basaltic melt can result in chromite precipitation (Hill and Roeder, 1974). This may bring the melt to saturation with respect to Ir (and presumably Os and Ru), thus precipitating IPGE alloys and/or sulphides. At the same time the background solubility of Pt (and Rh and Pt) may remain higher than their saturation level and PPGE will be continuously enriched in the melt until they are scavenged by sulphides.
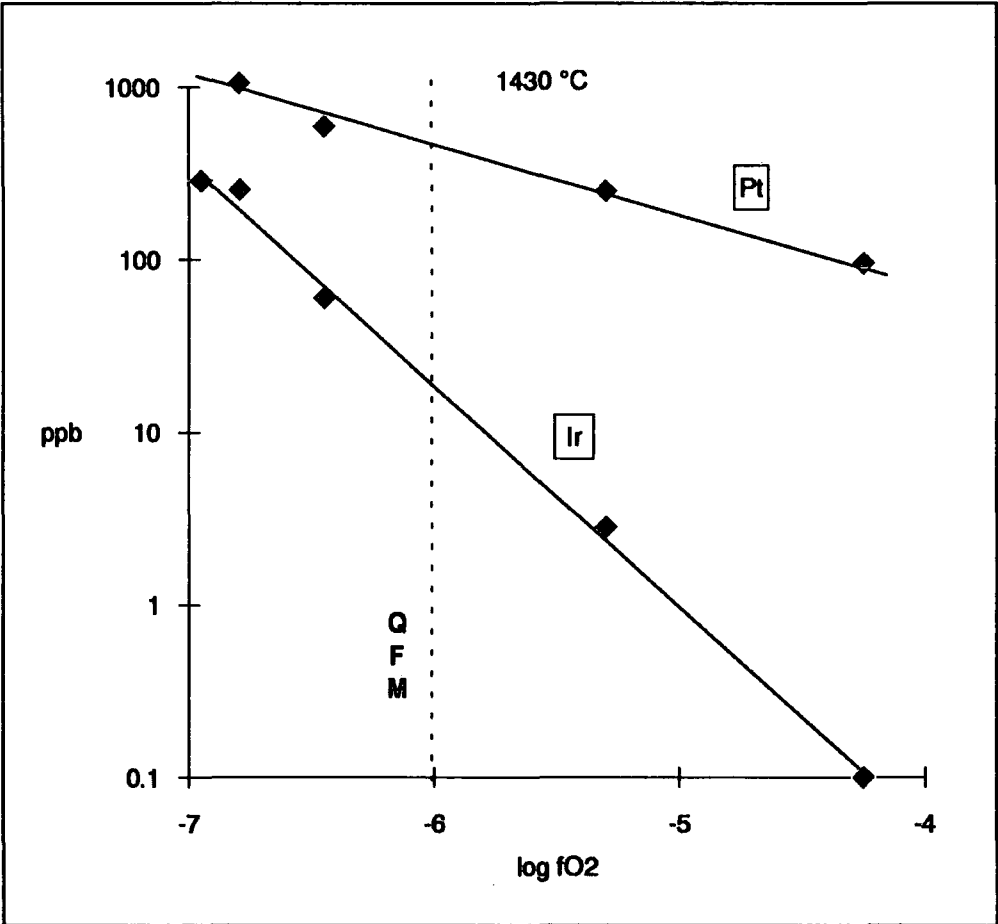
Figure_(4.9) Solubility of Ir and Pt in basaltic melt as a function of oxygen fugacity. Amossé et al. (1990).

4.6. Sulphur in the mantle

In view of the significance of sulphides as PGE collectors, their behaviour during partial melting and melt evolution must be examined. The sulphur content of mantle derived rocks is not an accurate indicator of the S content of the upper mantle (Lorand, 1987, 1990). Sun (1982) estimated the S abundance of the mantle to be in the range 350-1000 ppm, but . this value was probably too high. The more recent estimate of Morgan (1986) is lower at 200

ppm and is more widely acceptable. Assuming that sulphur resides in a sulphide phase containing ~35 wt.% S, it constitutes 0.058% of the total mass of the primitive mantle. This sulphide phase is likely to be a Fe-Ni-Cu sulphide interstitial to the silicate minerals (Lorand, 1987, 1989). Sulphides have low melting points; pyrrhotite starts to melt at 988°C, 1 bar (Craig and Scott, 1982) and this temperature is lowered in the presence of Cu (but not Ni, Naldrett, 1969). This ensures that sulphide is molten long before the onset of melting of the silicates, but it will not be able to segregate because it will be suspended in the "frozen" silicate matrix. Although the melt extraction mechanism is very efficient even for very low degrees of melting (McKenzie and Bickle, 1988), the presence of sulphides in·mantle derived rocks that have experienced partial melting (Mitchell and Keays, 1981, Garuti et al., 1984, Lorand, 1987, 1989, present study) indicates that they cannot be mechanically transported, possibly due to the combination of their high density and the low melt velocities in the melting region. The method of removal of sulphur from the mantle must be its dissolution in the silicate melt, and its solubility will determine the rate of its extraction.

The increased solubility of sulphur with increasing FeO content of the silicate melt is well established (MacLean, 1969, Haughton et al., 1974, Mathez, 1976, Wendlandt, 1982). Recently, Poulson and Ohmoto (1990) compiled the available data on sulphur experiments in synthetic and natural systems and arrived at models for the speciation of sulphur in silicate melts and mathematic expressions for its solubility in these melts. They distinguished three melt categories according to FeO content: melts with less than 1 wt.% FeO, melt with FeO between 1 and 10 wt.%, and melts with FeO higher than 10 wt.%. The first category involves experiments with albititic melts that are not relevant in the initial stages of melting. For melts with FeO > 10 wt.% they found that sulphur is dissolved as an Fe_3SO_2 (or $2FeO·FeS$) species according to the reaction:

$$\tfrac{1}{2}S_{(g)} + 2FeO_{(silicate\ melt)} = Fe_3SO_{2(silicate\ melt)} + \tfrac{1}{2}O_{2(g)} \tag{4.3}$$

$$\log K = \log X_S + \tfrac{1}{2}\log f_{O_2} - 3\log X_{FeO} - \tfrac{1}{2}\log f_{S_2} = -4.1 \ (at\ 1200\ ^\circ C,\ 1\ bar) \tag{4.4}$$

For silicate melts with intermediate FeO content, they found that sulphur is dissolved as an FeS species:

$$FeS_{(sulphide\ melt)} = FeS_{(silicate\ melt)} \qquad (4.5)$$

and determined the constant of the reaction:

$$\log K = \log X_S = -1.05 - 3000/T \ (^{\circ}K) \ (850-1200\ ^{\circ}C,\ 1bar-2.2\ kbar) \qquad (4.6)$$

According to Equation 4.6, the sulphur solubility in intermediate melts is temperature dependent. This is in apparent contradiction to the idea that sulphur solubility varies with the FeO content of the melt. Poulson and Ohmoto (1990) showed, however, that this is true only after a critical value of FeO in the melt is reached, which is also temperature dependant. Since primitive melts have FeO content of less than 10 wt.% (e.g. Shibata and Thompson, 1986), Equation 4.6 can be used to calculate the sulphur solubility of the melt during partial melting. The accuracy of this expression can be evaluated by comparing the calculated values with those encountered in an experimental study. The sulphur solubility of Grande Ronde basalt in the experiments of Wendlandt (1982) is ~0.15 wt.% S at 1420°C and ~0.9 wt.% S at 1300°C. The solubilities of sulphur calculated with Equation 4.6 at the same temperatures are 1500 and 1100 ppm respectively, a very good agreement. The ability to use a temperature-dependant expression for the sulphur solubility in silicate melts is of great advantage when modelling asthenospherically rising mantle, since the sulphide removal can be monitored very accurately without resorting to the use of a single solubility value throughout the melting episode.

Sulphur solubility is believed to increase with decreasing pressure (Helz, 1977; Wendlandt, 1982). Poulson and Ohmoto (1990) suggest that the constant of Equation 4.4 shows a positive pressure dependence (+0.1/kbar), they base this conclusion, however, on the experiments of Caroll and Rutherford (1985) that involved natural hydrous dacite melts from 1.06 to 2.90 kbar. Although they acknowledged the discrepancy, they offered no explanation. A possible reason for this apparent contradiction may be the different compositions considered by each study, as well as the different conditions, i.e. the

experiments of Wendlandt (1982) were performed at the much higher pressures of 12.5 to 30 kbar. In view of this contradiction, I favour the conclusion of Helz (1977), which is based on observations of natural MORB, that decompression enhances sulphur solubility.

MacLean (1969) found that the effect of increasing oxygen fugacity is to decrease the sulphur solubility in the silicate melt. He suggested that an increase in oxygen fugacity will deplete the ferrous iron content in the silicate melt by oxidizing it to ferric iron. Since sulphur is dissolved as FeS species (Equation 4.5) this will result in a decrease of the sulphur solubility in the melt. Haughton et al. (1974) also found that increasing f_{S_2} and f_{O_2} has the result of respectively increasing and decreasing sulphur solubility. In the experiments of Wendlandt (1982) the relative effects of f_{S_2} and f_{O_2} could not be evaluated and Wendlandt (op. cit.) cites the study of Haughton et al. (op. cit.) but actually reverses his conclusion (Wendlandt, 1982, pp 881-882). That f_{S_2} and f_{O_2} should have the effects described by MacLean (1969) and Haughton et al. (1974) is obvious when considering the products/reactants balance of Equation 4.3. If oxygen is added to the left-hand side of the equation (products) the Fe_3SO_2 activity of the silicate melt must decrease to maintain the balance. Similarly, an increase in sulphur fugacity will increase the amount of sulphur dissolved in the melt. Although the balance is maintained by an increase in oxygen fugacity, in practice the phase that will be most affected will be one that is not buffered in any way.

MacLean (1969) also showed that sulphur saturation can be attained by removal of ferrous iron from the silicate melt (e.g. olivine or chromite crystallization), by an increase in the SiO_2 content of the melt (silicate fractionation), and by temperature drop.
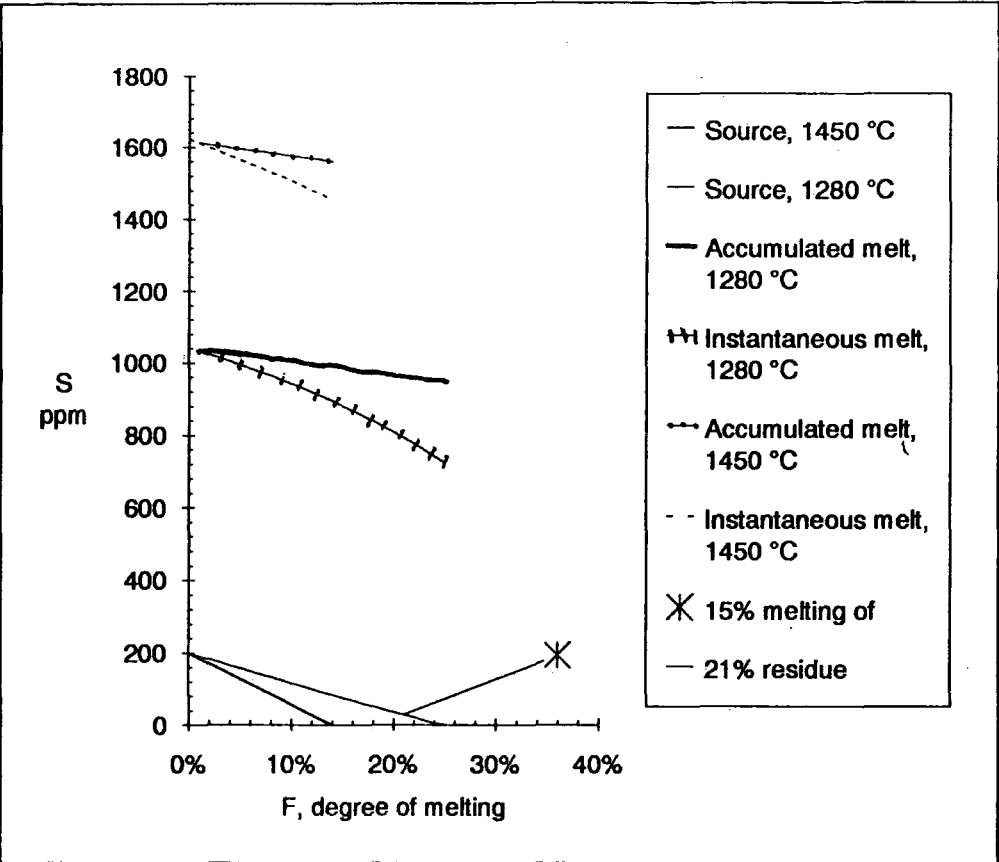
Figure (4.10) Sulphur content of the mantle and melts during partial melting. The asterisk represents 15% melting of the 21% melting residue, i.e. a total of 36% melting

The sulphur abundance of the mantle and melts generated by partial melting has been modelled using Equation 4.6. The melting model and calculations are presented in detail in Chapter 5. Briefly, a sequential equilibrium melting model with 1% intervals was used. Melts calculated at each interval are the instantaneous melt and their weighted average gives the accumulated (or pooled) melt of the melting interval. Figure 4.10 shows the sulphur compositions of residue, instantaneous and accumulated melts for two rising mantle diapirs with an initial temperature of 1280 and 1450°C. These are typical temperatures of normal MORB and hotspot related diapirs respectively (McKenzie and Bickle, 1988). The prediction for the disappearance of sulphide from the source at 24% melting, for the normal MORB diapir, is in excellent agreement with the estimates of 25% (J. W. Morgan, cited in Barnes et al., 1985) and Peach et al. (1990). The disappearance of the sulphide in the hotspot diapir occurs at 14% melting, because of the higher melt temperature which results in higher

sulphur solubility. Since the effect of pressure has not been taken into account this value is a lower limit of the degree of melting required to remove the sulphide.

In order to explain the high PGE values of low-Ti magnesian basalts relative to MORB, Hamlyn et al. (1985) suggested that the former were generated by partial melting of a peridotite that had already experienced MORB extraction and retained some residual sulphides that were consumed during the second melting episode. Their published sulphur data for the basalts they examined range from 20 to 1780 ppm S. They are however unreliable because sulphur is mobile during alteration. A more reliable indicator of the sulphur content is Se because it is not affected by alteration. The S/Se ratio of the mantle is 3509 (Morgan, 1986) and will change only if the melt interacts with sulphides during its evolution (e.g. achieves sulphur saturation). This is unlikely to have happened to the basalts examined by Hamlyn et al. (1985). The sulphur values calculated from the Se content of the basalts ranges from 15 to 708 ppm S with an average of 185 ppm S, which is consistent with the origin suggested by Hamlyn et al. (op. cit.). Figure 4.10 shows the sulphur content of a melt that is derived by 15% melting of a residue that has already experienced 21% melting, a typical value for MORB. The calculated value is 193 ppm S, which is in very good agreement with the average of the low-Ti basalts and is consistent with Hamlyn et al. (op cit.) hypothesis.

4.7. Modelling

The availability of distribution coefficients for the PGE makes possible the modelling of the PGE during partial melting and melt evolution. It has been argued that the presence of sulphides is the most important factor in controlling the PGE; their partitioning in chromite can also be examined, but there are no quantitative data on the partitioning of the PGE in silicates. In order to look at the behaviour of the PGE during partial melting, the three situations that were examined earlier with respect to sulphur in the mantle have been modelled using the partition coefficients of Stone et al. (1990). Since no partition coefficients for Ru and Rh exist, an arbitrary value of $4X10^4$ has been used. Figure 4.11 shows the results for the melts and residue. Note that the residue values are actually increased. This is because the very large distribution coefficients for the PGE make them behave compatibly,

however minute the sulphide fraction may be. Also, despite a difference of an order of magnitude of the distribution coefficients of Pd and Pt, the residue has a flat pattern. The effect of the different distribution coefficients is more obvious in the melt; it has Pd/Ir>1, since Ir is more compatible, and a positive Pt anomaly, due to its smaller distribution coefficient. These differences are eliminated in the 25% melt because the sulphide is no longer residual and the PGE enter the melt. The melt that comes from the subsequent melting of the restite that still retains some sulphides also does not show any anomalies and has a higher PGE content, since it represents a smaller (15%) degree of melting.

Figure 4.12 shows the three calculated melts in comparison to MORB and magnesian low-Ti basalts. All the MORB compositions are from localities near hotspots, but the sample from the Bouvet Triple Junction has very low abundances and may represent a smaller degree of melting. There is good agreement between the calculated and observed values for Pd for all models but the Pd/Ir ratio is very high in all basalts, which suggests that Ir has been depleted, probably due to IPGM crystallization during melt fractionation.
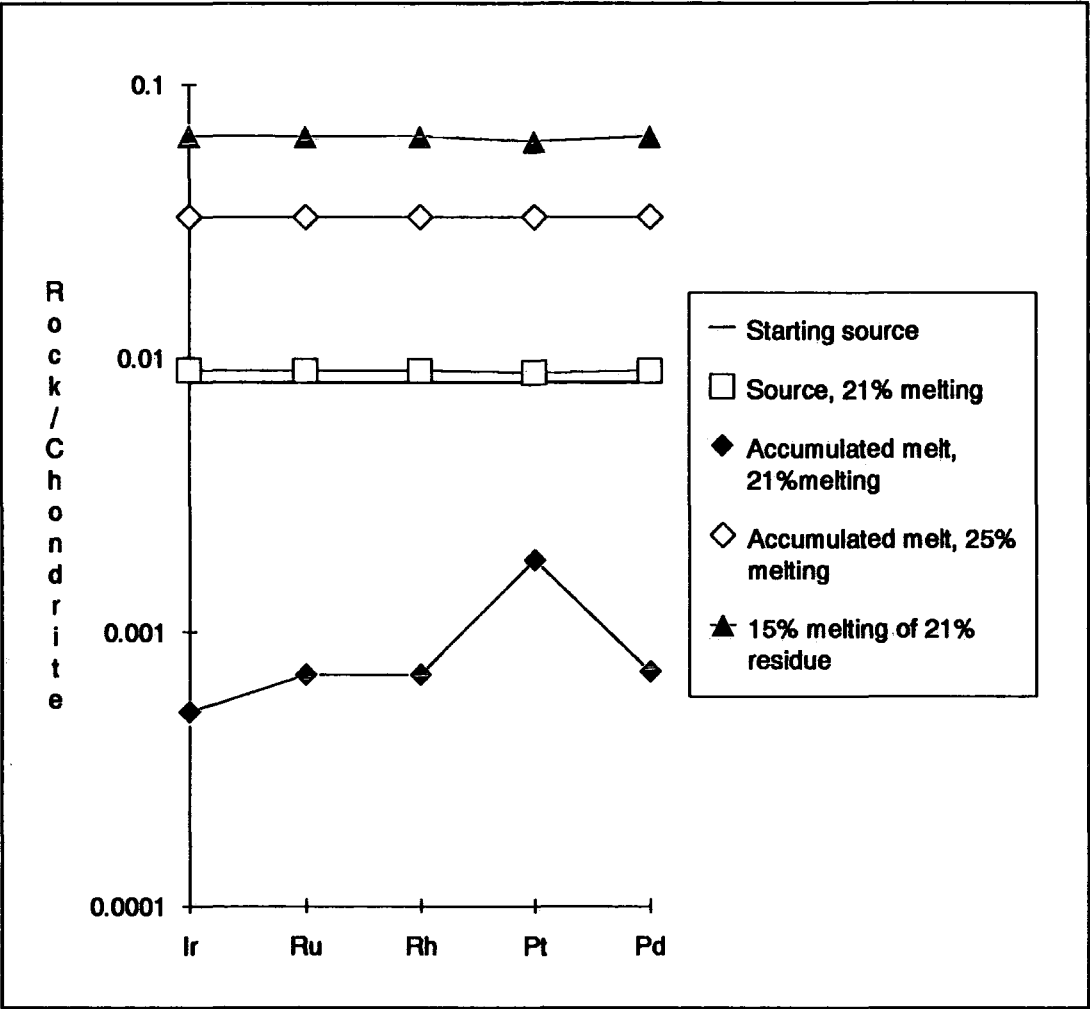
Figure (4.11) Melt and residue compositions for partial melting. Initial mantle values from Table 4.3. Distribution coefficients, see text. Same parameters as in Figure 4.10.
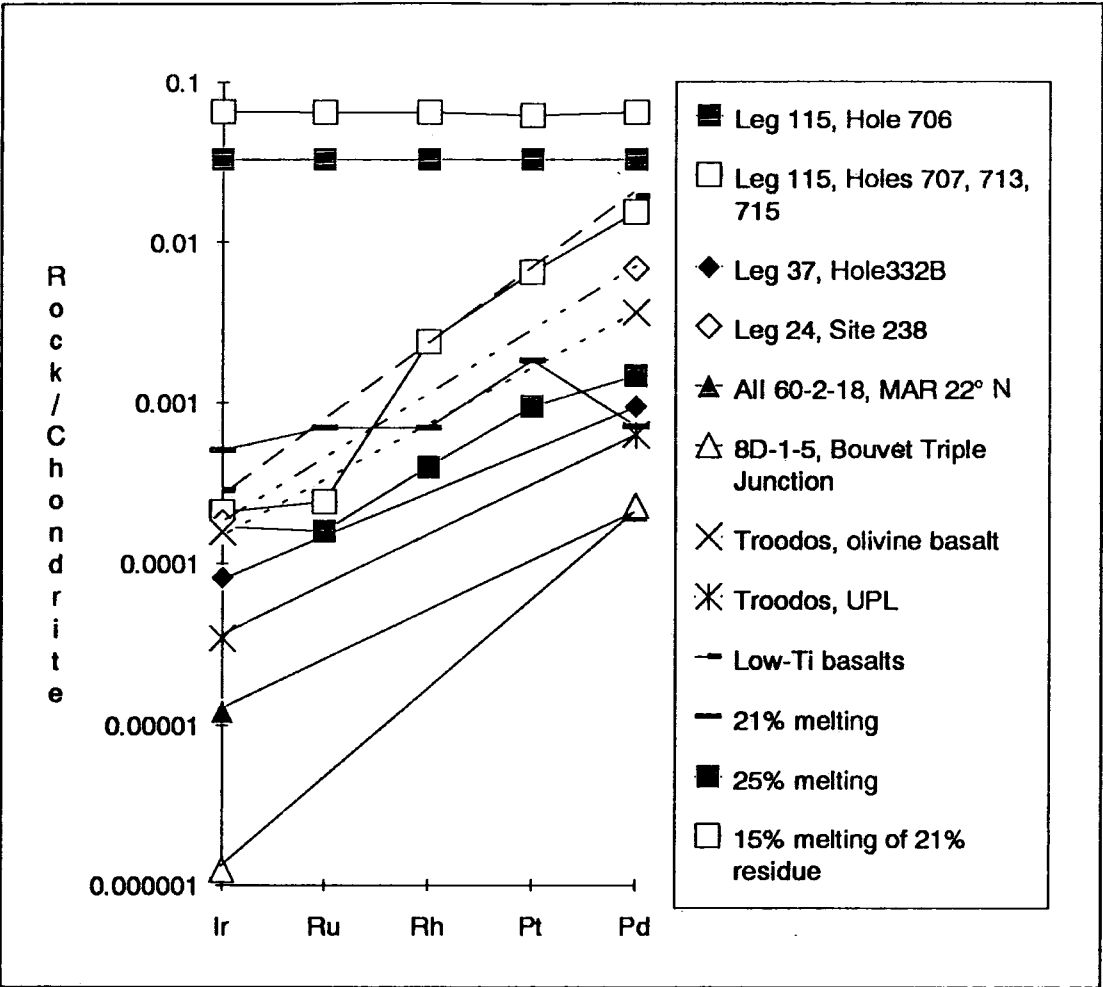
Figure (4.12) Comparison of the predicted melt compositions with MORB and magnesian low-Ti basalts. Data from Leg 115: Greenough and Fryer (1990), Leg 37: Crocket and Teruta, (1977), Leg 24, MAR, and Bouvet: Hertogen et al. (1980), low-Ti basalts: Hamlyn et al. (1985).

4.8. Summary

There are many uncertainties concerning the behaviour of PGE during partial melting and fractional crystallization, e.g. what is their host in the mantle, what fractionates Pd and Ir or Pd and Pt, what is the role of chromite etc. Although general characteristics are recognized, e.g. enrichment of IPGE in chromites, these are not universal and any theories have yet to be conclusively proved. Here, a model for the PGE abundances of the Pindos rocks will be presented that is consistent with the characteristics of the Pindos.

It has been argued that the silicate minerals cannot control the PGE abundances or patterns in mantle rocks. Instead, sulphides are the most likely candidate for this role. The

PGE absolute abundances in the Pindos harzburgites are consistent with the presence of residual sulphides. In addition, sulphides have been observed in most of the rocks, although they are usually badly affected by serpentinization and it is not clear whether they are primary or not. However, the decrease in the Pd/Ir ratio observed with increasing amount of melting cannot be reproduced by modelling the sulphide fraction alone, as both experimental studies and observations on natural rocks suggest that Pd and Ir are almost equally compatible in sulphides. An additional phase has to be present that is enriched preferentially in Ir over Pd. Mitchell and Keays (1981) suggested Ir-alloy as a possible candidate for the Ir host in the mantle. Such a phase, by virtue of its high melting point, would be more refractory than the Pd-hosting sulphide and would effectively fractionate the two. This Ir-alloy need not be present throughout the melting history of the mantle. The initial host of both Ir and Pd may be mantle sulphides. As these sulphides become enriched in Ir with increased melting they may exsolve an Ir-rich phase. This is consistent with the observed variation of the Pd/Ir ratio in the Pindos harzburgites, that is initially unchanged but starts to decrease with increased partial melting.

It is, however, more difficult to equate the suggestion of Hamlyn et al. (1985), that second-stage melting removes the residual sulphide from the mantle, with the relatively high Pd abundances of the Pindos harzburgites. It has been shown that most of the Pindos complex has experienced second-stage melting in a supra-subduction zone environment that resulted in the depleted harzburgites of Avgo and Livadi. A process that would satisfy the observations of Hamlyn et al. (1985) on second-stage melts with the residues of these melts is the presence of residual sulphide that has not equilibrated with melt. This could be achieved by the re-distribution of sulphides after initial melt extraction and their entrapment in silicates. Entrapment of spinel in silicate phases is a well established process during deformation of peridotites (Mercier and Nicolas, 1975) and silicate-hosted sulphides have been observed in the Pindos harzburgites. With the onset of second-stage melting, any interstitial sulphide would enter the melt and be exhausted from the peridotite, but the silicate-hosted sulphides would not do so unless their host also melted. In addition, being isolated from the melt, they would not equilibrate with it and deplete it from its PGE content.

The chromitite PGE abundances are more easy to explain, since their PGE mineralogy is better established. It was mentioned earlier that chromitites with positive chondrite-normalized patterns are associated with PGE sulphides, whereas those with negative patterns are associated with Os, Ir, Ru-minerals. It is significant that almost all processes that result in chromite precipitation (e.g. decreasing temperature, increased oxygen fugacity) also drive the melt to sulphide saturation. In addition, chromite fractionation itself can drive a melt to sulphide saturation, because it removes FeO. If, however, the melt is undersaturated with respect to sulphide, then a considerable amount of fractionation is required before immiscible sulphide is formed. In this case PGE solubility in the melt may be a more important factor than sulphide saturation. An increase in the oxygen fugacity will lower the solubility of Ir, thus depleting it from the melt. It is noteworthy that the fractionation of ferromagnesian silicates from a basic melt increases its Fe_2O_3 content (and its oxygen fugacity, Carmichael, 1991) until ferric-iron rich oxides precipitate.

It is concluded that the role of platinum-group minerals is frequently undetected because other phases (sulphides) may be abundant and dominate the magmatic processes. When the role of sulphides is diminished, platinum-group minerals start to control these processes.

Chapter 5. Modelling of major elements

5.1. Introduction

Basic magmas and their source regions are composed of the oxides of six major elements (Si, Al, Fe, Mg, Ca, Na) and several minor (Ti, Mn, K, P) and trace constituents. Major element oxide analyses have been extensively used to study the geometric path of partial melting processes in multicomponent systems (e.g., Bowen, 1914; O'Hara, 1968; Presnall, 1969). Systems with more than four components, however, are difficult to represent graphically. Consequently, petrologists have devised techniques to reduce the number of components by grouping them together into four sets; these sets can then be assigned to the four apices of a tetrahedron and projected onto a suitable plane (e.g. Yoder and Tilley, 1962; O'Hara, 1968). Nevertheless, in the process of reducing the number of components of a system, some information is inevitably lost. For example, by grouping FeO and MgO together, the effects of Fe-Mg partitioning between mafic minerals are not apparent. Significantly, the projectional algorithms that have been proposed so far by various workers (e.g., O'Hara, 1968; Walker et al., 1979; Elthon, 1983) involve methods of component reduction. The direct analysis of minerals and co-existing melt in partial melting or crystallization experiments allows a quantitative and detailed examination of melting and/or crystallization pathways, but the results are confined to the particular rock composition investigated and cannot be extrapolated to other rock types.

In contrast to the methods of studying igneous processes using major elements, trace elements can easily be modelled on a quantitative basis by means of relatively simple mathematical expressions (Gast, 1968; Shaw, 1970; Hertogen and Gijbels, 1976; Prinzhofer and Allègre, 1985). This does not imply that major elements cannot be modelled on a theoretical basis as well (see, for example, Ito, 1973; Maaløe, 1976), but rather that this approach is rarely followed, whereas there are hardly any trace element studies that are not accompanied by some sort of modelling.

The basis of formulating trace-elements models is the concept of the distribution (or partition) coefficient (Kd). This is the ratio of the concentration of an element in a phase to the concentration of that element in the co-existing liquid, and is constant over a wide range of temperatures and compositions of the phases provided that Henry's law[3] is obeyed. Although there is some controversy over the latter issue, Watson (1985) showed that most trace elements that are used in petrogenetic modelling do obey Henry's law at the concentrations observed in nature.

Hanson and Langmuir (1978) suggested that major elements need not be considered separately from traces and that all elements form a continuum of chemical behaviour. One end of the spectrum is occupied by the trace elements, whose abundance is so low that there is no stoichiometric constraint on their concentration in any phase. A trace element in an ideal solution will follow Henry's law, otherwise the activity coefficients will covary systematically in the phases involved (e.g. REE). The other end of the spectrum is occupied by elements that are essential structural constituents (ESC, Hanson and Langmuir, op. cit.) of minerals, completely filling a site. In this case, the abundance of an ESC in a liquid will be buffered by the composition of the mineral that hosts this element. For limited solid solution ESCs will follow Raoult's law (e.g. SiO_2 in pyroxenes). Intermediate elements lie between these end members. For a given Kd, the concentration of the elements in any phase will vary within the limits imposed by stoichiometry. Solid solutions may follow Raoult's or Henry's law, or be ideal or non-ideal. There may be elements occurring in critical concentrations, such that they are not stoichiometrically constrained by the composition of their host minerals, yet they do not fulfil the solution criteria to be considered trace elements (e.g. Ni in olivine). Hanson and

---

[3]In an ideal solution there is no enthalpy of mixing and the activity of a component mixing on one site is equal to its mole fraction in solution (Raoult's law). If the mixing components interact with one another, the activities will depart to a greater or lesser extent from the ideal mixing curve. With increasing dilution, however, elements become so dispersed that, although they may interact strongly with the other components present, small changes in their concentration do not significantly affect their average environment. The activity coefficient, therefore, remains constant and the activities of trace elements become proportional to their concentrations. This is known as Henry's law (Wood and Fraser, 1976).

Langmuir (op. cit.) used Roeder and Emslie's (1970) Kd's for MgO and FeO in olivine to model the composition of these elements in the liquid and co-existing residue during partial melting. Although Kd's for other minerals were not available, they overcame this problem through manipulation of the melting equations.

As Kd's became available (Nielsen and Drake, 1979; Nielsen, 1985; Weaver and Langmuir, 1990), the quantitative study of major elements was extended to more complex systems (Frenkel and Ariskin, 1985; Nielsen, op. cit.; Weaver and Langmuir, op. cit.). A different approach has been adopted by McKenzie and Bickle (1988) and Niu and Batiza (in press), who parameterized equilibrium melting experiments on peridotite compositions for which the extent of melting was known. Using this technique they were able to calculate the liquid composition at pressures, temperatures, and degrees of melting of interest.

In the present study the composition of the shallow upper mantle, generated during sequential partial melting will be modelled according to the method outlined by Hanson and Langmuir (1978), using solid/liquid distribution coefficients for all major and minor element oxides and for the most important dry mineral phases.

5.2. Mathematical expressions

Let us assume an assemblage of minerals in which element ι has an initial concentration C_0. When melting begins and a fraction of liquid (F) forms, mass balance dictates that:

$$C_0 = C^s (1-F) + C^l F \tag{5.1}$$

where C^l_i is the concentration of element ι in the liquid and C^s is the concentration of the element in the residual solid.

If we further assume that the initial solid consists of v phases it follows that:

$$C_0 = \sum_v C_\iota^\alpha X^\alpha \tag{5.2}$$

where C_ι^α is the concentration of element ι in phase α, X^α is the proportion of phase α, and $\sum_v X^\alpha = 1$.

The bulk distribution coefficient of element ι between the residual solid and the melt is, by definition, $D = \dfrac{C^s}{C^l}$.

(5.3)

Substituting 5.3 in 5.1 gives:

$$\frac{C^l}{C_0} = \frac{1}{D+F(1-D)} \quad \text{(Shaw, 1970)}$$

(5.4)

when the melt fraction remains at all times in equilibrium with the solid, and:

$$\frac{C^l}{C_0} = \frac{1}{D}(1-F)^{(\frac{1}{D}-1)} \quad \text{(Shaw, 1970)} \qquad \iota$$

(5.5)

when the melt fraction is continuously separated from preceeding liquids.

The two different melting modes described above are referred to as equilibrium (or batch) melting (Equation 5.4) and fractional melting (Equation 5.5). If the solid phases melt in proportions P^α different than those that occur in the solid, i.e. $P^\alpha \neq X^\alpha$, then it can be shown that:

$$D^{solid/melt} = D = \frac{D_0 - PF}{1-F}$$

(5.6)

where $P = \sum_\nu X^\alpha P^\alpha$ (7), $D_0 = \sum_\nu X^\alpha Kd_\iota^\alpha$ (8), and Kd_ι^α is the distribution coefficient of element ι between phase α and melt.

The expression for equilibrium melting then becomes:

$$\frac{C^l}{C_0} = \frac{1}{D+F(1-P)} \quad \text{(Shaw, 1970)}$$

(5.9)

and that for fractional melting becomes:

$$\frac{C^l}{C_0} = \frac{1}{D}\left(1-\frac{PF}{D}\right)^{(\frac{1}{P}-1)} \quad \text{(Shaw, 1970)}$$

(5.10)

5.3. Major elements distribution coefficients

The derivation of the previously described mathematical expressions is based solely on mass balance considerations and their application is not restricted to trace elements, as long as the distribution coefficients (Kd's) between the minerals and melt are known.

The Kd's of essential structural constituent (ESC) oxides of minerals are primarily temperature-dependent and can be expressed in the form of Arrhenius equations, that relate linearly the natural logarithm of the molar Kd with the inverse of the absolute temperature. The reason for this temperature dependence lies in thermodynamic principles. The classical theory for ideal solid solutions of ionic salts gives (Bradley, 1962):

$$R \, Ln(\frac{x_l}{x_s}) = \Delta H \, (\frac{1}{T_m} - \frac{1}{T}) + \Delta C_p \, Ln(\frac{T}{T_m}) - T_m \, \Delta C_p \, (\frac{1}{T_m} - \frac{1}{T})$$ (5.11)

where x_l and x_s are the mole fractions of a substance in liquid and solid solution respectively, ΔH is the molar heat of fusion of the substance at its melting point T_m (°K), and ΔC_p is the increase in specific heat at constant pressure per mole of melting substance.

For minerals that deviate from ideal solid solution models (e.g. spinels), additional thermodynamic parameters, such as mixing energies on different sites, must be introduced. In this case, Arrhenius equations are rather inadequate to describe accurately oxide partitioning. This has led to the treatment of minerals as a mixture of components, rather than oxides, for which Arrhenius equations were defined (Nielsen and Drake, 1979; Weaver and Langmuir, 1990).

The rigorous approach to derive major-element distribution coefficients is the thermodynamic analysis of solid solutions. This, however, is a formidable task, beyond the scope of the present thesis. Moreover, values for certain thermodynamic variables are still highly controversial (e.g. Nell and Wood, 1989; Sack and Ghiorso, 1991) even for the best studied minerals. For this reason, an empirical approach will be followed, using melting experiments on peridotites and crystallization experiments on basalts to calculate numerical expressions for the Kd's. To this end a database was compiled that contained most of the published dry experiments on natural compositions. Because distribution coefficients also

depend on the melt composition, only experiments related to basaltic liquids have been considered. The experimental conditions, initial compositions, phases analyzed and sources are presented in Table 5.1.

All melt and mineral compositions have been recalculated to mole fractions in order to facilitate comparison of the Kd's of oxides that occupy the same site in different minerals, e.g. Si in pyroxenes. It should be noted that these mole fractions are not based on one cation per mole (e.g., $AlO_{1.5}$, $NaO_{0.5}$ etc.) but on the gram formula weights of the oxides, i.e. Al_2O_3, Na_2O etc. To assist the reader, all the source, mineral, and melt compositions derived from modelling have been recalculated to weight percentages.

	Composition	T (°C)	P (kb)	fO$_2$	Olivine*	Opx*	Cpx*	Spinel*
Agee and Walker, 1990	Spinifex komatiite B-4, Zimbabwe	1960-1300	0.001-60	QFM	9			
Barnes, 1986	Bushveld chilled margin	1151-1334	0.001	NNO-IW		42		41
Bender et al., 1978	FAMOUS basalt 527-1-1	1208-1350	0.001-15	IW	18	1	5	
Bickle et al., 1977	NG 157, NG 7621, NG 152, NG 7638 peridotitic komatiites	1470-1850	15-40	C-CO	5	3		
Cawthorn and Davies, 1983	Fine grained feldspathic orthopyroxenite, Bushveld	1350	3	Pt-Fe capsule	1	1		
Duncan and Green, 1987	Inferred Troodos Upper Pillow Lava parent	1120-1400	0.001-10	Fe-FeO		3		
Elthon and Scarfe, 1984	Tortuga ophiolite, NT-23 basalt	1170-1500	10-30	C-CO	17	8		
Faloon and Green, 1987	MORB pyrolites MPY-87, MPY-90, MPY-90 minus 40% olivine, Tinaquillo lherzolite minus 40% olivine	1230-1420	10	C-CO	16	16	12	8
Fisk and Bence, 1980	As Bender et al., 1978	1175-1280	0.001	NNO+2-WCO				14
Fujii and Bougault, 1983	FAMOUS basalt ARP 74 10-16	1150-1325	0.001-15	10^{-8}atm.	1	1	1	
Grove and Bryan, 1983	FAMOUS (525-4 and 528-1-1), 23 °N (AII96-6-42) and 43 °N (AII32-12-6) basalts	1131-1245	0.001	QFM	37		19	5
Grove et al., 1990	ALV-1690-20 basalt 22 °N MAR	1108-1251	0.001-8	QFM	11		8	
Jaques, 1980	Pyrolite minus 40% olivine	1100-1550	2-15	C-CO		14	5	16
Jaques, 1980	Tinaquillo lherzolite minus 40% olivine	1100-1550	2-15	C-CO		14	4	15
Jaques, 1980	Lau basalt 95-1	1130-1480	0.0001-22	C-CO	29		14	4
Kinzler and Grove, 1985	Synthetic komatiite, two compositions	1173-1371	0.001	QFM	11			
Longhi et al., 1983	WSD-14 high-Mg chill margin, Montana	1180-1300	0.001	QFM-1		2	2	
Murck and Campbell, 1986	401 basalt	1150-1450	0.001	NNO-IW				22
Murck and Campbell, 1986	Jimberlana margin continental tholeiite, N-140	1250-1450	0.001	NNO-IW	11			22
Murck and Campbell, 1986	Kambalda komatiite, Z17054	1300-1500	0.001	NNO+1/ QFM-1	11			11

continued

Stolper, 1980	ALV-519-4-1 MORB +ol+opx	1250-1400	0.001-30	C-CO	4	3	1	
Takahashi, 1980	Alkali olivine basalt KRB	1270-1275	14.0	C-CO	2	2	1	
Takahashi, 1986	Peridotite KLB-1	1100-2300	0.001-140	NNO	4	2	4	1
Takahashi and Kushiro,1983	Peridotite HK66	1050-1600	0.001-51	C-CO	5	5	4	1
Tormey et al., 1987	22°-25 °N Kane Fracture Zone AII96-18-1, GS104-2-1, AII78-3-102, ALV528-1-1 basalts	1152-1230	0.001	QFM	19		5	1
Walker et al., 1979	V30-RD8-P12 & V30-RD8-P22 35 °N MAR basalts	1106-1199	0.001	QFM	8		10	

Table (5.1) Melting and crystallization experiments used in the calculation of major element distribution coefficients. *refers to the number of published analyses.

5.3.1. Olivine

5.3.1.1. Magnesium

Figure 5.1 is a plot of $LnKd_{Mg}^{ol/liq}$ against $1000/T^{\circ}C$. The regression line is calculated for experiments at 1 bar at the quartz-fayalite-magnetite (QFM) buffer. The regression of Roeder and Emslie (1970) is also included, showing good agreement in the range 1430 to 1200°C. A small deviation is observed at lower temperatures, and becomes maximum at 1100°C, where a difference of 1.15 in the $Kd_{Mg}^{ol/liq}$ value is observed (20% relative). This deviation is the result of the different and much more extensive data set used in this study.

In order to assess the effect of oxygen fugacity (f_{O_2}), the data of Bender et al. (1978) at the iron-wüstite (IW) buffer have been plotted in Figure 5.1. Roeder and Emslie (op. cit.) showed that the forsterite content of olivine is increased with increasing f_{O_2} at constant temperature, from Fo_{75} at the IW buffer to Fo_{95} at the heamatite-magnetite (HM) buffer. This change, however, is very small from IW to QFM (less than 6% relative, Roeder and Emslie, op. cit., their Figure 5.2b) and the data of Bender et al. (1978) at the IW show that $Kd_{Mg}^{ol/liq}$ is essentially the same with QFM.

The effect of pressure on $Kd_{Mg}^{ol/liq}$ is more difficult to discern. Hanson and Langmuir (1978) argued that $Kd_{Mg}^{ol/liq}$ (and $Kd_{Fe}^{ol/liq}$) must increase with pressure in order to be consistent with the solidus of pyrolite. They supported this suggestion with the experimental data of Longhi et al. (1978) and Bickle et al. (1977) on lunar basaltic and komatiitic compositions respectively. The data of Bickle et al. (op. cit.) at 15 and 30 kb pressure, as well as the 10 kb data of Falloon and Green (1987) and Jaques (1980) are plotted in Figure 5.1. The 30 kb data show a slight increase of $Kd_{Mg}^{ol/liq}$, but the 15 kb points are indistinguishable from the 1 bar experiments. The data of Falloon and Green (1987) at 10 kb show a larger shift towards higher $Kd_{Mg}^{ol/liq}$ values, but are at odds with the data of Jaques (1980) at the same pressure[4]. Examination of the Falloon and Green (1987) data $Kd_{Fe-Mg}^{ol/liq}$ (this is the

---

[4]The experiments of Jaques (1980) on the Tinaquillo lherzolite and Hawaian pyrolite were published by Jaques and Green (1980), and do not include olivine analyses (see Table 5.1). Because of Fe loss from the charge to the container, these authors calculated the equilibrium olivine composition using the formulation of Roeder and Emslie (1970). In

$\left[\dfrac{(Fe/Mg)_{ol}}{(Fe/Mg)_{liq}}\right]$ ratio between olivine and melt) has an average value of 0.34, instead of the

expected 0.30±0.01 at 10 kb (Roeder and Emslie, 1970; Takahashi and Kushiro, 1983),

suggesting that the olivine compositions in these experiments are out of equilibrium with the

co-existing liquid. In view of the uncertainty, and the fact that $Kd_{Mg}^{ol/liq}$ varies little with

pressure (Figure 5.1), no pressure correction was applied to $Kd_{Mg}^{ol/liq}$.

LnKdMg ol=4822.073/T°C-2.58156
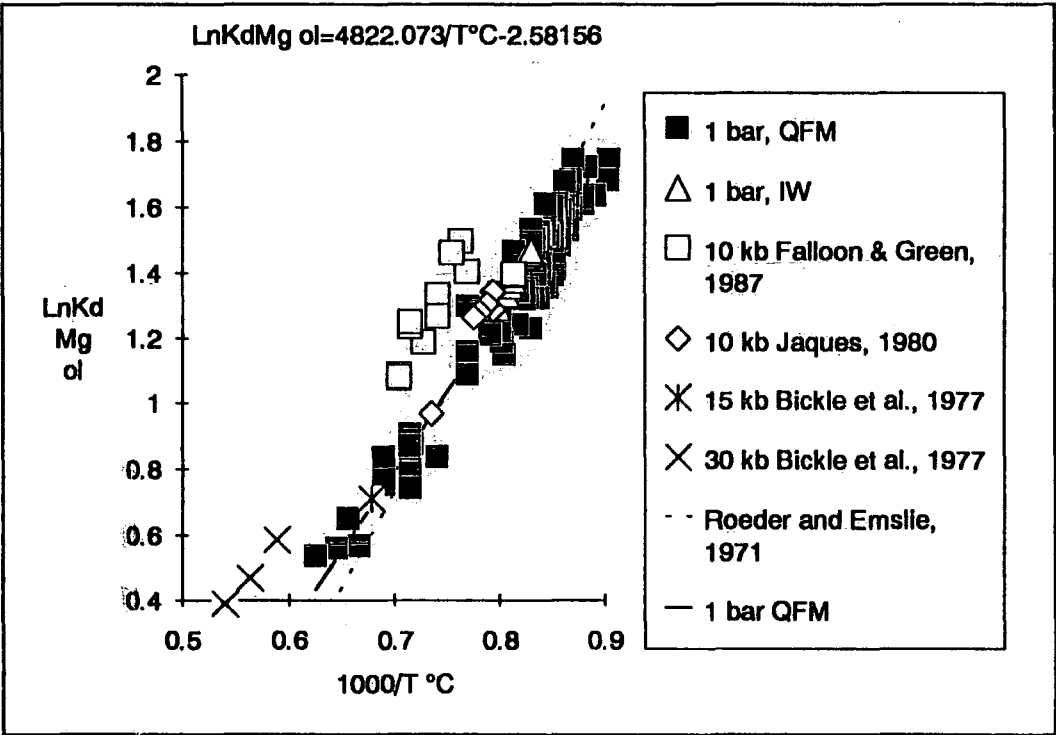
Figure (5.1) Plot of $LnKd_{Mg}^{ol/liq}$ vs. 1000/T°C. Dashed line is the regression of Roeder and Emslie (1970). Solid line corresponds to the expression shown and was calculated for the 1bar QFM experiments.

5.3.1.2. Iron

Figure 5.2 shows the effect of temperature on the partitioning of Fe between olivine

and liquid. It will be noted that the distribution coefficient has been calculated using total Fe in

addition, the melt composition of the charges was calculated from estimates of the degree of melting and mineral compositions by mass balance. Falloon et al. (1987) duplicated Jaques' (1980) experiments and showed that the calculated melt compositions of Jaques (1980), also published in Jaques and Green (1980), were in error. The olivine analyses used here are from experiments on a Lau Basin basalt composition (see Table 1) for which olivine and melt were directly analysed by probe (Jaques, 1980).

the melt and not the fraction of ferrous iron. This has been done in order to establish how varying f_{O_2} conditions affect the $Kd_{Fe}^{ol/liq}$. In theory as oxygen fugacity increases so does the Fe^{3+}/Fe^{2+} ratio of the liquid; since probe analysis cannot distinguish between the different valency states of an element, as the Fe^{3+}/Fe^{2+} ratio in the melt increases so $Kd_{Fe}^{ol/liq}$ should decrease. This however is not apparent in Figure 5.2, as the data of Bender et al. (1977) at the IW buffer are indistinguishable from those at the QFM buffer. The reason for this similarity in the $Kd_{Fe}^{ol/liq}$ is that the Fe^{3+}/Fe^{2+} ratio of the liquid increases slowly between IW and QFM and rapidly from QFM to HM (Roeder and Emslie, 1970). This change is sufficiently small (Figure 5.2) to be ignored. Figure 5.2 also shows the regression line of Roeder and Emslie (1970), which is subparallel to the one calculated in this study, but shifted to slightly higher $Kd_{Fe}^{ol/liq}$ values. This difference between the two trends is ascribed to the use by Roeder and Emslie (op. cit.) of the ferrous iron fraction of the melt to calculate $Kd_{Fe}^{ol/liq}$. This leads to a 15% relative difference in the calculated value of $Kd_{Fe}^{ol/liq}$, which is consistent with an average Fe^{3+}/Fe^{2+} ratio of the liquid of 0.15 at the conditions of the experiments (Roeder and Emslie, 1970; Kilinc et al., 1983).

The 10 kbar data of Falloon and Green (1987) and Jaques (1980), and the 15 and 30 kb data of Bickle et al. (1977) are also shown in Figure 5.2. Similarly to $Kd_{Mg}^{ol/liq}$, no pressure correction was applied to $Kd_{Fe}^{ol/liq}$.

LnKdFe ol=5286,158/T⁰C-4.21862

$$\text{LnKdFe ol} = 5286,158/T^\circ C - 4.21862$$
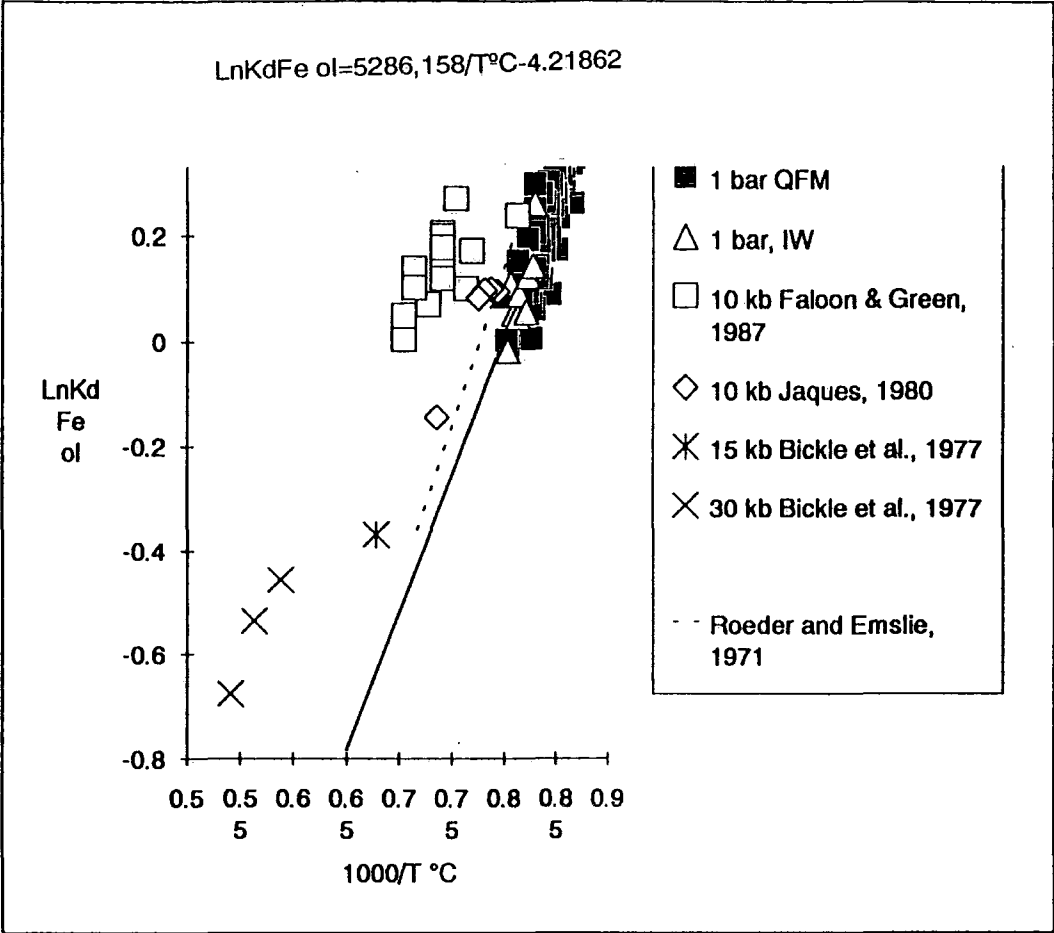
Figure (5.2) Plot of $LnKd_{Fe}^{ol/liq}$ vs. 1000/T°C. Iron is total iron in melt. Dashed line is the regression of Roeder and Emslie (1970). Solid line corresponds to the expression shown and was calculated for the experiments at 1bar QFM. The high temperature experiments of Bickle et al. (1977) and Agee and Walker (1990) were omitted from the regression.

5.3.1.3. Silica

Figure 5.3 is a plot of $LnKd_{Si}^{ol/liq}$ against 1000/T°C. The data of Bender et al. (1977) are shown in comparison with experiments at QFM. Since the mole fraction of SiO_2 in olivine is constant (33.33%) it is not expected to vary with f_{O_2}. This is confirmed by the relative position of the IW and QFM data.

As with $Kd_{Mg}^{ol/liq}$ and $Kd_{Fe}^{ol/liq}$, the effect of pressure on $Kd_{Si}^{ol/liq}$ is difficult to assess. Figure 5.3 includes the 10 kb data of Falloon and Green (1987) which define a distinct trend, but are at odds with the data of Jaques (1980) and Elthon and Scarfe (1984) at the same pressure. The reason for this disagreement is not clear. Although the olivines of Falloon and Green (op. cit.) may have only partially equilibrated with the liquid, as mentioned earlier, this is only true for the Fe-Mg exchange and should not affect SiO_2 partitioning, since the mole

fraction of SiO_2 in olivine is constant. Still, in view of the good agreement between the high pressure data points of Jaques (1980) and Elthon and Scarfe (1984) with the 1 bar experiments, no pressure correction will be introduced for $Kd_{Si}^{ol/liq}$.

$$LnKdSi\ ol = -1189.26/T°C + 0.534404$$
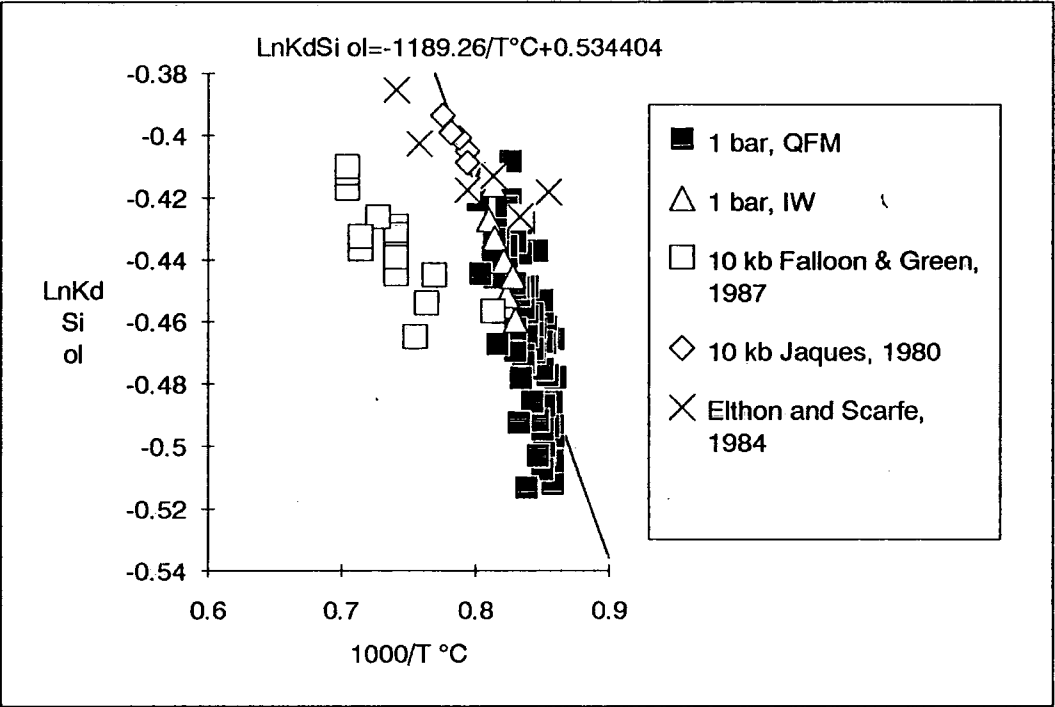
Figure (5.3) Plot of $LnKd_{Si}^{ol/liq}$ vs. 1000/T°C.

5.3.1.4. Further comments on the pressure effects on olivine

Klein and Langmuir (1987), in a global study of MORBs, suggested that the FeO and MgO content of basalts increases with increasing depth of melt generation, whereas at the same time their SiO_2 content decreases. They supported this suggestion with the experimental data of Jaques and Green (1980) and Takahashi (1986)[5], for which the extent of melting in the experimental charge was determined. Klein and Langmuir (1987) plotted the SiO_2 wt.% of experiments at 5, 10, 15, and 30 kb (calculated at 9 wt.% MgO) against the degree of melting. They observed that, for a given degree of melting, the SiO_2 content of the melt decreased with increasing pressure. They also observed that in a plot of MgO against

---

[5]Takahashi (1986) does not report the extent of melting in the experimental charges, but Klein and Langmuir (1987) calculated it by mass balance from the mineral analyses.

FeO (cation mole%), isobaric experiments defined distinct fields of increasing FeO and MgO with increasing pressure. Although Klein and Langmuir (1987) did not explicitly refer to partition coefficients (but rather to general characteristics of the chemistry of basalts) the implications of their suggestion is that the partition coefficients in olivine of FeO and MgO should decrease and for SiO_2 should increase with pressure[6]. However, as Figures 5.1, 5.2, and 5.3 show, $Kd_{Mg}^{ol/liq}$, $Kd_{Fe}^{ol/liq}$, and $Kd_{Si}^{ol/liq}$ either do not show any pressure dependence or change in exactly the opposite way than expected. An explanation for this discrepancy will be suggested here. In melting experiments the temperature and pressure are adjusted to roughly follow the solidus of the peridotite; this means that experiments conducted at high pressures are also at high temperatures. The Kd's variation that is consistent with Klein and Langmuir's (op. cit.) suggestions (i.e. $Kd_{Mg}^{ol/liq}$ and $Kd_{Fe}^{ol/liq}$ decrease and $Kd_{Si}^{ol/liq}$ increases with increasing pressure) is also consistent with the expected variation at increasing temperature. Normalizing the SiO_2 content to 9 wt.% MgO, as Klein and Langmuir (op. cit.) did, is not equivalent to comparing melts at the same temperature, so the effects of pressure and temperature cannot be distinguished in the diagrams that Klein and Langmuir (1987) used. The same argument applies to the natural basalts studied by Klein and Langmuir (op. cit.). Adiabatically rising mantle will cross its solidus at a depth that is determined by the peridotite potential temperature (McKenzie, 1984). Upwelling asthenosphere with a high potential temperature will start melting deeper and will, subsequently, experience higher degrees of melting and vice versa.

As already mentioned, the available the experiments show that $Kd_{Mg}^{ol/liq}$, $Kd_{Fe}^{ol/liq}$, and $Kd_{Si}^{ol/liq}$ either do not show any pressure dependence or they change in the opposite way than inferred by Klein and Langmuir's (1987) conclusions. The observed change is small compared to the change due to temperature variations and is likely to be masked by the

---

[6]Although the contribution of olivine to the melt is small, compared to that of the pyroxenes, it has a significant effect on the bulk distribution coefficients of SiO_2, MgO, and FeO because of its great abundance in mantle assemblages. In addition, the distribution coefficients of these elements in pyroxene are directly related to those of olivine, as will be shown later.

latter. Therefore, ignoring the pressure effect will not introduce a large error in the calculations.

5.3.1.5. Fe-Mg exchange between olivine and melt

Having calculated expressions for $Kd_{Fe}^{ol/liq}$ and $Kd_{Mg}^{ol/liq}$, it is easy to calculate the partitioning of Fe and Mg between olivine and liquid:

$$Kd_{Fe-Mg}^{ol/liq} = \frac{FeO^{ol}/MgO^{ol}}{FeO^{liq}/MgO^{liq}} = \frac{FeO^{ol}}{FeO^{liq}} \frac{MgO^{liq}}{MgO^{ol}} = \frac{Kd_{Fe}^{ol/liq}}{Kd_{Mg}^{ol/liq}} \Leftrightarrow$$

$$LnKd_{Fe-Mg}^{ol/liq/liq} = LnKd_{Fe}^{ol/liq} - LnKd_{Mg}^{ol/liq} = \frac{464}{T^{\circ}C} - 1.637 \tag{5.12}$$

The expression of Roeder and Emslie (1970) for $Kd_{Fe-Mg}^{ol/liq}$ is:

$$LogKd_{Fe-Mg}^{ol/liq} = \frac{171}{T^{\circ}K} - 0.63 \tag{5.13}$$

Equation 5.12 shows a larger temperature dependence of $Kd_{Fe-Mg}^{ol/liq}$ than Equation 5.13, obviously due to the different slopes of the regression lines for $Kd_{Fe}^{ol/liq}$ and $Kd_{Mg}^{ol/liq}$ (see Figures 5.1 and 5.2), resulting from the wider temperature range of the experiments considered in this study. Weaver and Langmuir (1990) also calculated expressions for Kd_{Fe}^{ol} and $Kd_{Mg}^{ol/liq}$ from which Equation 5.14 is derived.

$$LogKd_{Fe-Mg}^{ol/liq} = \frac{1515}{T^{\circ}K} - 1.583 \tag{14}$$

$Kd_{Fe-Mg}^{ol/liq}$ values, calculated from equations 5.12, 5.13, and 5.14 for the temperature range 1100-1400°C, are shown in Table 5.2. The expression of Weaver and Langmuir (1990) shows the largest temperature variation, whereas that of Roeder and Emslie (1970) is virtually independent of temperature. Equation 5.12 was derived from the largest data set and, being intermediate between the other two expressions, provides the best compromise.

T°C	$Kd^{ol/liq}_{Fe-Mg}$		
	Roeder and Emslie (1970)	Weaver and Langmuir (1990)	This work
1100	0.312	0.331	0.297
1200	0.306	0.279	0.286
1300	0.301	0.240	0.278
1400	0.297	0.210	0.271

Table (5.2) Variation of $Kd^{ol/liq}_{Fe-Mg}$ with temperature.

5.3.1.6. Nickel. Titanium. Chromium

Olivine is the major sink of nickel in the mantle (excluding sulphides) and its distribution coefficient has been the subject of many studies and some controversy (e.g. Hart and Davis, 1978, 1979; Elthon and Ridley, 1979; Mysen, 1979, 1981, 1982; Kinzler et al., 1988). Kostopoulos (1988) derived temperature-dependent equations for the Kds of Ni, Ti, and Cr between mantle phases and liquids of basaltic composition, and his expressions, adjusted for mole fractions, have been used here. The expression used for Ni is:

$$LnKd^{ol/liq}_{Ni}=8208.386/T°C-4.22685$$

That for Cr is:
$$LnKd^{ol/liq}_{Cr}=5255.96/T°C-4.17309$$

and that for Ti is:
$$LnKd^{ol/liq}_{Ti}=5528.57/T°C-8.51425$$

5.3.1.7. Aluminium

The Al_2O_3 content of olivines is always very low and does not greatly affect the Al_2O_3 abundance of the whole rock. This allows the use of an average $Kd^{ol/liq}_{Al}$ value without introducing significant error to the calculated melt and source compositions. In studies where olivine was analyzed for Al_2O_3, the average value for $LnKd^{ol/liq}_{Al}$ is -5 and this value will be used here for the modelling.

5.3.1.8. Manganese

Mn is geochemically similar to Fe and tephroite (Mn_2SiO_4) has similar thermodynamic properties to fayalite (Krauskopf, 1977). This suggests that the Mn distribution coefficient for olivine should be similar to that of Fe. This is supported by Figure

5.4, where $LnKd_{Mn}^{ol/liq}$ is plotted against $LnKd_{Fe}^{ol/liq}$. Watson (1977) studied the partitioning of Mn in forsterite in the iron-free system $MgO\text{-}CaO\text{-}Na_2O\text{-}Al_2O_3\text{-}SiO_2$ (+0.2% Mn) at atmospheric pressure, over the temperature range 1250-1450°C. He found that the Mn partition coefficient depends on liquid composition as well as temperature; in particular $Kd_{Mn}^{ol/liq}$ increases with increasing SiO_2 content of the coexisting melt and attains maximum values in rhyolitic melts. In this study, a temperature-dependent expression was formulated from the experiments of Watson (op. cit.) in which the liquid SiO_2 content was ~49 wt.%, which is an appropriate value for basaltic melts. The derived equation for $LnKd_{Mn}^{ol/liq}$ is:

$$LnKd_{Mn}^{ol/liq} = \frac{5500}{T°K} - 3.385$$

and it is compared with that for $LnKd_{Fe}^{ol/liq}$ in Figure 5.5. The result is in good agreement with Figure 5.4 supporting the conclusion of Watson (1977) that his work can be extended to iron-bearing assemblages.

The expression of Watson (1977) for $Kd_{Mn}^{ol/liq}$ will be used in the present modelling because of its better analytical accuracy.
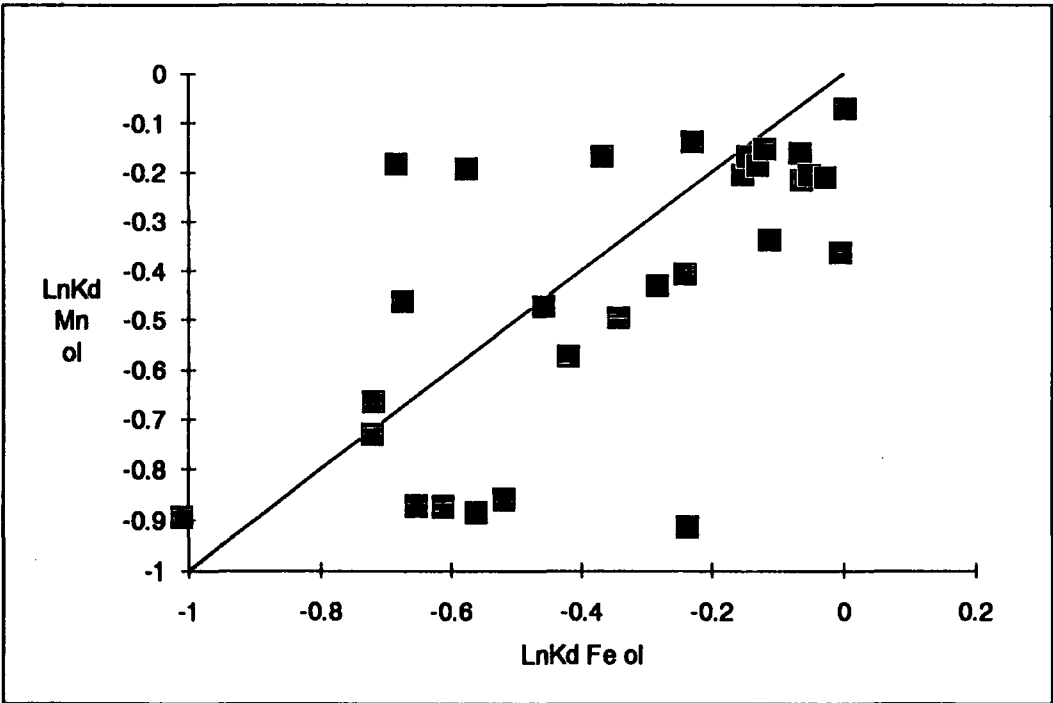
Figure (5.4) Plot of $LnKd_{Mn}^{ol/liq}$ vs. $LnKd_{Fe}^{ol/liq}$. 1:1 line shown for reference.
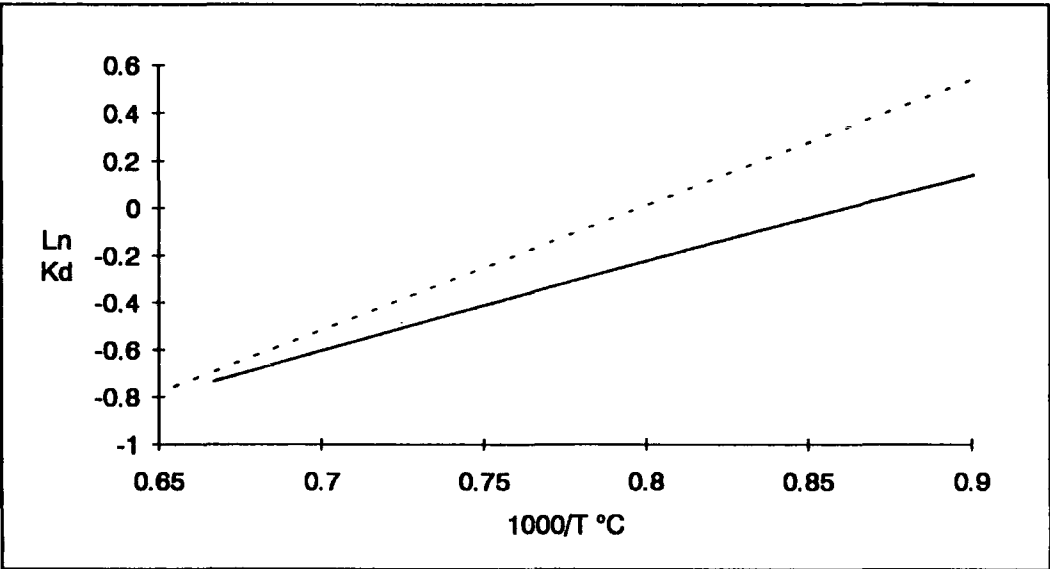
Figure (5.5). Dotted line is the temperature-dependent expression for $LnKd_{Fe}^{ol/liq}$ (Figure 5.2) and solid line is the temperature-dependent expression for $LnKd_{Mn}^{ol/liq}$, calculated from the data of Watson (1977).

5.3.1.9. Sodium. Potassium

Na and K are very incompatible elements and their very low concentrations in olivine result in a lack of data in the experiments considered. Because of their low concentrations, and the fact that they are rapidly depleted from the residue during melting, their partition coefficients can be approximated without introducing a large error in the calculations. For the purpose of the present modelling constant Kd values of 1×10^{-3} and 1×10^{-4} will be used for Na_2O and K_2O respectively.

5.3.1.10. Calcium

Calcium is a minor constituent of natural olivines and it is frequently omitted from microprobe analyses. Jurewicz and Watson (1988) studied the partitioning of Ca between olivine and melt in detail, and found that $Kd_{Ca}^{ol/liq}$ primarily depends on the CaO content of the melt and the relative iron activity of olivine, as indicated by its fayalite content. They found no direct effect from temperature or oxygen fugacity, and the effect of pressure was negligible below 20 kb. For melts with less than about 8 to 15 wt.% CaO, they derived the following empirical relation for $Kd_{Ca}^{ol/liq}$:

$$Kd_{Ca}^{ol/liq} = 0.01*\{(-0.08)*fo\% + 9.5\}$$

where fo is the forsterite % content of olivine. Note that this is weight % and not molar $Kd_{Ca}^{ol/liq}$.

The above expression gives a value for $Kd_{Ca}^{ol/liq}$ of 0.024 for coexisting Fo_{89} olivine and 0.021 for coexisting Fo_{92} olivine; since the CaO content of olivine is only a small fraction of the whole rock CaO abundance and the variation of $Kd_{Ca}^{ol/liq}$ is so small, the use of an average value of 0.022 is considered adequate. This can be converted to molar $Kd_{Ca}^{ol/liq}$ by dividing by 1.071 to give the $Kd_{Ca}^{ol/liq}$ value of 0.0205 used in the modelling .

5.3.2. Orthopyroxene

5.3.2.1. Magnesium

As has been shown in Chapter 3, the ratio of Mg# between olivine and orthopyroxene is virtually constant; this suggests that the Fe-Mg partitioning between the two minerals is interdependent. The linear correlation between $LnKd_{Mg}^{ol/liq}$ and $LnKd_{Mg}^{opx/liq}$ (Figure 5.6) demonstrates this point. The above approach is preferred over expressing $LnKd_{Mg}^{opx/liq}$ independently as a function of temperature, because it ensures that the calculated mineral compositions reflect those of the natural assemblages.

LnKdMg opx=1.019089*LnKdMg ol-0.38644
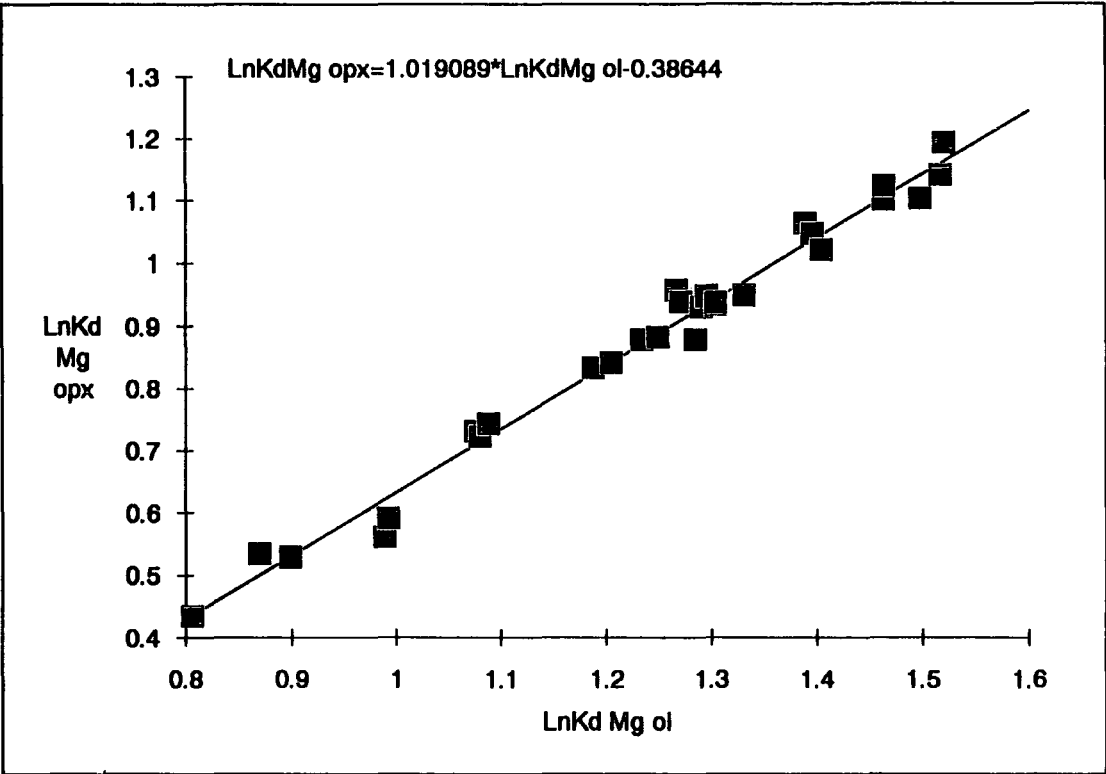
Figure (5.6) Plot of $LnKd_{Mg}^{ol/liq}$ vs. $LnKd_{Mg}^{opx/liq}$ for all available experiments with coexisting olivine and pyroxene.

LnKdMg opx=4470.69/T °C-2.50286
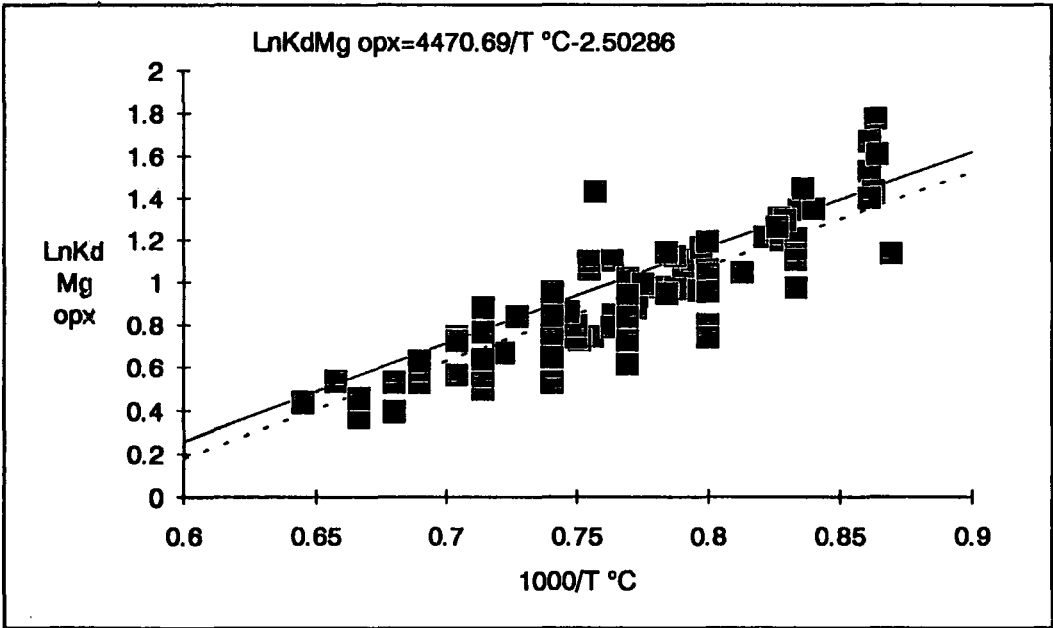
Figure (5.7) Dashed line corresponds to the equation and was calculated from all orthopyroxene data. Solid line is $LnKd_{Mg}^{opx/liq}$ calculated from $LnKd_{Mg}^{ol/liq}$ (see text and Figure 5.6).

The small deviation from linearity that inevitably occurs in calculating a temperature-dependent expression for $LnKd_{Mg}^{opx/liq}$ using all the available experiments (Figure 5.7), is

rather due to melt composition effects than to lack of robust correlation in the Fe-Mg exchange between olivine and orthopyroxene.

5.3.2.2. Iron

Similarly to $Kd_{Mg}^{opx/liq}$, $Kd_{Fe}^{opx/liq}$ has also been determined as a function of $Kd_{Fe}^{ol/liq}$ (Figure 5.8). The regression line so obtained has a shallower slope (0.773) compared to the regression for MgO, which is 1.019 (see Figure 5.6). The result of this is that calculated orthopyroxene compositions will have always greater Mg# than coexisting olivines, which is consistent with observation of natural assemblages (see Chapter 3, orthopyroxene chemistry).
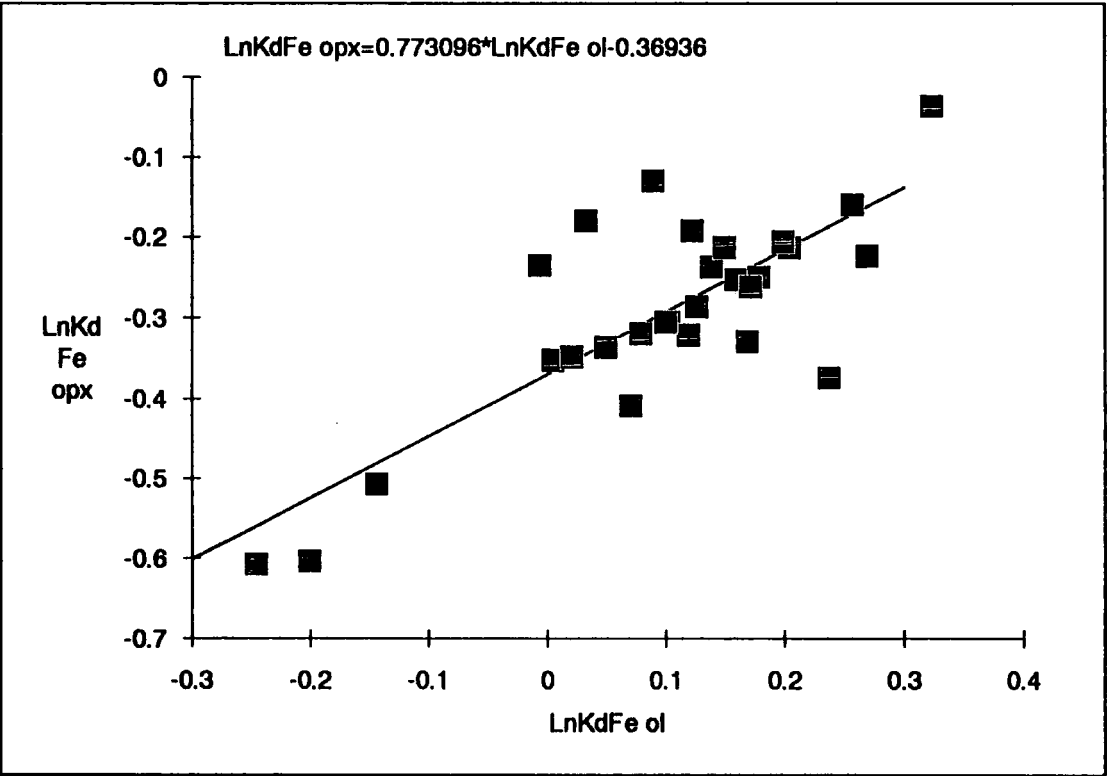
Figure (5.8) Plot of $LnKd_{Fe}^{ol/liq}$ vs. $LnKd_{Fe}^{opx/liq}$ for the same experiments as in Figure 5.6.

5.3.2.3. Silica

$LnKd_{Si}^{opx/liq}$ has been determined as a function of $LnKd_{Si}^{ol/liq}$ (Figure 5.9). The correlation observed between these parameters is the result of using mole fractions for the mineral compositions. From the mineral formulae:

$$(Mg,Fe)_2SiO_2 \qquad\qquad (Mg,Fe,Ca)SiO_2$$
olivine pyroxene
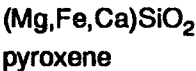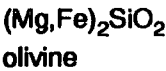
it follows that SiO_2 in olivine is 33.33 mole% and in pyroxene 50 mole%. This gives a

constant ratio of:

$$\frac{SiO_2{}^{opx}}{SiO_2{}^{ol}} = 1.5 \Leftrightarrow \frac{SiO_2{}^{opx}/SiO_2{}^{liq}}{SiO_2{}^{ol}/SiO_2{}^{liq}} = 1.5 \Leftrightarrow \frac{Kd_{Si}{}^{opx/liq}}{Kd_{Si}{}^{ol/liq}} = 1.5 \Leftrightarrow$$

$$Ln\left[\frac{Kd_{Si}{}^{opx/liq}}{Kd_{Si}{}^{ol/liq}}\right] = Ln(1.5) \Leftrightarrow LnKd_{Si}{}^{opx/liq} - LnKd_{Si}{}^{ol/liq} = Ln(1.5) \Leftrightarrow$$

$$LnKd_{Si}{}^{opx/liq} = LnKd_{Si}{}^{ol/liq} + 0.4055$$

The equation calculated in Figure 5.9 differs slightly from the above expression probably

because of the limited substitution of SiO_2 in orthopyroxene by Al_2O_3. This substitution

results in SiO_2 molar contents of orthopyroxene being always less than the ideal 50%.
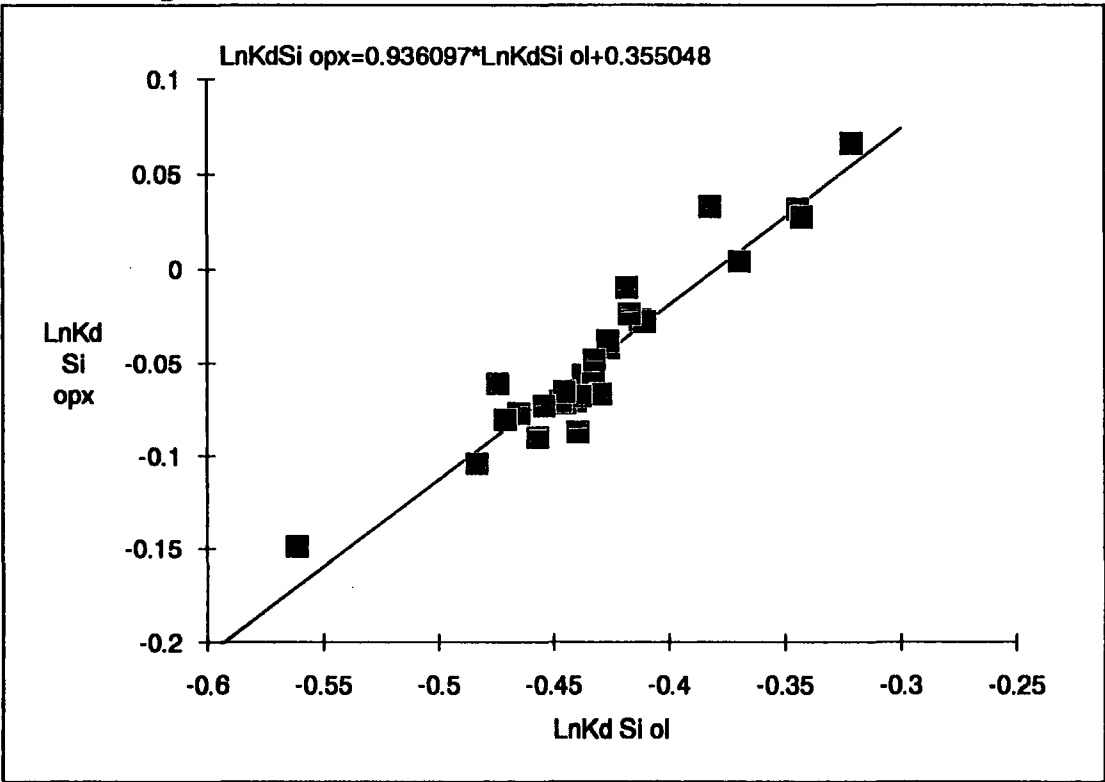
Figure (5.9) Plot of $LnKd_{Si}{}^{ol/liq}$ vs. $LnKd_{Si}{}^{opx/liq}$ for the same experiments as in Figures 5.6 and 5.8.

5.3.2.4. Aluminium

The Al content of orthopyroxene (and clinopyroxene) is both temperature and

pressure dependent. Figure 5.10 shows the plot of $LnKd_{Al}{}^{opx/liq}$ vs. $1000/T^\circ C$ for the isobaric

equilibrium melting experiments of Jaques (1980). Multiple linear regression shows that a

simple linear relation with pressure is sufficient to adequately reproduce the observed variation.

Comparison, however, of the experiments of Jaques (1980) with those of Barnes (1986) at 1 bar and Falloon and Green (1987) at 10 kb (Figure 5.11) shows significantly higher $Kd_{Al}^{opx/liq}$ values for the latter two data sets at any given temperature, while both the slope and relative position to pressure of the regression lines are almost the same with those of Jaques (op. cit.). Interlaboratory difference must be ruled out since the experiments of Falloon and Green (1987) were performed at the same laboratory as those of Jaques (op.cit.) (University of Tasmania) under the supervision of Professor D. H. Green; compositional dependence is also ruled out since the experiments were performed on similar compositions (see Table 5.1). The question of which experiments represent the true absolute Kd's is resolved in considering the way Jaques (1980) calculated the melt composition, viz. using the modal percentages and compositions of solid phases in the experimental charge and calculating the equilibrium melt composition by mass balance. Although this approach corrects for any Fe loss or gain of the melt to the capsule, uncertainties in the determination of the modal proportions of the phases, and whether true equilibrium compositions were probed, may lead to errors in the calculated liquid composition. This was confirmed by Falloon et al. (1988), who performed sandwich melting experiments on the calculated equilibrium melts of Jaques (1980) and found that the equilibrium melts were poorer in Al and Ca than the calculated equilibrium melts. This is consistent with the difference that is observed in Figure 5.11 and, therefore, the experiments of Falloon and Green (1987) and Barnes (1986) are considered closer to the true values of $Kd_{Al}^{opx/liq}$ and will be used to determine the expression used for the Kd.

LnKdAl opx=7478/T°C+0.1655*P(kb)-9.24755
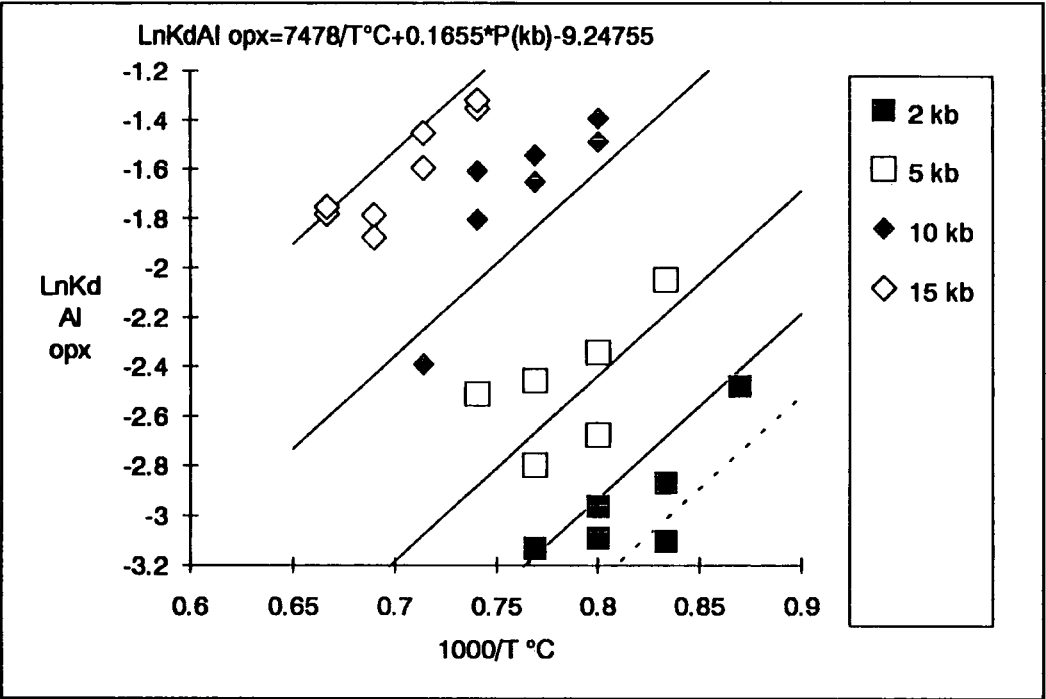
Figure (5.10) Plot of LnKd$_{Al}^{opx/liq}$ vs. 1000/T°C for the polybaric experiments of Jaques (1980). The dashed line is extrapolation of the regression equation for 1 bar pressure.
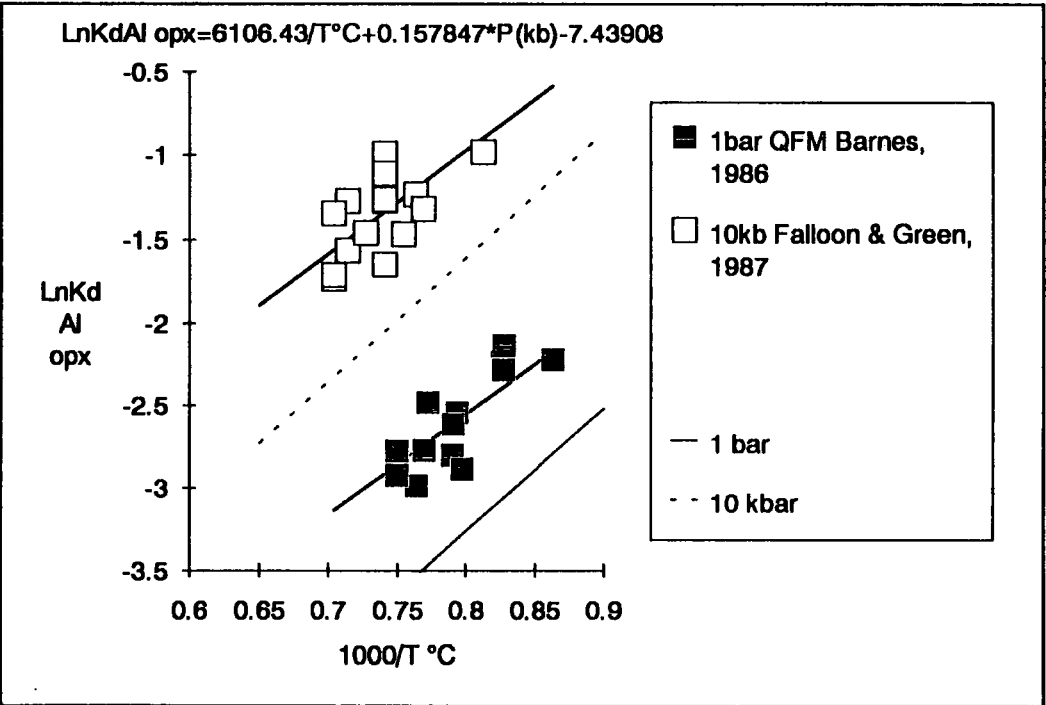
LnKdAl opx=6106.43/T°C+0.157847*P(kb)-7.43908

Figure (5.11) Plot of LnKd$_{Al}^{opx/liq}$ vs. 1000/T°C for the data of Falloon and Green (1987; open squares) and Barnes (1986; filled squares), from which the regression equation was derived and the best fits (thick lines) at 1 bar and 10 kbar were calculated. The thin line is the extrapolated 1 bar line from the equation of Figure 5.10 and the dashed line is the same for 10 kbar.

5.3.2.5. Calcium

The partitioning of Ca in orthopyroxene heavily depends on the presence of coexisting clinopyroxene. If both pyroxenes are in equilibrium, then the CaO content of orthopyroxene will be controlled by the position of the two-pyroxene solvus in the P-T space (e.g. Davidson and Lindsley, 1985). If orthopyroxene melts in the absence of clinopyroxene then $LnKd_{Ca}^{opx/liq}$ becomes strongly temperature and pressure dependent.

This dependence is demonstrated in Figure 5.12, which shows $LnKd_{Ca}^{opx/liq}$ vs. $1000/T°C$ for the isobaric equilibrium melting experiments of Jaques (1980). Multiple linear regression yields the expression:

$$LnKd_{Ca}^{opx/liq} = \frac{7384.2}{T°C} + 0.0662 * P\ kb - 8.0243$$

that reproduces the observed values quite well.

Figure 5.13 shows the experiments of Falloon and Green (1987) at 10 kb pressure and Barnes (1986) at atmospheric pressure. As was the case with Al_2O_3, the data of Falloon and Green (op. cit.) show higher $Kd_{Ca}^{opx/liq}$ values than those of Jaques (1980) at any given temperature, since the coexisting melts in the former study are poorer in CaO than the corresponding melts the latter. In contrast with Al_2O_3, however, the slopes of the best-fit lines for the three sets of experiments are different; the data of Barnes (1986) show a strong positive temperature dependence, the data of Jaques (1980) show a lees pronounced positive correlation with temperature, whereas the data of Falloon and Green (1987) show only a small positive temperature dependence. Considering that: i) the experiments of Barnes (op. cit.) did not crystallize any clinopyroxene at all; ii) only 8 out of the 28 experiments of Jaques (1980) contained clinopyroxene, and iii) 12 out of the 16 experiments of Falloon and Green (op. cit.) had coexisting ortho- and clinopyroxene, it seems that the presence of clinopyroxene minimizes the effects of temperature on the partitioning CaO between orthopyroxene and melt.

This is clearly shown in Figure 5.14, where $LnKd_{Ca}^{opx/liq}$ is plotted against $1000/T°C$ only for those experiments that contained coexisting pyroxenes. Although the data points are from 5 different experimental studies (and compositions, see Table 5.1) they scatter around an average $LnKd_{Ca}^{opx/liq}$ values of ~-1.5 and define a slightly negatively sloping array with no

obvious pressure effects. This is consistent with the control exerted by the two-pyroxene solvus on the Wo component of orthopyroxene as shown by the graphical thermometer of Lindsley and Andersen (1983),   As temperature decreases, orthopyroxene becomes Ca-poor (i.e. Kd becomes smaller) and the tight isotherms suggest that this compositional change is slow (reflected in the gently sloping regression line in Figure 5.14). Applying the pressure correction term suggested by Lindsley and Andersen (op. cit.), at the temperatures and compositions of interest the isotherms in Figure 5.15 shift by +3°C/kbar for clinopyroxene and +10°C/kbar for orthopyroxene, consistent with the small change of $Kd_{Ca}^{opx/liq}$ with pressure.

LnKdCa opx=7384.2/T°C+0.0662P(kb)-8.0243
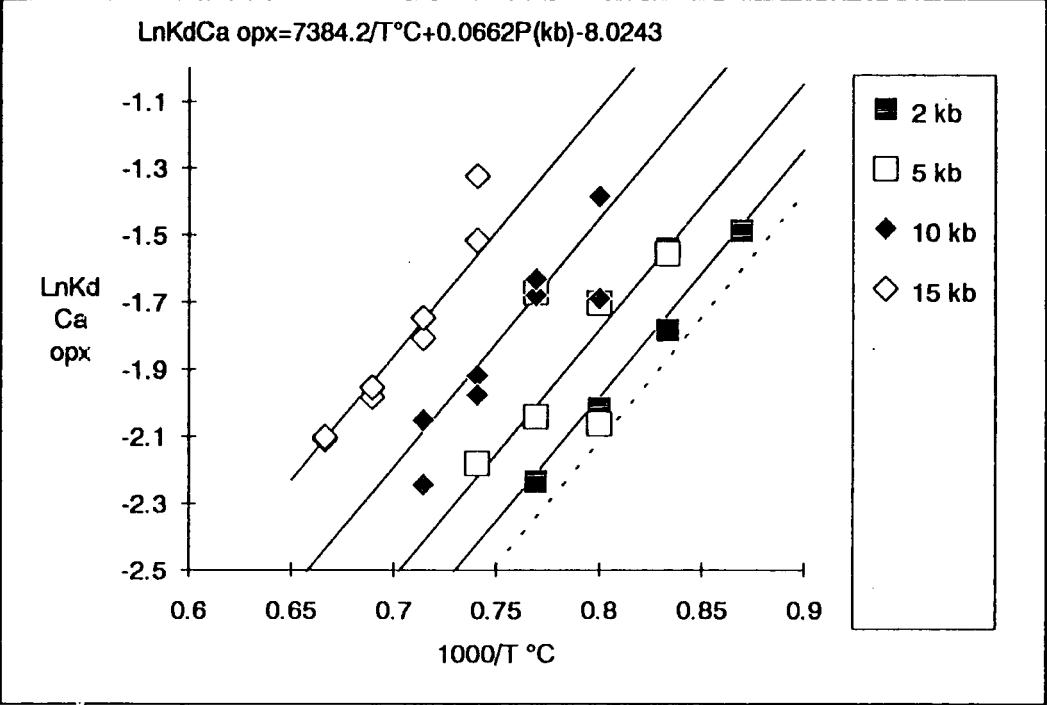
Figure (5.12) Plot of $LnKd_{Ca}^{opx/liq}$ vs. 1000/T°C for the isobaric equilibrium melting experiments of Jaques (1980). Dashed line is an extrapolation of the regression equation to 1 bar.

(1) LnKdCa opx=2998.979/T°C+0.0662*P(kb)-3.91318

(2) LnKdCa opx=18258.86/T°C-16.7463
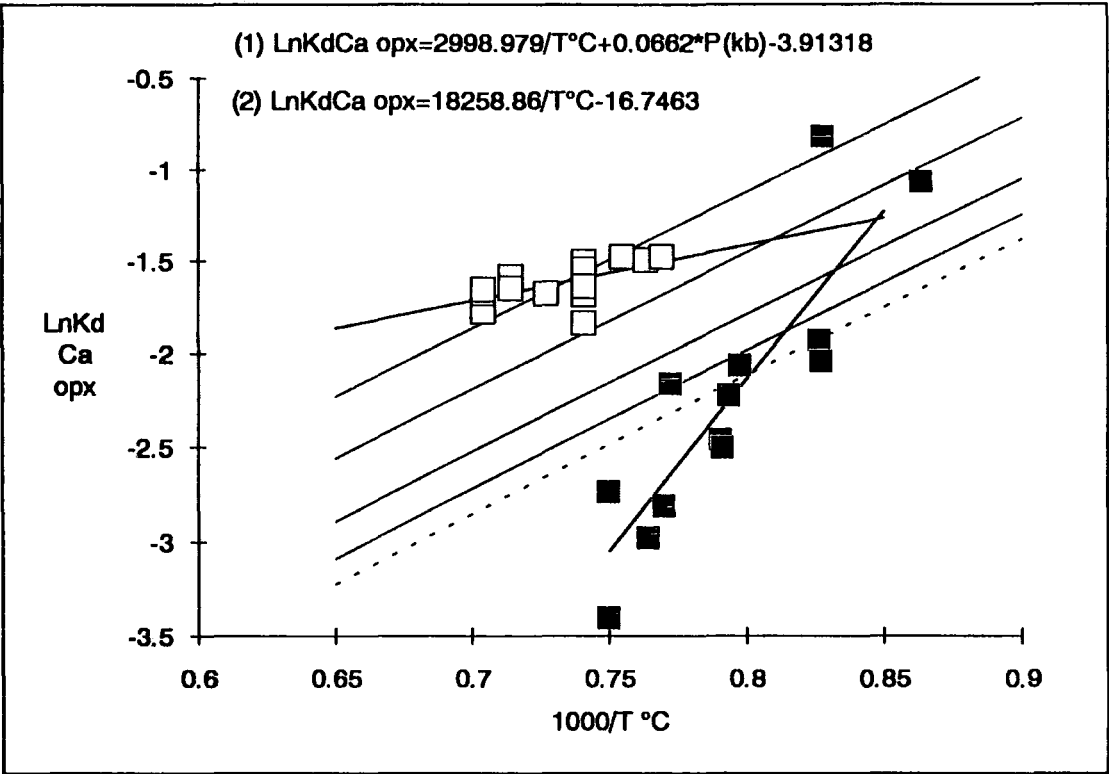
Figure (5.13) Plot of $LnKd_{Ca}^{opx/liq}$ vs. 1000/T°C for the data of Falloon and Green (1987; open squares) and Barnes (1986; filled squares). Equation (1) is the regression line for the former data set and equation (2) for the latter. Note that in the experiments of Barnes (op. cit.) orthopyroxene is not solvus constrained. Regression lines from Figure 5.12 are also shown for comparison. See text for the pressure term.

InKdCa opx=-110.05/T°C-1.48568
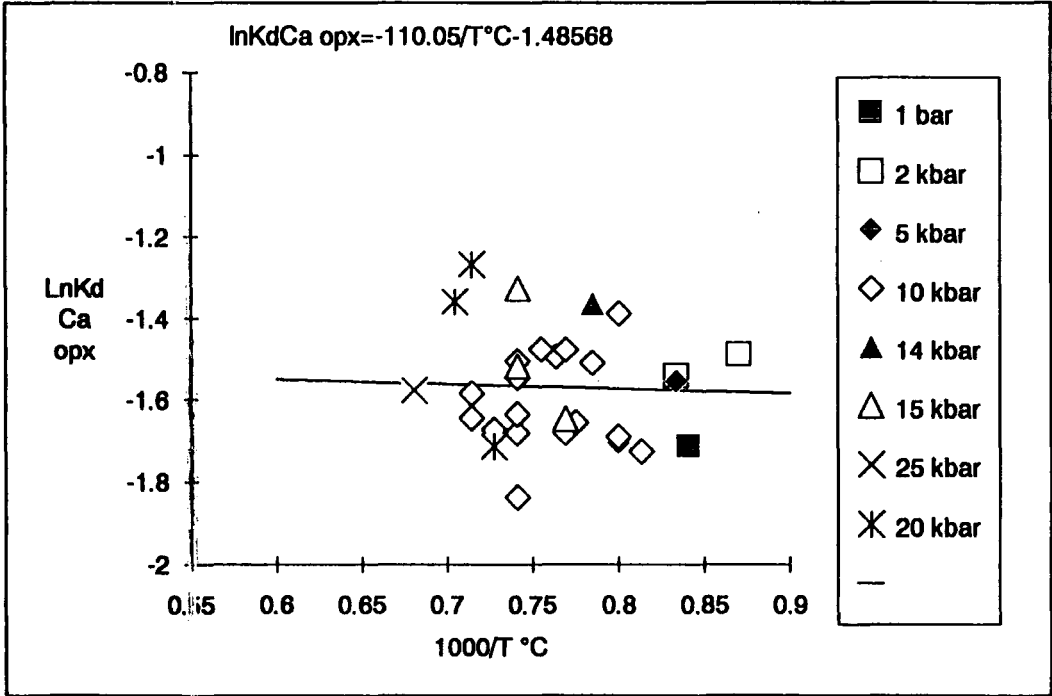
Figure (5.14) Plot of $LnKd_{Ca}^{opx/liq}$ vs. 1000/T°C for all available pairs of coexisting pyroxenes. Note the insignificant change in Kd with pressure.

5.3.2.6. Nickel, Titanium

The distribution coefficients of Ti and Ni for orthopyroxene are taken from Kostopoulos (1988), corrected for mole fractions. The expression used for Ti is:

$$LnKd_{Ti}^{opx/liq}=8912.29/T^{\circ}C-9.59445$$

and for Ni:

$$LnKd_{Ni}^{opx/liq}=3937.24/T^{\circ}C-1.8828$$

5.3.2.7. Manganese

Figure 5.16 is a plot of $LnKd_{Mn}^{opx/liq}$ vs. 1000/T°C for the data of Barnes (1986). The diagram shows considerable scatter, that is probably due to analytical uncertainty for both the mineral and melt compositions. Nevertheless, since Mn is only a minor element, the regression equation obtained is considered adequate for the present modelling.
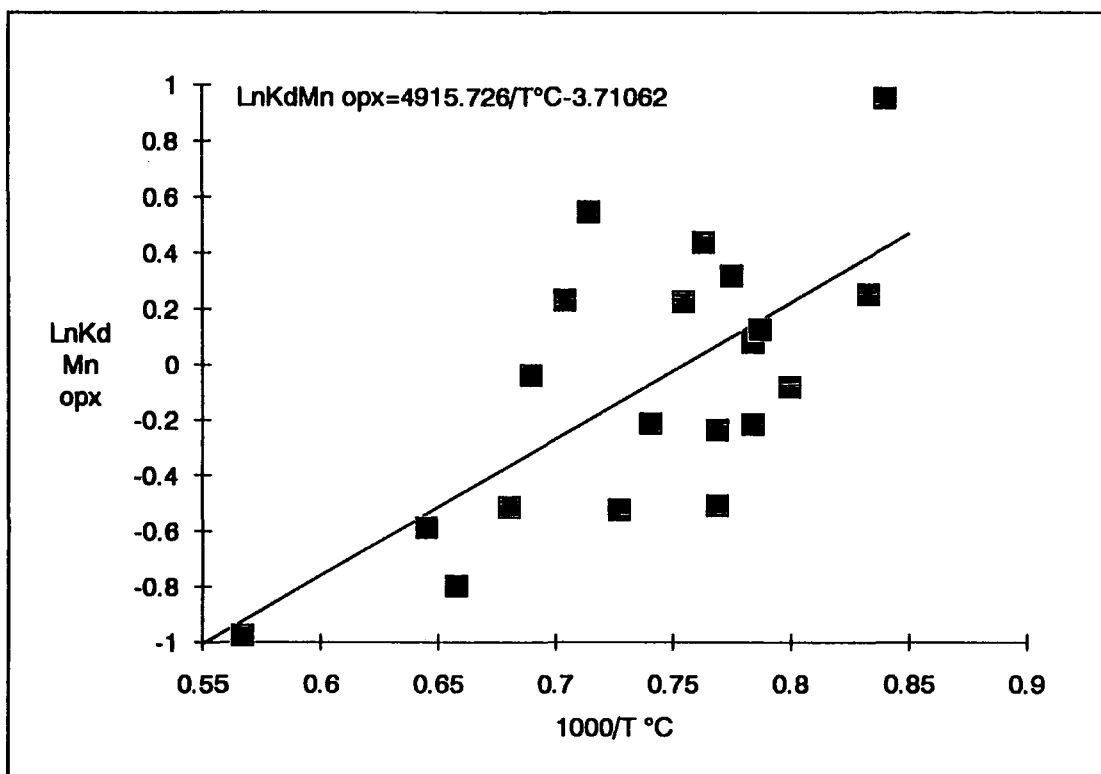
Figure (5.16) Plot of $LnKd_{Mn}^{opx/liq}$ vs. $1000/T^{\circ}C$.

The plot shows: LnKdMn opx=4915.726/T°C-3.71062, with axes LnKd Mn opx (y-axis, from -1 to 1) and 1000/T °C (x-axis, from 0.55 to 0.9).

5.3.2.8. Chromium

The distribution coefficient of Cr between orthopyroxene and melt is strongly dependent on temperature and oxygen fugacity, as is clearly evident from Figure 5.17. A decrease in oxygen fugacity will increase the Cr^{2+}/Cr^{3+} ratio in the melt, thus decreasing the concentration of Cr^{3+} in orthopyroxene. Since probe analyses of the melt do not discriminate between the two Cr species in the melt, $Kd_{Cr}^{opx/liq}$ will appear to decrease with decreasing f_{O_2}.
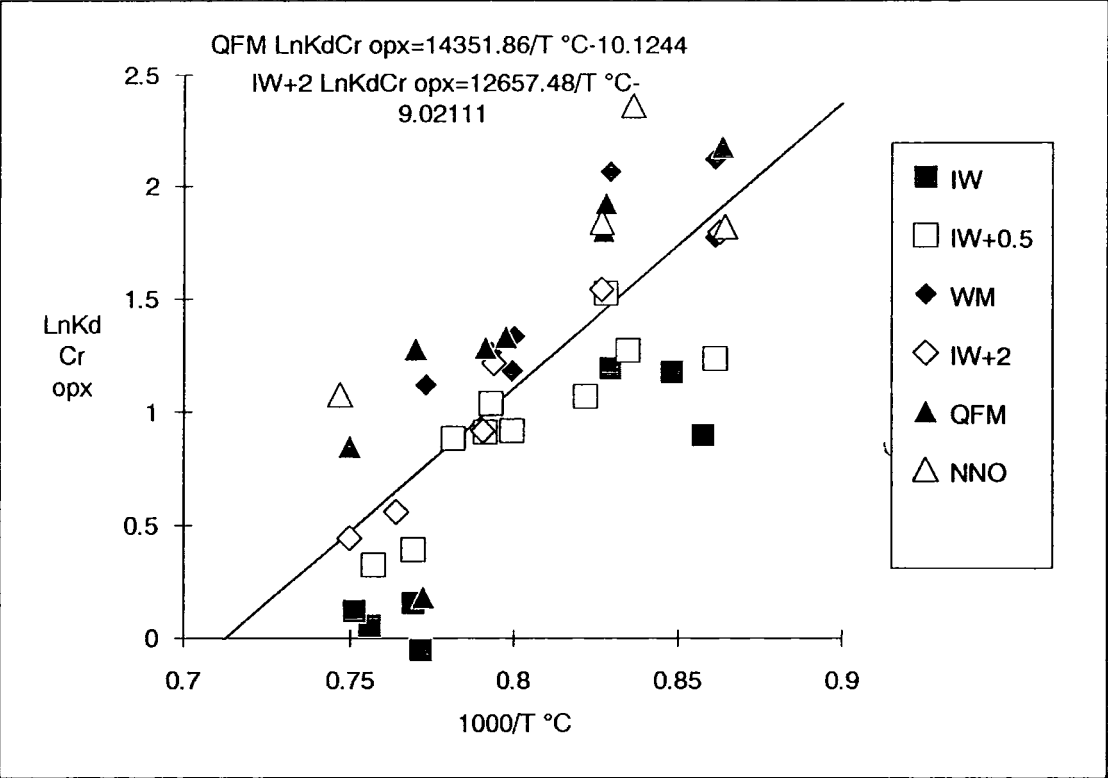
Figure (5.17) Plot of $LnKd_{Cr}^{opx/liq}$ vs. $1000/T°C$ for the 1 bar experiments of Barnes (1986). Regression line corresponds to the equation for the data at IW+2. The regression equation calculated for IW+2 is also given.

5.3.2.9. Sodium

Na is a very low-abundance element in orthopyroxene, therefore its analysis is subject to large analytical error, especially if the element has been determined by EDS. The simplest way to calculate $Kd_{Na}^{opx/liq}$ is to express it as a function of $Kd_{Na}^{cpx/liq}$. Figure 5.18 is a plot of $LnKd_{Na}^{opx/liq}$ vs. $Kd_{Na}^{cpx/liq}$ for the 7 pairs of coexisting pyroxenes that were both analyzed for Na. Since Na is rapidly exhausted in orthopyroxene, even a relatively large error in the estimation of the Kd will not greatly affect the calculated melt compositions. The available data cover a range of pressures from 10 to 30 kb, but no pressure dependence can be detected with confidence. The apparent lack of pressure dependence is ascribed to the similarity in the behaviour of Na in both ortho- and clinopyroxene.

LnKdNa opx=1.148042*LnKdNa cpx-0.91316
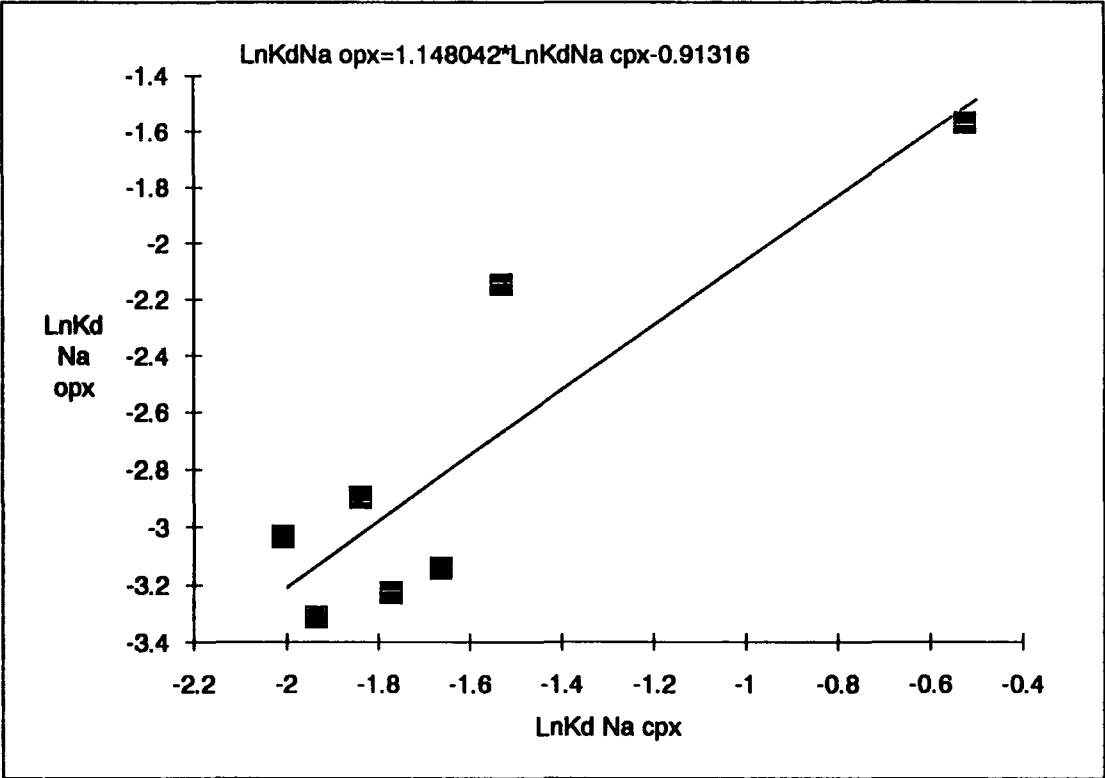
Figure (5.18) Plot of $LnKd_{Na}^{cpx/liq}$ vs. $LnKd_{Na}^{opx/liq}$.

5.3.2.10. Potassium

Similarly to Na, the analytical error for K in orthopyroxene is large. Unfortunately, there are no coexisting pyroxene pairs that were analyzed for K, so an average $LnKd_K^{opx/liq}$ value of -4.5, calculated from the data of Barnes (1986) will be used.
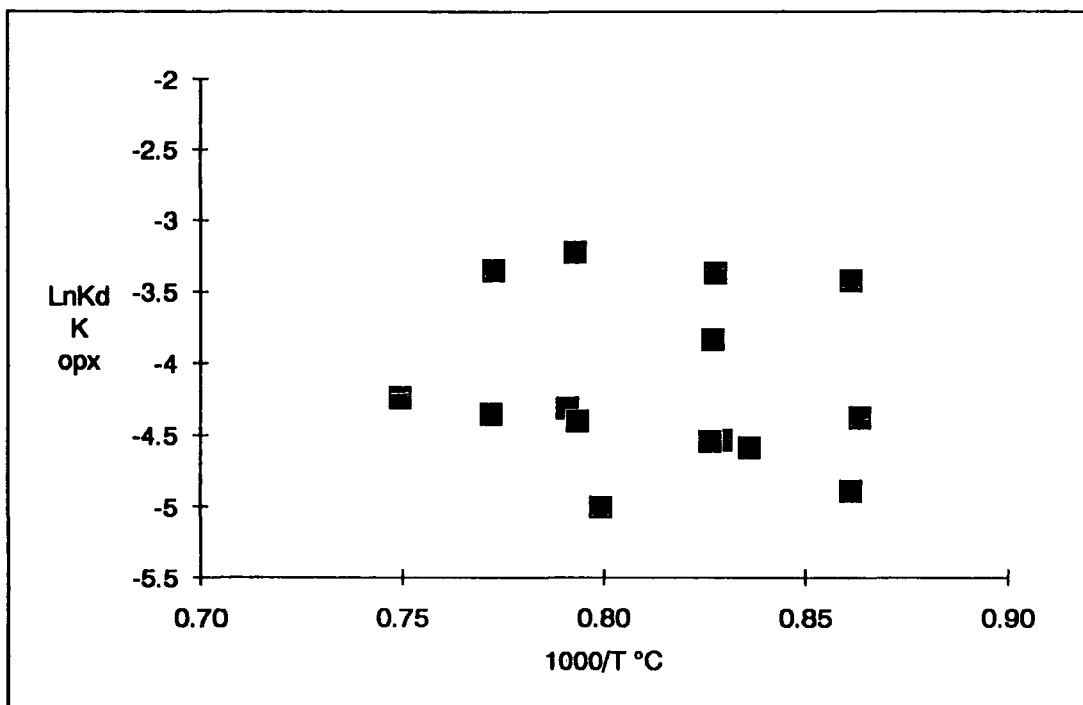
Figure (5.19) Plot of $LnKd_K^{opx/liq}$ vs. 1000/T°C for the data of Barnes (1986). Because there is no discernible temperature dependence, an average value of -4.5 is used in the modelling.

5.3.3. Clinopyroxene

5.3.3.1. Silica

Si occupies the same site in both ortho- and clinopyroxene. As the pyroxene formula suggests, the SiO_2 molar content in both ortho- and clinopyroxene is 50%, and $Kd_{Si}^{cpx/liq}$ is expected to be the same as $Kd_{Si}^{opx/liq}$. In practice, however, pyroxenes contain some Al_2O_3, which substitutes for SiO_2 in the tetrahedral site. Since clinopyroxene contains more Al_2O_3 than orthopyroxene, the SiO_2 molar content of the former is expected to be slightly less than that of the latter. This variation, however, is very small and probably smaller than analytical uncertainty, as a plot of $LnKd_{Si}^{opx/liq}$ against $LnKd_{Si}^{cpx/liq}$ testifies (Figure 5.20), therefore $Kd_{Si}^{cpx/liq}$ will be considered equal to $Kd_{Si}^{opx/liq}$ for the calculations.
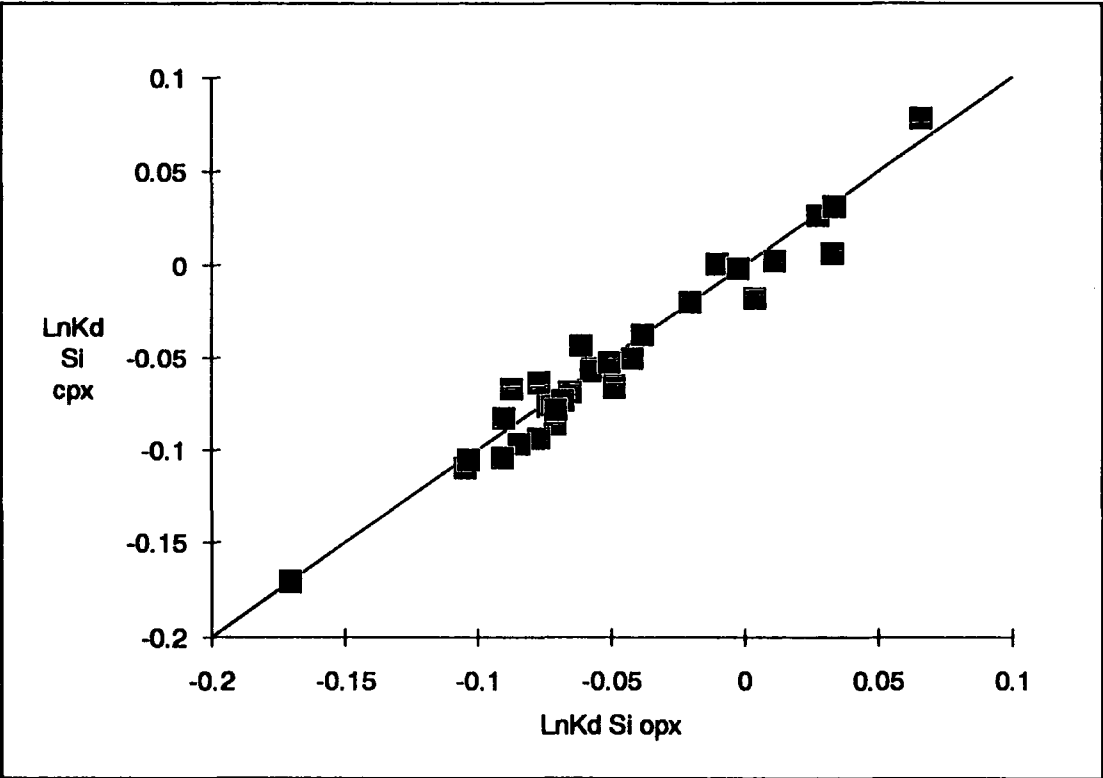
Figure (5.20) Plot of $LnKd_{Si}^{cpx/liq}$ vs. $LnKd_{Si}^{opx/liq}$. 1:1 line shown for reference.

5.3.3.2. Aluminium

Because there is a lack of experimental data that provide clinopyroxene compositions over a sufficiently wide range of pressures and temperatures to assess the effect of pressure on Al in clinopyroxene, $Kd_{Al}^{cpx/liq}$ will also be expressed as a function of $Kd_{Al}^{opx/liq}$. Figure 5.21 is a plot of $LnKd_{Al}^{cpx/liq}$ against $LnKd_{Al}^{opx/liq}$ showing a good positive correlation between the two parameters. This method of calculation also minimizes the effect of pressure, since pressure should have a similar effect on the Al_2O_3 content of both ortho- and clinopyroxene.
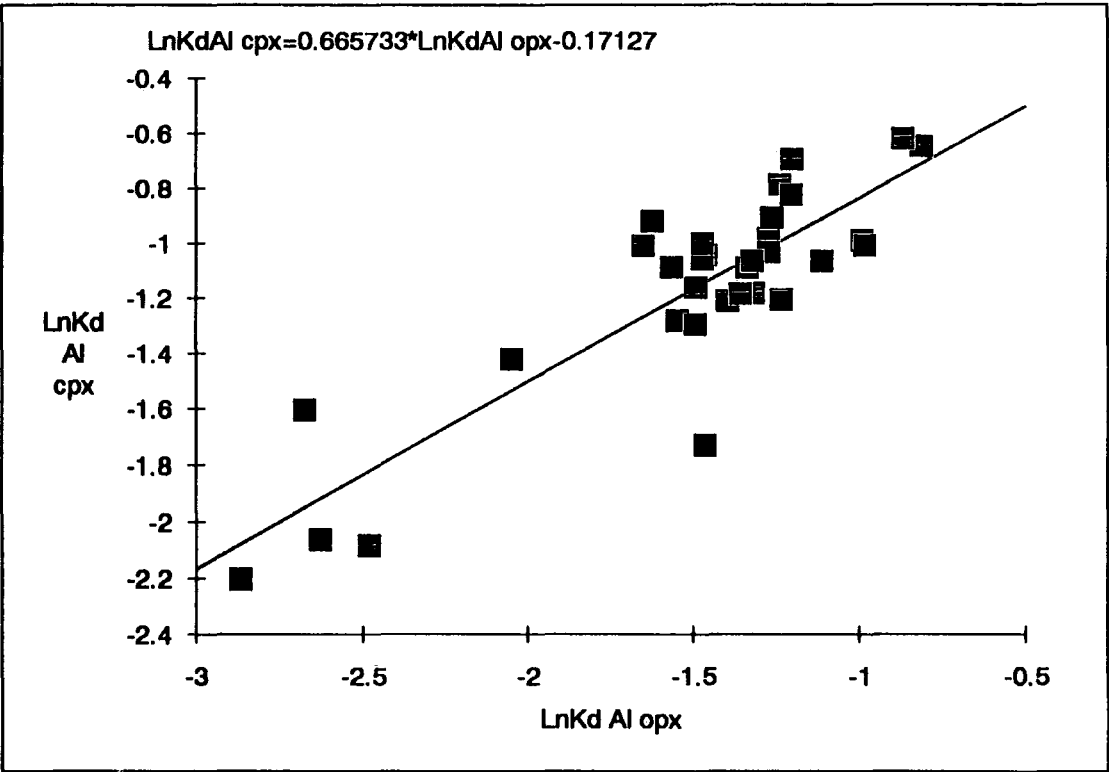
Figure (5.21) Plot of $LnKd_{Al}^{cpx/liq}$ vs. $LnKd_{Al}^{opx/liq}$ for coexisting pyroxenes.

5.3.3.3. Magnesium

Figure 5.22 is a plot of $LnKd_{Mg}^{cpx/liq}$ against 1000/T°C. In contrast to the 1 bar experiments, that show a coherent trend, the high-pressure experiments show a more scattered behaviour. The reason for this may be that many of the published high-pressure clinopyroxene analyses have abnormally high MgO contents and frequently the MgO content exceeds that of CaO (e.g. in the experiment T-2121 of Falloon and Green (1987) at 1230°C, 10 kbar, the clinopyroxene contains 18.57 wt.% MgO and 16.44 wt.% CaO, whereas in the experiment 329 of Elthon and Scarfe (1984) at the same pressure and temperature, the clinopyroxene contains 16.4 wt.% MgO and 19.24 wt.% CaO). This is too large a variation to be attributed to the different starting materials used by the two groups of workers and the high-Mg clinopyroxene in Falloon and Green's (1987) experiments probably represents an unequilibrated core composition with an abnormally large enstatite fraction. Because of this problem, $Kd_{Mg}^{cpx/liq}$ cannot be described as a function of $Kd_{Mg}^{opx/liq}$, since this will lead to a gross overestimation of the distribution coefficient and so it must be calculated from the 1 bar experiments.

Figure 5.22 is a plot of $LnKd_{Mg}^{cpx/liq}$ against 1000/ T°C for experiments conducted at atmospheric pressure. Also shown in Figure 5.22 is the regression line of Weaver and Langmuir (1990) derived from the experimental data of Grove and Bryan (1983). The close agreement of the two regression lines is expected since they are both based on crystallization experiments of abyssal tholeiites.

$$LnKdMgcpx=6089.212/T°C-4.43989$$
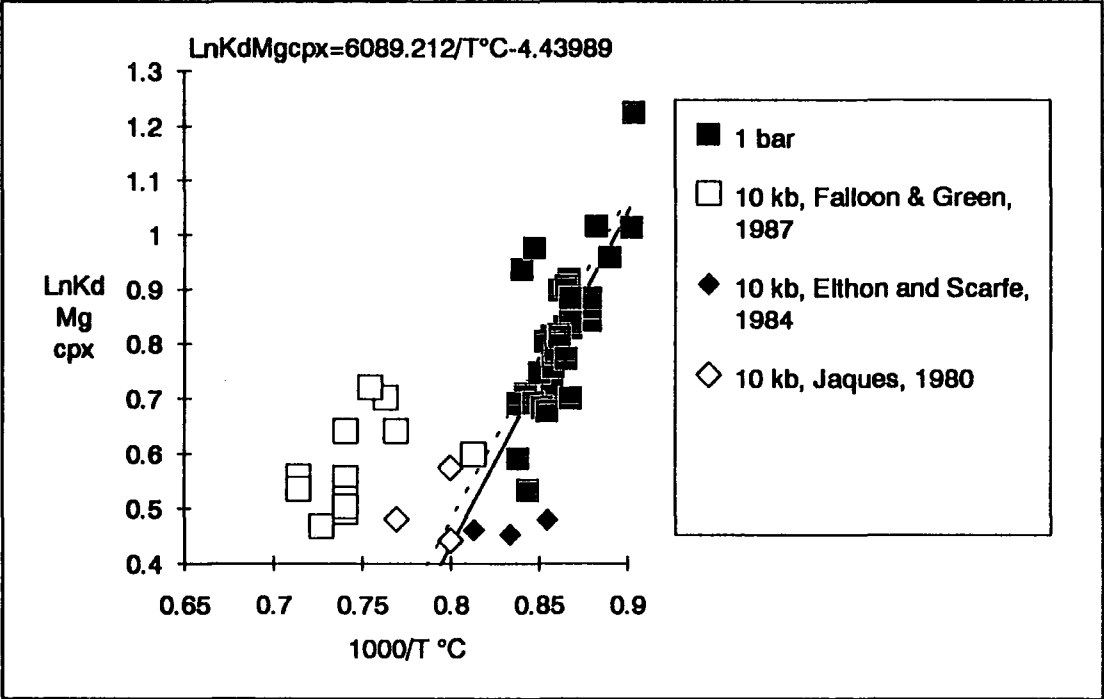
Figure.(5.22) Plot of $LnKd_{Mg}^{cpx/liq}$ vs. 1000/T°C. Filled squares are points at 1 bar pressure from which the regression line was calculated (see text). Also shown are three sets of experiments at 10 kb pressure exhibiting considerable scatter despite the similarity in starting materials. The dashed line is the equation of Weaver and Langmuir (1990).

5.3.3.4. Iron

In contrast to Mg, plots of $LnKd_{Fe}^{cpx/liq}$ vs. 1000/T°C show considerable scatter, even for experiments at 1bar for a single composition (Figure 5.23). The reason for this behaviour is not known but it has been encountered by other authors as well. Weaver and Langmuir (1990) tried to circumvent this problem by expressing $Kd_{Fe}^{cpx/liq}$ as a function of $LnKd_{Fe}^{ol/liq}$. Their expression however is just an average value, since $Kd_{Fe}^{cpx/liq}$ does not show any variation with $Kd_{Fe}^{ol/liq}$. Possible explanations include the loss of iron from the charge to the container during the experiment or the mistaking of quench clinopyroxene for liquidus crystals. In the present study $Kd_{Fe}^{cpx/liq}$ was expressed as a function of $Kd_{Fe}^{opx/liq}$. The

similarity in the FeO content of both pyroxenes suggests that any excess enstatite component in (partially equilibrated) clinopyroxene will not greatly increase its FeO content (Figure 5.24).
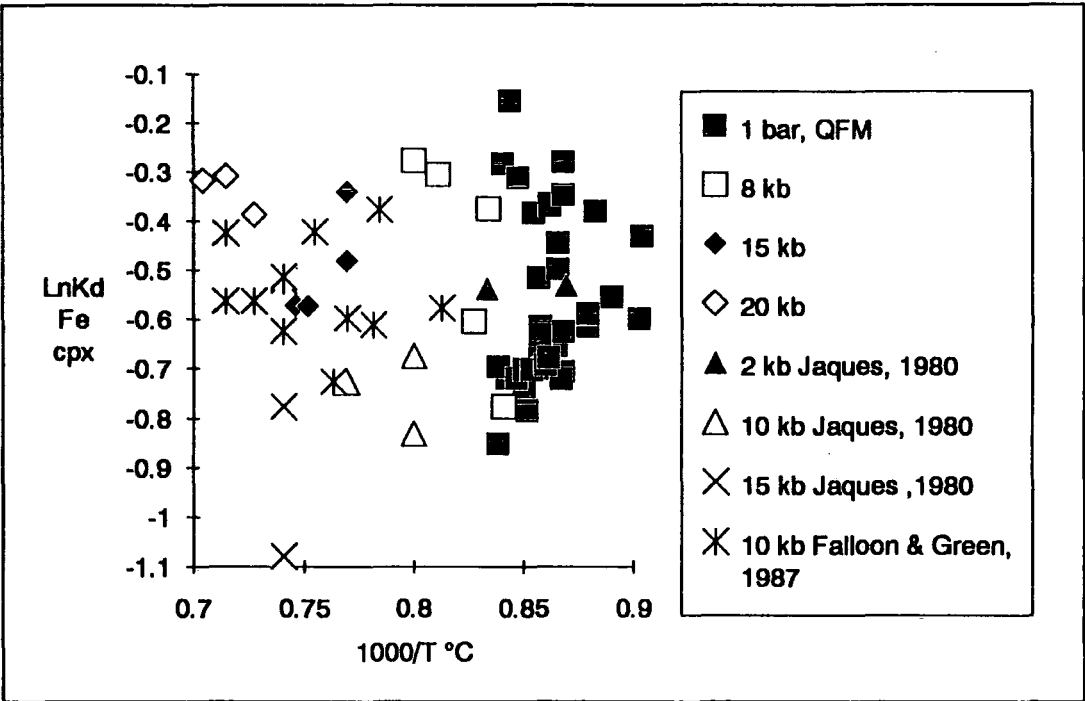
Figure (5.23) Plot of $LnKd_{Fe}^{cpx/liq}$ vs. $1000/T^{\circ}C$ demonstrating the absence of a coherent trend in the data set.

LnKdFe cpx=-0.28035*lnKdFe opx-0.68021
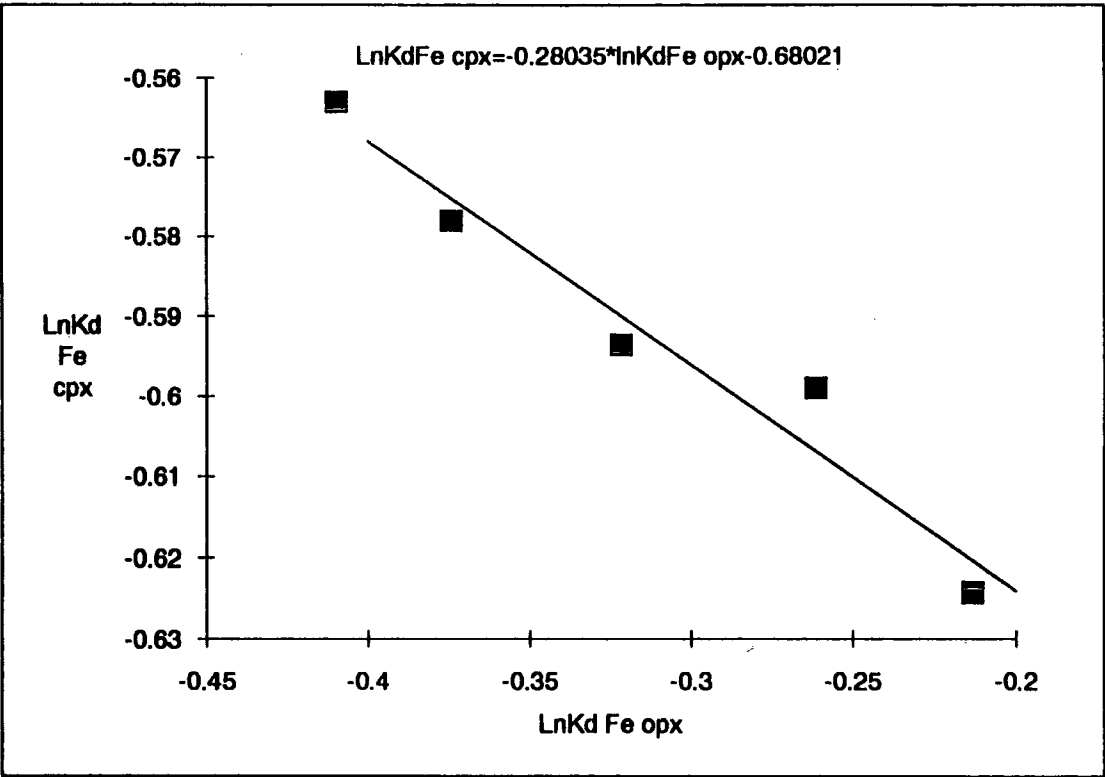
Figure (5.24) Plot of $LnKd_{Fe}^{opx/liq}$ vs. $LnKd_{Fe}^{cpx/liq}$ for coexisting pyroxenes in the 10 kbar experiments of Falloon and Green (1987).

5.3.3.5. Calcium

Figure 5.25 is a plot of $LnKd_{Ca}^{cpx/liq}$ vs. $1000/T^\circ C$ for the experiments at 1 bar and high pressure experiments that have coexisting orthopyroxene. The regression line has been calculated for the 1 bar experiments. The regression line has a positive slope, subparallel to the high pressure experiments, in contrast to the slightly negative slope of $Kd_{Ca}^{opx/liq}$. This is consistent with the increase of the Wo component in clinopyroxene with falling temperature (positive slope) and the widely spaced isotherms (large slope) of the two pyroxene solvus in Figure 5.15. Although the 10 kbar data of Falloon and Green (1987) are shifted to higher values, there is considerable scatter in the high pressure points, and, in view of the uncertainty, no pressure correction will be introduced.
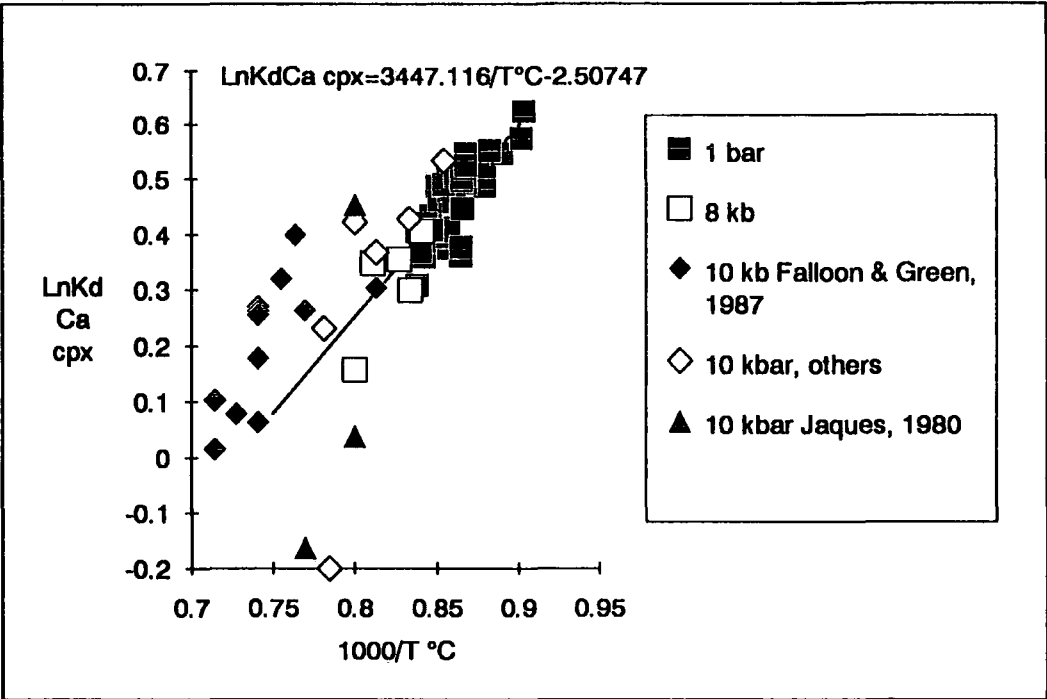
Figure (5.25) Plot of $LnKd_{Ca}^{cpx/liq}$ vs. 1000/T°C. Regression equation calculated from 1 bar data (solid squares).

5.3.3.6. Sodium

Na in clinopyroxene, as in orthopyroxene, has a large analytical error and is best expressed as a function of Ca. Figure 5.26 shows the $LnKd_{Na}^{cpx/liq}$ against $LnKd_{Ca}^{cpx/liq}$ for experiments carried out at atmospheric pressure. There is considerable scatter in the data and it is not clear if the slight negative correlation displayed is real. It will be noted, however, that, in a study of continental spinel lherzolites, Sachtleben and Seck (1981) observed a decreasing trend of the CaO atomic fraction in clinopyroxene with temperature of equilibration and a concomitant increase in its Na_2O atomic fraction, for which they provided no explanation. The observed behaviour of CaO and Na_2O in clinopyroxenes of spinel lherzolites is consistent with the variation of the distribution coefficients in Figure 5.26. A possible explanation for this behaviour is suggested here. The Wo fraction of clinopyroxene (and, hence, its CaO content) is rigidly fixed by the two-pyroxene solvus (Figure 5.15). Because CaO and Na_2O occupy the same clinopyroxene site, as the Wo fraction of clinopyroxene increases with decreasing temperature it "squeezes" out Na_2O and vice versa. Since Na_2O is

only a minor clinopyroxene constituent it has no stoichiometric constraints on its behaviour and can vary more freely than CaO.

InKdNacpx=-0.77994*InKdCacpx-1.93888
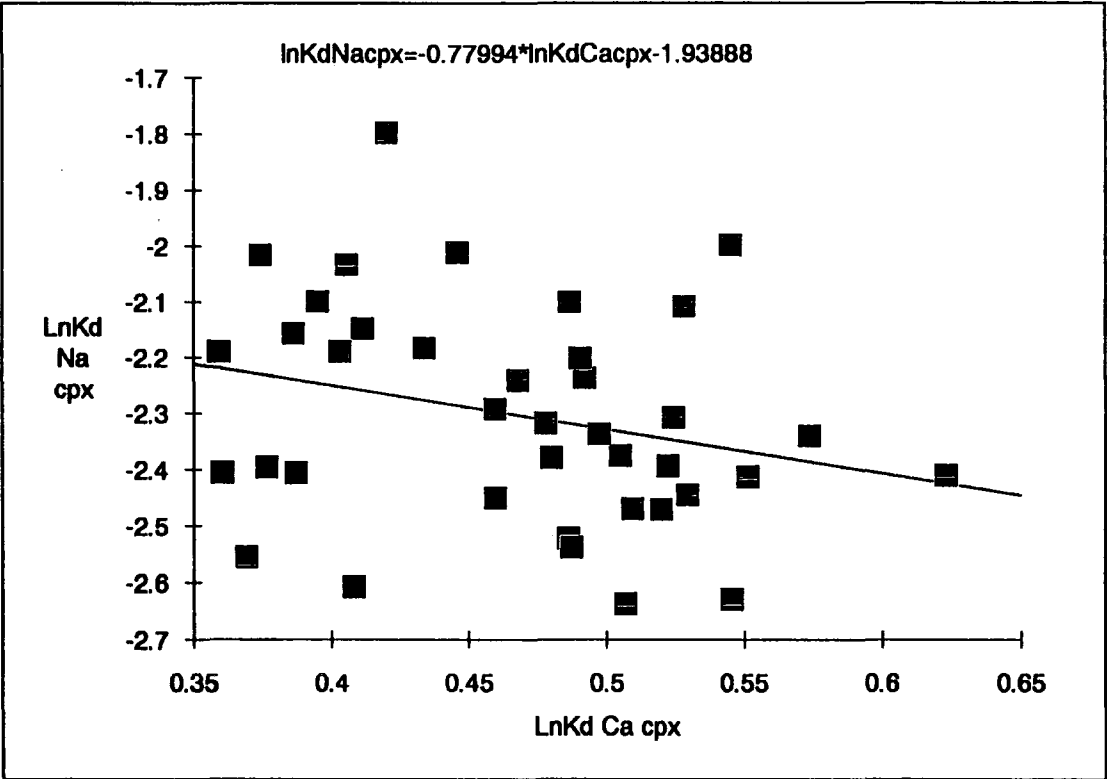
Figure (5.26) Plot of $LnKd_{Na}^{cpx/liq}$ vs. $LnKd_{Ca}^{cpx/liq}$.

5.3.3.7. Potassium

There is a scarcity of data for K in clinopyroxene, i.e. 9 analyses reported by Walker et al. (1979) and one by Takahashi (1980). Unfortunately, the analyses of Walker et al. (op. cit.) are on a small temperature range (1106-1185°C) to allow reliable extrapolation to higher temperatures, so the $Kd_{K}^{cpx/liq}$ will expressed as a function of Ca by taking the average ratio of $Kd_{K}^{cpx/liq}/Kd_{Ca}^{cpx/liq}$ from the data of Walker et al. (1979) which is 0.044, so:

$$Kd_{K}^{cpx/liq} = 0.044*Kd_{Ca}^{cpx/liq}$$

5.3.3.8. Chromium

The Cr distribution coefficient for clinopyroxene will be expressed as a function of its Kd in orthopyroxene. Using this method to calculate the $Kd_{Cr}^{cpx/liq}$ makes unnecessary considering the effects of oxygen fugacity, since it will affect both pyroxenes in the same manner.

LnKdCr cpx=1.023043*LnKdCr opx+0.097977
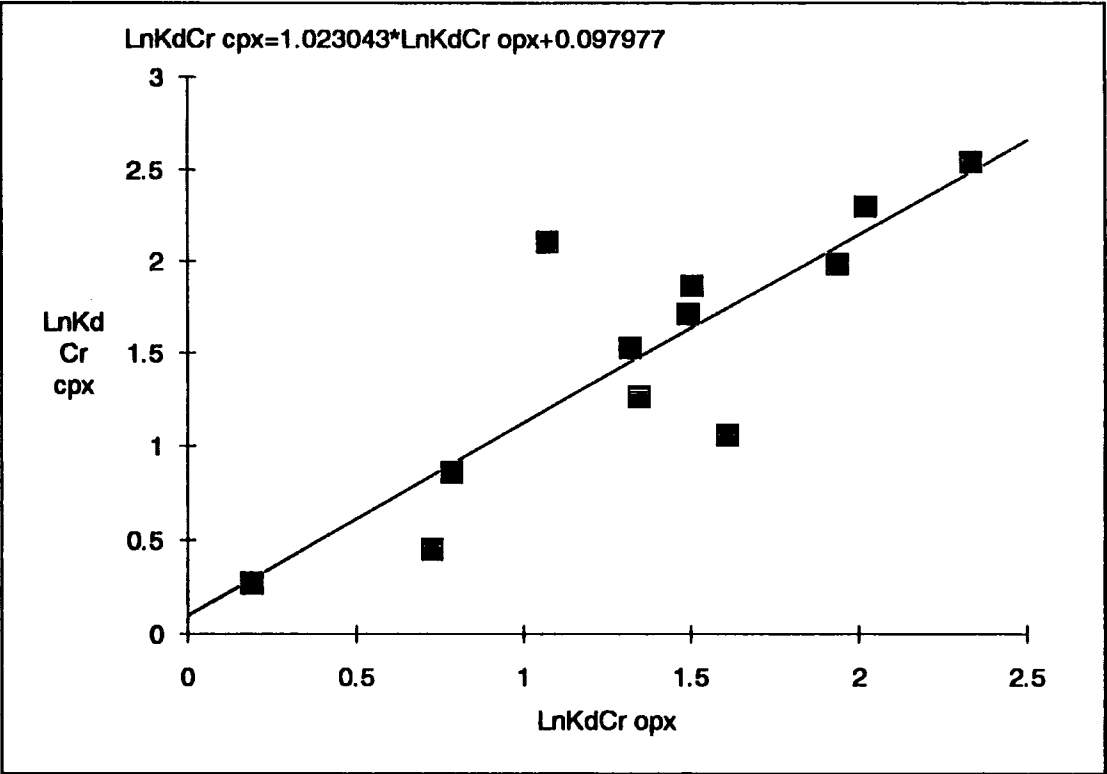
Figure (5.27) Plot of $LnKd_{Cr}^{opx/liq}$ vs. $LnKd_{Cr}^{cpx/liq}$ for coexisting pyroxenes. Note that this is a regression and not a 1:1 line.

5.3.3.9. Nickel. Titanium

The Ti and Ni distribution coefficients have been taken from Kostopoulos (1988) and adjusted for mole fractions. The expression used for Ti is:

$$LnKd_{Ti}^{cpx/liq}=9098.25/T^{\circ}C-9.0545$$

and for Ni:

$$LnKd_{Ni}^{cpx/liq}=6548.87/T^{\circ}C-4.4981$$

5.3.3.10. Manganese

The $Kd_{Mn}^{cpx/liq}$ in clinopyroxene does not show a discernible temperature dependence, but this may be due to analytical uncertainties. It displays, however, a sympathetic variation with $Kd_{Fe}^{cpx/liq}$ (Figure 5.28). Although there is still a considerable scatter the resulting equation is considered acceptable for the purposes of modelling.
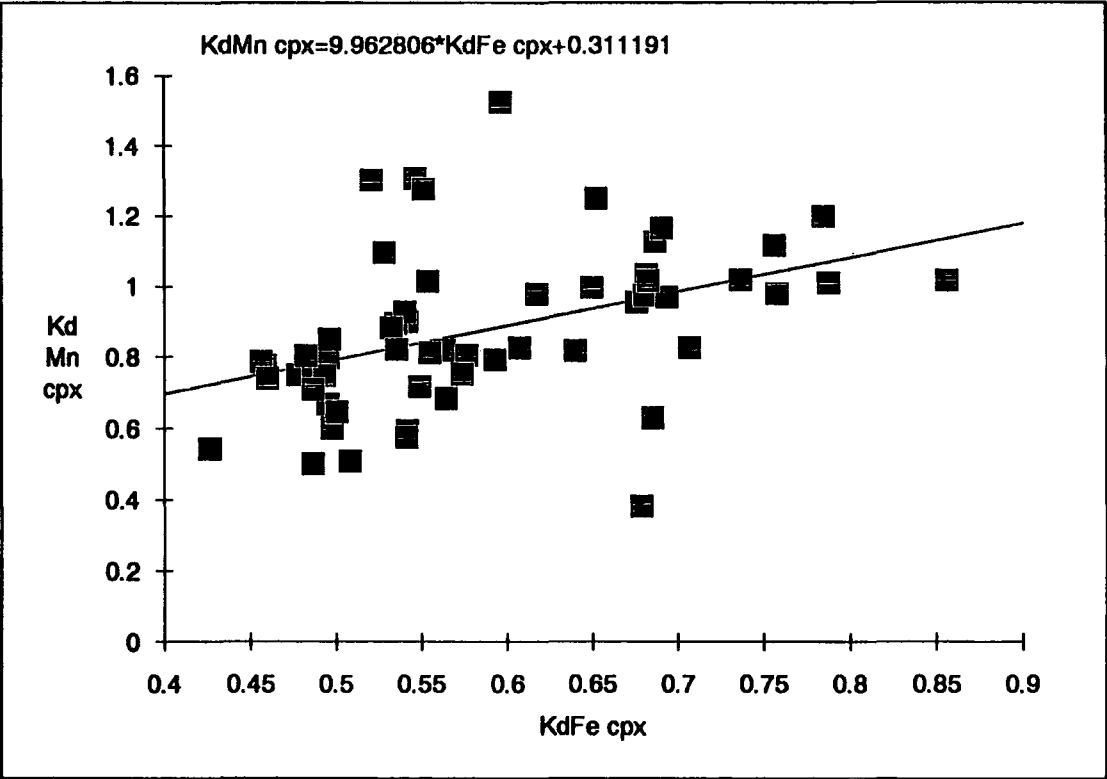
Figure (5.28) Plot of $LnKd_{Fe}^{cpx/liq}$ vs. $LnKd_{Mn}^{cpx/liq}$.

5.3.4. Spinel

The variation of partition coefficients for MgO, FeO, and Al_2O_3 in spinel are shown in Figure 5.29a-c. It is apparent from these plots (especially Al_2O_3), that Arrhenius equations do not describe the partitioning of these elements in spinel very accurately. This happens because spinels are better described as mixtures of components (e.g. hercynite, chromite etc.) than simple oxides. Fortunately the MgO, FeO, and Al_2O_3 systematics can be determined using different approaches, based on studies of the exchange of these elements between spinel and co-existing mantle minerals.
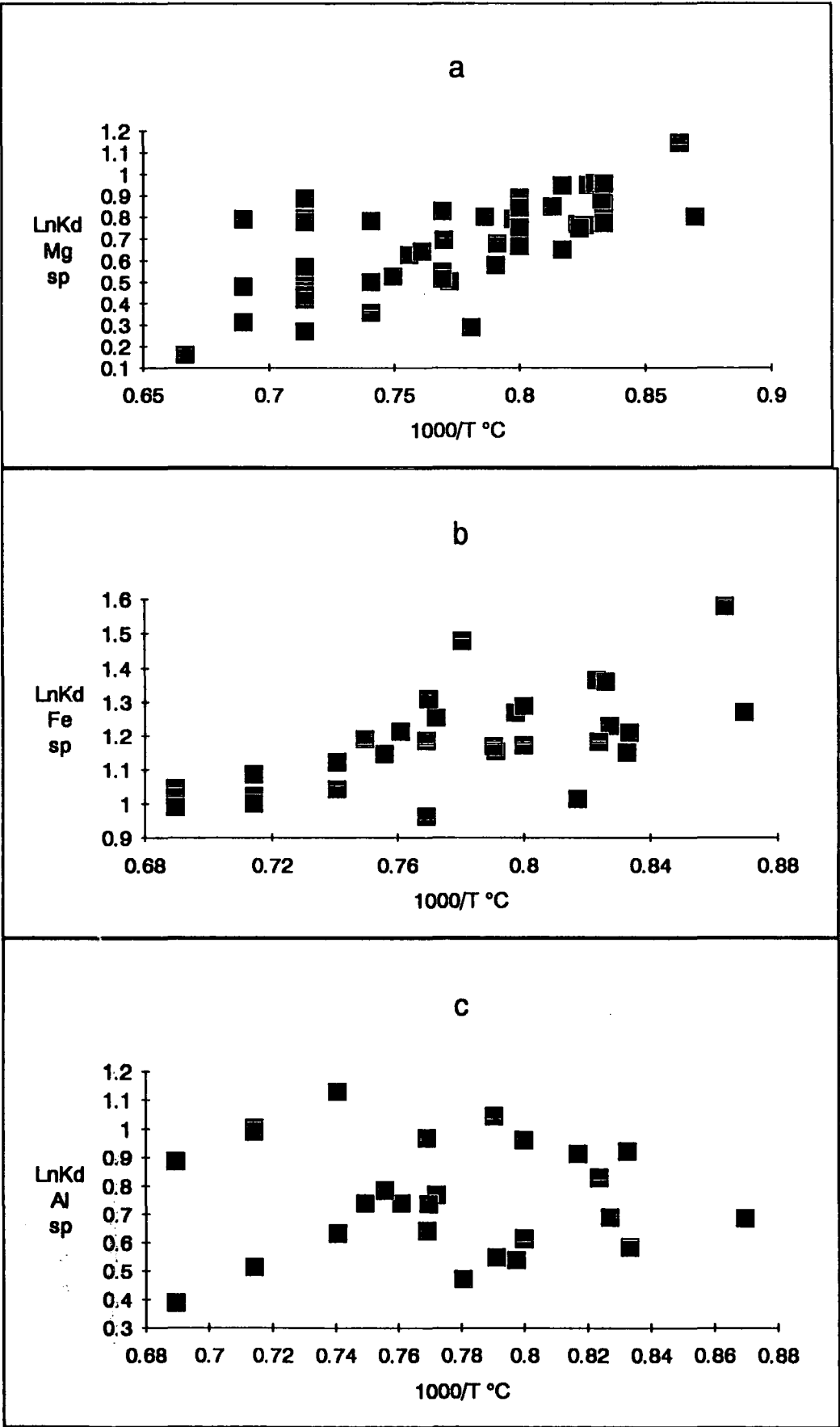
Figure (5.29) a-c. Plots of Mg, Fe, and Al in spinel vs. 1000/T.

5.3.4.1. Magnesium

The Fe-Mg exchange between olivine and spinel has been shown to be strongly dependent on temperature, the forsterite content of co-existing olivine, and the Cr/(Cr+Al) ratio in spinel (see Chapter 3, olivine-spinel thermometry). In Figure 5.30 the $Kd_{Mg}^{sp/liq}$ has been normalized to the Fo (i.e. Mg/(Mg+Fe)) fraction in olivine and the natural logarithm of $\dfrac{Kd_{Mg}^{sp/liq}}{Fo^{ol}}$ is plotted against $\dfrac{1000 \cdot Cr_{\#}^{sp}}{T^{\circ}C}$. The resulting line shows a minimum of scatter since it is effectively a reversed thermometric expression.
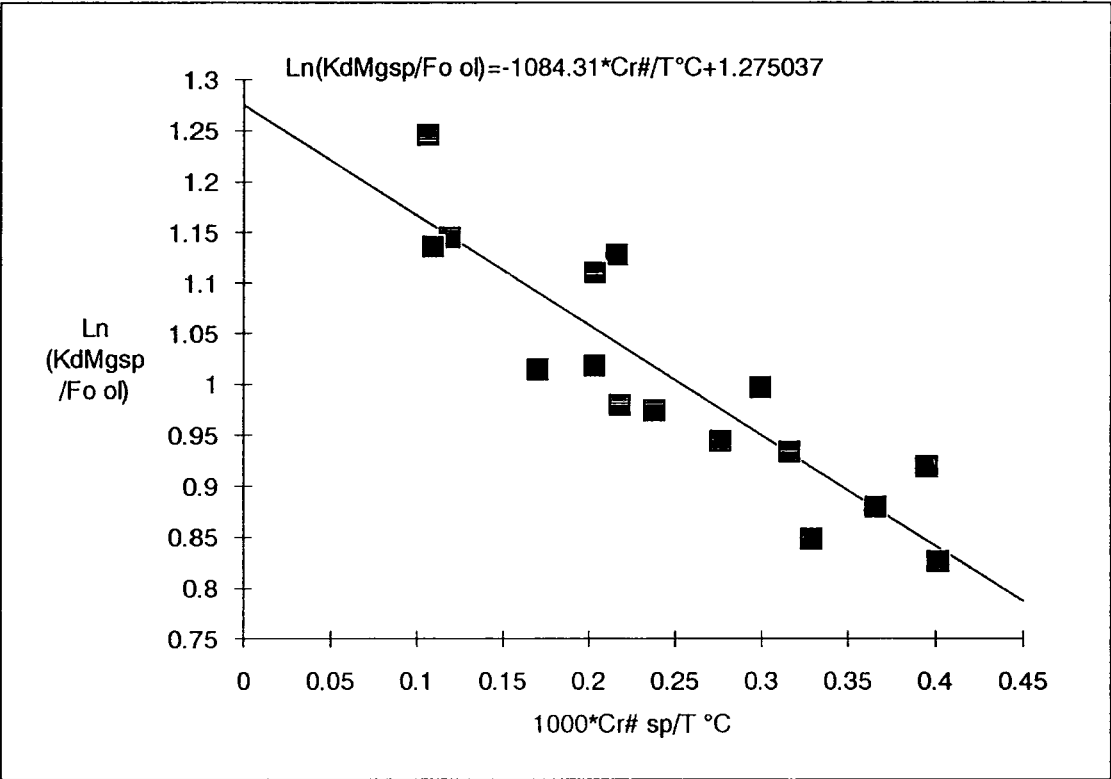
Figure (5.30) Plot of $Ln(Kd_{Mg}^{sp/liq}/Fo^{ol})$ vs. $\dfrac{1000 \cdot Cr_{\#}^{sp}}{T^{\circ}C}$.

5.3.4.2. Iron

As for $Kd_{Mg}^{sp/liq}$, the $Kd_{Fe}^{sp/liq}$ is normalized to the forsterite content of olivine and its natural logarithm plotted against $\dfrac{1000 \cdot Cr_{\#}^{sp}}{T^{\circ}C}$. The resulting line is shown in Figure 5.31. It has the opposite slope than that for $Kd_{Mg}^{sp/liq}$, since the two elements occupy the same spinel site.

Note that the total iron content of spinel is used in calculations. The Fe_2O_3 content of spinels depends on co-existing silicate composition, as well as oxygen fugacity (see Chapter 3, oxygen barometry), a simple expression for $Kd^{sp/liq}_{Fe_2O_3}$ cannot be calculated. At the experimental conditions, however, similar to mantle conditions, the Fe_2O_3 content of spinels is small and this omission is not likely to introduce large errors to calculated spinel compositions.

Ln(KdFesp/Fo ol)=1918.41*Cr#/T°C+0.34624
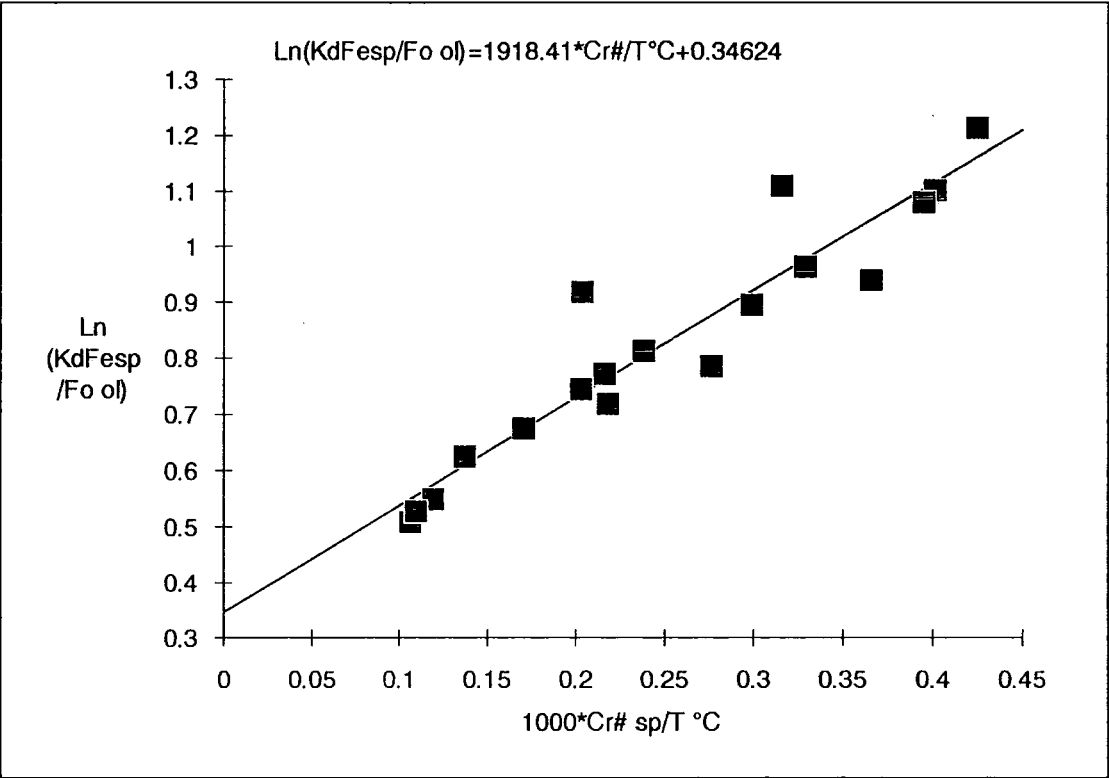
Figure (5.31) Plot of $Ln(Kd^{sp/liq}_{Mg}/Fo^{ol})$ vs. $\dfrac{1000*Cr^{sp}_{\#}}{T°C}$.

5.3.4.3. Aluminium

It is well established that there is a positive correlation between the Al_2O_3 content of orthopyroxene and co-existing spinel (e.g. Nagata et al., 1983; see also Chapter 3, mineral chemistry). The relation may be interpreted in terms of the reaction:

$Mg_2Si_2O_6$ + $MgAl_2O_4$ = $MgAl_2SiO_6$ + Mg_2SiO_4 (Nagata et al., 1983)
orthopyroxene   spinel   orthopyroxene   olivine
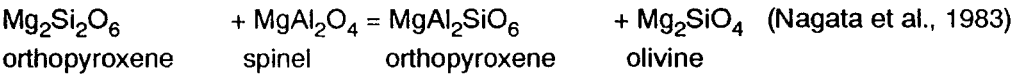
In view of the sympathetic variation of Al_2O_3 in orthopyroxene and spinel, it should be possible to express $Kd_{Al}^{sp/liq}$ in terms of $Kd_{Al}^{opx/liq}$, which is very well constrained. In Figure 5.32 the $LnKd_{Al}^{sp/liq}$ shows a simple linear relation between the two partition coefficients, but the data still show some scatter. This is because the Cr-Al exchange between orthopyroxene and spinel depends on temperature as well as the Cr# of spinel (See Chapter 3, olivine-orthopyroxene-spinel thermometry). Figure 5.33 shows a plot of $LnKd_{Al}^{sp/liq}$ against $\dfrac{1000 \ast Cr_{\#}^{sp}}{T^{\circ}C}$, which gives better results than Figure 5.32. Note that this expression is in effect the reversed thermometric expression of Sachtleben and Seck (1981).

KdAl sp=458.914*LnKdAl opx+1.667411
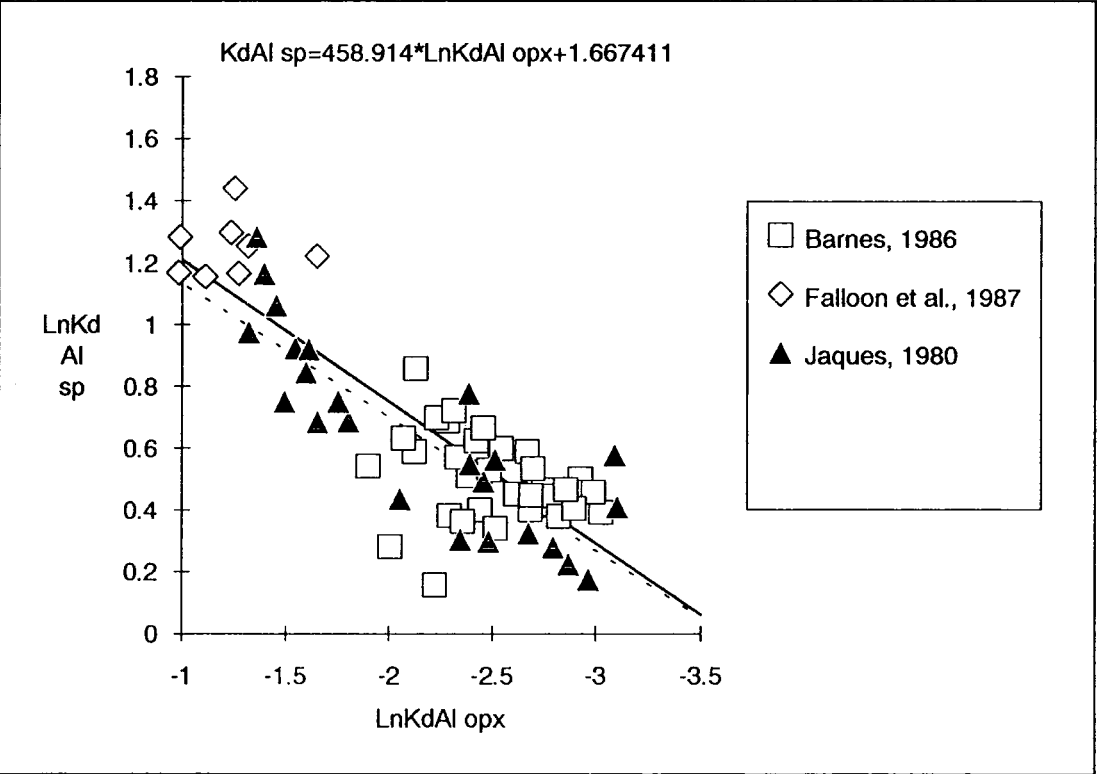
Figure (5.32) Plot of $LnKd_{Al}^{opx/liq}$ vs. $LnKd_{Al}^{sp/liq}$. The dashed line was calculated from the data of Jaques (1980). The solid line was calculated from all points and corresponds to the equation shown.

LnKdAl sp=595.762*LnKdAl opx * Cr# sp/T °C+1.327173
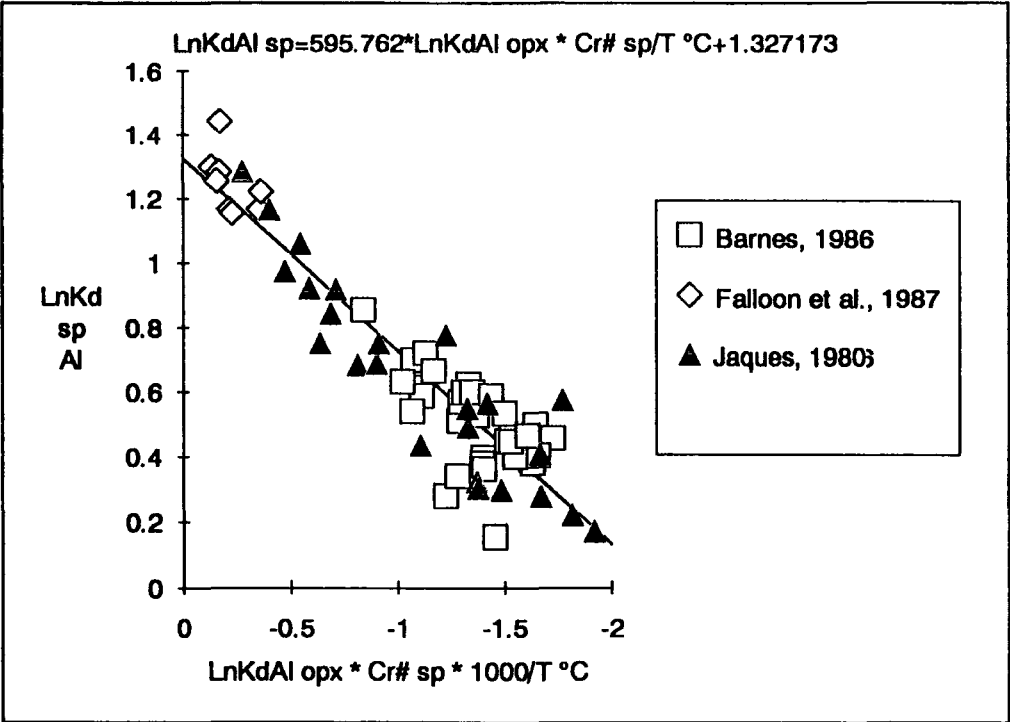
Figure (5.33) Plot of $LnKd_{Al}^{opx/liq}$ * Cr/(Cr+Al)sp * 1000/T°C vs. $LnKd_{Al}^{sp/liq}$. The regression line was calculated from all points.

5.3.4.4. Chromium

Schreiber and Haskin (1976) and Schreiber (1977) first examined Cr partitioning in spinel and the effect of oxygen fugacity (f_{O_2}). As with other elements (e.g. Fe, V, Eu) that have more than one possible valency state at the conditions of interest, $Kd_{Cr}^{sp/liq}$ is strongly dependent on f_{O_2}, and in particular $Kd_{Cr}^{sp/liq}$ increases with increasing f_{O_2}. The reasons for this increase were discussed in the Cr partitioning in orthopyroxene. In Figure 5.34 $LnKd_{Cr}^{sp/liq}$ is plotted against 1000/T°C at four different fugacity buffers: NNO, QFM, IW+2, and IW. The data plotted are from Fisc and Bence (1980), Barnes (1986), and Murck et al. (1986), since these experiments have well constrained f_{O_2} and do report spinel compositions. Kostopoulos (1988) also determined the $Kd_{Cr}^{sp/liq}$ using a slightly larger data set. The temperature-dependent expressions he calculated at different buffers are in good agreement with this study, showing only a small deviation at very high temperatures.
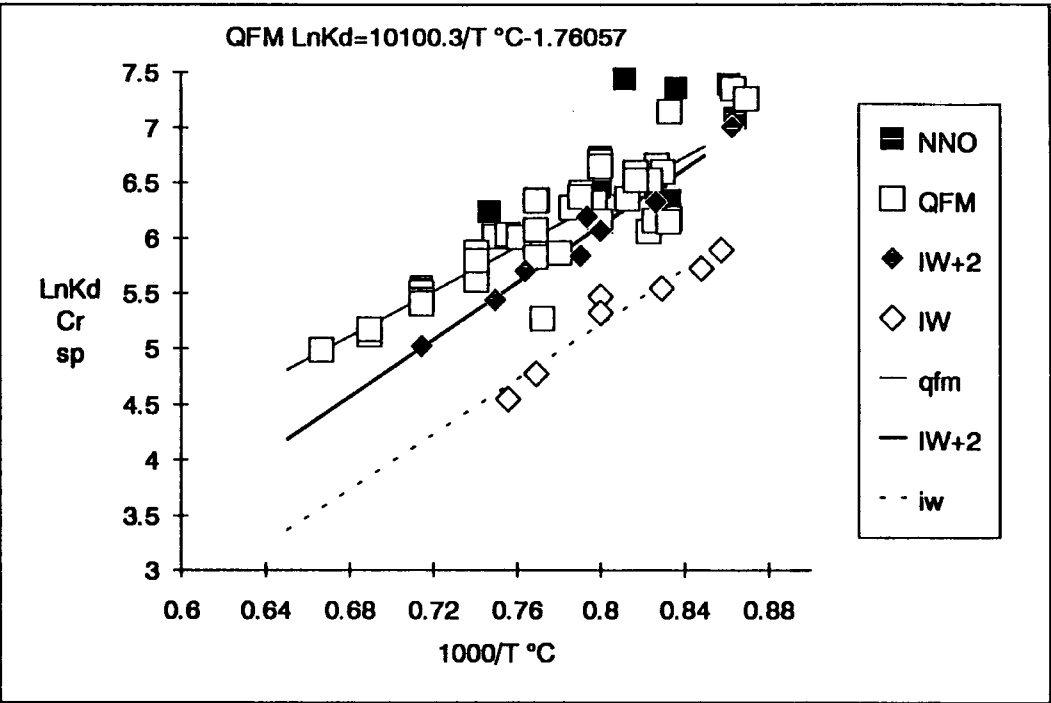
Figure (5.34) Plot of $LnKd_{Cr}^{sp/liq}$ vs. 1000/T°C for experiments at different oxygen fugacity buffers. Note the increase of the partition coefficient with increasing oxygen fugacity. The regression equation has been calculated at the QFM buffer. Data from Fisk and Bence (1980), Barnes (1986), and Murck and Campbell (1986).

In a recent study, Roeder and Reynolds (1991) also examined chromium solubility in basic magmas across a range of temperatures and oxygen fugacities. Unfortunately their work was published too late for their experiments to be included in the evaluation of partition coefficients in spinel. Their results, however, are in close agreement with the experiments already considered (Figure 5.35) and their effect on the equation for $LnKd_{Cr}^{sp/liq}$ would be minimal.
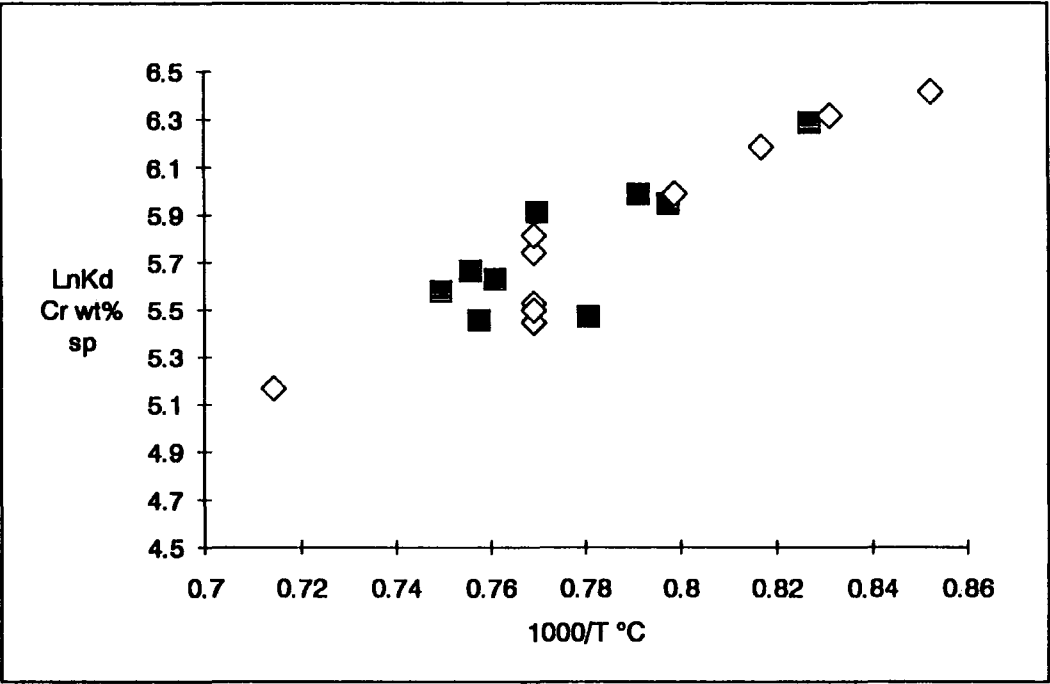
Figure (5.35) Plot of $LnKd_{Cr}^{sp/liq}$ vs. $1000/T°C$. Filled squares are the QFM data of Barnes (1986) at 1 bar pressure. Rhombs are data from Roeder and Reynolds (1991) at the same oxygen fugacity and pressure.

5.3.4.5. Manganese

As Figure 5.36 shows, $Kd_{Mn}^{sp/liq}$ in spinel shows a wide range of values and no apparent temperature dependence. Since spinel is only a minor phase no accuracy is lost if an average value is used. The average $Kd_{Mn}^{sp/liq}$ of all the available data is 1.95 and is the value used for the modelling.
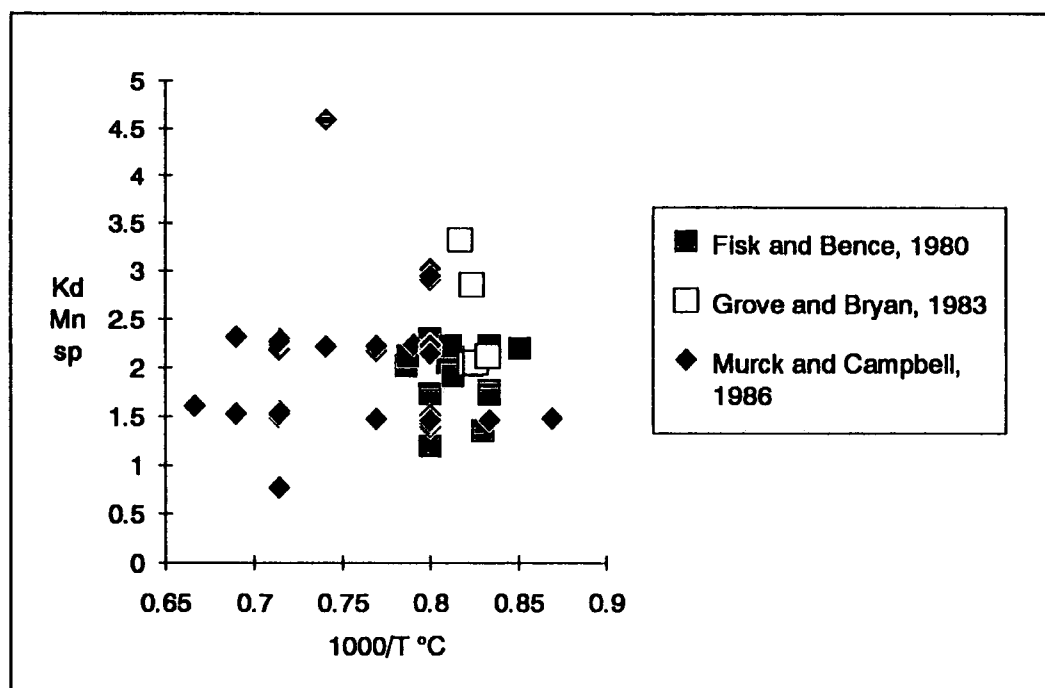
Figure (5.36) $Kd^{sp/liq}_{Mn}$ vs. 1000/T°C. All experiments are at 1 bar pressure.

5.3.4.6. Nickel, Titanium

The expression for $LnKd^{sp/liq}_{Ti}$ and $LnKd^{sp/liq}_{Ni}$ is taken from Kostopoulos (1988) after adjusting for mole fractions. For Ti the regression equation is:

$$LnKd^{sp/liq}_{Ti}=5287.57/T°C-4.9519$$

and for Ni:

$$LnKd^{sp/liq}_{Ni}=7353.17/T°C-3.1315$$

5.3.4.7. Silica, Calcium

SiO_2 and CaO partitioning in spinel is not of critical importance in the calculations, because of the very low abundance of these elements in spinel. The average values for $LnKd^{sp/liq}_{Si}$ and $LnKd^{sp/liq}_{Ca}$ for all the experiments are -5 and -3.4 respectively, and will be used instead of temperature-dependent expressions.

5.3.4.8. Sodium, Potassium

Although there are no data regarding the abundance of alkalies in spinel, it is reasonable to assume that they do not enter the spinel lattice. Therefore, perfect incompatibility between the alkalies and spinel is assumed and the Kd's are taken as zero.

5.4. Conditions of mantle melting

The variation of the major-element distribution coefficients with temperature, pressure and oxygen fugacity discussed above requires prior knowledge of these parameters for the construction of rigorous petrogenetic models. It was shown in Chapter 3 that the majority of the Pindos mantle sequence is composed of rocks more depleted than oceanic peridotites and their composition is similar to peridotites from ancient and present-day supra-subduction zone (SSZ) settings. A history of MORB extraction at an accreting margin, followed by subsequent melting episodes is also supported by the presence of basalts with mid-ocean ridge, island-arc tholeiitic, and boninitic compositions (Kostopoulos, 1988). The conditions of genesis of magmas at mid-ocean ridges and supra-subduction zones and the parameters of modelling will be briefly described below.

5.4.1. Mid-ocean ridges.

Melting of upwelling asthenosphere is the result of adiabatic decompression above the peridotite solidus. McKenzie and Bickle (1988) showed that spreading ridges are passive features underlain by mantle of constant potential temperature of ~1280°C (when not in the vicinity of a hotspot); beneath them melting will start at ~50 km depth (15 kb), i.e. in the spinel-lherzolite field. Since MORB compositions from Pindos do not show any evidence of garnet involvement in the source (Kostopoulos, 1988), only melting beneath such a 'normal' ridge will be considered. The pressure, temperature, and degree of melting during upwelling of MORB mantle have been calculated, using the equations of Kostopoulos and James (in press). According to their parameterization, isentropically upwelling asthenosphere of normal (1280°C) potential temperature will experience 21% partial melting before being emplaced at the base of the oceanic crust (compare McKenzie and Bickle, 1988).

Because Cr partitioning is significantly affected by the oxygen fugacity conditions prevailing during partial melting, knowledge of these conditions is necessary to calculate accurately spinel compositions. The oxygen fugacity beneath mid-ocean ridges was discussed in Chapter 3. All evidence increasingly points to fugacities between the iron-wüstite and quartz-fayalite-magnetite buffers (see Chapter 3 for references) with an average value of

~1 log unit below QFM at normal ridges. The partition coefficients for Cr between mantle minerals and melt have been accordingly adjusted to such f_{O_2} conditions.

Regarding the source of MORB, it is now generally accepted that a relatively undepleted spinel lherzolite (commonly referred to as MORB pyrolite or Depleted MORB Mantle) is the most appropriate candidate. Although many estimates of the composition of MORB pyrolite exist (e.g. Carter, 1970; Ringwood, 1975; Jagoutz et al., 1979; Maaløe and Steel, 1980; Hart and Zindler, 1986), the major-element abundances do not vary appreciably. In the present study the starting composition of Kostopoulos and James (in press) will be used and is shown in Table 5.3. Modal proportions and mineral compositions for DMM were also taken from Kostopoulos and James (in press) and Kostopoulos (pers. comm.)

	SiO_2	TiO_2	Al_2O_3	Cr_2O_3	FeO	MnO	NiO	MgO	CaO	Na_2O	K_2O
wt.%	44.5	0.19	4.06	0.38	8.52	0.13	0.25	38.29	3.28	0.34	0.03
mol%	38.51	0.12	2.07	0.13	6.17	0.10	0.17	49.39	3.04	0.29	0.02

Table (5.3) Composition of the MORB pyrolite used for modelling. From Kostopoulos and James (in press).

5.4.2. Supra-subduction zones

Mantle melting in an SSZ environment may produce four different types of magmas: alkaline, calc-alkaline, tholeiitic (IAT), and boninitic (BSV). Of these only the last two are encountered in Pindos (Kostopoulos, 1988). A common feature of SSZ melting is the presence of water (as deduced from the associated magmas). In an intra-oceanic subduction zone (such as Pindos) water is probably introduced in the mantle wedge by dehydration of the subducted, hydrothermally altered oceanic lithosphere. The presence of water will promote melting in two ways: firstly, the presence of volatiles lowers the peridotite solidus, and, secondly, it reduces the peridotite density, triggering gravitational instability that causes diapiric upwelling of the peridotite. In addition water will introduce elements like LREE, alkalies etc., to the peridotite that will affect the melt composition; however, since these are mostly trace elements, they will not be considered here. A more significant effect of the water is that it changes the melt structure (Mysen, 1986) which, in turn, affects the distribution

coefficients between the residual minerals and coexisting melt. Unfortunately most of the hydrous experiments published are focused on the andesitic members of the calc-alkaline series and cannot be used here. Of the wet melting experiments on compositions of interest (Green, 1973, 1976; Nicholls, 1974; Mysen and Boettcher, 1975; Umino and Kushiro, 1989; Van der Laan, et al., 1989; Kelemen et al., 1990) very few were focused on the composition of phases coexisting with the melt, thus limiting severely their use in the derivation of Kd's. At the present time the affect of water on the distribution coefficients cannot be quantitatively assessed. Still, as will be shown later, the use of the distribution coefficients derived from dry experiments produces plausible results.

Another feature of SSZ magmas is their elevated oxygen fugacity (f_{O_2}) compared to that of MORBs. The oxygen fugacity of the Pindos and other SSZ-related peridotites is discussed in Chapter 3. It is shown that, with the exception of Pindos which has an average value of f_{O_2} of ~QFM+1, other SSZ-related peridotites have virtually the same f_{O_2} as mantle beneath ocean ridges. The reasons for this difference, and whether it is real or not, are discussed in Chapter 3. For the purpose of the present modelling it will be assumed that the prevailing f_{O_2} is that of the QFM buffer. In practice, underestimation of the oxygen fugacity by 1-2 log units will not appreciably affect the Cr_2O_3 content of calculated liquid or residual compositions, except for spinel, in which case the calculated Cr# will represent a minimum.

The pressure and temperature conditions, and the source composition of SSZ magmas are not as well constrained as for MORB. In practice, the linear variation of the peridotite chemistry in Pindos may indicate a simple melting regime of repeated melting episodes of a progressively depleted source. This is consistent with the order of eruption of basalts, with MORB being the oldest and BSV the youngest (Kostopoulos, 1988). Kostopoulos (op. cit.) reviewed the petrogenetic models for island-arc tholeiite and boninite petrogenesis. His suggested solidus conditions for IAT genesis were ~1250°C at ~15 kb, and for boninites ~1250°C at pressures of 5 kb or less. In the absence of mathematical formulation describing mantle upwelling at SSZ settings, for the purposes of the present modelling it will be assumed that, after MORB extraction, the average residual peridotite will melt at a nominal temperature of 1250°C and a pressure of 5 kb.

5.4.3. The melting regime

The modal mineralogy of the source peridotite and the amount that each mineral contributes to the melt fraction (melting proportion) are of great importance in the calculations of both the liquid and the residual compositions. This makes necessary the use of a model that accurately depicts the mantle melting behaviour. The model that will be used here is that of Kostopoulos (1991) and will be briefly described below.

Kostopoulos (op. cit.) examined quantitatively the melting behaviour of mantle minerals with the use of ternary diagrams and observations on natural peridotite assemblages. He showed that the mantle melting regime is not linear and can be essentially divided into three domains: The first domain relates to the melting of a fertile spinel lherzolite (FSL) where diopside dominates the melt fraction. The second domain relates to the melting of depleted spinel lherzolites (DSL) and diopside-bearing harzburgites where enstatite starts contributing significantly to the melt, and the third domain relates to the melting of diopside-free harzburgites where enstatite is the major melting phase. Table 5.4 shows the compositions and melting proportions of minerals for these domains. It will be noted that in this model diopside persists in the residue until about 35-40% melting, a much higher value than is usually quoted in other melting models or observed in pyrolite melting experiments (e.g. Jaques, 1980). This difference is partly due to the inability of the isobaric, isothermal melting experiments to accurately approximate the supra-solidus isentropic rise of asthenosphere, which is a polybaric, polythermal phenomenon. In addition, this model implicitly accommodates the melting of pigeonite, which appears in pyroxene phase relation diagrams, but is absent from natural peridotite assemblages. It will be noted that, as the presence of exsolved diopside in enstatite indicates, Pindos harzburgites are saturated with respect to clinopyroxene. As will become apparent later, the persistence of clinopyroxene in the residue to large degrees of melting is consistent with the observed peridotite and basalt compositions in Pindos.

Modal abundances (wt.%)					
Degree of melting	Ol	Opx	Cpx	Sp	
0%	57.00	25.50	15.00	2.50	Fertile Spinel Lherzolite (FSL)
13.4%	65.00	28.00	6.20	0.80	Depleted Spinel Lherzolite (DSL)
42%	84.10	15.55		0.35	Depleted Spinel Harzburgite (DSH)
Melting proportions (wt.%)					
	1.21	8.06	76.37	14.36	FSL
	9.55	63.88	24.47	2.10	DSL
	12.73	85.17		2.10	DSH

Table (5.4) Modal abundances and melting proportions of the source peridotite used in the melting model. (From Kostopoulos, 1991)

The last consideration is the right choice of type of melting, i.e. equilibrium versus fractional melting. McKenzie (1984) showed that buoyancy of the melt and deformation of the matrix quickly separates the former, and that the melt fraction is unlikely to exceed a few per cent anywhere in the mantle during melting. Although this rules out equilibrium melting, at least for large degrees of melting, fractional melting, where the melt fraction is instantaneously separated from the matrix, seems an equally unlikely proposition. A more realistic model is one where a small melt fraction is generated in equilibrium with the residue and is continuously separated from it, as employed in Kostopoulos (1988). For the purposes of modelling, the non-modal equilibrium melting equations (Equations 5.5 and 5.8) have been used for 1% melting intervals, recalculating the mode of the residue to 100% after each step. This procedure has the added advantage of permitting the change of distribution coefficients and melting proportions, where appropriate, without making necessary the use of complex equations (as those of Hertogen and Gijbels, 1976). In practice, the choice of model is relevant only to incompatible elements. Figure 5.37a shows that the liquid (and whole-rock) compositions calculated with the sequential equilibrium melting model approach those for fractional melting. For the limited degrees of melting used in the calculations, the choice of melting model does not perceptibly influence the concentrations of compatible elements (Figure 5.37b).
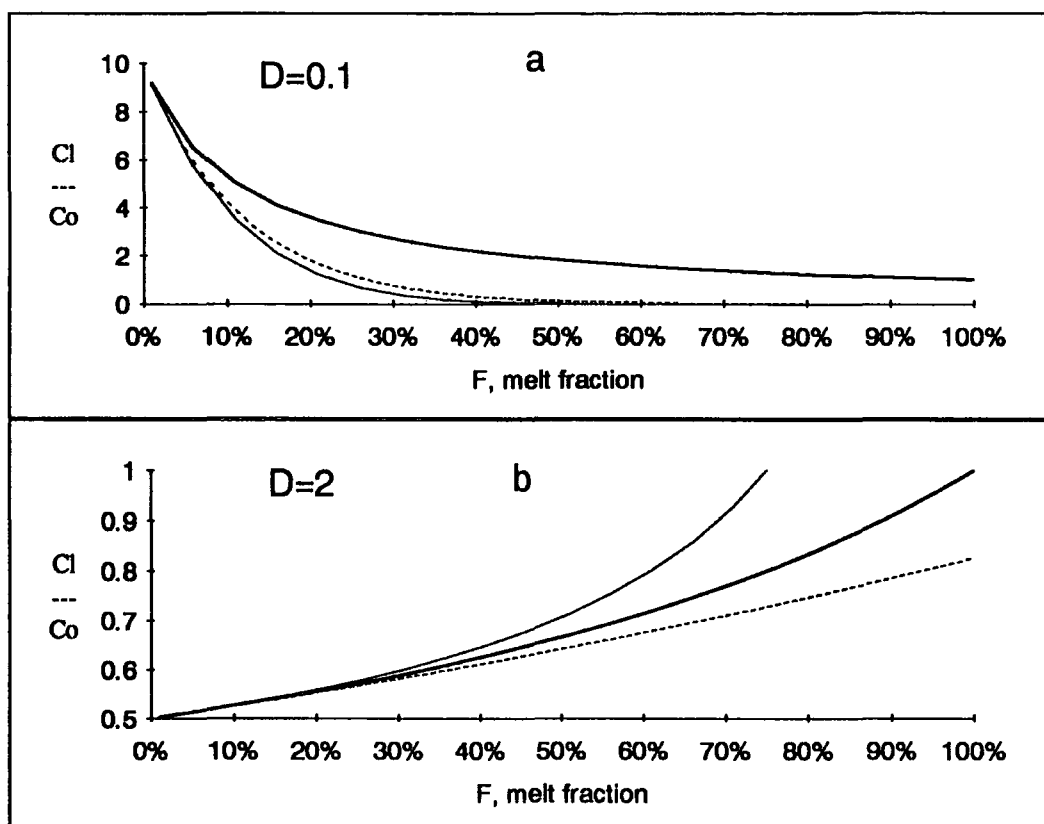
Figure (5.37) Comparison of the theoretical variation of element concentrations during equilibrium (thick line), fractional (thin line), and sequential equilibrium (dotted line) melting for an incompatible (a) and a compatible (b) element. D is the bulk distribution coefficient. Cl is the liquid concentration and Co is the initial source concentration. The same relations apply to the variation of the source composition Cs.

In order to assess the success of the modelling the calculated whole rock, liquid, and mineral compositions are compared to those of natural rocks in the following sections.

5.5. Whole rock composition

Peridotites dredged from the ocean floor are believed to be the residues of melting that produced MORBs at oceanic spreading centres (e.g. Dick, 1984; Dick et al., 1984; Michael and Bonatti, 1985; Bonatti and Michael, 1989; Dick, 1989). The peridotites have a relatively
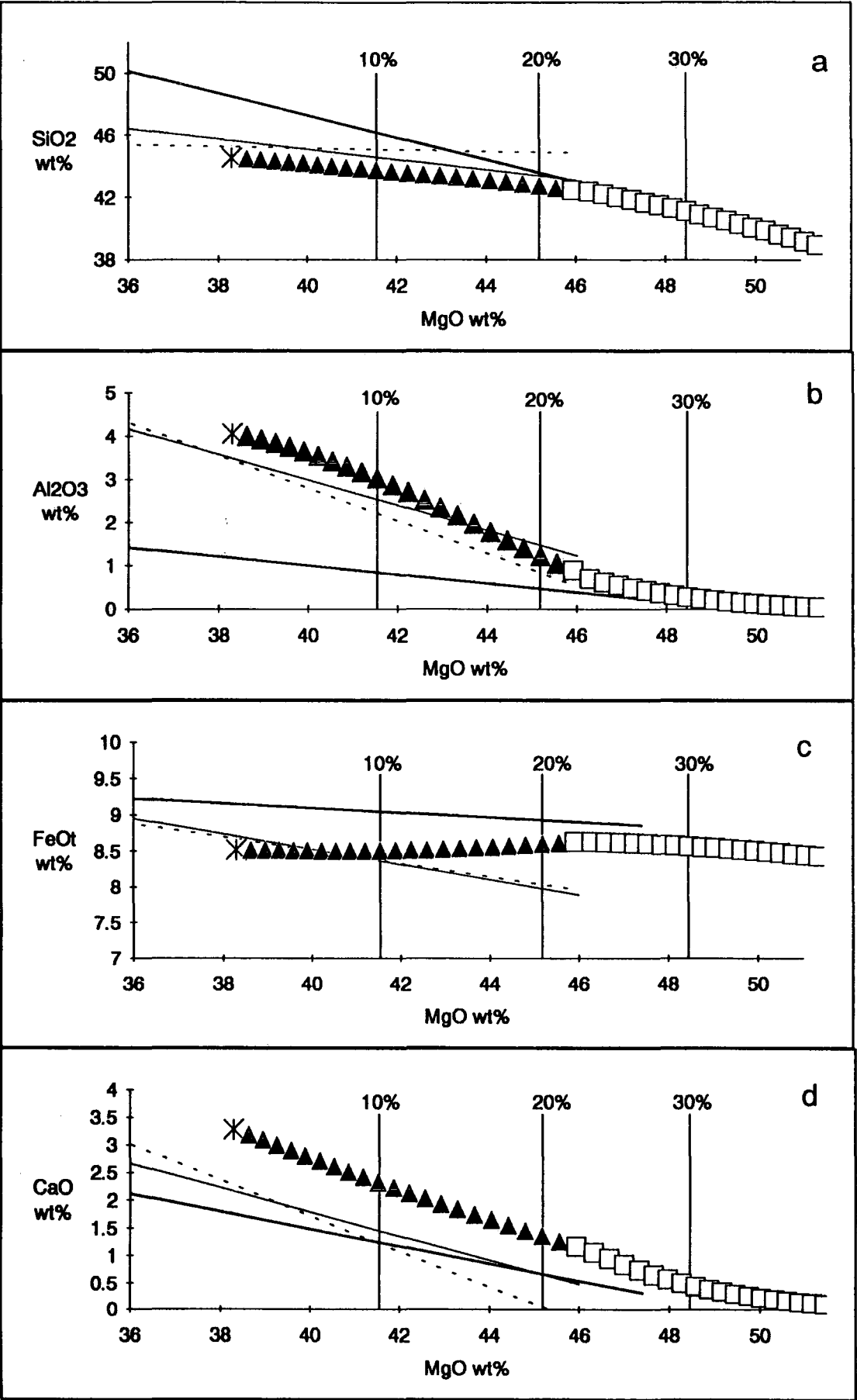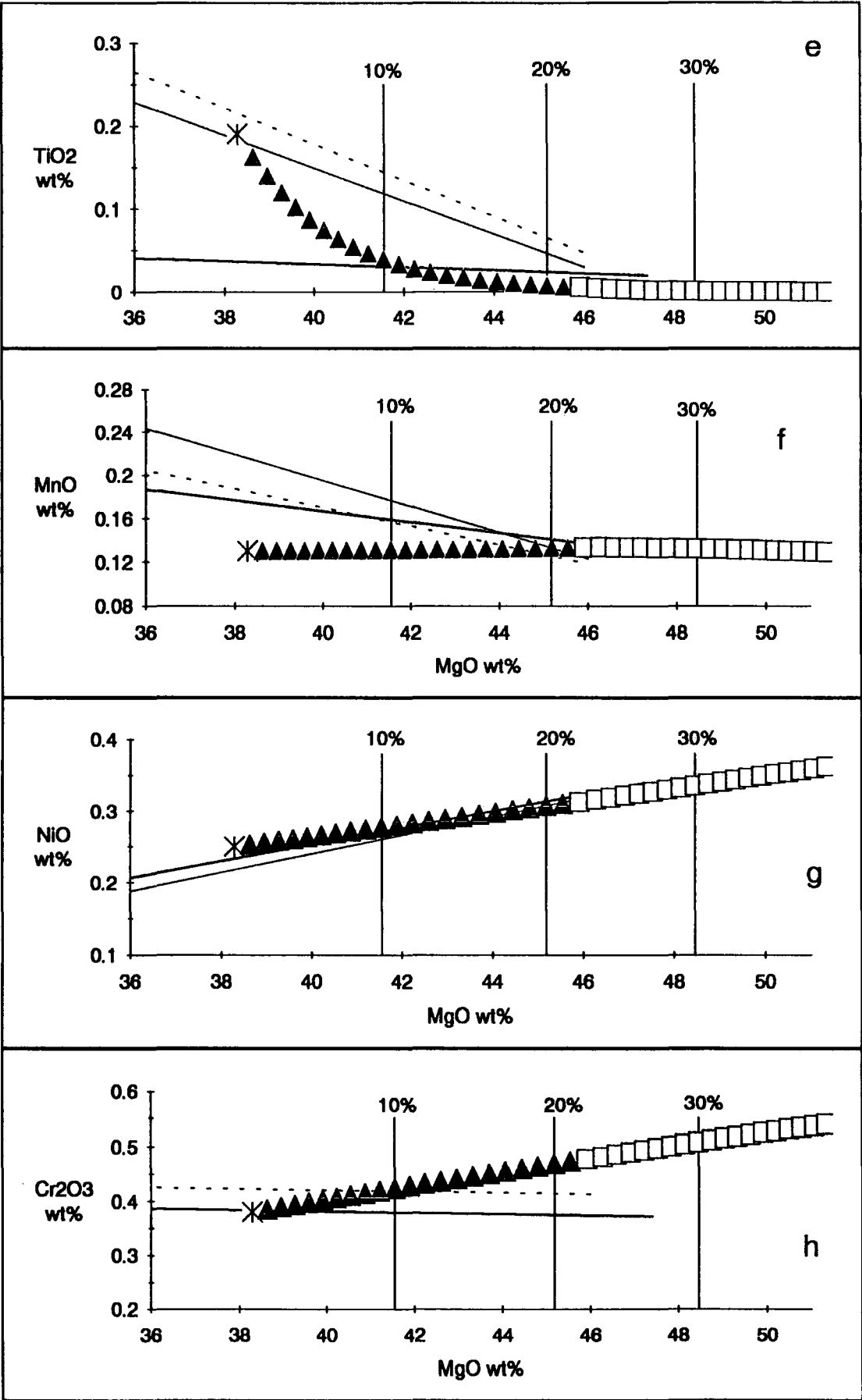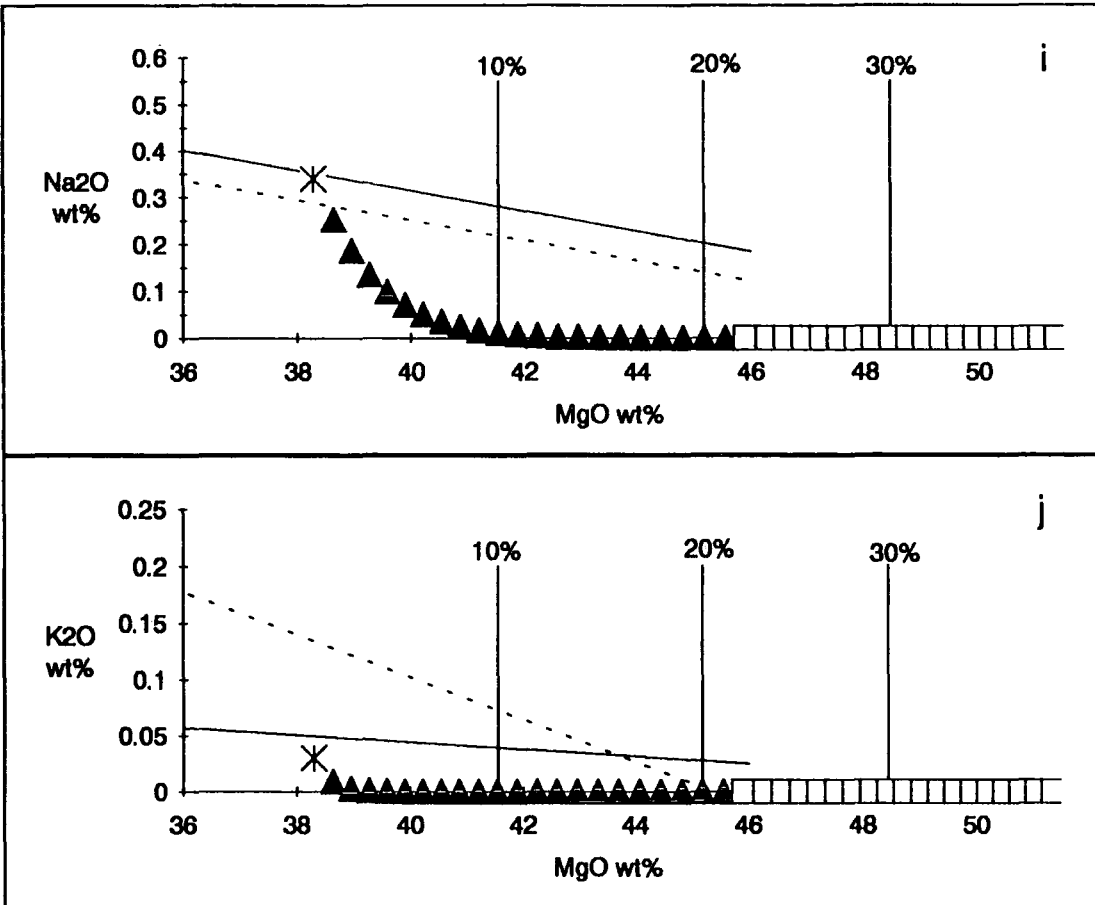
Figure (5.38) Binary diagrams of oxide wt.% plotted against MgO wt.%. Thin line is calculated from 83 oceanic peridotites (Maaløe and Aoki, 1977), except for Cr_2O_3 and K_2O where the regression for 302 continental spinel lherzolites is used. Dashed line is calculated from 99 oceanic peridotites (Shibata and Thompson, 1986). Thick line is a regression of 40 representative Pindos peridotites (this study); note that no best-fit line was calculated for Na_2O and K_2O since these elements are below the detection limit in the samples considered. The ends of the lines correspond to the minimum and maximum MgO wt.% abundances of the peridotites for which they were calculated. Solid triangles represent the first 21% of melting of isentropically upwelling asthenosphere underneath a mid-ocean ridge. Open squares represent a further 19% of melting at constant pressure and temperature after which clinopyroxene disappears from the residue (see text). Star is the starting source composition (Table 5.3). Every point represents 1% melting. Vertical lines mark the 10%, 20%, and 30% partial melting points. Calculated oxide values are recalculated to 100%. Full analyses can be found in Appendix B.

restricted range of major element compositions and MgO contents greater than 47 wt.% or less than 36 wt.% are rarely observed; they exhibit, nevertheless, distinctive chemical trends that are consistent with various degrees of melt extraction or accumulation (Maaløe and Aoki, 1977; Maaløe and Steel, 1980; Shibata and Thompson, 1986). Maaløe and Aoki (op. cit.) studied the composition of sub-oceanic mantle in simple binary plots of MgO weight per cent against all other major- and minor-element oxides and calculated the corresponding regression lines. Shibata and Thompson (1986) used a slightly larger data base of peridotites and calculated regression lines for SiO_2, TiO_2, Al_2O_3, FeO, MnO, MgO, CaO, Na_2O, K_2O, and P_2O_5 in a similar manner. These regressions will be used to define the oceanic melting regime and compare it with the calculated compositions peridotite compositions. Peridotite depletion trends were also calculated for Pindos using a representative subset of 40 selected samples. All best-fit lines are shown as Figures 5.38a-j together with the calculated peridotite compositions for the first 40% of melting.

Three points are immediately apparent in these plots:

a) There is a large overlap in the MgO wt.% contents between the abyssal and the Pindos peridotites, although the latter extend to more MgO-rich compositions.

b) The slopes of the two regression lines computed for the abyssal peridotites differ slightly for all oxides but this difference is larger for SiO_2, CaO, Na_2O, and K_2O.

c) The slope of the Pindos best-fit line is quite distinct from that calculated for the abyssal peridotites for all elements considered.

With regard to point (a) above, it will be noted that samples containing less than 5% modal orthopyroxene were not included in the Pindos data base. These samples were excluded not only because their compositional range is very restricted (i.e. dunitic) and would probably bias the regressions, but also because their origin may have involved processes other than partial melting, namely, olivine accumulation, incongruent melting of enstatite, or mechanical mixing between dunite and harzburgite.

The occurrence of compositions more fertile than the starting pyrolite composition (<38.29 wt % MgO) is due to the presence of variable amounts of trapped melt, a process

that has been established both for Pindos (see Chapter 1) and for abyssal peridotites (Dick, 1984, 1989).

With respect to point (b) above, the data set from which the regression lines were derived must be examined. Shibata and Thompson (1986) used a data set of 99 samples compared to that of 83 samples of Maaløe and Aoki (1977). Maaløe and Aoki (op. cit.) used the PETROS library (Mutschler et al., 1976) and do not mention individual sources, so it is difficult to establish where the two data bases differ. Still, this difference of 16 samples represents one fifth of the data set and is sufficient to cause the discrepancy. Notably, the largest differences occur for SiO_2, CaO, Na_2O, and K_2O[7] which are mobile during sea-floor alteration (see Chapter 2) hence, are the most likely elements to behave erratically.

Finally, with respect to point (c) made earlier, the difference in the calculated slopes between Pindos and the abyssal data set may reflect differences in their melting regimes. As discussed previously, melting beneath a mid-ocean ridge involves volatile-free melting of fertile peridotite with clinopyroxene dominating the melt fraction. Pindos has, however, experienced additional melting in the harzburgite field where H_2O was probably important and orthopyroxene was the most significant melting phase. This difference in the melting regime is best reflected in the concentrations of SiO_2, Al_2O_3, and CaO. In the case of CaO, Figure 5.38d shows that the regressions for the abyssal peridotites completely miss the starting composition by 1 wt.%. Although this may result from the MORB pyrolite composition used (Table 5.3) being too rich in CaO, a more likely explanation is that the abyssal peridotites have experienced CaO loss due to sea-floor alteration (see Chapter 2).

FeO is the only element that displays an enrichment trend in successive residues at degrees of melting less than 21% and a depletion trend at degrees of melting greater than about 21%. This is because below ~1300°C the behaviour of FeO changes from incompatible with olivine to compatible during melting (Figure 5.2). Although the depletion trend is consistent with the Pindos data, it is inconsistent with the observed enrichment trend for the

---

[7]Note that the regression line of Maaløe and Aoki (1977) for K_2O was calculated from continental spinel lherzolites that are usually much less altered than abyssal peridotites.

abyssal peridotites. A possible explanation is that the data set from which the regression lines for FeO for the abyssal peridotites were calculated was dominated by rocks that had experienced melting at temperatures in excess of 1300°C. However, since the calculated slopes for the abyssal peridotite trends are very shallow, this difference may not be statistically significant (the data also show a large scatter about the regression lines). An additional source of error, peculiar to FeO analyses, results from the combination of two practices. The first is that a sample may be analyzed for ferric and ferrous iron separately and then report total iron as ferric or ferrous. The second is that, because peridotites are usually altered, their analyses are recalculated on a volatile-free basis. This involves the way ignition losses are determined and, depending on the true amount of ferrous iron in the samples, they may have been underestimates, thus introducing an error to the recalculated volatile-free analyses. Although for most elements such error is negligible, for iron it may be amplified because the sum of the oxides changes depending on whether iron is reported as ferric or ferrous iron.

The rapid depletion in TiO_2, Na_2O, and K_2O in the residual peridotites (Figures 38e,i,j) is the result of the incompatible nature of these elements. It will be noted, however, that, because of their low concentrations (subjected to large analytical uncertainties), there are large 2σ-standard errors to the least-squares fits. In addition, Na_2O and K_2O are mobile during sea-floor alteration and this may have affected the slopes of the regression lines. This is especially true for Na_2O, which Maaløe and Aoki (1977) found to be 0.1 wt.% higher in abyssal peridotites than in continental spinel-lherzolites.

MnO shows an almost horizontal trend (Figure 38f), suggesting a bulk distribution coefficient of near unity, which is consistent with the lack of variation of MnO abundances that peridotites generally show. Although the calculated regression lines for the abyssal and Pindos peridotites have negative slopes, it should be borne in mind that the data show large scatter about the regression lines, which may have affected their slopes. This is supported by the fact that both the abyssal peridotite trends miss the starting MORB-pyrolite composition by 0.08 to 0.11 wt.% (Figure 5.38f).

NiO clearly shows an enrichment trend with a slightly shallower slope than that of the calculated regression lines (Figure 5.38g). This suggests that the bulk distribution coefficient for Ni is slightly larger than the calculated one. It is suggested here that, because of the very large partition coefficient of Ni in sulphide (e.g. Naldrett, 1981a), the presence of even minute sulphides in the mantle (which were omitted in the model) will increase the bulk distribution coefficient of Ni and, consequently, increase the slope of the calculated trend.

The calculated Cr_2O_3 increases with increasing melting, in contrast to the horizontal to slightly negative trends observed for the abyssal and Pindos peridotites (Figure 5.38h). The reason for this is not entirely clear. Liang and Elthon (1990) noted the horizontal trend to be common to all the Alpine peridotites and peridotite xenoliths in alkali basalts that they examined. They ascribed this lack of variation to a bulk distribution coefficient for Cr near 1 during mantle melting and suggested that all primary mantle melts are picritic to komatiitic in composition, containing high amounts of Cr_2O_3, equal to those in the peridotites with which they had equilibrated. The suggestion of Liang and Elthon (1990) is very difficult to equate with the presence of residual spinel and the behaviour of Cr during melting. Even at a temperature of $1400^{\circ}C$ and oxygen fugacity conditions as reducing as the iron-wüstite buffer, the $Kd_{Cr}^{sp/liq}$ has a value of ~110, implying that even a small fraction of residual spinel is sufficient to make the bulk distribution coefficient of Cr larger than unity. Moreover, it has been shown (see Chapter 3, oxygen geobarometry) that Pindos peridotites experienced melting at lower temperatures and higher oxygen fugacities than those above, which should increase $Kd_{Cr}^{sp/liq}$ to even higher values. Additional evidence against the proposition of Liang and Elthon (1990) comes from the observed Pindos basalts. For example, there is no evidence for the existence of picritic liquids in Pindos; furthermore, the existence of different magmatic units becoming progressively enriched in Cr_2O_3 with increasingly younger ages requires variation in the Cr_2O_3 abundance of their source region. Although Cr is affected by re-equilibration at sub-solidus temperatures (see Chapter 3, geothermometry), this exchange has high blocking temperatures and should not affect the whole rock Cr_2O_3 abundance. Nor can alteration be responsible for the difference in the Cr_2O_3 content between calculated and observed peridotite compositions, since Cr_2O_3 is immobile during alteration (see Chapter 2,

serpentinization). At the present time the discrepancy is attributed to the distribution of Cr_2O_3 in the rock. Unlike Ni, most of which occurs in solid solution in mantle minerals and its distribution is relatively homogeneous, Cr_2O_3 is strongly concentrated in a minor phase (spinel). In addition, spinel grains tend to form clusters, that increase the inhomogeneity of the rock with respect to Cr_2O_3. This is not apparent in other spinel constituents because their contribution to the whole rock is very small. It is, therefore, suggested that the difficulty in obtaining and analyzing a representative rock sample is the main reason for the contrasting Cr_2O_3 pattern between the calculated and observed peridotite compositions. The above conclusion is supported by Figures 5.39 and 5.40. Figure 5.39 is a plot of MgO wt.% in the whole rock against Cr_2O_3 wt.% in the spinel for the Pindos peridotites. The data show a positive correlation in agreement with the model calculations. Figure 5.40 is a plot of Cr_2O_3 wt.% in the spinel against Cr in whole rock for the Pindos peridotites. Since spinel is the major Cr-bearing phase, a strong positive correlation is expected. However, such a correlation is not observed. The scatter shown by the whole-rock Cr values suggests inhomogeneous distribution of modal spinel according to the discussion above, rather than to analytical error or peculiarities in the melting regime.
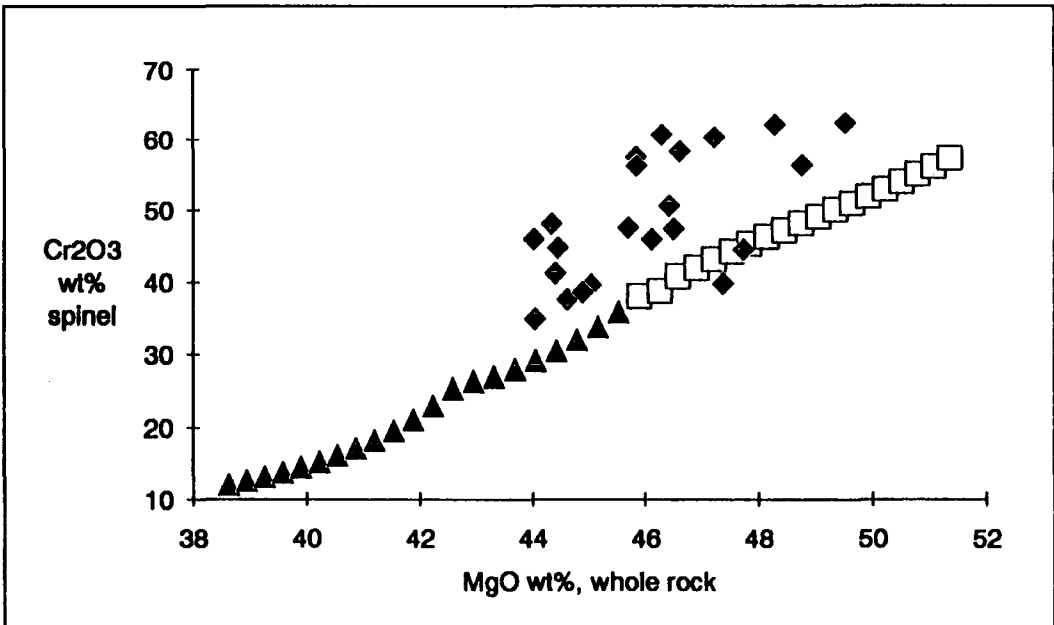
Figure (5.39) Plot of MgO wt.% in the whole rock vs. Cr_2O_3 wt.% in the spinel for the Pindos peridotites (filled rhombs). Other symbols as in Figure 5.38. A positive correlation is displayed.
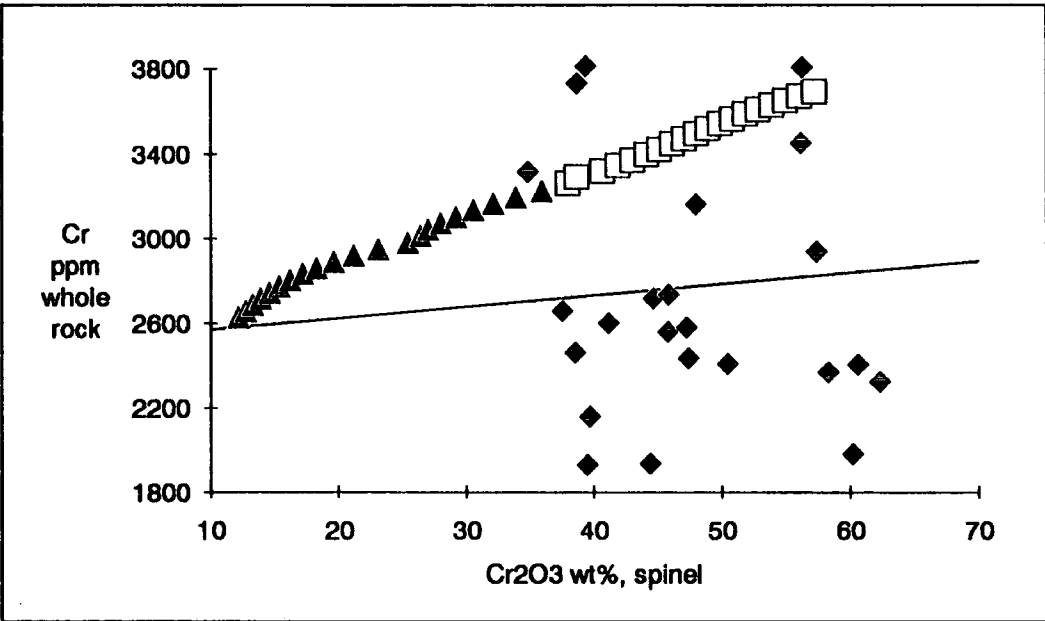
Figure (5.40) Plot of Cr_2O_3 wt.% in spinel vs. Cr in whole rock for the Pindos peridotites, for which the regression line was calculated. Only a weak positive correlation is displayed. Symbols as in Figure 5.39.

5.6. Liquid compositions

Although the major-element partition coefficients were evaluated in the present thesis aiming at modelling the composition of melting residues, a by-product of the calculations is the composition of the liquid in equilibrium with the residual peridotite. Comparison of the calculated melts with natural basalts provides a measure of the validity of the modelling.

In the melting model used, an equilibrium liquid composition is calculated for every melting step (instantaneous melt). Natural basalts, however, are mainly the products of accumulation of instantaneous liquids in some reservoir (pooled melts; Klein and Langmuir, 1987; McKenzie and Bickle, 1988; Kostopoulos and James, in press). For this reason, the calculated composition of the instantaneous melts have been "pooled" according to the method of Kostopoulos and James (in press) over the chosen melting intervals and are shown in Tables 5.5 and 5.6.

5.6.1. Melting beneath an ocean ridge

The first 21 increments of melting were calculated for isentropically upwelling mantle of normal (1280°C, McKenzie and Bickle, 1988) potential temperature beneath a mid-ocean

ridge. Pooling of these melt fractions should produce a melt composition that corresponds to primary MORB. and the calculated pooled melt is that of primary MORB (Kostopoulos, in press). There is considerable debate, however, over what is the composition of primary MORB. Several workers believe that magnesian MORBs (MgO>9.5 wt.%) represent near-primary basalts generated at moderate (5-11 kb) pressures (e.g. Bender et al., 1978; Hart and Davis, 1978; Takahashi and Kushiro, 1983; Fujii and Bougault, 1983; Presnall and Hoover, 1984; Shibata and Thompson, 1986; Klein and Langmuir, 1987; McKenzie and Bickle, 1988), whereas others believe that they derive from high-pressure (15-30 kb) picritic liquids (MgO>16 wt.%) through extensive olivine fractionation (e.g. O'Hara, 1968; Jaques and Green, 1980; Stolper, 1980; Elthon and Scarfe, 1984; Duncan and Green, 1987; Falloon and Green, 1987, 1988; Falloon et al., 1988; Liang and Elthon, 1990). Arguments for each theory were recently reviewed in Kostopoulos (in press), who was in favour of the first theory, and will not be reiterated here, except to say that the results of the present modelling strongly favour the former alternative. The composition of the pooled melt for the first 21 melting increments is shown in Table 5.5, together with the calculated melt composition of McKenzie and Bickle (1988) and a range of observed primitive MORBs. McKenzie and Bickle (op. cit.) used parameterized melting experiments of pyrolite to calculate the instantaneous and accumulated melts generated by isentropically upwelling lithosphere. The composition shown in Table 5.5 is calculated for the same mantle conditions that were used in this study. The pooled melt calculated here shows good agreement, both with McKenzie and Bickle's (1988) melt, and with the natural basalts in Table 5.5, especially considering the variety of processes that were involved in the generation of the natural basalts (olivine fractionation or accumulation, magma mixing etc.). The calculated CaO/Al_2O_3 ratio for the pooled melt is 0.726 (Table 5.5) and compares favourably with that for 84 depth-averaged abyssal tholeiites from all mid-ocean ridges (Klein and Langmuir, 1987; 0.756±0.057). The overall similarity between calculated and observed liquid and residual peridotite compositions may be regarded as a measure of the adequacy of the melting regime chosen and the derived expressions for the distribution coefficients.

	A	B	SD-7-MG	DB	RH	3-18	ARP74-10-6
SiO_2	50.92	51.89	50.93	50.26	49.5	50.3	50.26
TiO_2	1.15	0.92	1.01	0.61	0.81	0.73	0.82
Al_2O_3	14.75	14.57	17.27	14.21	15.7	16.6	15.05
FeO	8.16	8.53	7.67	6.82	7.45	7.99	8.04
MnO	0.11	N/A	0.20	0.10	0.15	0.12	0.14
MgO	11.45	10.27	11.03	11.89	10.0	10.2	10.13
CaO	10.71	11.01	11.36	13.46	13.0	13.2	12.09
Na_2O	2.44	2.16	0.36	1.42	1.95	2.00	2.07
K_2O	0.25	0.25	N/A	0.07	0.17	0.01	0.16
Cr_2O_3	0.034	N/A	N/A	N/A	N/A	N/A	N/A
NiO	0.031	N/A	N/A	N/A	N/A	N/A	N/A
Mg#	0.715	0.683	0.720	0.757	0.706	0.695	0.692

Table (5.5) A: the calculated pooled melt composition using the first 21 increments of melting. B: depth and point average melt composition of McKenzie and Bickle (1988) for partial melting of mantle of normal temperature (1280°C). SD-7-MG, DB, RH, 3-18, and ARP74-10-6 are primitive abyssal tholeiite glasses, ranging from picrite to olivine tholeiite, and were compiled by Shibata and Thompson (1986). N/A: not analyzed.

5.6.2. Second-stage melting

Second-stage melting in SSZ mantle involves a variety of source compositions and melting conditions. For the sake of modelling the peridotite at the top of the MORB melting column (i.e. the peridotite that experienced 21% melt extraction) is taken as the source of the SSZ magmas. In Table 5.6, melts C and D are calculated after 10% and 19%[8] melting respectively of the depleted source peridotite explained above. Also shown in Table 5.6 are a range of compositions for two Pindos boninite units (Kostopoulos, 1988). Once again, the calculated pooled melts show good agreement with the natural compositions, reflected in the high SiO_2, MgO, Cr_2O_3, and Mg# and the low TiO_2, Na_2O, and K_2O of the calculated liquids.

---

[8]This is the maximum melting extent of the previously depleted peridotite after which clinopyroxene disappears from the residue.

	C	D	N50E BSV		
	C	D	12	620	83
SiO_2	57.30	59.20	54.87	56.25	56.77
TiO_2	0.11	0.09	0.21	0.20	0.21
Al_2O_3	10.71	8.51	10.97	10.81	9.53
FeO	8.83	9.04	8.22	8.54	8.69
MnO	0.13	0.13	0.15	0.15	0.18
MgO	14.00	14.67	14.26	13.90	14.09
CaO	8.71	8.12	7.46	7.38	9.16
Na_2O	0.04	0.04	2.83	1.58	1.28
K_2O	0.05	0.05	0.12	0.27	0.02
Cr_2O_3	0.094	0.109	0.156	0.116	0.152
NiO	0.037	0.039	0.036	0.025	0.030
CaO/Al_2O_3	0.813	0.954	0.680	0.683	0.961
Mg#	0.739	0.744	0.756	0.744	0.743

Agia Sotira BSV				
	118	309	302c	302r
SiO_2	56.33	58.20	57.33	54.84
TiO_2	0.25	0.33	0.32	0.33
Al_2O_3	10.36	13.22	12.95	10.58
FeO	8.81	5.93	7.74	9.42
MnO	0.18	0.16	0.14	0.21
MgO	12.70	10.46	12.79	15.09
CaO	9.61	6.63	4.91	6.56
Na_2O	1.09	3.93	3.46	1.30
K_2O	0.09	0.02	0.06	0.06
Cr_2O_3	0.104	0.051	0.084	0.077
NiO	0.021	0.016	0.027	0.013
CaO/Al_2O_3	0.928	0.502	0.379	0.620
Mg#	0.720	0.759	0.747	0.741

Table (5.6) Columns labelled C and D are the calculated pooled melt compositions after 10% and 19% respectively of a source peridotite that underwent 21% melt extraction beneath a mid-ocean ridge. Model melting conditions: T=1250°C, P=5kb. N50E and Agia Sotira are two boninite units from Pindos (Kostopoulos, 1988).

An interesting result of the modelling is the contrasting behaviour of CaO and Al_2O_3. Melts C and D (Table 5.6), for example, have very similar CaO contents but the Al_2O_3 content of melt D is much lower than that of melt C. This suggests that the CaO/Al_2O_3 ratio in these melts increases with increasing degree of partial melting. The reason for this lies in the choice

of melting model, and particularly to the persistence of clinopyroxene in the source up to ~40% melting. CaO is an essential structural constituent (ESC, see Introduction of this Chapter) of clinopyroxene and buffers the CaO content of the equilibrium liquids. In contrast, Al_2O_3 substitutes in both tetrahedral and octahedral clinopyroxene sites and is rapidly depleted, especially in the former, with progressive melting. The good agreement in the CaO/Al_2O_3 ratio and the CaO content between calculated melts and natural Pindos boninites suggests that the latter were in equilibrium with clinopyroxene in their source regions. This agrees with the suggestion, made by Kostopoulos (1988), that the Pindos boninites are of the eutectic type, i.e. their genesis did not involve incongruent melting of orthopyroxene.

The good agreement between the calculated melts and the natural Pindos boninites is somewhat surprising, because the partition coefficients were calculated from dry experiments. This suggests that the effect of water on major-element partitioning is not large, therefore the change in 'wet' Kds can be accommodated within the uncertainty of the 'dry' partition coefficients.

5.7. Model dependencies

Having calculated the whole-rock and liquid compositions for the chosen melting model, a brief examination of how the initial assumptions affect these compositions will be made. Considerable effort was put in the choice of all the modelling variables, so that results were, as much as possible, free of uncertainty. Variables like the MORB pyrolite composition, or the pressure and temperature path of isentropically upwelling asthenosphere are as best constrained as possible, and there is no point in considering alternatives. Perhaps the only controversial assumption is the choice of melting model, and it is necessary to establish how much the results depend on this.

The consequences of choosing equilibrium, fractional, or sequential equilibrium melting have already been discussed in the description of the melting regime. The chosen sequential equilibrium melting model will give the same results as the other models where compatible elements are concerned. Incompatible elements will be more rapidly depleted from the source, than if equilibrium melting had been chosen (Figure 5.37a). While this

variation is insignificant for elements like Ti, Na, or K, that are rapidly depleted to ppm concentrations, it is substantial for elements like Si, Al, or Ca. It has been shown, however, (Figures 5.38a,b,d) that, far from being exhausted in the residues, the Si, Al, and Ca abundances of the residual peridotites match well the concentrations of these elements in the natural rocks. In addition, independent evidence in favour of a fractional melting model for the mantle is presented in recent studies on REE geochemistry of oceanic peridotites and basalts (Johnson et al., 1989; McKenzie and O'Nions, 1991). The good results of the modelling so far indicate that the chosen model is a good approximation of the mode of mantle melting.

Because the residue, liquid, and mineral compositions are all calculated from the initial whole rock composition (Equations 5.2 and 5.8), for any given temperature, pressure, and oxygen fugacity, the only factor affecting these compositions is the non-modal bulk distribution coefficient, which depends on the mineralogy of the residual peridotite and the melting proportions of minerals. As remarked earlier, one of the unusual aspects of the melting model is the persistence of clinopyroxene in the residue for large (~40%) degrees of partial melting. The arguments for its justification have been presented elsewhere (Kostopoulos, 1991) and will not be reiterated here. It will, however, be noted that the persistence of clinopyroxene in the residue during isentropic upwelling of the mantle for larger degrees of melting than equilibrium melting experiments suggest, has been independently suggested (Duncan and Green, 1987; Falloon and Green, 1988; MacKenzie and Bickle, 1988). In practice, if the sum of the melting proportions and the sum of the modes of ortho- and clinopyroxene are constant, the calculated liquid and residue compositions remain almost unaffected. This is due to the choice of 1% melting intervals that make the non-modal bulk distribution coefficient fairly insensitive to the parameter P (Equation 5.7). This means that the model is fairly robust to fluctuations of initial parameters and is not critically dependent on any of them, although the results obviously depend on the particular set of conditions chosen.

5.8. Residual mineral compositions

Having calculated the equilibrium instantaneous melt composition for every melting step, it is a simple matter to calculate the compositions of the residual minerals using their

partition coefficients. These calculations provide a measure of the accuracy of individual distribution coefficients for a given mineral. In addition, natural mineral compositions are free of the effects of serpentinization that is an added complication regarding whole-rock compositions.

In the following sections some of the diagrams that were presented in Chapter 3 will be used to illustrate how the calculated and natural mineral compositions compare.

5.8.1. Fe-Mg exchange between olivine and orthopyroxene

Figure 5.41 is a plot of Mg# of olivine against the Mg# of orthopyroxene. Data from Pindos peridotites show very good agreement with the calculated mineral compositions. The Fe-Mg ratio between olivine and orthopyroxene has a semi-logarithmic relation with temperature. From the partition coefficient equations for Fe and Mg in olivine and orthopyroxene (Figures 5.1, 5.2, 5.6, 5.8) the following temperature-dependent equation can be calculated:

$$\frac{(Fe/Mg)_{opx}}{(Fe/Mg)_{ol}} = \frac{-1291}{T^{\circ}C} + 1.00$$

This relatively strong temperature dependence is the cause of the slight underestimation of orthopyroxene Mg# for residues of second stage melting (Figure 5.41). These would shift to lower values of orthopyroxene Mg# for higher temperatures and vice versa. The temperature that actually fits the data best is rather low (1180°C) and probably results from the low-temperature re-equilibration that has affected the peridotites.
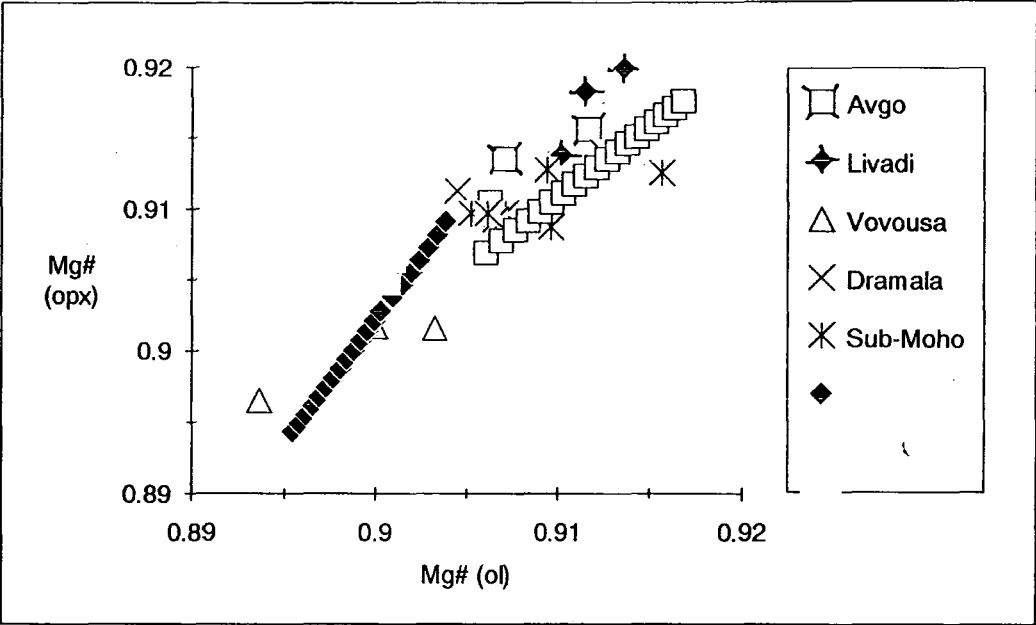
Figure (5.41) Plot of Mg/(Mg+Fe) of olivine vs. Mg/(Mg+Fe) of orthopyroxene. Filled rhombs are the first 21% of melting. Open squares represent an additional 19% of melting (see text). The rest of the symbols are compositions of mineral from Pindos peridotites.

5.8.2. Al₂O₃ content of orthopyroxene versus Mg#.

Figure 5.42 is a plot of Mg/(Mg+Fe) in orthopyroxene against its Al_2O_3 content. As expected a negative correlation is displayed. The failure of the modelled compositions to match the natural ones at low degrees of melting is caused by clinopyroxene exsolution. In peridotites that have not experienced re-equilibration at temperatures as low as Pindos, more aluminous orthopyroxene is preserved (Figure 5.43). Note that the S-shaped trend of the model compositions resembles that of the whole rock Al_2O_3 content (Figure 5.38b) and is also exhibited by the abyssal peridotites. The underestimation of orthopyroxene Mg# towards higher degrees of melting, that was mentioned in the previous paragraph, is also responsible for the small shift of the calculated trend towards smaller Al_2O_3 contents.
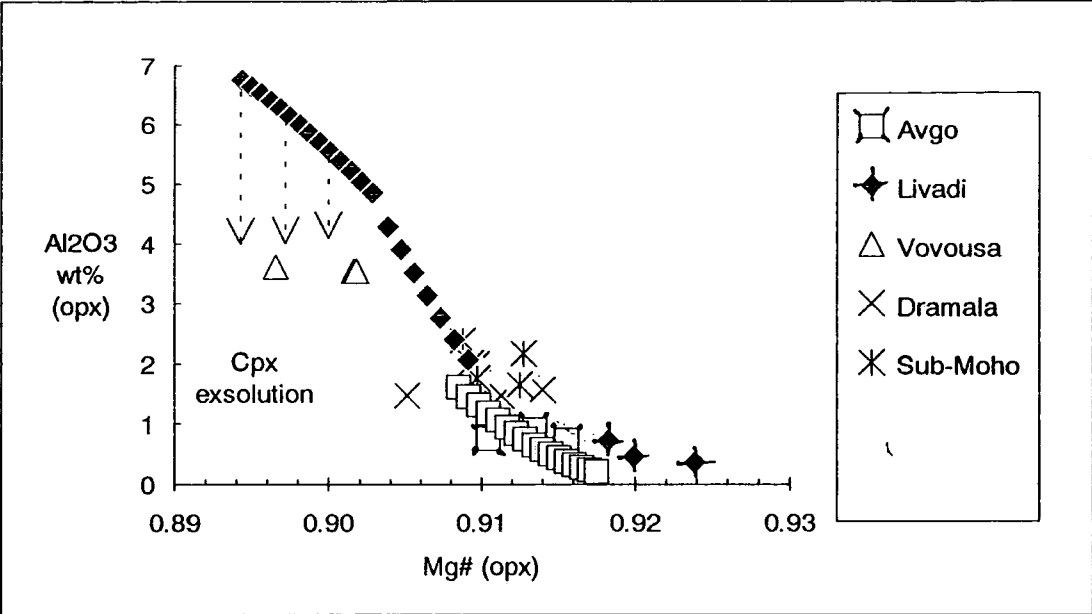
Figure (5.42) Plot of Mg/(Mg+Fe) vs. Al_2O_3 wt.% content of orthopyroxene. Symbols as in Figure 5.41.
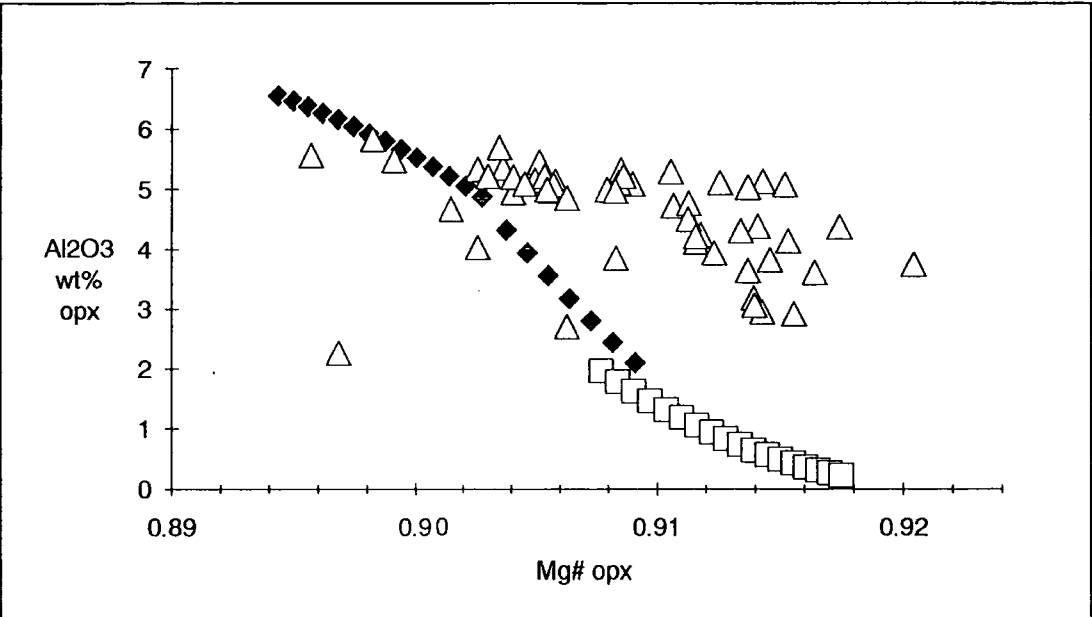
Figure (5.43) Plot of Mg/(Mg+Fe) vs. Al_2O_3 wt.% content of orthopyroxene. Symbols as in Figure 5.41. Triangles are orthopyroxene compositions from ocean floor peridotites from fracture zones (Dick, 1989).

5.8.3. Al_2O_3 content of co-existing pyroxenes

Figure 5.44 is a plot of the Al_2O_3 content of co-existing pyroxenes. The overestimation of the Al_2O_3 content of clinopyroxenes at any degree of melting suggests that

the calculated $Kd_{Al}^{cpx/liq}$ may be overestimated. Examination of the relative Al_2O_3 wt.% abundance in coexisting pyroxenes shows that, for example, abyssal peridotites have an average Al_2O_3cpx/Al_2O_3opx ratio of 1.22±0.09, whereas the pyroxene pairs used to calculate $Kd_{Al}^{cpx/liq}$ (Figure 5.21) have an average ratio of 1.38±0.39. The lower Al_2O_3 wt.% content of natural clinopyroxenes, compared to experiments, is the result of the low temperature re-equilibration that typically affects the former. Although this difference leads to apparently high Al_2O_3 abundances of calculated clinopyroxenes, the calculated $Kd_{Al}^{cpx/liq}$ is appropriate for the calculation of liquid compositions. Note that the lowest value of Al_2O_3 in orthopyroxene is ~1 wt.%, compared to less than 0.5 wt.% in Figure 5.42. The reason for this is not the complete absence of clinopyroxene from very depleted rocks, but its presence as increasingly thinner lamellae in orthopyroxene. Still, clinopyroxene grains large enough to be probed, persist until ~30% melting.
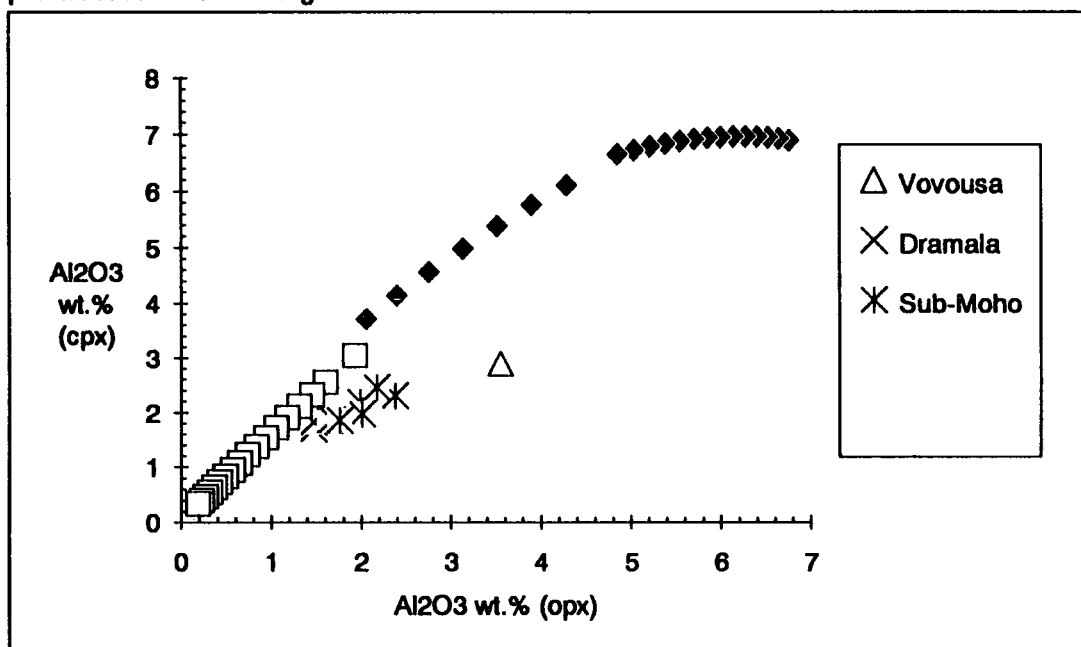
Figure (5.44) Plot of Al_2O_3 wt.% content of orthopyroxene vs. that of clinopyroxene. Symbols as in Figure 5.41.

5.8.4. Al_2O_3 between orthopyroxene and co-existing spinel

Figure 5.45 is a plot of Al_2O_3 wt.% in orthopyroxene against $Cr/(Cr+Al)$ in spinel. As mentioned earlier, at low degrees of melting the calculated orthopyroxenes have more Al_2O_3 than the natural ones, due to the effects of clinopyroxene exsolution on the latter. At higher

degrees of melting, however, the calculated trend shows excellent agreement with the natural compositions.
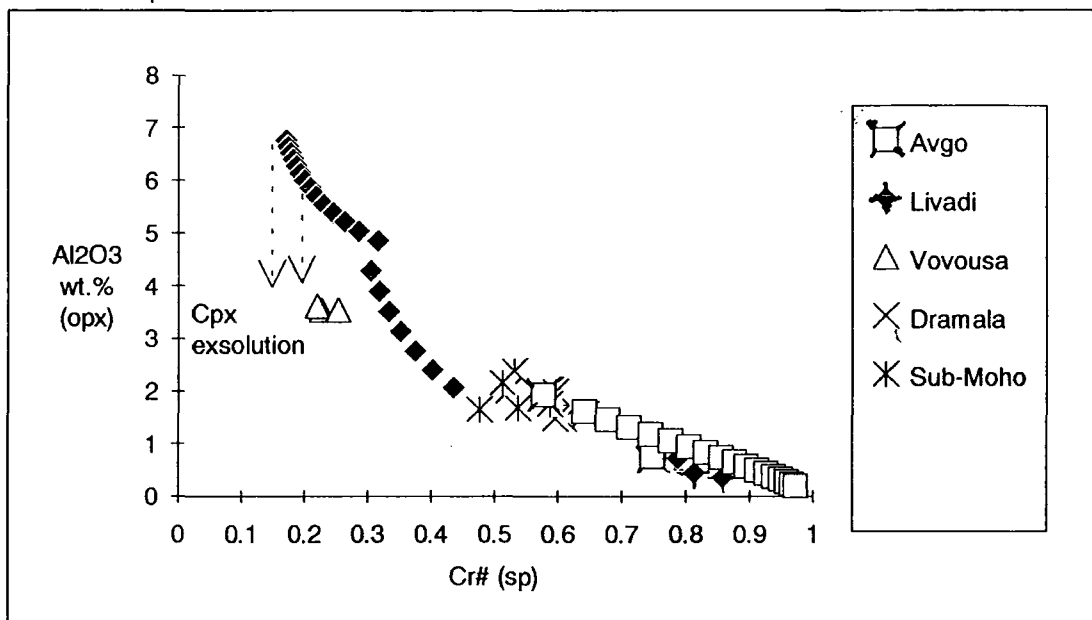
Figure (5.45) Plot of Al_2O_3 wt.% content of orthopyroxene vs. Cr/(Cr+Al) of spinel. Symbols as in Figure 5.41.

5.8.5. Cr-Al exchange between orthopyroxene and co-existing spinel

Figure 5.46 is a plot of Cr/(Cr+Al) between orthopyroxene and co-existing spinel. Despite the good agreement between modelled and natural compositions the Cr# of orthopyroxene (and, hence, its Cr_2O_3 content) is not predicted very accurately. For the first stage melting, the Cr# of orthopyroxene is underestimated, compared to the natural minerals; this is consistent with the earlier comments on Al_2O_3 in orthopyroxene, and its overstimation leads to the observed underestimation of the Cr#. With increasing degree of melting, however, the Cr# of orthopyroxene increases to values much higher than those observed in the minerals. Although orthopyroxenes with such high Cr# do exist (Jaques, 1980), they are the products of extreme degrees of melting, and do not justify the observed model trend. The reason why natural peridotites do not have orthopyroxenes with such high Cr# is that the Cr_2O_3 is controlled by the Cr# in co-existing spinel. Nagata et al. (1983) showed that the Cr fraction in the M1 site of orthopyroxene increases with increasing Cr# in spinel, until the latter is ~0.40, when Cr_{M1}^{opx} starts to decrease. In a plot of

Cr^{opx}_{M1} against Cr# in spinel this creates a parabolic trend (see also Chapter 3, orthopyroxene chemistry). Nagata et al. (op. cit.) also found a similar effect in clinopyroxene. The expression for Cr partitioning in orthopyroxene does not show any dependence on the Cr# of co-existing spinel, so this characteristic of Cr-Al exchange between the two minerals is difficult to reproduce in modelling.
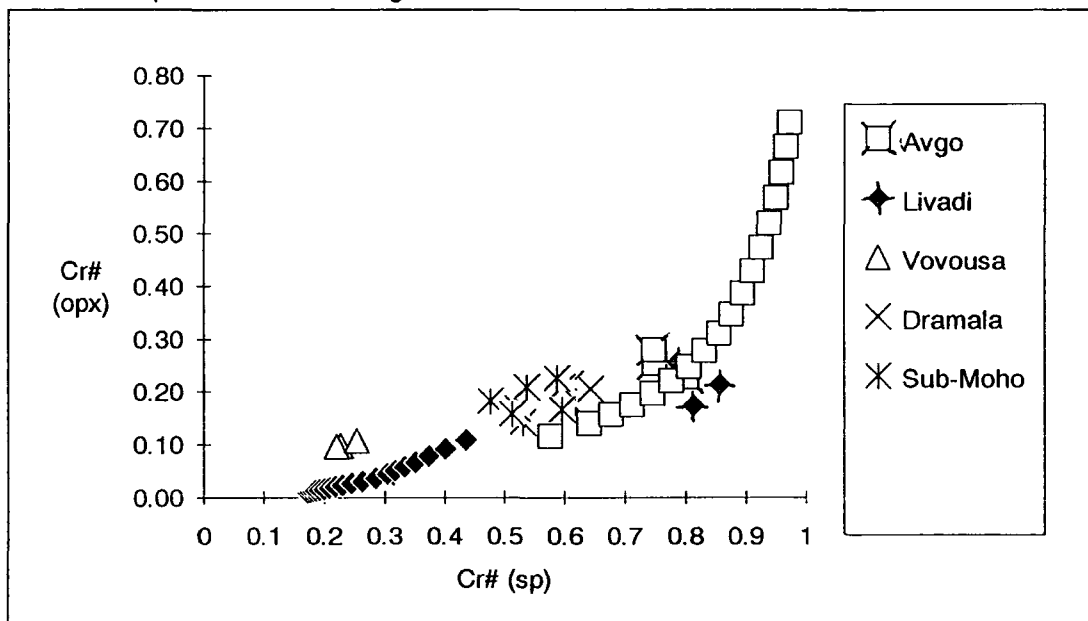
Figure (5.46) Plot of Cr/(Cr+Al) of orthopyroxene vs. Cr/(Cr+Al) of spinel. Symbols as in Figure 5.41.

5.8.6. Spinel in the Fe-Mg-Cr-Al plane

Figure 5.47 is a plot of Mg# against Cr# in spinel. As mentioned in Chapter 3, the Mg# in spinel is strongly affected by low-temperature re-equilibration; this results in the offset of the natural mineral compositions in Figure 5.47 to slightly lower Mg# than calculated, although there is good agreement for the Cr#. The spinel compositions have been calculated at two different oxygen fugacities to assess the effect of f_{O_2} on the Cr#. The very small difference between the two trends shows that a difference of 1 log unit has a very small effect on spinel. Note that the calculated trends resemble the s-shaped trend calculated independently from a thermometric expression (see Chapter 3, olivine spinel thermometry).
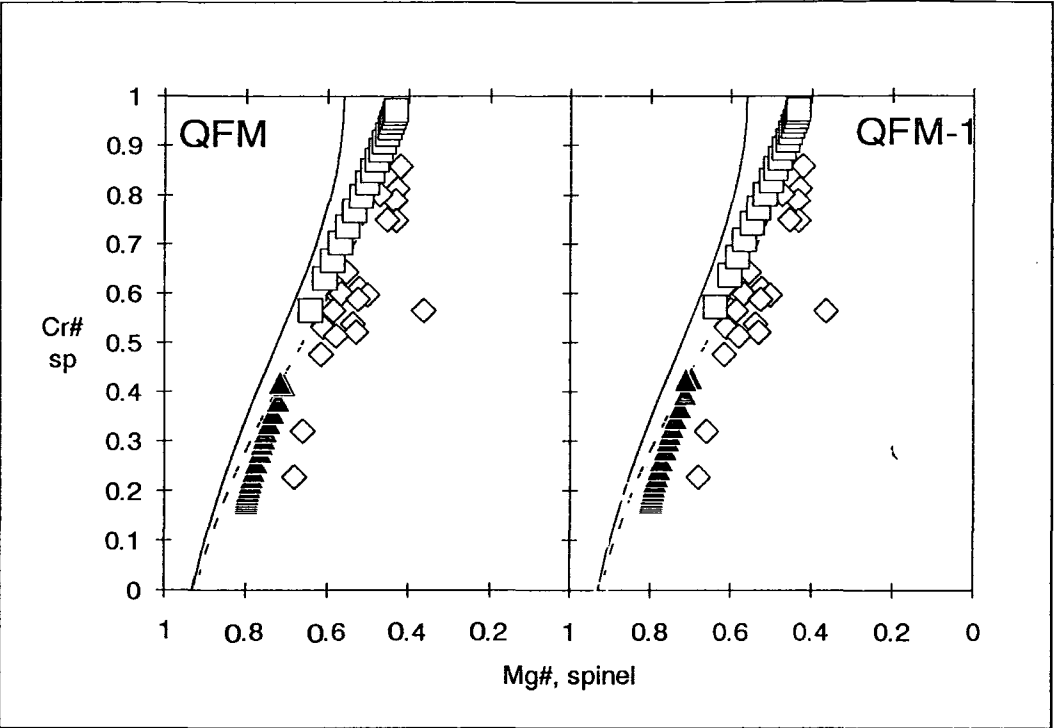
Figure (5.47) Plot of Mg/(Mg+Fe) vs. Cr/(Cr+Al) of spinel. Dashed line is the theoretical composition of spinel coexisting with olivine of Fo_{90} at 1200°C and solid line the same at 1300°C (see Chapter 3, olivine-spinel thermometry, for derivation).

5.9. Summary

Distribution coefficients between melt of basic composition and co-existing dry mantle minerals (olivine, orthopyroxene, clinopyroxene, spinel) were evaluated from dry melting experiments on natural rock compositions. This allowed the quantitative modelling of mantle melting using trace element approaches. The composition of peridotite, co-existing liquid, and residual minerals were calculated using an equilibrium partial melting model of 1% intervals for two mantle melting scenarios: under a mid-ocean ridge, and in a supra-subduction zone-related environment. The first setting involved mantle of MORB pyrolite composition with a normal initial temperature (1280°C) that starts to melt at a depth of 15.3 kb and experiences a total of 21% partial melting. Melting in a supra-subduction zone-related environment assumed that the residual peridotite after MORB extraction experiences a further 19% partial melting in static conditions at a temperature of 1250°C and a depth of 5 kb until the clinopyroxene disappears from the residue. Although this setting involves the

introduction of volatiles to the melting region, their effect on the major element partitioning was not evaluated, and the dry partition coefficients were used.

The calculated residual peridotite compositions were compared with observed compositions of oceanic and Pindos peridotites in simple binary diagrams of MgO wt.% against oxides. The modelled compositions showed good agreement with the natural rocks for most elements. Uncertainties in the calculated partition coefficients (MnO) or rock analyses (K_2O), involvement of other phases (NiO), and sampling difficulties (Cr_2O_3) accounted for most of the discrepancies.

In order to compare the calculated liquid composition with natural rocks, the instantaneous melts of each melting interval were used to calculate the weighted average of the melting column. The resulting pooled melt showed good agreement with calculated primary MORB and primitive abyssal basalts. The relatively low MgO content (11.45 wt.%) and Mg# (71.5) of this melt lend support to the theory that magnesian MORB (MgO>9.5 wt.%) are near primary melts generated at moderate (5-11 kb) pressures.

The calculated pooled melt produced by 10-20% partial melting of depleted peridotite compared very well with Pindos boninites, both in range of compositions and in general characteristics. It was also demonstrated that SiO_2, MgO, and Mg# in boninites increase with increasing extent of partial melting, whereas Al_2O_3 at the same time decreases. The CaO abundance depends on the presence of residual clinopyroxene, in which case it is almost constant, or its absence, in which case it behaves like Al_2O_3.

The modelled compositions of residual minerals also showed good agreement with the chemistry of minerals in the Pindos peridotites. The latter, however, have been subjected to low-temperature re-equilibration, which resulted in some differences. These discrepancies ranged from small (Al_2O_3 in co-existing pyroxenes) to very large (Cr_2O_3 exchange between spinel and co-existing orthopyroxene).

The results of the modelling support the conclusions of Chapter 3, where the Pindos peridotites were compared with mantle-derived rocks from a variety of settings, and allow quantitative comparisons to be made. Thus, the Vovousa peridotite, for which a mid-ocean ridge origin was inferred, has experienced ~12-15% partial melting. The rest of the complex is

more depleted and shows a wider range of compositions. A supra-subduction zone evolution was suggested for this part, with heterogeneously distributed water-induced second-stage melting resulting in variable degrees of depletion of the peridotites. The total degree of partial melting ranges from ~18% to ~40%, although the less depleted peridotites were probably re-fertilized by melt impregnation. Whereas all peridotites underwent melting in a mid-ocean ridge environment, some experienced additional melting episodes and eventually produced boninites.

Appendix A. Sample location maps

Scale 1:20,000

Arkoudas rema

gc1

Gucamisios

·kk34
·kk33
kk32
·kk31
·kk30

·gc2

·dr20
·dr19

dr18

·dr17
dr16

·dr29

dr28
dr27
·dr26

dr25

dr24

dr23·

dr22·
dr21

·dr13

·dr14
·dr15

kk8811
kk8812

kk8813-4

dr11

·dr8

4

dr7
·dr6

dr5

1611
×

·dr12

kk8817
kk8821

kk8822
·kk8823

·kk17

kk39

dr1

dr2

dr3

kk37-8

·kk8824

kk36

kk35

1433
×

Scale 1:20,000

Scale 1:50,000
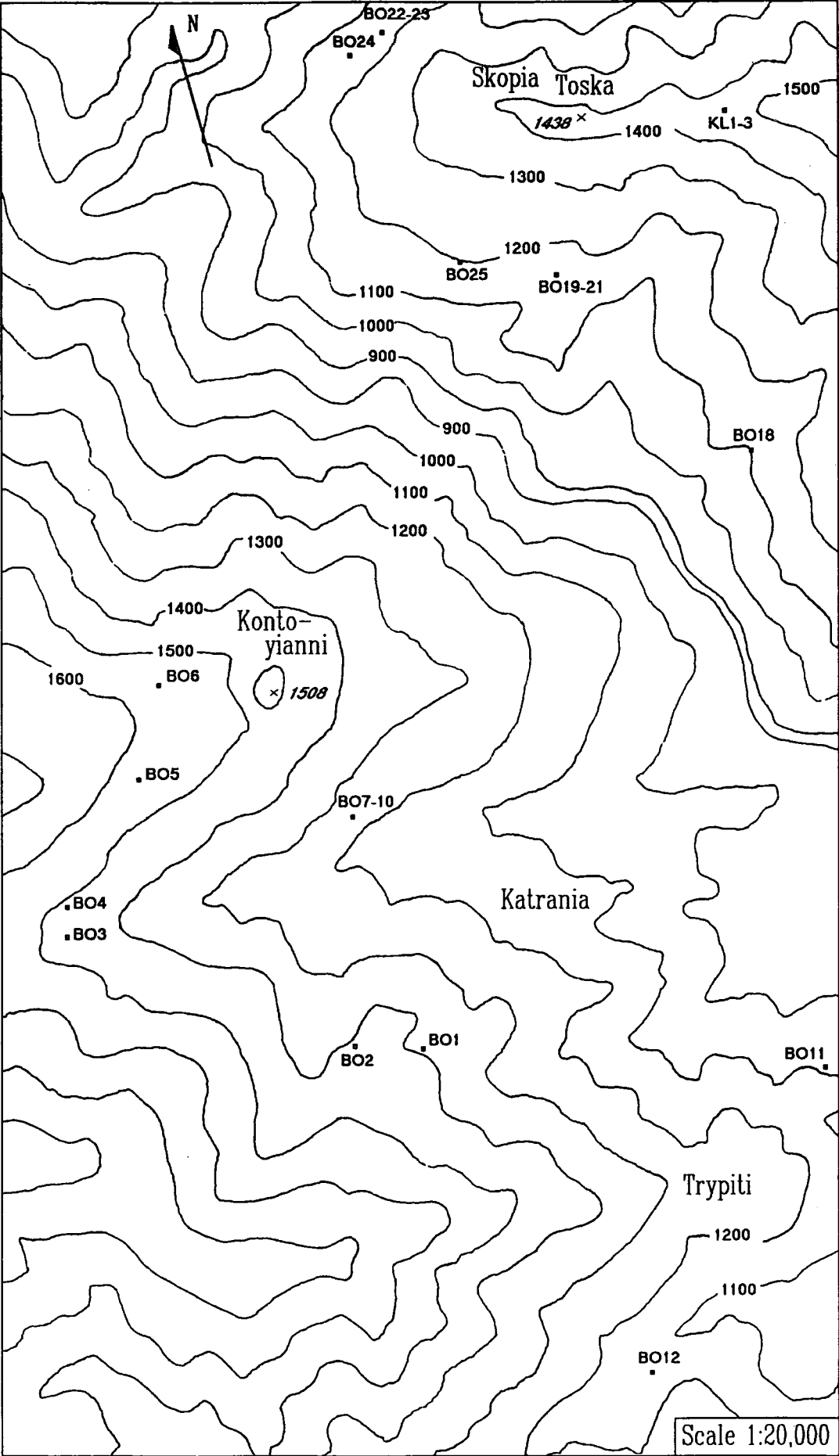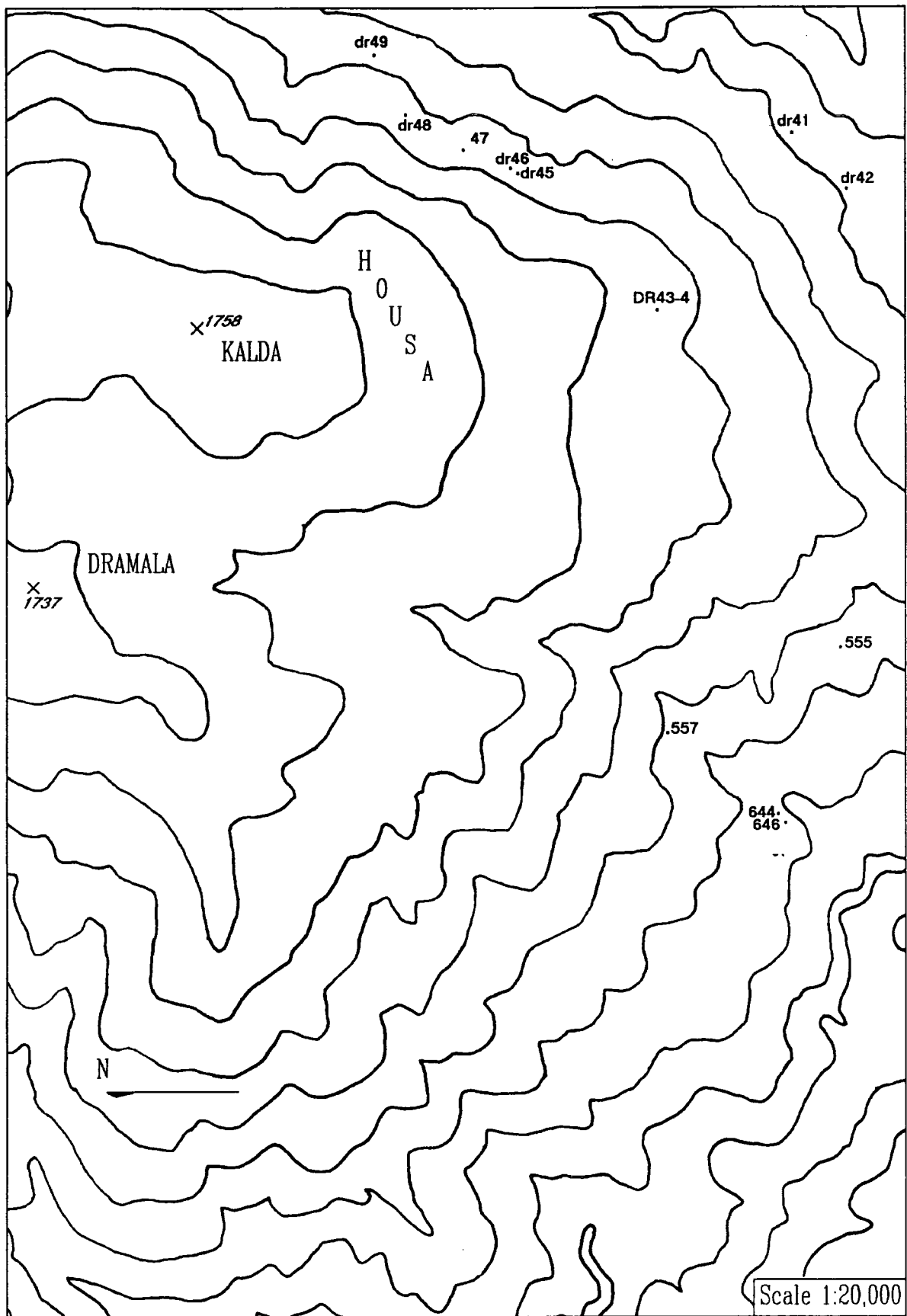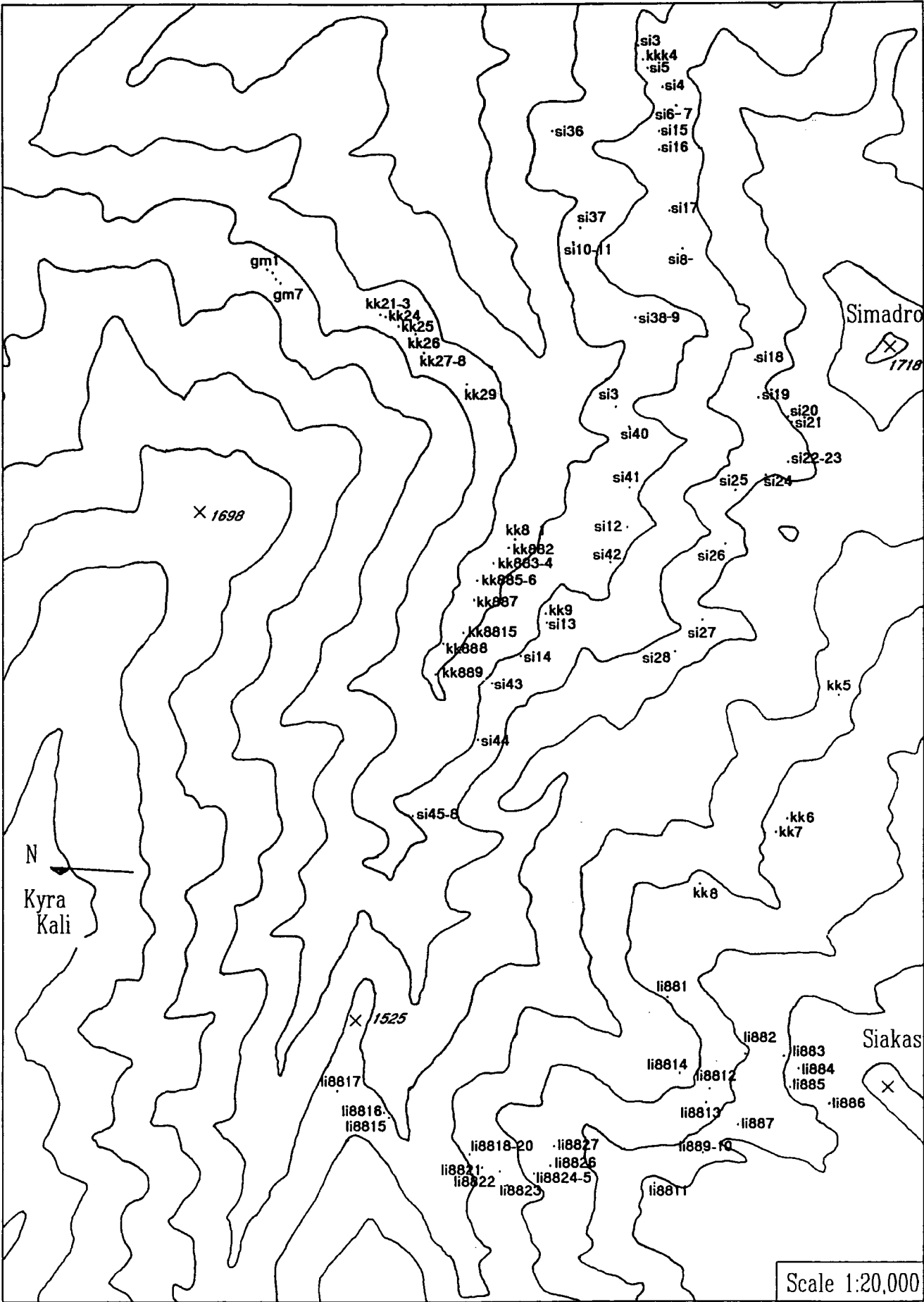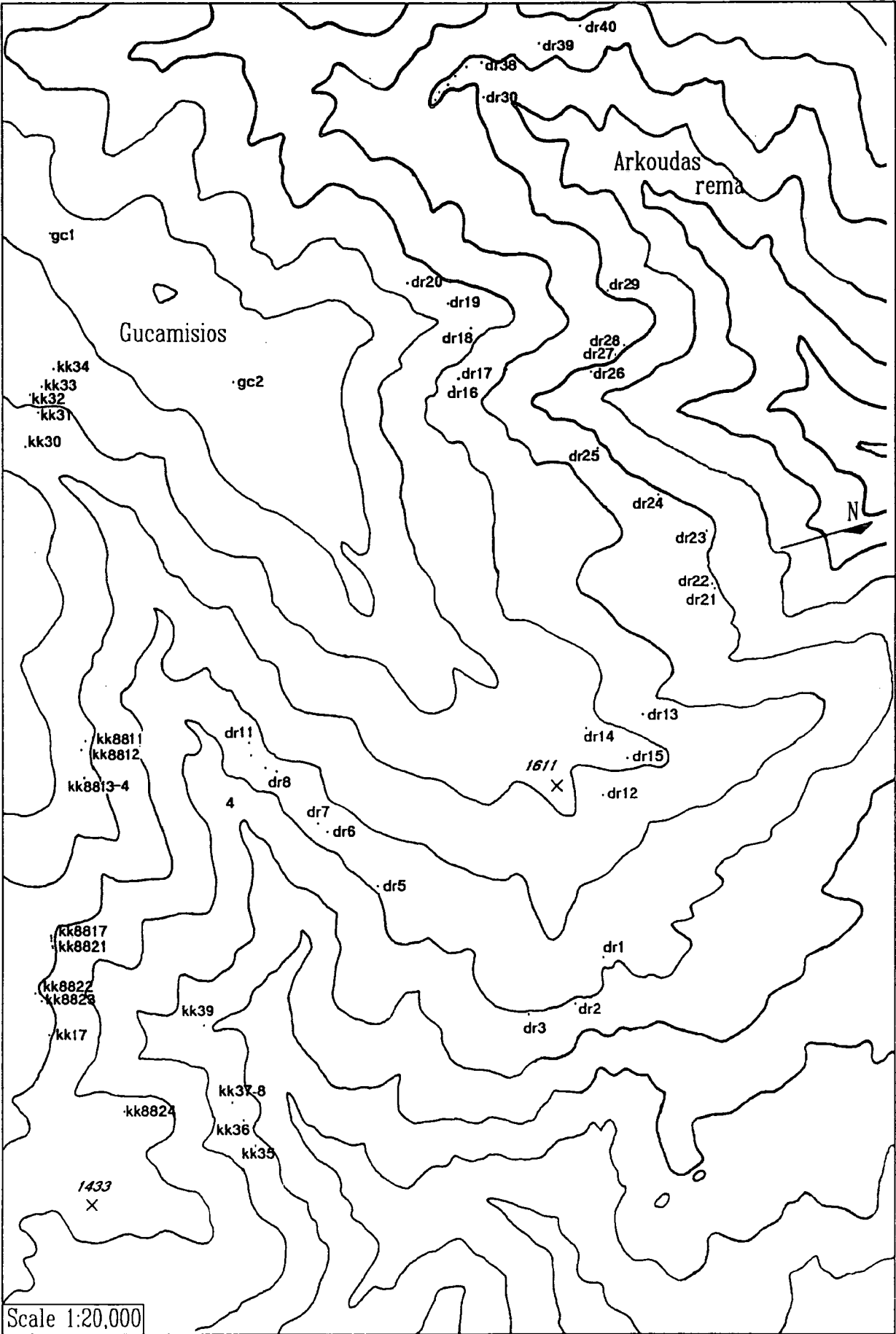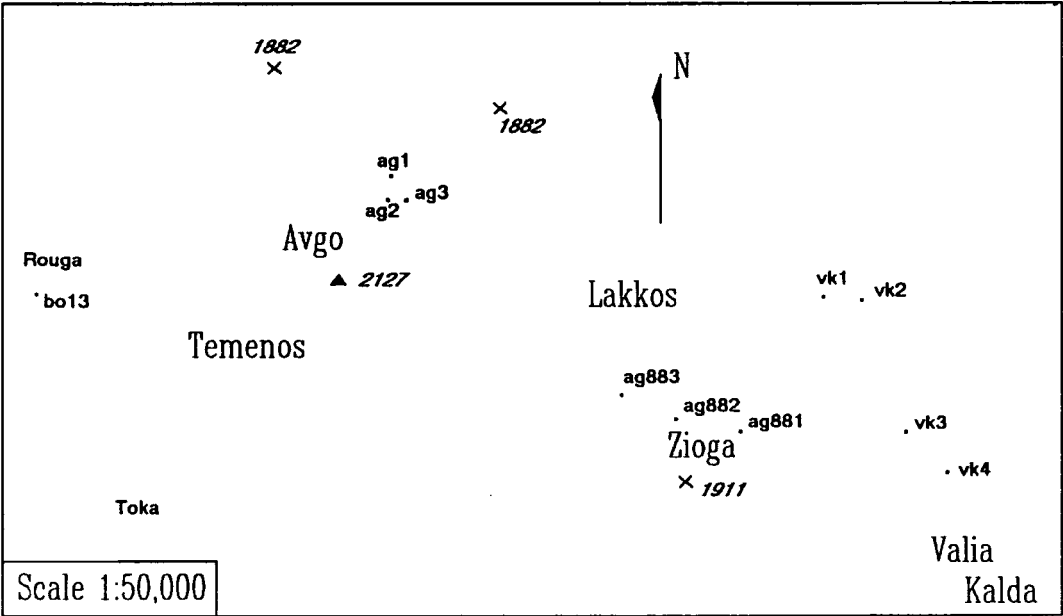
Appendix B. Calculated peridotite compositions

F	SiO$_2$	TiO$_2$	Al$_2$O$_3$	FeO*	MnO	MgO	CaO	Na$_2$O	K$_2$O	NiO	Cr$_2$O$_3$
0%	44.51	0.190	4.06	8.52	0.130	38.30	3.28	0.340	0.030	0.250	0.380
1%	44.48	0.163	3.99	8.52	0.130	38.64	3.19	0.253	0.009	0.253	0.385
2%	44.42	0.140	3.91	8.52	0.130	38.96	3.09	0.186	0.003	0.255	0.389
3%	44.35	0.120	3.82	8.52	0.130	39.28	2.99	0.136	0.001	0.258	0.393
4%	44.28	0.103	3.72	8.51	0.131	39.60	2.90	0.098	tr	0.261	0.397
5%	44.20	0.088	3.62	8.51	0.131	39.92	2.80	0.070		0.263	0.402
6%	44.12	0.075	3.50	8.51	0.131	40.24	2.70	0.050		0.266	0.406
7%	44.03	0.064	3.39	8.51	0.131	40.56	2.60	0.035		0.269	0.410
8%	43.95	0.054	3.26	8.51	0.131	40.89	2.50	0.024		0.271	0.415
9%	43.86	0.046	3.12	8.51	0.131	41.22	2.40	0.017		0.274	0.419
10%	43.77	0.039	2.98	8.51	0.131	41.56	2.30	0.011		0.277	0.423
11%	43.68	0.033	2.83	8.51	0.131	41.90	2.20	0.007		0.280	0.428
12%	43.59	0.028	2.67	8.52	0.132	42.25	2.10	0.005		0.283	0.432
13%	43.50	0.024	2.50	8.52	0.132	42.61	1.99	0.003		0.286	0.436
14%	43.41	0.020	2.31	8.53	0.132	42.97	1.89	0.002		0.289	0.441
15%	43.31	0.017	2.13	8.54	0.132	43.34	1.79	0.001		0.292	0.445
16%	43.21	0.014	1.95	8.55	0.132	43.70	1.69	0.001		0.295	0.450
17%	43.10	0.012	1.76	8.56	0.132	44.07	1.60	tr		0.298	0.454
18%	42.99	0.010	1.58	8.57	0.133	44.44	1.51			0.301	0.459
19%	42.87	0.009	1.40	8.59	0.133	44.81	1.43			0.304	0.463
20%	42.74	0.008	1.23	8.60	0.133	45.18	1.34			0.307	0.468
21%	42.60	0.006	1.06	8.61	0.133	45.55	1.26			0.310	0.472
22%	42.45	0.006	0.90	8.63	0.133	45.91	1.19			0.313	0.477
23%	42.33	0.004	0.73	8.63	0.133	46.27	1.11			0.316	0.481
24%	42.17	0.004	0.64	8.62	0.133	46.60	1.03			0.319	0.485
25%	42.01	0.003	0.56	8.61	0.133	46.92	0.95			0.321	0.489
26%	41.84	0.002	0.49	8.61	0.133	47.23	0.88			0.324	0.493
27%	41.66	0.002	0.43	8.60	0.133	47.54	0.81			0.327	0.496
28%	41.48	0.001	0.37	8.59	0.133	47.85	0.74			0.330	0.500
29%	41.29	0.001	0.32	8.58	0.132	48.16	0.68			0.333	0.504
30%	41.10	0.001	0.28	8.57	0.132	48.46	0.62			0.335	0.507
31%	40.90	0.001	0.24	8.55	0.132	48.76	0.56			0.338	0.511
32%	40.70	0.001	0.20	8.54	0.132	49.06	0.51			0.341	0.514
33%	40.50	tr	0.17	8.53	0.131	49.35	0.46			0.343	0.518
34%	40.29		0.14	8.52	0.131	49.65	0.41			0.346	0.521
35%	40.07		0.12	8.50	0.131	49.94	0.36			0.349	0.524
36%	39.86		0.10	8.49	0.130	50.22	0.32			0.351	0.528
37%	39.63		0.08	8.47	0.130	50.51	0.28			0.354	0.531
38%	39.41		0.07	8.46	0.130	50.80	0.25			0.357	0.534
39%	39.18		0.06	8.44	0.129	51.08	0.21			0.359	0.537
40%	38.95		0.04	8.43	0.129	51.36	0.18			0.362	0.540

Table (B.1) Compositions of residual peridotite (whole rock wt.% recalculated to 100%) calculated using pressure- and temperature dependent equations for major elements distribution coefficients. See Chapter 5 for details. F is the degree of melting. tr = trace.

Appendix C. PGE analytical method

Because of their very low abundances in silicate rocks, determination of the PGE requires special analytical procedures. With the exception of instrumental or radiochemical neutron activation analysis, virtually all methods of PGE analysis include a preconcentration stage (Beamish and Van Loon, 1977, Crocket and Cabri, 1981). Despite the disadvantage of introducing added complexity, a preconcentration step allows the use of a large sample size which, in addition to improving the limit of detection for the PGEs, reduces sampling errors, overcomes inhomogeneity and separates the PGE from a complex silicate or ore matrix concentrating them into a simpler one. The increased reactivity of the PGEs at elevated temperatures, their solubility in molten alkalies and their chalcophilic behaviour makes fusion in the presence of a collector ideal for PGE preconcentration. Although many different procedures have appeared in the literature, the choice of flux and collector have two things in common: to release the PGEs from their matrix and to concentrate them in the collector.

A variety of metals that are closely associated with the PGE in natural assemblages have been used as collectors. These include PbO with Au or Ag, Ni (e.g. Hoffman et al., 1978), Te (Shazali et al. 1988), and Sn (Crocket and Cabri, 1981). The fusion with PbO and Au or Ag as collectors is one of the earliest and best established techniques (e.g. Page et al., 1980, Crocket and Cabri, 1981) but presents several problems, notably that a skilled analyst is required for consistent results. In contrast, collection in NiS, as first examined by Robèrt et al. (1971), offers the advantages of being much simpler and still quantitative for all PGE, Au and Ag. These advantages made it the optimum choice for analysis of the PGE by ICP-MS. The procedure described below in based on the literature as well as test fusions undertaken in the period 1989-1990. A list of the reagents used can be found in Table C.1.

The samples are dried at 110°C for at least 1 hour. The sample, Ni, S and flux are weighed accurately on weighing paper, transferred into the clay crucible and thoroughly mixed with a teflon rod. For silicates the flux:sample ratio is 4:1 and the flux consists of Na_2CO_3 and $Li_2B_4O_7$ in a ratio of 1:2 together with 5 g. of silica, irrespective of the sample mass. For chromitites the flux:sample ratio is increased to 10:1 and the flux consists of

Na_2CO_3, $Li_2B_4O_7$ and NaOH in a ratio 1:2:1 to which 8 g. of silica are added. The mass of the collector is always 2.00 g. of Ni and 1.50 g. of S. The crucibles are placed in the furnace and kept for $1\frac{1}{4}$ hrs at a temperature of 1150°C after which they are removed and left to cool.

After cooling to room temperature the crucibles are broken and the NiS buttons are retrieved. The buttons have a pyrite-yellow colour and are usually shiny on the side that was in contact with the melt. Exceptionally PGE-rich samples (e.g. Pt+) produced buttons with a reddish tint. Buttons from chromitite fusions were pitted where undissolved chromite grains were in contact with them. Sometimes the nickel sulphide buttons had a bluish iridescent surface, reminiscent of the alteration products of copper sulphides. However, no systematic link was found between such buttons and rock type, flux, and fusion conditions. These buttons did not present any dissolution problems.

Some nickel sulphide beads were polished and examined microscopically in reflected light. The buttons took a very good polish and had very few melt inclusions (<1%), even when silicate rocks were fused (compare Wilson et al., 1991). The buttons usually showed exsolution of an unidentified phase (Fe-sulphide?) that was distributed uniformly throughout the button surface. The shape of the exsolution spots was irregular with sizes varying from 1 to 20 μm. Wilson et al. (1991) observed eutectic intergrowths of a Ni-S and a Fe-Ni-S liquid in buttons prepared in a similar way to that described here. Such intergrowths were not observed in this study at a magnification of up to X1000. However, one of the early fusions produced a button with large (50-400 μm) round to ovoid pools of an immiscible liquid (S-poor?). This was probably caused by a deficiency of sulphur that promoted liquid immiscibility.

After retrieval from the cooled crucibles, the buttons are placed in a 100 ml beaker with 50 ml conc. HCl, covered with a watch-glass and heated on a hotplate until all H_2S is released and no effervescence is observed. Sometimes a residue of PGE is visible, but usually the solutions are clear.

While the solutions are still warm 1 ml of a 1000 ppm Te solution is added, which is reduced by the addition of 5 ml of freshly prepared 12.5 wt.% $SnCl_2$ solution. The solutions

are then left near the boiling point for at least 1/2 hr for the Te to coagulate, after which 5 ml of the $SnCl_2$ solution are added again and the solutions are removed from the hotplate.

The PGE and Te are then filtered under vacuum (cellulose nitrate or Whatman 542 filters) and the filter is washed with ~300 ml warm HCl 6M and an equal amount of H_2O. The filter is placed in the original beaker, 3 ml conc. HNO_3 and 1 ml HCl are added and the beaker is heated on the hotplate for at least 20 mins or until the filter and Te are dissolved. If paper filters are used, the solution is filtered again to remove the paper pulp before proceeding. The solution is transferred in the appropriate volumetric flask, the acidity is adjusted as necessary and internal standards are added. The final dilution depends on the expected PGE content of the solution. In order to keep memory effects, non-linear response and wash times to a minimum, the final dilution is adjusted so the concentration of the PGE in solution does not exceed that of the 50 ppb artificial standard. All solutions are spiked with 50 ppb of Nb, In, Re and Tl.

Nickel	carbonyl nickel powder, INCO type 123
Sulphur	sublimed sulphur powder, BDH GPR
Silica	precipitated SiO2 powder, acid washed, BDH GPR
Sodium carbonate	Anhydrous, granular, BDH Analar
Lithium tetraborate	di-lithium tetraborate, Johnson Matthey, Spectroflux
Sodium hydroxide	sodium hydroxide pearl, BDH, Analar
conc. HCl	BDH, Analar
conc. HNO_3	BDH, Analar
Stannous chloride	Tin (II) chloride 2-hydrate, BDH Analar
Te, Ni, Nb, In, Re, Tl solutions	1000 ppm Te standard solution, BDH Spectrosol
Os, Ir, Ru, Rh, Pt, Pd, Au, Ag solutions	1000 ppm AA Specpure standard solutions, Johnson Matthey

Table (C.1) Reagents used for the preconcentration and preparation of solutions.

Artificial standard solutions were prepared from an 1 ppm Os, Ir, Ru, Rh, Pt, Pd, Au, Ag stock solution by dilution to 2, 5, 10, and 50 ppb and spiking with 50 ppb of Nb, In, Re and Tl. Acids were added to each solution to match the acidity of the unknowns.

The operating conditions of the ICP-MS for a typical run can be found in Table C.2.

Samples were run in the following way: The four artificial standards were run first, in order of increasing concentration, to construct the calibration curve, then the acid and reagents blanks, five unknowns, 5ppb artificial standard as drift monitor, acid blank, five unknowns, etc. The data from each sample are transferred to an IBM compatible computer and processed using spreadsheet software.

Collector	4.36	Argon gas flow:	
External	0.60	Coolant	13.5 lt/min
1	5.24	Auxiliary	0.5 lt/min
2	4.50	Nebulizer	0.768 lt/min
3	4.90	Incident power	1320 Watts
4	3.28	Reflected power	3 Watts
P.B.	5.76	Measurement mode	Multichannel
D.A.	1.54	Dwell time	320 ms
F.P.	5.04	No. of sweeps	250
P.F.	4.06	Wash time	~3 mins.

Table (C.2) Typical operating conditions of the ICP-MS during a run.

The following modifications have been made to the fusion technique described by Robèrt et al. (1971).

The size of the collector has been reduced to 2 g. of Ni in order to minimize dissolution times, the amount of acid used and to keep the PGE concentration levels of the reagent blank to a minimum. Asif et al. (1988) showed that recovery of the PGE remains quantitative to 0.5 g. of Ni. It was found, however, that more than 1 g. of Ni was required to consistently produce a good NiS button.

The amount of S used varies with each published method, but it is always more than that needed to produce stoichiometric NiS. The reason is that the lower melting point of S together with its volatile nature leads some losses before it reacts with Ni. Although a large excess of S is undesirable, because it leads to the production of NiS_2 which does not dissolve in HCl, the results of more than 100 fusions indicates that, as long as the Ni/S molar ratio is 0.7-0.9, any excess S is boiled away. This figure however depends on a number of things that cannot be easily controlled, such as crucible size, total mass in the crucible, furnace power, and it is bound to be different between laboratories.

$Na_2B_4O_7$ has been substituted with $Li_2B_4O_7$, since the latter improves dissolution of chromite (Borthick and Naldrett, 1984). Massive chromitites however may still present dissolution problems, even with an increased flux:sample ratio of 10:1. Substitution of half of the $Li_2B_4O_7$ with NaOH, as reported by Parry et al. (1988), improved chromite dissolution, although very finely ground samples were still required for best results.

The amount of silica was not critical in any way for a successful fusion, as far as NiS button production and recoveries are concerned, but its absence may lead to the rapid attack and decomposition of crucibles along pre-existing cracks, resulting in spillages and furnace corrosion.

The NiS button was not crushed in order to avoid losses and contamination. Despite this, dissolution times are not excessive, due to the reduced button size of ~2.5 g., and buttons are usually completely dissolved within 24 hrs.

The taking into solution of the final PGE residue may present some problems. It is assumed that PGE are present in solid-solution or sub-micron scale exsolution in the NiS button. Wilson et al. (1991) investigated the homogeneity of nickel sulphide buttons with respect to PGE using accelerator mass spectrometry. At a spatial resolution of 100 μm they found that the button was homogeneous. Although this is consistent with the presumed mode of distribution of the PGE, a much smaller resolution is needed for conclusive results. It is further assumed that the PGE precipitate as sulphides during the dissolution of the NiS button in HCl. Because of the low pH and low Eh conditions of the HCl solution, the sulphides the PGE sulphides expected are (Burns et al., 1981, Westland, 1981), RuS_2, OsS_2, Ir_2S_3, Rh_2S_3, PdS and PtS. The choice of acid is thus dictated by its ability to attack these PGE sulphides. According to Burns et al. (1981) all of the above sulphides (with the exception of PtS) are soluble in hot HNO_3. Aqua regia can dissolve Rh_2S_3 and PdS, whereas hot conc. HCl can only dissolve PdS. Platinum sulphide is more insoluble. Although PtS_2 is "readily dissolved in aqua regia", PtS is "insoluble in acids and bases" (Burns et al., 1981). Robèrt et al. (1971) and Date et al. (1987) used conc. $HCl+H_2O_2$ for the final dissolution, but both encountered incomplete attack. In test fusions, hot HNO_3 appeared to attack the PGE residue completely but presented two problems. Firstly, all of Os and much of Ru were lost due to their

conversion to volatile tetroxides, and, secondly, it was found that Pd, and possibly Pt, concentrations in the final solution decreased with time to less than 20% within a week. The probable cause of this decrease in concentration with time is that Pd and Pt exist as hydrated oxidized complexes in an HNO_3 medium that are apparently less stable than the corresponding chloride complexes. Aqua regia appears to be the best acid combination to dissolve the PGE residue, effectively attacking the PGE sulphides and providing Cl⁻ ions to stabilize Pd and Pt in solution. The problem of the volatility of Os and Ru is not solved but can be overcome by the use of teflon screw-top beakers in the final dissolution stage.

Although the PGE residue is washed with warm HCl, traces of Ni remain on the filter and carried in the final solution. Its presence can present problems in the determination of the PGE by ICP-MS, by signal suppression and Ni-Ar species overlaps on Ru^{101}. Semi-quantitative determination of Ni showed that its concentration is 1-2 ppm for a 50 ml final volume (cf. Jackson, 1990). Artificial standards without Ni and with matched Ni levels showed the same response for all PGE and internal standards, suggesting that at these levels Ni does not cause any suppression of signal. The overlap of Ni^{61}-Ar on Ru^{101} that Jackson et al. (1990) reported was not observed, as the comparison of Ru isotope ratios in Table C.3 shows. The explanation for the absence of this overlap may be the low concentration of Ni, compared with that of Jackson et al. (op. cit.), although the differences of the VG PQ1 instrument compared to the SCIEX Elan model 250 of Jackson et al. (op. cit.) may play an important role in suppressing Ar species.

	n	Ru^{100}/Ru^{99}	Ru^{101}/Ru^{99}	Ru^{102}/Ru^{99}	Ru^{104}/Ru^{99}
Natural ratio		0.99	1.35	2.49	1.46
Artificial standards	8	1.03	1.42	2.66	1.62
1σ error		0.03	0.06	0.06	0.05
Unknowns	17	1.03	1.40	2.58	1.54
1σ error		0.07	0.09	0.18	0.12

Table (C.3). The ratios of 5 Ru isotopes as determined in 8 artificial standards without Ni and in 17 unknowns with 1-2 ppm of Ni. The natural isotopic ratios are shown for comparison.

Appendix D. Whole-rock chemical analyses (XRF)

XRF analysis was carried out on pressed powder pellets for trace elements and on fused discs for major elements. Loss on ignition was determined gravitometrically by heating ~0.5 g. of pre-dried sample at 700°C for 3 hrs.

Pressed powder pellets were made by mixing 8-10 g. of sample powder with up to 10 drops of a PVA ('Mowiol') binder solution. This was pressed in a hydraulic press at a pressure of the order of1000 kg/cm^{-2} for about 30 sec. to produce a flat disc. The pellets were dried at room temperature and stored in polyethelene bags.

Fused discs were prepared using 0.4500 g. of dried (but not ignited) sample powder, weighed into platinum crucibles. Precisely 5 times as much lanthanum oxide-doped lithium tetraborate/lithium carbonate (Johnson Matthey Spectroflux 105) was added and the two were carefully mixed with a polyethene stirring rod. The dilution of the sample by the flux together with the presence of lanthanum oxide (which acts as a heavy absorber), produces discs of similar composition, thus minimizing matrix effects during analysis. The crucibles were then placed into a preheated electric muffle furnace and fused for 1 hour at 1250°C. The elevated temperature and extended fusion time were found necessary in order to dissolve chromite grains. After this period the crucibles were removed from the furnace and the molten fused beads poured into graphite discs and pressed into shape with an aluminium plunger in a steel collar. The discs were then labelled and stored in polyethelene bags.

All analyses were carried out on a Phillips PW1400 wavelength dispersive X-ray spectrometer, with a rhodium tube, equipped with a PW1500/10 sample changer. The spectromemter was controlled by the dedicated Phillips software package X41. Accelerating potential was 80kV and the electron current was 35mA. Other operating conditions are given in Table D.1.

Analytical runs consisted of up to 120 analyses, 24 of which were calibration standards and the rest of which were run as unknowns. The PW1400 spectrometer corrects for drift by utilizing four internal monitor samples. The spectrums were stored on hard disk and processed offline using the software package ALPHAS (Phillips Analytical). The data

correction used for major elements used influence coefficients (de Jongh, 1973) to correct for interelements effects. For trace elements, the rhodium Compton scatter method was used (Jenkins and de Vries, 1970), by taking the ratioo of the net (peak-background) element intensity to the gross intensity of the rhodium Compton scatter line (Kα).

Table D.2 shows the analysis of two standard geological materials that were included in an analytical run as unknowns.

The abbreviations in Table D.3 are:

Hz	Harzburgite
D	Mantle sequence dunite
Pxnite	Pyroxenite
Pl Hz	Plagioclase Harzburgite (Transition zone)
Pl D	Plagioclase Dunite
Serp	Serpentinite
Cum D	Cumulate Dunite
Troct	Troctolite
Gb	Gabbro
Dol	Dolerite dyke

Element	Crystal	Angle	+bkg	-bkg	Peak time	bkg time
Si	3	109.14	4.80	4.20	40	20
Al	3	145.07	1.40	5.10	40	20
Fe	2	57.580	2.30	2.00	40	20
Mg	6	23.325	2.30	2.40	40	20
Ca	2	113.260	4.30	2.00	40	20
Na	6	28.11	2.92	-	100	40
K	2	136.885	3.00	-	40	20
Ti	2	86.28	5.00	-	40	20
Mn	1	95.415	4.6.	-	40	20
Zr	1	32.155	0.90	-	80	20
Sr	1	35.925	0.90	-	80	20
Cu	1	65.645	1.10	-	80	20
Ni	1	71.355	2.00	-	80	20
V	1	13.335	-	2.00	80	20
Cr	1	107.305	-	2.00	80	20
Sc	1	97.895	2.00	2.00	80	20
Co	1	77.940	2.00	3.50	80	20
Zn	1	60.520	1.20	0.80	80	20

Table (D.1) Analytical conditions for the Phillips PW1400 wavelength dispersive X-ray spectrometer. The X-ray fluorecence line used is the Ka line. Crystals used are: 1 - LiF$_{220}$; 2 - LiF$_{200}$; 3 - PE; 4 - THAP; 5 - Ge; 6 - PX1. Angle refers to the 2θ at which the crystal was set for measurement of the line concerned. Positive and negative background

angular offsets, where used, are given relative to the position of the peak angle. Count times are in seconds.

	PCC-1	Recomended*	NIM-D	Recomended*
SiO_2	41.40	41.67	39.09	38.96
TiO_2	0.008	0.013	0.015	0.020
Al_2O_3	0.83	0.67	0.29	0.30
Fe_2O_{3total}	8.58	8.25	17.38	16.96
MnO	0.116	0.119	0.197	0.220
MgO	42.73	43.43	42.82	43.51
CaO	0.56	0.52	0.30	0.28
Ni	2400	2380		
Cr	2697	2730		
Sc	8.35	8.4		
V	37	31		
Co	118	112		

Table (D.2) Analysis of two standard geological samples that were included as unknowns during an analytical run. Recomended values from Govindaraju (1989).

Appendix D Whole-rock chemical analyses (XRF)

SAMPLE	655	AG1	AG2	AG3	AG881	AG882	AG883	AG885
	Hz	Hz	Hz	Hz	Hz	Hz	Hz	Hz
SiO_2	38.52	41.13	41.87	40.86	39.29	36.19	40.46	39.93
TiO_2	0.01	0.00	0.00	0.01	0.03	0.00	0.01	0.02
Al2O3	0.34	0.78	0.36	0.44	0.31	0.21	0.35	0.25
Fe_2O_2*	7.93	8.29	8.64	8.93	8.66	8.97	8.04	8.99
MnO	0.12	0.11	0.11	0.11	0.12	0.09	0.11	0.13
MgO	42.20	43.89	47.36	45.52	40.02	45.03	42.36	39.05
CaO	0.30	0.57	0.27	0.30	0.44	0.14	0.40	0.19
Na_2O								
K_2O								
L.O.I.	10.75	5.26	1.57	2.05	10.83	8.37	7.08	11.34
Total	100.16	100.04	100.19	98.21	99.69	99.00	98.81	99.89
Mg#	0.914	0.913	0.916	0.910	0.902	0.909	0.913	0.896
Ni	2515	2398	2557	2583	2288	2511	2380	2330
Cr	1803	2573	2317	2915	2435	4914	2475	2546
V	26	31	14	24	34	24	21	25
Sc	1	7	2	3	9		6	7
Co	118	115	122	128	109	134	111	111
Zr								
Sr								
Zn	50	44	42	45	45	51	44	44
Cu	12	14	12	12	14	11	13	12

SAMPLE	BAK1	BO13	BO9	DR10	DR11	DR14	DR19H	DR23
	Hz	Hz	Hz	Hz	Hz	Hz	Hz	Hz
SiO_2	43.03	41.50	41.00	41.29	41.00	37.71	47.95	40.26
TiO_2		0.01	0.02	0.01	0.01		0.02	0.02
Al2O3	1.53	0.61	0.40	0.76	0.57	0.63	0.85	0.16
Fe_2O_2*	8.63	8.56	9.03	7.48	7.82	7.95	7.06	8.40
MnO	0.12	0.12	0.12	0.11	0.11	0.11	0.06	0.11
MgO	46.43	44.58	46.86	38.62	41.08	41.00	37.43	44.76
CaO	0.47	0.51	0.35	1.09	0.86	0.55	0.57	0.28
Na_2O								
K_2O								
L.O.I.	0.07	3.63	2.20	10.10	8.41	11.18	6.44	4.71
Total	100.29	99.51	99.97	99.46	99.86	99.12	100.37	98.69
Mg#	0.914	0.912	0.912	0.911	0.913	0.911	0.913	0.914
Ni	2424	2350	2548	2047	2383	2424	2057	2418
Cr	2534	3499	3128	2763	2575	2398	8633	2405
V	34	43	28	49	40	36	77	25
Sc	9	3		12	10	1	15	4
Co	119	118	128	99	107	114	76	126
Zr								
Sr								
Zn	43	46	45	41	45	46	40	49
Cu	12	13	13	12	17	19	48	13

SAMPLE	DR3	DR31	DR32	DR34	DR36	DR4	DR42	DR44
	Hz	Hz	Hz	Hz	Hz	Hz	Hz	Hz
SiO_2	40.00	39.75	41.11	43.54	39.13	40.74	42.73	43.47
TiO_2	0.01	0.01	0.03	0.01	0.01	0.00	0.00	0.01
Al2O3	0.67	0.83	0.75	0.91	0.44	0.44	0.57	0.41
$Fe_2O_2{}^*$	7.90	7.73	8.38	8.49	9.23	8.14	8.78	8.37
MnO	0.11	0.10	0.12	0.11	0.12	0.12	0.13	0.11
MgO	39.06	40.06	41.55	43.83	46.97	39.61	46.69	46.09
CaO	0.85	0.82	0.75	0.97	0.19	1.31	0.53	0.46
Na_2O								
K_2O								
L.O.I.	10.24	9.61	6.23	1.61	3.86	9.15	0.44	0.20
Total	98.84	98.91	98.91	99.48	99.94	99.52	99.87	99.12
Mg#	0.908	0.911	0.908	0.911	0.910	0.906	0.914	0.916
Ni	2268	2266	2254	2315	2570	2118	2431	2394
Cr	2748	2428	2616	3099	2788	2596	2579	2955
V	42	40	41	37	22	54	30	29
Sc		10	15	10	4	11	1	7
Co	108	109	113	112	132	108	120	117
Zr								
Sr								
Zn	46	38	46	46	53	48	47	44
Cu	13	13	12	12	13	14	11	12

SAMPLE	DR9	KK12	KK24	KK25	KK6	KK7	KK8812	KK8813
	Hz	Hz	Hz	Hz	Hz	Hz	Hz	Hz
SiO_2	39.49		39.56	41.53	42.90	42.53	39.81	40.27
TiO_2	0.00			0.02	0.03	0.01	0.02	0.00
Al2O3	0.76		0.62	0.26	0.97	1.03	1.23	0.83
$Fe_2O_2{}^*$	7.51		7.80	8.42	8.74	8.51	8.05	7.80
MnO	0.11		0.11	0.11	0.13	0.12	0.11	0.10
MgO	40.91		39.61	44.61	43.73	43.30	39.54	40.67
CaO	0.71		0.97	0.34	2.44	1.38	0.88	0.81
Na_2O								
K_2O								
L.O.I.	10.53		10.87	3.89	0.99	2.22	8.78	10.34
Total	100.01		99.54	99.17	99.93	99.09	98.41	100.82
Mg#	0.915		0.910	0.913	0.909	0.910	0.907	0.912
Ni	2328	2221	2253	2330	2301	2277	2258	2232
Cr	2370	2670	2512	2490	2734	2508	2687	3250
V	36	35	38	29	43	42	42	39
Sc	7	10	6	4	13	6	8	4
Co	104	112	109	119	114	112	111	107
Zr								
Sr								
Zn	46		45	47			44	
Cu	14		14	13			14	

Appendix D Whole-rock chemical analyses (XRF)

SAMPLE	KK8820	LI881	LI8811	LI8812	LI8813	LI8816	LI8827H	LI885
	Hz	Hz	Hz	Hz	Hz	Hz	Hz	Hz
SiO_2	39.00	38.80	41.24	41.41	38.45	38.45	38.51	42.54
TiO_2	0.01	0.00	0.02	0.00	0.01	0.01	0.00	0.01
Al2O3	0.60	0.16	0.57	0.54	0.25	0.47	0.22	0.76
Fe_2O_2*	7.99	7.88	7.96	8.05	8.49	8.17	7.89	8.46
MnO	0.11	0.10	0.12	0.11	0.11	0.10	0.10	0.12
MgO	41.12	45.60	43.21	43.89	48.23	44.72	44.82	43.79
CaO	0.73	0.15	0.52	0.41	0.16	0.17	0.24	1.11
Na_2O								
K_2O								
L.O.I.	10.17	7.79	6.31	5.23	3.76	6.74	8.39	3.33
Total	99.73	100.49	99.94	99.64	99.46	98.83	100.17	100.10
Mg#	0.911	0.920	0.915	0.915	0.919	0.916	0.919	0.911
Ni	2359	2668	2427	2466	2326	2654	2393	2266
Cr	2021	2268	2416	2348	2931	2018	2594	2735
V	31	15	32	33	35	16	35	42
Sc	8	2	2	6	4	3	3	4
Co	116	124	110	115	112	122	109	11
Zr								
Sr								
Zn	46	41	45	43	41	45	40	48
Cu	14	13	12	12	13	12	11	12

SAMPLE	LI886	SI13	SI21	SI25	SI27	SI33	SI43	SI46A
	Hz	Hz	Hz	Hz	Hz	Hz	Hz	Hz
SiO_2	42.23	39.80	38.60	39.46	41.34	38.31	39.24	38.18
TiO_2	0.01	0.01	0.01	0.01	0.01	0.01	0.01	0.01
Al2O3	0.73	0.53	0.65	0.71	0.47	0.66	0.73	0.59
Fe_2O_2*	8.42	8.42	7.55	7.96	7.82	7.74	7.80	8.10
MnO	0.12	0.12	0.10	0.12	0.11	0.10	0.11	0.12
MgO	43.29	40.45	39.60	40.91	42.41	39.28	39.81	41.55
CaO	0.83	0.82	0.61	1.08	0.95	0.42	0.96	0.56
Na_2O								
K_2O								
L.O.I.	3.03	9.69	12.01	9.76	6.41	12.23	10.17	10.68
Total	98.65	99.84	99.13	100.00	99.50	98.75	98.83	99.78
Mg#	0.911	0.905	0.912	0.911	0.915	0.910	0.910	0.911
Ni	2304		2335	2298	2344	2400	2288	
Cr	2726		2676	2490	3156	2595	2935	
V	42		34	27	36	40	49	
Sc	11		4	12	12	14	11	
Co	111		108	110	105	107		
Zr								
Sr								
Zn	47	53	45	45	42	41	45	45
Cu	13	13	13	11	12	12	16	12

SAMPLE	DR18	SI31	SI14A	SI15	SI35
	Hz	Hz	Pl Hz	Pl Hz	Serp
SiO_2	42.14	38.46	36.76	38.69	36.73
TiO_2	0.01	0.00	0.03	0.03	0.03
Al2O3	0.52	0.27	1.67	0.81	1.32
$Fe_2O_2{}^*$	8.67	7.61	9.30	8.82	11.13
MnO	0.13	0.10	0.12	0.12	0.12
MgO	44.81	42.78	41.66	39.74	36.26
CaO	0.58	0.24	1.12	0.95	0.02
Na_2O					
K_2O					
L.O.I.	3.09	10.22	9.11	9.60	14.22
Total	99.95	99.69	99.77	98.75	99.84
Mg#	0.911	0.918	0.899	0.899	0.866
Ni	2395	2525			2547
Cr	2346	2193			3236
V	37	11			64
Sc	4	6			11
Co	117	115			151
Zr					
Sr					
Zn	45	42	46	51	62
Cu	13	12	22	13	15

SAMPLE	DR17	KK30	KK32	DR1	DR13	DR16	DR19D	DR20
	Pxnite	Pxnite	Pxnite	D	D	D	D	D
SiO_2	51.30	50.76	51.15	34.81	33.31	34.15	39.91	36.14
TiO_2	0.04	0.05	0.05	0.02	0.02	0.01		
Al2O3	0.97	0.90	0.96	0.12	0.72	0.32	0.14	0.24
$Fe_2O_2{}^*$	5.51	10.45	7.45	8.65	9.45	8.64	8.38	6.75
MnO	0.15	0.23	0.19	0.11	0.10	0.12	0.11	0.09
MgO	24.29	25.48	23.47	42.41	40.60	41.73	45.15	46.00
CaO	16.89	11.54	15.94	0.18	0.25	0.24	0.19	0.09
Na_2O								
K_2O								
L.O.I.	0.66	0.34	0.60	13.05	14.93	13.51	6.05	9.95
Total	99.82	99.75	99.81	99.34	99.39	98.71	99.93	99.26
Mg#	0.897	0.829	0.862	0.907	0.895	0.906	0.914	0.931
Ni	393	256	272	2384	2418	2243	2584	3058
Cr	2520	778	1230	2350	3322	1998	1405	2406
V	98	139	127	19	16	21	16	11
Sc	45	54	62	5			6	2
Co	16	63	26	130	142	126	125	110
Zr								
Sr								
Zn	32	51	41	47	50	46	37	41
Cu	13	13	14	13	47	92	13	11

SAMPLE	DR22	DR26	DR35	DR6	DR8	KK8817	LI8810	LI8815
	D	D	D	D	D	D	D	D
SiO_2	36.58	34.75	34.66	34.95	35.52	34.58	35.60	42.48
TiO_2	0.02	0.01	0.01	0.02	0.04	0.01	0.02	0.01
$Al2O3$	0.24	0.15	1.26	0.17	0.67	0.23	0.26	0.86
Fe_2O_2*	7.98	6.67	8.78	9.44	9.20	9.12	6.49	8.23
MnO	0.09	0.10	0.11	0.13	0.11	0.12	0.11	0.11
MgO	45.56	43.47	42.98	42.78	42.28	41.88	45.07	42.71
CaO	0.02	0.09	0.16	0.12	0.26	0.09	0.13	0.68
Na_2O								
K_2O								
L.O.I.	8.43	14.33	11.59	11.14	11.03	13.72	12.28	4.67
Total	98.91	99.58	99.55	98.77	99.11	99.75	99.96	99.75
Mg#	0.919	0.928	0.907	0.900	0.901	0.901	0.932	0.912
Ni	2701	2806	2497	2129	2260	2326		2858
Cr	3830	899	1767	2260	2987	1497		2418
V	21	2	18	16	21	27		17
Sc	2			2	1	2		
Co	123	114	130	139	128	136		134
Zr								
Sr								
Zn	40	35	50	44	47		37	48
Cu	12	27	184	13	12		16	12

SAMPLE	LI8817	LI882	LI8820	LI8823	LI8824	LI8826	LI8827D	LI883
	D	D	D	D	D	D	D	D
SiO_2	37.54	37.53	37.32	35.59	36.74	36.25	39.31	37.04
TiO_2	0.03	0.01	0.00	0.00	0.01	0.01	0.02	0.01
$Al2O3$	0.27	0.24	0.17	0.06	0.52	0.22	0.18	0.35
Fe_2O_2*	7.64	8.36	9.02	7.05	7.68	7.73	8.33	7.13
MnO	0.10	0.10	0.11	0.12	0.07	0.08	0.12	0.10
MgO	46.90	45.36	45.88	45.19	45.42	44.38	44.18	47.04
CaO	0.13	0.19	0.25	0.07	0.37	0.12	0.36	0.14
Na_2O								
K_2O								
L.O.I.	6.97	6.49	7.28	10.82	8.30	10.04	7.18	4.66
Total	99.59	98.28	100.02	98.88	99.10	98.82	99.67	96.45
Mg#	0.924	0.915	0.910	0.927	0.922	0.919	0.913	0.929
Ni	2823	2727	2695	3215	2756	2759	2669	3055
Cr	2642	2871	2274	726	5878	4496	2576	1892
V	13	21	16	11	28	13	28	11
Sc		1	2		1	4	5	
Co	120	126	142	118	119	120	119	115
Zr								
Sr								
Zn	42	47	50	40	43	40	44	38
Cu	12	11	12	13	12	12	13	12

Appendix D Whole-rock chemical analyses (XRF)

SAMPLE	LI884	KK8816	SI10	SI16	SI16A	SI17	SI18	SI19
	D	Cum D	Cum D	Cum D	Cum D	Cum D	Cum D	Cum D
SiO_2	35.86	35.77	37.34	37.18	39.48	38.87	33.44	34.18
TiO_2	0.02	0.02	0.07	0.06	0.01	0.03	0.01	0.03
Al2O3	0.23	0.59	3.41	3.76	0.83	0.70	0.49	0.31
$Fe_2O_2^*$	7.75	9.93	9.40	9.11	8.07	9.83	9.36	9.05
MnO	0.12	0.10	0.13	0.12	0.12	0.14	0.11	0.12
MgO	45.06	38.57	35.80	36.97	40.20	37.97	41.21	40.84
CaO	0.15	0.12	1.57	0.69	0.60	0.05	0.13	0.11
Na_2O								
K_2O								
L.O.I.	11.51	13.23	11.88	12.38	10.24	12.15	13.99	14.40
Total	100.70	98.33	99.60	100.27	99.56	99.75	98.74	99.05
Mg#	0.920	0.885	0.883	0.890	0.908	0.885	0.897	0.900
Ni	2817	2249	1944		2228			
Cr	1824	2171	2213		2537			
V	14	27	40		42			
Sc	1	4	11		9			
Co	122	145	120		113			
Zr								
Sr								
Zn	45	52			49	53	44	47
Cu	13	14			13	21	15	15

SAMPLE	SI23	SI31A	SI37	SI38	SI40	SI7	SI8	SI9
	Cum D	Cum D	Cum D	Cum D	Cum D	Cum D	Cum D	Cum D
SiO_2	37.21		38.25	38.71	36.34	39.24	39.51	37.27
TiO_2	0.05		0.05	0.02	0.03	0.02	0.01	0.06
Al2O3	1.91		2.47	0.66	3.42	1.02	0.95	3.13
$Fe_2O_2^*$	11.67		8.97	10.00	9.75	7.82	7.51	9.28
MnO	0.12		0.13	0.10	0.12	0.10	0.11	0.12
MgO	35.83		36.22	37.18	36.29	38.34	37.33	38.08
CaO	0.21		0.16	0.42	0.19	0.04	0.04	1.28
Na_2O								
K_2O								
L.O.I.	11.72		12.49	11.53	14.60	12.62	14.58	9.71
Total	98.71		98.73	98.61	100.74	99.20	100.04	98.92
Mg#	0.859		0.889	0.881	0.881	0.907	0.908	0.891
Ni	1709	255	2231	2119	2032	2433	1977	
Cr	3964	657	2626	1980	3374	2711	2569	
V	48	80	51	34	33	41	48	
Sc	12	26	10	11	13	6	6	
Co	148	10	127	132	115	112	122	
Zr								
Sr								
Zn	58		51	47		49	41	
Cu	29		14	15		12	12	

Appendix D Whole-rock chemical analyses (XRF)

SAMPLE	KK887	GM4	KK28	KK8821	SI20	SI39	KK886	KK8811
	Cum D	Pl D	Pl D	Pl D	Pl D	Pl D	Pl D	Pl D dyke
SiO_2	38.21	37.46	35.81	33.91	36.05	42.35	37.19	38.44
TiO_2	0.06	0.04	0.08	0.02	0.02	0.09	0.06	0.05
Al2O3	2.83	2.48	1.39	1.75	2.15	1.17	2.72	3.68
$Fe_2O_2^*$	8.23	9.69	10.09	9.16	10.31	8.09	8.37	8.95
MnO	0.11	0.11	0.13	0.08	0.13	0.15	0.11	0.11
MgO	36.49	36.20	38.73	40.12	39.26	32.25	37.17	36.22
CaO	0.53	0.53	1.32	0.09	1.18	8.77	1.94	3.39
Na_2O								
K_2O								
L.O.I.	12.12	12.08	10.53	12.98	9.92	6.89	10.47	8.31
Total	98.56	98.59	98.07	98.11	99.01	99.75	98.03	99.16
Mg#	0.898	0.881	0.884	0.897	0.883	0.888	0.898	0.889
Ni	1946	1471	1967	2322	1870	1058	1885	1728
Cr	3685	3109	3393	6172	3247	2687	3628	3142
V	53	36	46	43	31	99	57	48
Sc	7	2	8	10	4	29	10	11
Co	112	139	132	127	135	64	107	108
Zr								
Sr								
Zn	46	43	53	49	54	40	48	48
Cu	16	12	29	20	23	32	17	14

SAMPLE	KK16	KK18	KK20	KK33	KK36	KK19	KK46	SI41
	Wehrlite	Wehrlite	Wehrlite	Wehrlite	Wehrlite	Troct	Troct	Troct
SiO_2	40.94	40.80	40.10	37.84	41.40	41.00	38.27	37.96
TiO_2	0.10	0.05	0.07	0.07	0.04	0.07	0.04	0.07
Al2O3	2.40	3.03	9.03	6.56	1.01	13.94	7.23	6.02
$Fe_2O_2^*$	8.19	8.19	7.65	9.64	7.33	5.08	10.68	9.22
MnO	0.12	0.14	0.12	0.13	0.11	0.08	0.15	0.14
MgO	32.19	32.49	29.76	32.61	37.92	21.66	31.08	31.49
CaO	5.22	6.12	5.53	4.00	1.22	10.83	3.85	5.08
Na_2O			0.47			0.74		
K_2O								
L.O.I.	9.97	8.94	7.05	7.62	9.67	6.50	8.65	9.63
Total	99.13	99.77	99.79	98.46	98.70	99.91	99.95	99.61
Mg#	0.886	0.887	0.885	0.870	0.911	0.894	0.852	0.872
Ni	1015	1138	1233	1384	2083	845	1155	1111
Cr	1876	3984	2025	1976	3117	1022	1786	1435
V	62	79	42	33	64	45	27	53
Sc	19	22	14	7	15	15	4	22
Co	92	72	70	111	95	30	106	91
Zr				6	2	10	2	2
Sr				42	5	100	13	6
Zn	45	43	51	50	42	32	57	48
Cu	21	30	21	26	19	18	27	39

SAMPLE	SI6	GM5	KK1	KK15	KK21	KK50	KK8810	SI11
	Troct	Gb	Gb	Gb	Gb	Gb	Gb	Gb
SiO_2	38.63	39.61	49.05	43.35	43.22	46.40	47.32	44.57
TiO_2	0.13	0.04	0.41	0.09	0.06	0.15	0.28	0.05
Al2O3	5.13	16.41	15.61	12.71	21.19	24.75	15.06	25.03
$Fe_2O_2^*$	9.20	4.77	7.29	4.25	3.73	3.53	5.83	2.11
MnO	0.12	0.07	0.16	0.10	0.07	0.07	0.13	0.04
MgO	34.34	19.90	10.05	19.00	13.86	6.58	12.64	4.66
CaO	2.30	12.34	12.81	15.96	13.28	15.37	15.89	18.80
Na_2O		0.55	2.38	0.57	1.05	1.42	1.10	0.86
K_2O		0.01	0.21		0.01			0.16
L.O.I.	8.35	5.72	1.16	3.44	3.11	1.10	0.92	3.27
Total	98.20	99.41	99.12	99.46	99.59	99.37	99.17	99.55
Mg#	0.881	0.892	0.732	0.899	0.881	0.787	0.812	0.814
Ni	1671	851	162	446	383	201	223	117
Cr	2585	797	374	1986	324	435	726	134
V	64	25	173	73	28	56	125	28
Sc	17	19	36	35	24	24	47	28
Co	110	26	17	11	10		10	
Zr	4	7	19	8	9	11	15	22
Sr	6	81	93	80	95	80	57	263
Zn	54	32	46	21	24	30	35	13
Cu	15	13	28	13	29	21	29	16

SAMPLE	SI3	SI36	SI5	DR15	SI42B	KK23	SI32	SI4
	Gb	Gb	Gb	Gb dyke	Gb dyke	Dol	Dol	Dol
SiO_2	45.85	43.84	42.98	44.20	46.01	43.02	44.65	49.74
TiO_2	0.24	0.14	0.17	0.05	0.16	0.62	0.10	0.19
Al2O3	17.25	18.94	14.76	16.63	18.12	16.49	15.01	10.94
$Fe_2O_2^*$	5.99	6.03	8.18	6.71	4.04	11.90	3.83	10.57
MnO	0.13	0.11	0.14	0.14	0.08	0.17	0.07	0.17
MgO	12.45	14.24	18.83	13.44	12.31	6.39	16.55	15.65
CaO	15.41	13.62	11.00	14.21	16.17	18.65	15.09	7.51
Na_2O	1.03	0.94	0.89	1.48	1.09		0.80	1.33
K_2O		0.01			0.01			0.29
L.O.I.	1.05	1.79	2.53	2.83	1.07	2.67	3.00	2.64
Total	99.40	99.66	99.48	99.69	99.04	99.91	99.10	99.02
Mg#	0.805	0.824	0.820	0.799	0.858	0.516	0.896	0.746
Ni	247	364	400	342	319	82	353	208
Cr	733	470	518	372	992	78	695	800
V	118	64	83	131	79	306	86	231
Sc	34	25	28	42	35	41	39	36
Co	15	23	47	21		28	1	46
Zr	3	10	12	26	21	45	16	14
Sr	43	71	65	336	206	106	187	53
Zn	37	39	43	41	25	57	20	68
Cu	37	31	29	12	23	14	11	41

Table (D.3) Major and trace element composition of Pindos ultramafic and mafic rocks.

Appendix E. Microprobe analyses

Mineral analyses were obtained using a modified Cambridge Instruments Geoscan microprobe, fitted with a Link 860 energy-dispersive detector system centred on a silicon solid-state detector. The microprobe was operated at a beam current of 5nA with an accelerating voltage of 15kV, and used Lidoped Sidetectors, maintained at the temperature of liquid nitrogen to reduce electronic noise. A 'livetime' of 100 sec (corresponding to ~120 sec real-time) was used for each analysis. Processing was carried out using a Link Systems AN 10/56AS unit. Spectra of the standards are held on hard disc in the on-line computer. These are compared with the unknown spectra, calibrated using a cobalt metal standard for the calculation of element concentrations. The Co analysis thus corrects for any longterm drift, acting as a 'monitor' sample. In addition, the Co calibration was monitored with natural olivine, jadeite, and wollastonite standards during each analytical run. The analyses were performed on standard, carbon-coated, polished thin sections. Si, Ti, Al, Mg, Fe, Ca, Na, K, Mn, Ni and Cr were all analysed simultaneously, using the $K\alpha$ peak in all cases (Fe $L\alpha$ was also measured but only for correction purposes). ZAF corrections were applied using Link-supplied software that uses a procedure based on the TIM1 program of Duncumb and Jones (1969). The atomic number correction described by Duncumb and Reed (1968) is used, together with Reed's (1965) fluorescence correction. The absorbtion effects are calculated using Philibert's (1963) equation, using Heinrich's (1967) absorbtion coefficients, and bulk mass absorbtion coefficients as calculated by Yakowitz et al. (1973).

In the following tables the first column identifies the mineral that was probed. The first 3-6 digits are the sample name, followed by a two digit mineral identifier (i.e. OL, OX, CX, or SP), followed by a serial analysis number. C and R refer to core and rim of a grain respectively and may be followed by a number if more than one places were probed. A and B refer to different analyses of the same grain.

	SiO$_2$	Cr$_2$O$_3$	FeO*	MnO	MgO	NiO	Total
ag2OL8C	41.1	0.14	8.3	0.04	48.4	0.42	98.35
ag2OL8R	41.7	n.d.	8.5	0.08	49.4	0.42	100.14
ag2OL9	41.8	0.02	8.9	n.d.	48.1	0.24	99.00
ag2OL10	43.2	0.05	8.0	0.12	46.9	0.55	98.88
ag2OL11	41.3	0.03	8.6	0.05	48.9	0.37	99.21
ag2OL12	41.5	n.d.	8.5	0.03	49.3	0.16	99.49
ag3OL6	41.5	0.20	9.0	0.14	49.1	0.50	100.44
ag3OL7C	41.8	n.d.	8.6	0.19	49.1	0.54	100.19
ag3OL7R	41.6	n.d.	9.0	0.16	49.7	0.46	100.92
ag3OL8C	41.8	0.05	8.8	0.09	48.8	0.42	100.05
ag3OL9	41.8	0.18	9.0	0.22	49.0	0.33	100.57
ag3OL10	40.9	n.d.	9.0	0.10	47.9	0.46	98.43
ag3OL11	41.6	0.04	8.8	0.19	48.8	0.36	99.75
ag3OL12	41.5	n.d.	9.1	0.07	48.9	0.30	99.87
ag3OL13	42.2	n.d.	8.7	0.27	48.3	0.45	99.86
ag883OL1	41.2	n.d.	8.3	0.14	50.4	0.36	100.36
bak1OL1	41.3	0.07	8.4	0.12	48.1	0.27	98.27
bak1OL1B	41.5	0.04	8.8	n.d.	48.5	0.54	99.36
bak1OL1R	43.3	0.26	8.2	0.07	47.1	0.16	99.04
bak1OL2	41.5	n.d.	8.9	0.17	48.5	0.32	99.35
bak1OL2B	41.2	0.04	8.5	0.17	47.9	0.59	98.46
bak1OL3	41.1	n.d.	8.3	0.07	48.5	0.38	98.36
bak1OL3R	43.4	0.01	8.1	0.24	47.5	0.28	99.52
bak1OL4C	41.3	0.02	7.8	0.06	48.7	0.57	98.45
bak1OL4R	41.8	0.06	8.2	0.15	49.7	0.48	100.27
bak1OL5C	41.8	0.03	8.9	0.08	48.7	0.38	99.84
bak1OL5R	41.4	n.d.	8.7	0.14	48.6	0.57	99.45
bak1OL6	41.7	0.09	8.1	0.20	49.7	0.40	100.25
bo13OL1	41.3	0.03	8.9	0.18	48.5	0.50	99.43
bo13OL2	42.0	0.01	9.1	0.07	48.2	0.22	99.55
bo13OL3	40.8	0.04	8.9	0.11	48.8	0.54	99.17
bo13OL4	40.9	0.10	8.8	0.18	48.0	0.52	98.44
bo13OL5	40.9	0.06	8.9	0.10	47.8	0.45	98.17
bo14OL1	41.2	n.d.	8.4	0.04	48.6	0.43	98.58
bo14OL2	41.4	n.d.	8.4	0.06	48.2	0.44	98.52
bo14OL3	42.1	n.d.	8.8	0.06	48.8	0.17	99.98
bo14OL4	42.1	0.01	8.4	0.27	48.5	0.25	99.56
bo18OL5	41.9	0.03	9.1	0.19	47.0	0.48	98.70
bo18OL7	41.4	n.d.	9.7	0.23	47.8	0.35	99.45
bo18OL8	41.4	n.d.	9.0	0.19	47.7	0.55	98.80
bo22OL6	41.1	n.d.	10.3	0.03	47.6	0.54	99.50
bo22OL7	41.4	n.d.	10.0	0.28	47.1	0.50	99.28
bo22OL8	40.9	n.d.	10.0	0.17	47.0	0.12	98.16
bo22OL9	41.3	0.09	9.8	0.14	47.7	0.41	99.38
bo6OL5	40.8	0.05	9.2	0.22	47.5	0.54	98.37
bo6OL6	41.5	n.d.	9.7	0.06	48.4	0.29	99.96
bo6OL7	41.3	0.13	9.7	0.05	48.3	0.59	100.19
bo6OL8	41.0	0.04	9.5	0.18	47.6	0.27	98.52
cmt730OL2	42.0	n.d.	7.9	0.16	50.0	0.55	100.66
cmt730OL3	41.8	n.d.	7.4	0.07	49.5	0.39	99.23
cmt730OL4	41.9	0.02	7.5	0.24	50.0	0.50	100.18
cmt730OL5	42.3	n.d.	7.8	0.06	50.0	0.51	100.67
dr11OL6	42.1	0.01	8.9	0.16	49.0	0.47	100.56
dr11OL7	41.8	n.d.	8.5	0.24	49.0	0.37	99.87

	SiO$_2$	Cr$_2$O$_3$	FeO*	MnO	MgO	NiO	Total
dr16OL1	41.3	0.25	9.5	0.10	48.5	0.47	100.11
dr16OL2	41.4	n.d.	8.5	0.20	48.0	0.05	98.09
dr16OL3	42.2	0.07	8.8	0.09	49.3	0.09	100.50
dr16OL4	41.5	0.01	9.2	0.23	48.1	0.30	99.35
dr16OL5	41.7	n.d.	9.1	0.36	49.2	0.31	100.71
dr16OL6	41.0	0.04	9.0	0.24	47.7	0.42	98.43
dr20OL1	42.1	0.10	6.9	n.d.	49.9	0.15	99.14
dr20OL2	41.6	0.17	6.6	0.16	50.0	0.42	98.91
dr20OL3	41.9	0.10	7.0	0.06	50.1	0.50	99.65
dr20OL4	41.5	0.00	7.0	0.23	49.5	0.46	98.72
dr22OL4	41.0	0.17	7.7	n.d.	48.8	0.33	98.01
dr22OL5	41.2	0.53	7.8	0.16	48.8	0.07	98.52
dr22OL6C	41.3	0.03	7.7	0.13	48.5	0.46	98.10
dr22OL6R	41.9	n.d.	8.1	0.12	48.9	0.26	99.28
dr22OL7	41.3	0.15	8.1	0.02	49.5	0.69	99.76
dr23OL10	41.3	0.03	8.5	0.17	48.3	0.44	98.70
dr23OL7	41.2	0.14	8.7	0.18	48.0	0.38	98.64
dr23OL8	41.1	0.06	8.2	0.27	48.6	0.46	98.69
dr23OL9	41.7	n.d.	9.1	0.14	48.5	0.53	99.99
dr23OL1	41.7	0.67	7.8	0.14	49.8	0.41	100.60
dr23OL2	41.6	n.d.	8.6	0.15	48.8	0.30	99.45
dr23OL3	41.8	n.d.	8.3	0.13	48.9	0.43	99.54
dr23OL9	41.0	n.d.	8.0	0.13	48.8	0.72	98.71
dr23OL10	41.2	n.d.	7.9	0.28	49.1	0.46	98.98
dr3OL7	42.0	n.d.	9.2	0.39	49.2	0.58	101.33
dr3OL8	41.6	n.d.	8.7	0.16	48.9	0.49	99.90
dr34OL6	41.3	0.13	9.3	0.21	48.0	0.45	99.40
dr34OL7	40.8	0.01	9.4	0.13	47.7	0.41	98.44
dr42OL1	41.8	0.05	9.1	0.13	48.4	0.46	99.99
dr42OL2	41.4	n.d.	9.5	0.11	47.9	0.24	99.11
dr42OL3	41.1	n.d.	8.8	0.14	47.9	0.42	98.44
dr42OL4	41.9	0.08	8.7	0.19	48.0	0.58	99.48
dr42OL5	41.2	n.d.	9.0	0.15	47.9	0.21	98.46
dr6OL5	40.7	0.07	9.6	0.18	47.4	0.27	98.26
dr6OL6	41.1	n.d.	9.6	0.09	47.3	0.06	98.10
dr9OL1	41.7	0.02	7.9	0.01	48.4	0.39	98.37
dr9OL2	41.6	0.05	8.1	0.09	48.5	0.22	98.51
dr9OL3	42.2	n.d.	8.2	0.18	49.1	0.16	99.88
dr9OL4	41.4	n.d.	7.9	0.23	48.8	0.42	98.71
dr9OL5	41.2	0.03	8.0	0.16	48.5	0.54	98.37
kk28OL11	40.5	0.05	11.5	0.22	46.0	0.30	98.53
kk28OL12	40.4	n.d.	11.2	0.38	45.9	0.36	98.29
kk28OL13	40.3	n.d.	11.1	0.23	46.0	0.44	98.02
kk7OL1	41.7	0.02	8.7	0.14	48.4	0.32	99.30
kk7OL2	41.2	n.d.	8.6	0.29	48.6	0.51	99.23
kk7OL3	41.8	0.11	8.6	0.15	47.9	0.42	98.98
kk8812OL1	41.1	n.d.	9.2	0.18	48.3	0.60	99.43
kk8812OL2	41.5	n.d.	9.2	0.05	48.4	0.23	99.29
kk8812OL3	41.3	n.d.	8.8	0.20	48.2	0.24	98.66
kk8812OL5	41.4	0.09	8.8	0.15	48.2	0.50	99.23
kk8813OL5	41.3	n.d.	8.6	0.18	48.6	0.31	99.00
kk8813OL6	41.7	n.d.	8.8	0.13	49.2	0.37	100.19
kk8813OL7	41.4	n.d.	8.8	0.11	49.1	0.40	99.80
kk8813OL8	41.4	0.02	8.4	0.15	48.4	0.04	98.50

	SiO_2	Cr_2O_3	FeO*	MnO	MgO	NiO	Total
kk8819OL8	40.8	n.d.	9.2	0.32	48.1	0.25	98.72
kk8819OL9	41.0	n.d.	9.1	0.30	47.5	0.15	98.06
kk8819OL10	41.0	n.d.	9.4	0.17	47.5	0.32	98.45
kk8829OL1	41.3	n.d.	8.9	0.10	47.9	0.53	98.68
kk8829OL2	41.5	n.d.	8.7	0.23	48.7	0.48	99.72
kk8829OL2B	41.6	n.d.	9.0	0.13	49.0	0.58	100.24
kk8829OL3	41.1	n.d.	9.1	0.14	48.4	0.46	99.13
kk8829OL4C	41.4	0.00	8.7	0.21	48.3	0.12	98.76
kk8829OL4R	41.3	n.d.	9.1	0.31	48.5	0.41	99.64
kk8824OL1	41.6	0.04	7.7	0.31	48.8	0.50	98.98
li8811OL1	41.2	0.07	8.5	0.18	48.5	0.40	98.82
li8811OL4	41.5	0.09	8.5	0.23	48.9	0.40	99.65
li8811OL6	41.5	0.02	8.6	0.15	48.4	0.41	99.10
li8816OL6	41.3	n.d.	8.2	0.18	48.3	0.47	98.46
li8816OL7	41.8	0.00	8.2	0.13	48.9	0.35	99.41
li8819OL1C	41.5	n.d.	8.7	0.09	48.9	0.58	99.77
li8819OL1R	40.6	0.08	8.9	0.24	48.0	0.42	98.12
li8819OL2	42.1	0.18	8.1	0.25	49.0	0.34	99.94
li8819OL3	41.2	0.02	9.1	0.06	48.5	0.56	99.41
li8821OL1	41.0	n.d.	8.3	0.21	48.4	0.54	98.48
li8821OL2	40.9	n.d.	8.6	0.20	48.2	0.33	98.17
li8821OL3	41.3	0.08	8.5	0.22	48.6	0.37	99.07
li8821OL4	42.0	0.06	8.2	0.18	49.2	0.39	99.96
li8824OL1	41.2	0.02	7.3	0.20	49.5	0.50	98.75
li8824OL2	41.5	0.04	7.1	0.25	49.3	0.30	98.54
li8824OL3	41.3	0.03	6.9	0.14	49.4	0.32	98.17
li8824OL4	41.5	0.03	7.2	0.20	49.9	0.43	99.22
li8824OL5	41.3	0.02	7.4	0.07	49.1	0.29	98.20
li8824OL6	41.8	0.01	7.3	0.30	50.0	0.50	99.85
li8824OL7	41.9	0.00	7.4	0.27	49.6	0.31	99.41
li8824OL8	41.4	0.01	7.0	0.16	49.6	0.53	98.73
li8824OL9	41.8	0.09	7.4	0.21	49.6	0.44	99.50
li8824OL10	41.5	n.d.	6.8	0.15	49.4	0.39	98.21
li8824OL11	41.3	0.04	6.9	0.29	49.8	0.24	98.58
li8824OL12	41.6	n.d.	7.4	0.20	49.4	0.23	98.88
li8824OL12A	41.9	0.04	7.3	0.11	49.5	0.48	99.35
li8824OL13C	41.4	0.09	7.0	0.19	49.0	0.51	98.24
li8824OL13R	41.4	0.04	7.2	0.14	49.7	0.42	98.92
li8826OL1	41.6	0.02	8.2	0.01	49.4	0.52	99.70
li8826OL2	41.2	n.d.	7.9	0.01	48.9	0.51	98.53
li8826OL3	41.5	n.d.	8.0	0.05	49.9	0.47	99.92
li8826OL4	41.4	0.10	7.9	0.01	48.8	0.38	98.48
li8826OL5	41.3	0.10	7.9	0.12	48.5	0.20	98.06
si43OL4	41.4	n.d.	9.0	0.18	48.3	0.46	99.23
si43OL5	40.9	0.04	8.8	0.36	47.9	0.40	98.38
si45OL14	41.5	0.06	9.0	0.15	48.3	0.49	99.53
si45OL15	40.7	0.02	8.9	0.05	48.2	0.29	98.10
si45OL16	40.9	0.10	9.2	0.05	47.9	0.34	98.48

Table (E.1) Olivine analyses.

Appendix E Microprobe analyses

	SiO_2	TiO_2	Al_2O_3	Cr_2O_3	FeO^*	MnO	MgO	CaO	NiO	Total
ag2OX1	57.2	n.d.	0.58	0.19	5.56	0.18	33.8	0.50	0.05	98.07
ag2OX2	58.0	0.06	0.85	0.34	5.53	0.25	33.5	1.26	n.d.	99.75
ag2OX3	58.0	0.04	0.75	0.46	5.49	0.18	33.7	1.21	0.03	99.94
ag3OX1C	58.0	0.04	0.86	0.51	5.66	0.09	33.0	1.40	n.d.	99.51
ag3OX1R	58.2	0.01	0.97	0.38	5.69	0.13	33.9	0.92	0.14	100.35
ag3OX2C	57.9	n.d.	0.97	0.47	5.68	0.21	33.8	1.08	0.25	100.37
ag3OX2R	58.4	0.10	0.94	0.55	5.77	0.10	33.9	1.01	0.35	101.08
ag3OX3C	57.6	0.06	0.71	0.55	5.53	0.03	33.2	1.45	0.15	99.31
ag3OX3R	57.6	0.08	0.45	0.45	5.47	n.d.	33.5	0.75	0.28	98.58
ag3OX4C	58.3	n.d.	0.98	0.40	5.78	0.11	33.9	1.17	0.22	100.79
ag3OX4R	57.6	0.06	0.66	0.29	5.80	0.09	33.7	0.83	0.20	99.29
ag3OX4B	55.5	0.03	1.19	0.44	5.93	0.19	34.3	1.12	0.20	98.98
ag883OX1C	58.3	n.d.	1.28	0.41	5.63	0.17	35.0	0.77	0.21	101.72
ag883OX1R1	57.0	0.01	1.58	0.44	5.72	0.25	34.3	0.74	n.d.	99.97
ag883OX1R2	58.5	n.d.	1.32	0.52	4.90	0.08	33.2	0.68	0.15	99.38
ag883OX2	53.5	0.01	0.86	0.13	6.38	0.35	38.8	0.49	0.42	100.89
ag883OX3R	55.6	n.d.	1.01	0.26	6.16	0.11	34.0	0.92	n.d.	98.10
ag883OX3C	57.8	0.09	0.94	0.35	5.42	0.17	34.6	1.07	0.03	100.49
ag883OX4	58.6	0.08	0.94	0.40	5.37	0.05	35.7	0.66	n.d.	101.82
bak1OX1	56.3	0.07	1.86	0.61	5.39	0.17	32.8	1.09	n.d.	98.28
bak1OX1R	56.4	0.04	1.83	0.54	5.80	0.16	32.7	0.69	0.08	98.27
bak1OX1C	57.1	n.d.	1.52	0.25	5.57	0.18	33.7	0.48	0.02	98.90
bak1OX2	57.2	0.04	1.91	0.60	5.55	0.19	32.9	1.29	0.18	99.81
bak1OX2R	57.4	n.d.	1.95	0.55	5.43	0.19	33.5	0.79	0.02	99.87
bak1OX2R2	57.3	0.00	2.04	0.77	5.48	0.21	33.1	0.91	0.03	99.79
bo13OX1	57.1	0.10	0.70	0.51	5.69	0.13	32.8	1.20	0.26	98.49
bo13OX2	57.0	0.03	0.75	0.37	5.62	0.26	32.7	1.11	0.23	98.06
bo13OX3	57.4	0.05	0.82	0.46	6.02	0.11	33.2	1.04	0.33	99.37
bo13OX4	57.5	0.02	0.88	0.39	5.78	0.21	32.8	1.08	0.01	98.65
bo18OX2C	55.8	0.09	4.02	0.65	6.26	0.11	32.4	0.93	0.17	100.42
bo18OX3C	55.4	0.12	3.61	0.49	6.30	0.24	32.2	0.88	0.13	99.33
bo18OX3R	55.4	n.d.	3.34	0.36	5.90	0.31	32.1	0.62	0.14	98.12
bo18OX4C	56.5	0.07	3.11	0.37	6.26	0.31	32.7	0.66	0.02	100.01
bo18OX4R	56.0	n.d.	2.99	0.30	6.31	0.19	32.9	0.68	0.00	99.39
bo18OX5	56.8	n.d.	3.37	0.60	6.50	0.18	33.1	0.59	0.10	101.17
bo18OX7	55.8	0.04	3.80	0.79	6.31	0.05	32.2	0.60	0.06	99.67
bo22OX5	53.5	0.10	3.88	0.59	6.58	0.01	31.4	3.20	0.14	99.41
bo22OX6	54.7	0.18	3.76	0.55	6.44	0.22	31.2	1.20	0.09	98.27
bo22OX7	55.0	0.06	3.50	0.56	6.98	0.08	31.9	0.74	0.03	98.90
bo22OX8	54.3	n.d.	3.81	0.73	5.96	0.31	29.5	4.12	0.18	98.89
bo22OX9	54.9	0.08	3.43	0.48	6.21	0.23	31.9	0.63	0.24	98.07
bo6OX4	55.5	0.08	3.04	0.53	6.38	0.28	32.4	0.47	0.04	98.68
bo6OX5	55.6	0.03	4.07	0.86	6.02	0.11	31.8	1.30	0.00	99.84
bo6OX6	54.9	0.18	4.15	0.65	6.23	0.17	30.8	1.41	0.16	98.61
bo6OX6	56.1	n.d.	3.86	0.51	6.17	0.17	31.5	1.62	n.d.	99.85
bo6OX7	55.3	0.10	3.28	0.53	6.24	0.08	31.9	1.38	0.16	98.95
bo6OX8	55.5	0.12	3.69	0.80	6.21	0.22	32.2	0.59	n.d.	99.27
bo6OX9	55.6	0.10	3.31	0.64	6.26	0.17	31.7	0.92	0.22	98.94
dr11OX5	56.8	n.d.	1.93	0.35	5.89	0.28	32.8	1.17	n.d.	99.26
dr11OX6	56.8	0.04	2.05	0.62	5.86	0.26	32.9	1.49	0.04	100.04
dr11OX7	56.8	n.d.	1.32	0.59	5.62	0.07	33.1	0.87	0.14	98.55
dr17OX8	56.2	0.00	0.85	0.39	8.67	0.22	30.8	1.37	0.05	98.58
dr17OX9	56.2	n.d.	1.09	0.30	9.98	0.16	30.0	1.59	0.15	99.46

	SiO_2	TiO_2	Al_2O_3	Cr_2O_3	FeO*	MnO	MgO	CaO	NiO	Total
dr23OX2	56.7	n.d.	1.26	0.62	5.44	0.18	32.9	0.98	n.d.	98.05
dr23OX3	57.0	n.d.	1.48	0.71	5.68	0.06	33.0	1.25	0.27	99.46
dr23OX4	57.2	n.d.	1.66	0.46	5.73	0.12	33.0	1.03	n.d.	99.17
dr23OX1	56.0	0.03	1.20	0.40	5.98	0.16	34.2	0.64	0.20	98.80
dr23OX2	57.6	0.04	1.56	0.63	5.61	0.09	32.8	1.29	0.06	99.67
dr23OX2B	56.7	0.04	1.59	0.65	5.40	0.13	33.3	0.86	0.02	98.69
dr23OX3	56.4	n.d.	1.49	0.73	5.31	0.12	33.0	1.03	0.14	98.16
dr23OX10	56.9	n.d.	1.58	0.40	5.45	0.06	33.4	0.75	0.21	98.75
dr3OX1	56.6	n.d.	1.50	0.49	5.81	0.23	32.9	1.05	0.05	98.55
dr3OX2	55.3	0.09	1.33	0.54	6.39	0.20	33.5	2.26	0.06	99.70
dr3OX3	57.6	n.d.	1.50	0.38	5.99	0.10	33.7	0.62	n.d.	99.90
dr3OX4	57.1	n.d.	1.85	0.59	5.89	0.29	33.4	0.60	n.d.	99.69
dr3OX5	57.2	n.d.	1.77	0.51	5.89	0.15	33.4	0.67	0.19	99.77
dr34OX5	56.3	0.05	1.71	0.92	6.02	0.17	32.6	0.89	0.14	98.78
dr34OX6	56.7	n.d.	1.29	0.38	6.37	0.07	33.0	1.16	0.22	99.15
dr34OX7	56.9	n.d.	1.45	0.51	6.13	0.30	33.4	0.50	0.03	99.20
dr42OX1C	57.2	n.d.	1.52	0.55	5.74	0.16	33.7	0.92	0.19	99.95
dr42OX1R	57.1	0.07	1.44	0.72	5.43	0.10	32.6	1.10	0.34	98.86
dr42OX2	56.8	0.09	1.63	0.64	5.72	0.24	32.9	0.97	0.01	98.98
dr42OX3	57.3	0.05	1.71	0.56	6.13	0.19	33.0	1.15	0.06	100.16
dr42OX4	56.4	0.12	1.54	0.62	5.56	0.25	32.5	0.99	0.10	98.13
dr9OX1	56.5	n.d.	2.01	0.31	5.74	0.17	33.5	0.67	n.d.	98.85
dr9OX2	56.0	0.01	1.98	0.60	5.68	0.21	32.8	1.04	0.08	98.48
dr9OX3	56.5	0.04	2.80	0.98	5.41	0.04	32.0	2.36	n.d.	100.12
dr9OX4	57.2	0.10	2.26	0.66	5.09	0.30	32.8	1.50	0.11	99.98
kk30OX5	55.1	n.d.	1.19	0.02	12.28	0.30	26.6	2.77	0.07	98.28
kk30OX6	55.3	0.07	1.00	0.17	12.77	0.35	28.3	1.04	n.d.	99.07
kk7OX1	56.7	0.02	2.86	0.70	5.76	0.17	32.8	0.82	0.15	99.98
kk8812OX1	57.7	0.03	1.73	0.56	5.86	0.11	33.3	0.90	n.d.	100.20
kk8812OX2	57.1	0.01	2.02	0.79	5.71	0.16	32.5	2.17	0.05	100.47
kk8812OX3	57.3	0.03	1.43	0.57	6.01	0.17	33.0	0.87	n.d.	99.40
kk8812OX7C	56.1	0.07	1.56	0.75	5.57	0.06	32.1	1.96	0.12	98.25
kk8812OX7R	56.4	0.16	1.74	0.74	5.61	0.10	32.1	1.79	0.08	98.68
kk8812OX8	56.7	0.01	1.80	0.63	5.64	0.22	33.0	1.23	0.01	99.28
kk8812OX9	55.8	0.01	2.05	0.88	5.74	0.08	32.4	1.24	n.d.	98.29
kk8813OX7	57.6	0.03	2.56	0.61	5.68	0.18	33.0	1.43	n.d.	101.13
kk8813OX8	56.8	n.d.	2.28	0.76	5.35	0.13	32.0	2.72	0.17	100.23
kk8813OX5	57.4	0.03	2.06	0.56	5.77	n.d.	33.3	0.85	0.30	100.34
kk8813OX6	57.1	0.02	2.25	0.72	5.76	0.09	33.0	0.88	n.d.	99.86
kk8813OX6	56.7	0.11	1.66	0.41	5.88	0.14	33.1	0.78	0.09	98.91
kk8813OX9	56.0	n.d.	2.27	0.58	5.28	0.22	32.3	1.73	n.d.	98.40
kk8820OX1	55.8	0.01	1.77	0.73	5.60	0.05	31.7	2.39	0.09	98.08
kk8820OX2	57.0	0.05	2.03	0.60	5.84	0.11	33.0	1.51	0.05	100.21
kk8820OX3	57.0	0.04	1.93	0.69	5.76	0.07	32.5	2.26	0.02	100.19
kk8820OX4	57.1	0.01	2.08	0.55	5.94	0.33	33.1	1.18	0.24	100.54
li8811OX5	57.2	n.d.	1.78	0.44	5.60	0.17	33.5	1.09	0.08	99.92
li8811OX1C	57.7	n.d.	1.43	0.47	5.76	0.12	32.7	1.10	n.d.	99.26
li8811OX1R	57.2	0.09	1.58	0.50	5.69	0.06	33.3	0.90	0.06	99.35
li8811OX2C	57.0	0.03	1.56	0.49	5.50	0.12	33.4	0.77	0.13	99.05
li8811OX2R	56.8	n.d.	1.64	0.45	5.56	0.17	33.0	0.96	0.12	98.72
li8811OX3R	56.7	n.d.	1.72	0.73	5.48	0.21	33.0	1.15	n.d.	98.97
li8811OX3R	56.9	n.d.	1.35	0.54	5.57	0.05	33.2	1.05	n.d.	98.69
li8811OX4	56.9	0.10	1.76	0.52	5.48	0.28	33.1	1.03	0.10	99.34

	SiO$_2$	TiO$_2$	Al$_2$O$_3$	Cr$_2$O$_3$	FeO*	MnO	MgO	CaO	NiO	Total
li8816OX5	57.5	n.d.	0.46	0.16	5.47	0.11	35.3	0.43	0.04	99.43
li8816OX7	54.0	0.00	1.02	0.12	6.05	0.08	36.5	0.36	n.d.	98.19
li8821OX1	57.5	0.04	0.52	0.39	5.41	0.19	33.7	0.97	0.24	98.97
li8821OX2	57.7	n.d.	0.90	0.45	5.41	0.27	33.8	0.59	0.16	99.34
li8821OX3	57.6	n.d.	0.80	0.30	5.42	0.21	35.0	0.61	n.d.	99.89
li8826OX1	58.0	0.03	0.37	0.14	4.99	0.17	34.2	0.66	0.06	98.66
li8826OX2	57.9	0.12	1.19	0.15	5.14	0.25	33.6	0.93	0.08	99.34
li8826OX5	58.5	n.d.	0.29	0.16	5.22	0.11	34.2	0.76	0.05	99.29
si43OX4	56.7	n.d.	1.88	0.85	5.66	0.12	32.3	1.88	n.d.	99.31
si43OX5	57.2	n.d.	1.51	0.68	6.12	0.19	32.7	1.49	n.d.	99.86
si43OX6	56.3	0.06	1.94	0.81	5.45	0.09	32.2	1.48	0.00	98.30

Table (E.2) Orthopyroxene analyses.

	SiO_2	TiO_2	Al_2O_3	Cr_2O_3	FeO*	MnO	MgO	CaO	NiO	Total
bo18CX1	53.1	0.25	2.84	0.56	2.31	0.11	16.9	24.3	n.d.	100.56
bo18CX3	52.6	0.20	2.46	0.41	2.18	0.06	17.2	23.7	0.02	99.09
bo18CX4	51.8	0.21	3.31	0.71	2.09	0.10	16.1	23.9	n.d.	98.55
bo18CX5	51.6	0.23	2.97	0.52	2.10	0.10	16.4	24.0	n.d.	98.21
bo22CX1	52.0	0.25	3.34	0.69	2.39	n.d.	15.7	24.0	0.01	98.71
bo22CX2	51.8	0.27	2.92	0.65	2.36	0.04	16.1	24.1	0.18	98.55
bo22CX3	45.2	0.23	9.13	3.24	4.27	0.06	17.5	19.4	n.d.	99.33
bo22CX4	49.5	0.17	5.02	1.24	3.53	0.14	18.4	20.5	0.11	98.89
bo6CX1	51.3	0.31	4.37	1.33	2.18	0.01	16.4	23.6	n.d.	99.80
bo6CX2	52.2	0.16	2.75	0.88	1.83	0.24	16.2	24.8	0.03	99.26
bo6CX3	52.6	n.d.	2.13	0.48	2.19	0.13	17.3	23.5	0.08	98.55
dr11CX4	53.3	0.03	2.16	0.76	2.22	0.01	17.2	24.0	n.d.	99.79
dr11CX5	52.2	n.d.	2.23	0.99	2.28	0.06	17.3	23.3	0.11	98.77
dr23CX1	52.3	0.06	1.72	0.84	2.38	0.15	18.3	22.1	0.27	98.37
dr3CX6	53.3	n.d.	1.96	0.88	2.37	0.17	17.1	23.0	0.03	99.20
dr3CX7	54.2	0.08	2.06	1.13	2.28	n.d.	17.3	23.7	0.06	101.00
dr3CX7	53.0	0.14	1.71	0.77	2.23	0.17	17.5	22.8	n.d.	98.76
dr3CX8	52.1	0.03	1.89	0.82	3.00	0.20	20.3	19.9	n.d.	98.65
dr3CX9	52.0	0.05	1.73	0.90	2.91	0.20	20.5	19.1	0.24	98.14
dr34CX1	53.4	0.05	1.82	1.07	2.51	0.04	19.2	21.3	0.16	99.77
dr9CX2	52.5	n.d.	1.99	0.82	2.33	n.d.	17.8	22.6	n.d.	98.37
dr9CX3	52.4	n.d.	2.36	1.13	2.25	0.12	17.1	22.4	0.01	98.00
dr9CX1	53.0	n.d.	2.57	1.32	2.12	0.01	17.1	23.1	0.25	99.76
kk30CX5	53.7	0.13	1.18	0.26	4.95	0.04	16.1	23.5	0.23	100.44
kk30CX6	52.9	n.d.	1.11	0.21	5.32	0.24	16.3	22.7	0.16	99.15
kk30CX7	53.6	0.02	1.16	0.22	5.06	n.d.	16.4	23.4	0.11	100.19
kk8812CX1	52.6	n.d.	1.64	1.11	2.45	0.13	17.6	23.2	0.06	98.91
kk8812CX5	52.2	n.d.	2.08	0.78	2.49	0.14	17.0	23.2	n.d.	98.10
kk8813CX7	52.9	0.01	2.52	1.30	2.27	0.12	17.3	23.1	n.d.	100.05
kk8813CX4	53.5	n.d.	2.15	1.04	2.22	0.01	17.4	23.3	n.d.	100.02
kk8813CX5	53.7	0.12	2.44	1.00	2.01	0.03	17.1	23.6	0.19	100.65
kk8813CX6	53.1	n.d.	2.70	1.28	2.14	n.d.	16.5	23.7	0.16	99.93
kk8819CX1	49.8	0.26	1.79	1.01	4.34	0.06	21.5	19.8	0.04	98.65
kk8820CX1	52.1	0.04	2.35	0.92	2.62	0.03	17.0	23.5	0.06	98.83
kk8820CX2	52.6	0.08	1.79	0.57	2.30	0.14	17.4	23.3	n.d.	98.30
kk8820CX3	53.1	n.d.	1.82	0.56	2.49	0.18	17.9	22.8	0.21	99.42
si43CX1	53.0	0.07	1.58	0.81	2.62	n.d.	17.6	22.8	0.36	99.13
si43CX4	52.8	n.d.	1.86	0.81	2.78	0.05	19.0	21.4	0.15	99.28
si43CX2	52.4	n.d.	2.19	0.88	2.65	0.07	17.8	21.9	0.13	98.38

Table (E.3) Clinopyroxene analyses.

	SiO$_2$	TiO$_2$	Al$_2$O$_3$	Cr$_2$O$_3$	FeO*	MnO	MgO	NiO	Total
ag2SP15C	0.35	0.10	9.9	60.8	19.3	n.d.	9.6	n.d.	100.12
ag2SP15R	1.69	0.08	10.5	57.8	20.4	0.24	10.4	n.d.	101.14
ag2SP16C	0.41	0.04	9.9	61.3	19.4	0.21	9.8	0.05	101.13
ag2SP16R	0.65	0.02	10.7	58.6	20.6	0.43	9.1	0.09	100.11
ag2SP17	0.68	0.12	10.5	60.4	20.0	n.d.	9.8	n.d.	101.50
ag3SP10	0.23	n.d.	12.9	58.6	21.5	0.17	9.0	n.d.	102.45
ag3SP11	0.31	0.11	13.0	57.0	20.9	0.32	9.2	n.d.	100.79
ag3SP12C	0.32	0.06	13.2	58.0	20.0	n.d.	9.7	0.24	101.47
ag3SP12R	0.35	0.06	14.0	56.4	20.3	n.d.	9.7	n.d.	100.82
ag3SP13C	1.42	0.15	13.2	57.3	20.6	n.d.	9.6	0.25	102.52
ag3SP13R	0.35	0.11	13.5	54.3	24.2	0.17	8.6	0.19	101.40
ag3SP14	0.23	0.09	12.9	57.7	20.7	0.26	9.4	n.d.	101.34
ag3SP15C	0.07	n.d.	12.8	57.5	19.1	0.04	9.9	0.17	99.66
ag3SP15R	0.11	0.06	13.7	56.8	20.8	n.d.	9.8	n.d.	101.24
ag883SP1	0.76	0.07	13.8	56.3	18.7	0.46	11.4	n.d.	101.36
ag883SP2	0.82	n.d.	14.3	55.5	18.7	0.21	11.1	0.46	101.00
ag883SP3	0.88	n.d.	14.4	54.6	19.8	0.33	11.0	0.17	101.13
ag883SP4	0.36	0.12	13.6	57.4	19.2	n.d.	11.2	0.03	101.85
ag883SP5	0.94	0.13	13.6	56.3	18.6	0.03	12.0	0.03	101.69
ag883SP6	0.23	0.13	13.7	56.2	19.1	n.d.	11.0	0.04	100.35
ag883SP7	0.25	n.d.	13.6	56.1	19.0	n.d.	11.0	0.16	100.11
ag883SP8	0.24	0.03	13.5	55.6	18.9	n.d.	10.9	0.18	99.36
ag883SP9	0.11	n.d.	13.5	55.3	18.8	n.d.	11.3	0.20	99.23
ag883SP10	0.87	n.d.	13.5	53.9	18.8	n.d.	11.3	0.05	98.40
bak1SP1	0.17	n.d.	24.4	44.8	16.2	n.d.	13.2	0.01	98.65
bak1SP1B	0.20	0.11	23.5	45.8	16.1	0.44	12.8	0.09	99.07
bak1SP3	0.40	0.08	23.9	45.3	16.7	0.39	12.8	0.05	99.63
bak1SP4	0.21	0.21	23.3	46.9	16.6	0.36	12.9	0.06	100.56
bak1SP5	0.26	0.14	24.0	46.5	17.2	n.d.	13.2	n.d.	101.27
bak1SP6	0.22	0.14	24.0	46.4	16.5	0.33	13.2	n.d.	100.65
bak1SP7	0.29	0.07	23.7	47.3	16.3	0.16	13.4	0.21	101.40
bak1SP7B	0.14	0.05	23.1	47.3	16.3	0.14	13.2	0.18	100.43
bak1SP8	0.17	0.07	24.4	46.5	16.3	0.22	13.3	0.12	101.14
bak1SP9	1.09	0.06	24.1	43.8	17.0	0.22	13.5	0.11	99.95
bak1SP3R	0.33	0.08	25.0	43.5	16.3	n.d.	13.1	0.25	98.56
bak1SP4R	0.48	0.06	23.9	47.1	16.9	0.14	13.3	0.02	101.94
bak1SP4R2	0.17	0.10	23.8	47.4	17.3	0.14	13.3	0.20	102.49
bak1SP21	1.33	n.d.	25.5	43.3	15.7	n.d.	14.6	n.d.	100.44
bak1SP22	0.23	0.03	24.1	46.4	16.3	0.10	14.1	0.16	101.42
bak1SP23	1.25	0.09	25.5	42.8	15.9	0.13	14.8	0.04	100.50
bak1SP24	0.31	n.d.	23.4	46.1	16.6	0.07	13.5	0.09	100.09
bak1SP25	0.35	0.09	24.0	46.2	16.4	0.16	13.9	n.d.	100.95
bak1SP26	0.19	0.03	23.9	45.5	15.7	0.13	13.7	0.21	99.48
bak1SP27	0.14	n.d.	23.8	46.1	16.4	0.21	13.9	0.10	100.61
bak1SP28	0.19	n.d.	24.1	45.6	16.5	n.d.	14.3	0.08	100.73
bak1SP29	0.27	0.01	23.8	45.9	16.7	n.d.	14.0	0.01	100.64
bak1SPB30	0.26	0.10	24.1	45.1	15.9	n.d.	14.5	0.08	100.02
bo13SP1	0.21	0.08	12.8	56.6	21.8	0.56	9.3	n.d.	101.37
bo13SP2	0.17	0.06	12.9	55.6	21.5	0.61	9.1	0.01	100.01
bo13SP3	0.23	0.08	12.5	56.7	21.6	0.66	9.1	0.08	101.04
bo14SP1	0.28	0.09	21.6	45.7	20.5	0.63	11.5	n.d.	100.42
bo14SP2	0.34	0.12	21.6	46.3	19.7	0.13	12.1	n.d.	100.29
bo14SP3	0.26	0.12	21.6	46.2	20.0	0.56	11.7	n.d.	100.42
bo14SP4	1.34	0.16	17.9	45.8	23.3	0.56	10.6	n.d.	99.69
bo14SP5	2.65	0.14	14.4	45.9	25.8	0.34	9.6	n.d.	98.73

	SiO_2	TiO_2	Al_2O_3	Cr_2O_3	FeO*	MnO	MgO	NiO	Total
bo18SP2C	0.41	0.14	45.7	19.9	14.4	0.02	17.1	0.59	98.24
bo18SP2R	0.47	0.16	46.6	19.8	14.5	0.01	17.4	0.31	99.25
bo18SP3C	0.19	n.d.	45.6	20.7	14.7	0.12	17.2	0.33	98.94
bo18SP3R	1.00	0.05	45.6	20.0	14.7	0.04	16.9	0.08	98.39
bo18SP4C	0.44	n.d.	45.9	20.0	14.8	n.d.	17.5	0.18	98.86
bo18SP4R	21.31	n.d.	29.9	13.5	11.3	n.d.	24.7	0.46	101.15
bo18SP5	0.27	0.04	46.4	19.4	14.5	0.17	17.7	0.22	98.73
bo22SP4	0.03	0.10	47.1	19.8	14.5	0.06	17.7	0.15	99.40
bo22SP5	1.53	0.12	45.1	19.8	14.3	0.25	18.0	0.52	99.68
bo22SP6	1.84	0.06	45.7	19.1	13.2	n.d.	18.2	0.28	98.29
bo22SP7	0.49	0.09	47.3	19.2	13.9	0.05	17.4	0.50	98.81
bo6SP5	0.74	0.13	48.3	19.4	13.5	0.08	17.5	n.d.	99.59
bo6SP6	0.83	0.09	44.2	22.8	15.0	n.d.	16.7	0.37	99.88
bo6SP7	0.50	n.d.	43.7	23.9	15.2	0.09	16.3	0.42	100.13
bo6SP8	0.99	0.02	45.0	20.5	14.1	0.13	17.5	0.09	98.33
cmt730SP7	0.35	0.12	20.5	48.9	17.6	0.46	14.0	0.11	101.97
cmt730SP8	0.14	0.02	20.0	48.4	18.1	0.21	13.5	0.12	100.56
cmt730SP9	0.21	0.06	20.5	48.7	17.3	n.d.	14.3	0.09	101.17
cmt731SP2R	0.26	0.21	18.7	51.0	14.9	n.d.	13.8	n.d.	98.92
cmt731SP4R	0.46	0.17	19.3	49.5	15.8	0.13	13.9	0.17	99.35
cmt731SP5R	0.22	0.24	18.7	51.9	15.4	0.13	14.4	0.08	101.12
cmt731SP6R	5.80	0.25	17.5	44.1	14.0	0.11	17.5	0.06	99.38
dr11SP4	3.94	0.03	26.1	29.6	14.8	0.33	23.1	0.23	98.11
dr11SP5	15.63	n.d.	17.2	19.6	12.6	0.17	34.3	0.40	99.93
dr16SP1	0.41	0.29	19.1	45.3	23.4	0.38	10.2	0.30	99.44
dr16SP2	2.05	0.44	15.0	44.2	27.6	0.63	8.9	0.10	98.92
dr16SP3	0.22	0.45	19.4	45.9	22.7	0.26	10.6	0.08	99.61
dr16SP4	1.99	0.45	18.7	45.3	22.1	0.17	10.6	0.32	99.62
dr16SP5	0.29	0.44	19.1	45.5	22.0	0.27	10.7	n.d.	98.36
dr16SP6	0.41	0.45	18.9	45.1	24.5	0.21	9.9	0.02	99.44
dr16SP7	1.83	0.29	17.1	43.4	25.7	0.17	9.5	0.12	98.16
dr16SP1R	0.47	0.32	20.1	44.0	23.1	0.60	10.5	n.d.	99.08
dr17SP11	3.35	0.10	20.4	39.3	27.2	n.d.	8.7	0.29	99.22
dr20SP1	0.65	n.d.	8.9	61.7	16.9	0.86	10.5	0.22	99.63
dr20SP2	0.49	0.04	8.5	62.8	17.7	0.84	10.0	n.d.	100.40
dr20SP3	0.49	n.d.	8.9	62.8	17.0	1.19	10.1	n.d.	100.40
dr22SP12	0.77	0.08	12.7	57.1	19.4	0.18	11.2	0.02	101.40
dr22SP13C	0.77	0.14	13.9	56.1	18.1	0.01	10.8	0.30	100.12
dr22SP13R	1.11	0.06	12.6	56.6	19.0	0.08	11.3	0.11	100.80
dr22SP14C	0.84	0.01	12.1	56.3	20.2	0.15	10.9	0.06	100.57
dr22SP14R	2.28	0.11	11.0	53.0	20.5	0.10	11.9	0.08	99.05
dr23SPb7	0.26	0.22	18.6	51.0	17.6	0.34	12.2	n.d.	100.20
dr23SPb7B	0.24	0.20	18.2	51.1	18.0	0.52	12.1	0.20	100.58
dr23SPb8	0.33	0.08	18.5	51.6	17.5	0.45	11.9	0.13	100.44
dr23SP9C	0.13	0.16	19.3	50.2	17.2	0.14	12.9	0.10	100.13
dr23SP1C	0.20	0.26	19.8	49.5	17.1	0.44	12.1	0.01	99.46
dr23SP2C	0.13	0.19	19.0	50.4	17.5	0.37	12.0	0.19	99.85
dr23SP9R	0.23	0.12	19.7	48.3	17.3	0.07	12.5	n.d.	98.16
dr23SP1R	0.53	0.25	20.7	47.1	17.0	0.42	12.2	n.d.	98.12
dr23SP2R	0.19	0.06	19.3	48.9	17.8	0.29	12.1	0.13	98.80
dr3SP10	0.31	0.13	18.0	49.9	19.7	n.d.	12.3	0.06	100.32
dr3SP11	0.33	0.11	20.3	46.8	19.9	n.d.	12.1	n.d.	99.53
dr3SP12	1.02	0.03	21.9	41.3	22.3	n.d.	12.0	0.03	98.58
dr3SP8	1.17	0.18	21.0	43.8	20.5	0.26	12.3	0.34	99.46
dr3SP9	1.09	0.11	20.9	42.6	22.7	0.19	10.7	n.d.	98.22

	SiO_2	TiO_2	Al_2O_3	Cr_2O_3	FeO^*	MnO	MgO	NiO	Total
dr34SP5	1.95	0.01	20.6	45.6	18.4	0.41	12.7	n.d.	99.68
dr34SP6	0.26	n.d.	21.7	47.6	20.6	n.d.	11.4	0.01	101.62
dr34SP7	0.14	n.d.	19.8	50.2	19.5	0.12	12.0	0.05	101.84
dr34SP7R	0.22	0.13	20.9	48.3	20.0	0.10	11.8	n.d.	101.46
dr34SP8	0.17	0.12	20.9	49.2	19.5	0.21	12.4	0.03	102.57
dr42SP1	0.26	0.07	22.1	49.5	18.0	0.38	12.4	n.d.	102.73
dr42SP2	5.09	n.d.	19.2	42.8	17.4	0.57	16.2	0.15	101.45
dr42SP3	0.36	0.15	23.1	48.1	17.9	0.50	12.6	n.d.	102.67
dr42SP4	0.38	0.11	22.2	49.2	17.7	0.37	12.4	n.d.	102.39
dr6SP6	0.52	0.43	18.4	36.8	32.2	0.54	9.3	n.d.	98.13
dr6SP6B	0.31	0.49	18.9	42.9	26.8	0.43	9.4	0.12	99.44
dr9SP1C	0.59	0.02	30.3	37.5	16.4	0.28	14.5	0.21	99.81
dr9SP2	3.71	n.d.	28.3	34.1	17.9	0.22	15.2	0.06	99.36
dr9SP3C	0.17	n.d.	28.0	41.2	15.9	n.d.	14.4	0.20	99.89
dr9SP1R	1.21	0.09	30.2	35.9	16.5	0.47	14.7	0.08	99.15
dr9SP3R	0.26	n.d.	27.2	39.6	17.2	0.11	13.6	0.22	98.12
kk28SP9	3.77	0.22	20.3	30.7	33.0	0.37	10.8	0.26	99.41
kk28SP10	0.19	1.04	17.6	39.7	31.1	0.43	8.3	0.15	98.53
kk49SP3	0.26	0.13	29.1	32.8	23.7	0.29	13.7	0.21	100.11
kk49SP4	0.36	0.25	28.9	34.0	23.1	0.33	13.8	0.24	100.95
kk49SP6	0.26	0.30	28.9	34.4	21.4	0.45	13.9	n.d.	99.66
kk7SP1C	0.69	0.06	38.8	29.1	14.9	0.18	16.3	0.12	100.03
kk7SP1R	1.30	0.09	39.4	25.8	15.1	0.37	16.3	0.24	98.72
kk8812SP1C	0.45	n.d.	23.3	43.0	19.4	0.41	12.5	0.19	99.18
kk8812SP2C	1.12	0.10	24.4	40.9	19.6	0.40	12.8	n.d.	99.35
kk8812SP2R	1.03	n.d.	25.6	40.5	19.9	0.65	13.0	0.01	100.61
kk8812SP1R	0.48	n.d.	23.8	42.0	19.2	0.36	12.4	0.04	98.28
kk8812SP3	0.57	0.09	24.6	40.7	18.9	1.04	12.4	0.12	98.35
kk8813SP4	0.24	0.04	25.7	41.9	18.0	0.06	13.7	0.15	99.81
kk8813SP5	0.35	n.d.	25.6	40.8	18.3	n.d.	13.8	0.19	99.02
kk8813SP6	0.13	0.05	24.5	42.2	17.7	n.d.	13.7	0.20	98.46
kk8813SP7	0.57	0.07	26.1	40.4	17.6	0.05	13.9	0.31	99.16
kk8813SP8	1.30	0.04	27.8	37.4	18.2	0.15	14.3	0.05	99.30
kk8813SP6R	0.25	0.04	26.0	40.5	18.1	n.d.	13.8	0.09	98.77
kk8819SP10	0.52	0.62	16.0	45.1	25.1	0.09	11.7	0.21	99.28
kk8819SP8	1.51	0.43	16.1	45.5	22.6	n.d.	11.9	0.09	98.18
kk8819SP9	2.13	0.38	14.7	41.5	26.6	0.18	12.9	0.24	98.67
kk8820SP1	4.00	0.09	22.6	37.4	19.2	0.34	14.7	0.31	98.67
kk8820SP2	0.89	0.12	25.6	40.2	20.2	0.13	12.8	0.02	99.98
kk8820SP3	0.69	0.11	24.1	40.0	20.2	0.31	12.7	0.17	98.33
kk8824SP1C	0.27	0.25	26.9	41.8	17.0	0.48	14.4	0.09	101.11
kk8824SP2C	0.23	0.05	26.5	41.6	16.8	n.d.	14.2	0.08	99.48
kk8824SP3C	0.35	0.10	26.7	42.0	17.1	0.15	14.2	0.08	100.66
kk8824SP4	0.19	0.10	26.7	41.5	18.2	0.16	13.6	0.24	100.72
kk8824SP5	0.19	n.d.	26.7	42.4	15.3	0.46	15.2	0.15	100.42
kk8824SP6	0.18	0.12	26.2	42.3	15.9	n.d.	14.6	0.50	99.67
kk8824SP1R	0.30	0.12	26.7	40.7	19.3	0.28	12.8	0.07	100.35
kk8824SP2R	0.18	0.05	26.8	40.1	17.1	0.12	13.8	0.27	98.35
kk8824SP3R	0.12	n.d.	26.9	40.3	18.4	0.41	13.8	n.d.	99.92
li8811SP1	0.36	0.10	22.4	48.9	17.1	0.47	12.7	n.d.	102.07
li8811SP2	0.52	0.19	20.6	48.5	17.4	0.25	11.9	0.25	99.67
li8811SP3C	0.29	0.02	21.0	49.4	17.7	0.19	12.1	n.d.	100.66
li8811SP3R	2.70	0.15	22.0	43.1	16.6	0.21	14.3	0.16	99.20
li8811SP4C	0.29	0.12	21.4	48.8	17.6	0.24	12.4	0.05	100.98
li8811SP4R	1.13	0.06	22.5	45.7	16.6	0.27	12.8	0.02	99.12
li8811SP5C	0.26	n.d.	20.8	48.7	17.5	0.43	11.6	n.d.	99.33

	SiO_2	TiO_2	Al_2O_3	Cr_2O_3	FeO*	MnO	MgO	NiO	Total
li8811SP5R	0.46	n.d.	22.4	46.5	17.4	0.50	12.0	n.d.	99.20
li8816SP5	0.93	0.10	10.6	58.8	21.2	0.50	8.8	0.08	100.98
li8816SP6	5.35	0.10	8.4	50.6	22.0	0.32	12.4	n.d.	99.28
li8816SP7	0.57	n.d.	8.2	62.2	21.2	0.20	9.0	0.26	101.64
li8819SP10C	0.33	0.26	15.4	52.8	20.6	0.39	10.5	0.08	100.30
li8819SP10R	1.21	0.42	15.1	50.4	23.0	0.51	10.2	0.46	101.27
li8819SP11	0.76	0.26	16.3	52.0	20.0	0.10	11.3	0.26	101.03
li8819SP7	0.93	0.42	2.9	52.1	37.8	1.19	2.8	0.21	98.37
li8819SP8C	0.29	0.36	16.1	52.7	20.0	0.20	11.0	0.11	100.77
li8819SP8R	0.52	0.25	15.6	51.7	20.1	0.51	10.9	0.16	99.67
li8819SP9	0.37	0.28	15.5	52.2	22.5	0.21	9.6	0.05	100.65
li8821SP1	0.75	0.08	11.4	57.7	20.8	0.38	8.7	n.d.	99.92
li8821SP2	0.48	0.09	10.3	58.4	21.7	0.32	9.1	0.05	100.36
li8821SP3	0.30	n.d.	10.0	59.1	20.5	0.25	9.4	0.07	99.74
li8821SP4	0.56	0.14	10.7	58.9	21.3	0.19	9.1	n.d.	100.85
li8824SP10	0.13	0.15	10.5	57.3	20.3	0.17	10.0	n.d.	98.49
li8824SP8C	0.22	0.08	10.4	59.2	20.4	n.d.	9.9	0.01	100.19
li8824SP9C	0.22	n.d.	10.9	59.7	18.0	0.13	11.2	0.07	100.17
li8824SP11C	0.24	0.04	10.8	59.0	19.6	n.d.	10.3	0.42	100.46
li8824SP12C	0.20	0.07	10.8	59.2	18.9	0.05	10.7	0.25	100.23
li8824SP13C	0.15	0.10	10.8	59.6	18.4	n.d.	11.0	n.d.	99.98
li8824SP14C	0.28	0.09	10.7	58.6	19.7	n.d.	10.0	0.02	99.36
li8824SP15C	0.01	0.11	10.8	58.2	18.1	n.d.	11.1	0.27	98.44
li8824SP8R	0.32	0.02	10.3	57.5	22.3	0.21	9.0	0.12	99.70
li8824SP9R	0.20	0.13	11.0	57.9	19.6	0.21	10.6	n.d.	99.61
li8824SP11R	0.25	0.16	11.1	58.1	20.6	n.d.	9.9	0.32	100.42
li8824SP12R	0.15	0.22	11.6	58.1	19.2	n.d.	10.8	0.41	100.50
li8824SP13R	0.19	0.17	11.3	57.0	19.5	n.d.	10.6	0.02	98.79
li8824SP14R	0.30	n.d.	12.5	54.5	21.4	n.d.	9.8	0.31	98.87
li8824SP15R	0.08	n.d.	10.6	58.2	18.6	n.d.	10.7	n.d.	98.15
li8826SP1	0.83	0.16	7.0	62.7	20.3	0.38	8.7	0.26	100.33
li8826SP1R	5.09	0.01	6.2	55.3	19.6	0.49	11.4	0.03	98.09
li8826SP2C	0.72	0.03	6.1	63.1	20.7	0.29	8.2	n.d.	99.17
li8826SP2R	1.98	n.d.	8.1	58.7	19.9	0.52	9.1	0.08	98.40
li8826SP3	1.04	n.d.	6.8	63.1	21.0	0.19	8.5	n.d.	100.71
li8826SP4	1.78	0.02	8.0	59.7	21.0	0.49	8.4	n.d.	99.45
si23SP9	0.31	0.57	19.2	41.0	28.3	0.03	8.7	0.03	98.23
si23SP10	0.53	0.60	21.7	39.0	26.3	0.25	9.6	0.07	98.07
si23SP11	0.78	0.57	19.6	38.6	30.1	0.37	8.1	0.13	98.27
si43SP3	0.43	0.30	21.7	46.5	19.5	0.15	12.4	0.18	101.15
si43SP2B	0.45	0.18	21.8	45.7	20.0	0.51	12.1	n.d.	100.73
si43SP4	0.76	0.10	23.9	41.9	20.5	0.23	12.8	0.21	100.34
si43SP5	2.43	0.03	22.1	38.3	22.0	0.18	13.2	n.d.	98.11
si45SP11	0.27	0.33	23.5	43.6	18.5	0.06	12.9	0.17	99.33
si45SP12	0.23	0.16	23.9	44.2	18.6	0.14	13.5	0.26	101.02
si45SP13	0.21	0.10	23.6	43.9	18.0	0.01	13.5	0.19	99.57
si45SP14	0.44	0.12	23.5	42.1	20.6	0.16	12.5	0.23	99.76

Table (E.4) Spinel analyses.

References

Agee, C.B., and Walker, D.A., 1990. Aluminium partitioning between olivine and ultrabasic silicate liquid to 6 GPa. Contrib. Mineral. Petrol., 105, 243-254.

Agiorgitis, G., and Wolf, R., 1978. Aspects of osmium, ruthenium and iridium contents in some Greek chromites. Chem. Geol., 23, 267-272.

Amossé, J., Allibert, M., Fischer, W., and Piboule, M., 1990. Experimental study of the solubility of platinum and iridium in basic silicate melts - Implications for the differentiation of platinum-group elements during magmatic processes. Chem. Geol., 81, 45-53.

Arai, S., 1987. An estimation of the least depleted spinel peridotite on the basis of olivine - spinel mantle array. N. Jb. Miner. Mh., 8, 347-354.

Arai, S., and Fujii, T.,1978. Petrology of ultramafic rocks from Site 395, DSDP. In: Melson, W.G., and Rabinowitz, P.D., et al., Init. Rep. Deep Sea Drill. Project, 45, Washington, 595-602.

Arculus, R.J., 1985. Oxidation status of the mantle: Past and present. Ann. Rev. Earth Planet. Sci., 13, 75-95.

Arculus, R.J., 1987. The significance of source versus process in the tectonic controls of magma genesis. J. Volcanol. Geotherm. Res., 32, 1-12.

Arculus, R.J., and Powell, R., 1986. Source component mixing in the regions of arc magma generation. J. Geophys. Res., 91, 5913-5926.

Arculus, R.J., Johnson, R.W., Chappell, B.W., McKee, C.O., and Sakai, H., 1983. Ophiolite-contaminated andesites, trachybasalts, and cognate inclusions of Mount Lamington, Papua New Guinea: Anhydrite-amphibole-bearing lavas and the 1951 cumulodome. J. Volcanol. Geotherm. Res., 18, 215-247.

Asif, M., and Parry, S.J., 1988. Elimination of reagent blank problems in the fire-assay pre-concentration of the platinum group elements and gold with a nickel sulphide bead of less than one gram mass. Analyst, 114, 1057-1059.

Aubouin, J., 1965. Geosynclines. Elsevier, Amsterdam, 335pp.

Aubouin, J., Bonneau, M., Celet, P., Charvet, J., Clement, B., Degardin, J.M., Dercourt, J., Fèrriere, J., Fleury, J.J., Guernet, C., Maillot, H., Mania, J.H., Mansy, J.L., Terry, J., Thiebault, P., Tsoflias, P., and Verriex, J.J., 1970. Contribution à la géologie des Hellenides: le Gavrovo, le Pinde et la zone ophiolitique subpelagonienne. Annal. Soc. Géol. du Nord, 90, 277-306.

Augé, T., 1988. Platinum-group minerals in the Tiebaghi and Vourinos ophiolitic complexes: Genetic implications. Can. Mineral., 26, 177-192.

Aumento, F., and Loubat, H., 1971. The Mid-Atlantic Ridge near 45°N. XVI. serpentinized ultramafic intrusions. Can. J. Earth Sci., 8, 631-662.

Bacuta, G.C., Robert, W.K., Gibbs, A.K., and Lipin, B.R., 1990. Platinum-group element abundance and didtribution in chromite deposits of the Acoje Block, Zambales ophiolite complex, Philippines. J. Geoch. Explor., 37, 113-145.

Ballhaus, C., Berry, R.F., and Green, D.H., 1990. Oxygen fugacity controls in the Earth's upper mantle. Nature, 348, 437-440.

Ballhaus, C., Berry, R.F., and Green, D.H., 1991. High pressure experimental calibration of the olivine-orthopyroxene-spinel oxygen geobarometer: Implications for the oxidation of the upper mantle. Contrib. Mineral. Petrol., 107, 27-40.

Barnes, S.J., 1986. The distribution of chromium among orthopyroxene, spinel and silicate liquid at atmospheric pressure. Geochim. Cosmochim. Acta, 50, 1889-1909.

Barnes, I., and O'Neil, J.R., 1969. The relationship between fluids in some fresh Alpine-type ultramafics and possible modern serpentinization, Western US. Bull. Geol. Soc. Am., 80, 1947-1960.

Barnes, I., Rapp, J.B., and O'Neil, J.R., 1972. Metamorphic assemblages and the direction of flow of metamorphic fluids in four instances of serpentinization. Contrib. Mineral. Petrol., 35, 263-276.

Barnes, S-J., Boyd, R., Korneliussen, A., Nilsson, L.P., Often, M., Pedersen, R., and Robins, B., 1988. The use of mantle normalization and metal ratios in discriminating between the effects of partial melting, crystal fractionation and sulphide segregation on platinum-group elements, gold, nickel and copper: examples from Norway. In: Prichard, H.M., Potts, P.J., Bowles, J.F.W., and Cribb, S., (eds). Geoplatinum 87, Elsevier, Barking, 113-143.

Barnes, S-J., Naldrett, A.J., and Gorton, M.P., 1985. The origin of the fractionation of platinum-group elements in terrestrial magmas. Chem. Geol., 53 303-323.

Basu, A.R., 1977. Textures, microstructures and deformation of ultramafic xenoliths from San Quintin, Baja California. Tectonophysics, 43, 213-246.

Beamish, F.E., and Van Loon, J.C., 1977. Analysis of noble metals: Overview and selected methods, Academic Press, New York, 327 pp.

Beblen, J., Ohnenstetter, D., Ohnenstetter, M., and Vergely, P., 1980. Diversity of the Greek ophiolites: birth of oceanic basins in transcurrent systems. Ofioliti, Spec. Iss. Teth. Oph., 2, 129-197.

Bédard, J.H., 1991. Cumulate recycling and crustal evolution in the Bay of Islands ophiolite. J. Geol., 99-225-249.

Bender, J.F., Hodges, F.N., and Bence, A.E., 1978. Petrogenesis of basalts from the project FAMOUS area: Experimental study from 0 to 15 kbars. Earth Planet. Sci. Lett., 41, 277-302.

Berlincourt, L.E., Hummel, H.H., and Skinner, B.J., 1981. Phases and phase relations of the platinum-group elements. In: Cabri, L.J., (ed). Platinum-group elements: mineralogy, geology, recovery. Can. Inst. Miner. Metal., Spec. Iss. 23, 5-18.

Bertolani, M., Capedri, S., and Giacobazzi, C., 1980. Sulphide ore deposit in the ophiolite at Mount Kodra (Northern Pindos, Perivoli, Grevena). Proc. Int. Symp. on Metallogeny of Mafic and Ultramafic Complexes. I.G.C.P., 169, 185-195.

Bertolani, M., Capedri, S., and Giacobazzi, C., 1982. Opaque phases in the ophiolitc rocks from the Aspropotamos Valey (Northern Pindos). Chem. Erde, 41, 103-110.

Bickle, M.J., Ford, C.E., and Nisbet, E.G., 1977. The petrogenesis of peridotitic komatiites: Evidence from high-pressure melting experiments. Earth Planet. Sci. Lett., 37, 97-106.

Bloomer, S.H., and Fisher, R.L., 1987. Petrology and geochemistry of igneous rocks from the Tonga Trench - A non-accreting plate boundary. J. Geol., 95, 469-495.

Bloomer, S.H., and Hawkins, J.W., 1983. Gabbroic and ultramafic rocks from the Marianna trench: An island arc ophiolite. Geoph. Monograph, 27, 294-317.

Bodinier, J.L., Guiraud, M., Dupuy, C., and Dostal, J., 1986. Geochemistry of basic dykes in the Lanzo massif (Western Alps): Petrogenetic and geodynamic implications. Tectonophysics, 149, 67-88.

Bonatti, E., and Michael, P.J., 1989. Mantle peridotites from continental rifts to ocean basins to subduction zones. Earth Planet. Sci. Let., 91, 297-311.

Bonatti, E., Ottonello, G., and Hamlyn, P.R., 1986. Peridotites from the island of Zabargad, (St.John), Red Sea : Petrology and geochemistry. J. Geoph. Res., 91, 599-631.

Borthick, A.A., and Naldrett, A.J., 1984. Neutron activation analysis for platinum group elements and gold in chromitites. Anal. Lett., 17, 265-275.

Bowen, N.L., 1914. The ternary system: Diopside-forsterite-silica. Am. J. Sci., 38, 207-264.

Bowen, N.I., and Tuttle, O.F., 1949. The system $MgO-SiO_2-H_2O$. Bull. Geol. Soc. Am., 60, 430-460.

Bradley, R.S., 1962. Thermodynamic calculations on phase equilibria involving fused salts. Part II. Solid solutions and application to the olivines. Am. J. Sci., 260, 550-554.

Brey, G.P., and Köhler, T.P., 1990. Geothermobarometry in natural four-phase lherzolites, part II: New geothermobarometers and practical assessment of existing thermobarometers. J. Petrology, 31, 1353-1378.

Brogniart, A., 1813. Essai d'un classification minéralogique des roches mélangées. J. des Mines, Paris, 199, 5-48.

Brown, M.A., 1982. Chromite deposits and their ultramafic host rocks in the Oman ophiolite. Ph.D Thesis, Open University, 263pp.

Browning, P., 1984. The petrology, geochemistry and structure of the plutonic rocks of the Oman ophiolite, Ph.D. thesis, Open University, 404pp.

Brunn, J.H., 1956. Contribution à l' étude géologique du Pinde septentrional et d' une partie de la Macedonie occidentale, Annal. Geol. Pays Hell., 7, 358pp.

Brunn, J.H., 1960. Mise en place et differentiation de l' association pluto-volcanique du cortège ophiolitique. Rev. Geogr. Phys. Dyn., 3, 115-132.

Brunn, J.H., 1961. Les sutures ophiolitiques. Contribution à l' étude des les relations entre phenomenes magmatic et orogeniques. Rev. Geogr. Phys. Geol. Syn., 4, 181-202.

Bryndzia, L.T., and Wood, B.J., 1990. Oxygen thermoberometry of abyssal peridotites: The redox state and C-O-H volatile composition of the earth's sub-oceanic mantle. Am. J. Sci., 190, 1093-1116.

Bryndzia, L.T., Wood, B.J., and Dick, H.J.B., 1989. The oxidation state of the earth's sub-oceanic mantle from oxygen thermoberometry of abyssal peridotites. Nature, 341, 526-527.

Burgath, K.P., and Mohr, M., 1985. Chromitites and platinum-group minerals in the Meratus-Bobaris Ophiolite zone, southeast Borneo. In: Metallogeny of basic and ultrabasic rocks, Gallagher, M.J., Ixer, R.A., Neary, C.R., and Prichard, H.M., (eds). 333-350.

Burns, D.T., Townshend, A., and Carter, A.H., 1981. Inorganic reaction chemistry. Volume 2: Reactions of the elements and their compounds, Parts A and B. John Wiley, Chichester, 300pp.

Butler, J.C., 1979. Trends in ternary petrologic variation diagrams-facts or fantasy? Am. Mineral., 64, 1115-1121.

Cabri, L.J., 1976. Gloassary of platinum-group minerals. Econ. Geol., 71, 1476-1480.

Cabri, L.J., 1981. The platinum-group minerals. In: Cabri, L.J., (ed). Platinum-group elements: mineralogy, geology, recovery. Can. Inst. Miner. Metal., Spec. Iss. 23, 83-150.

Cabri, L.J., and Laflamme, J.H.G., 1981. Analyses of minerals containing platinum-group elements. In: Cabri, L.J., (ed). Platinum-group elements: mineralogy, geology, recovery. Can. Inst. Miner. Metal., Spec. Iss. 23, 151-174.

Campbell, I.H., and Barnes, S.J., 1984. A model for the geochemistry of the platinum group elements in magmatic sulphide deposits. Can. Mineral., 22, 151-160.

Canil, D., Virgo, D., and Scarfe, C.M., 1990. Oxidation state of mantle xenoliths from British Columbia, Canada. Contrib. Mineral. Petrol., 104, 453-462.

Cann, J.R., 1970. New model for the structure of ocean crust. Nature, 226, 928-930.

Cann, J.R., 1974. A model for oceanic crustal structure developed. Geophys. J. R. Astr. Soc., 39, 169-187.

Cannat, M., and Hébert, R., 1990. Plastic deformation and magmatic impregnation in serpentinized ultramafic rocks from the Garett transform fault (East Pacific Rise). Earth Panet. Sci. Lett., 101, 216-232.

Capobianko, C.J., and Drake, M.J., 1990a. Partitioning of ruthenium, rhodium, and palladium between spinel and silicate melt and implications for the platinum group element fractionation trends. Geochim. Cosmochim. Acta, 54, 869-874.

Capobianko, C.J., and Drake, M.J., 1990b. (abstract), Trans. Am. Geoph. Union, EOS.

Caroll, M.R., and Rutherford, 1985. Sulphide and sulfate saturation in hydrous silicate melts, J. Geoph. Res., 90, 601-612.

Carter, J.L., 1970. Mineralogy and chemistry of the Earth's upper mantle based on the partial fusion-partial crystallization model. Geol. Soc. Am. Bull., 81, 2021-2034.

Cassard. D., Nicolas, A., Rabinowitz, M., Moutte, M, Leblanc, M., and Prinzhofer, A., 1981. Structural classification of chromite pods in southern New Caledonia. Econ. Geol., 76, 805-831.

Cawthorn, R.G., and Davies, G., 1983. Experimental data at 3 kbars pressure on the parental magma to the Busheld complex. Contrib. Mineral. Petrol., 83, 128-135.

Chernosky, J.V., 1973. The stability of chrysotile, $Mg_3Si_2O_5(OH)_4$, and the free energy of formation of talc, $Mg_3Si_4O_{10}(OH)_2$ (abstract). Geol. Soc. Am. Abstr., 1973 Meet.

Christie, D.M., Carmichael, I.S.E., and Langmuir, R.H., 1986. Oxidation states of mid-ocen ridge basalt glasses. Earth Panet. Sci. Lett., 79, 397-411.

Chyi, L.L., and Crocket, J.H., 1983. Partition of platinum, palladium, iridium and gold among coexisting minerals from the deep ore zone Srathcona Mine, Sudbury, Ontario. Econ. Geol., 71, 1196-1205.

Cocherie, A., Augé, T., and Meyer, G., 1989. Geochemistry of the platinum-group elements in various types of spinels from the Vourinos ophiolitic complex, Greece. Chem. Geol., 77, 27-39.

Coleman, R.G., 1977. Ophiolites ancient oceanic lithosphere? Springer-Verlag, 229pp.

Coleman, R.G., and Keith, T.E., 1971. A chemical study of serpentinization - Burro Mountain, California. J. Petrology, 12, 311-328.

Constandinides, C.C., Kingston, G.A., and Fisher, P.C., 1979. The occurrence of platinum group minerals in the chromitites of the Kokkinorotsos chrome mine, Cyprus, in: Ophiolites, Panayiotou, A., (ed). Proceedings International Ophiolite Symposium, Cyprus, 93-101.

Corrivaux, L, and Laflamme, J.H.G., 1990. Minéralogie des éléments du groupe du platine dans les chromitites de l' ophiolie de Thetford Mines, Québec. Can. Mineral., 28, 579-595.

Craig, J.R and Scott, S.D., 1982. Sulphide phase equilibria. In: Ribbe, P.H., (ed). Reviews in Mineralogy 1. Sulphide mineralogy. Mineral. Soc. Am., CS1-CS109.

Crocket, J.H., 1979. Platinum-group elements in mafic and ultramafic rocks: A survey. Can. Mineral., 17, 391-402.

Crocket, J.H., 1981. Geochemistry of the platinum-group elements. In: Cabri, L.J., (ed). Platinum-group elements: mineralogy, geology, recovery. Can. Inst. Miner. Metal., Spec. Iss. 23, 47-64.

Crocket, J.H., and Cabri, L.J., 1981. Analytical methods for the platinum- group elements. In: Cabri, L.J., (ed). Platinum-group elements: mineralogy, geology, recovery. Can. Inst. Miner. Metal., Spec. Iss. 23, 71-82.

Crocket, J.H., and Teruta, Y., 1977. Palladium, iridium, and gold contents of mafic and ultramafic rocks drilled from the Mid-Atlantic Ridge, Leg 37, Deep Sea Drilling Project. Can. J. Earth Sci., 14, 777-784.

Date, A.R., Davis, A.E., and Cheung, Y.Y., 1987. The potential of fire assay and inductively coupled plasma-mass spectrometry for the determination of platinum group elements in geological materials. Analyst, 112, 1217-1222.

Davidson, P.M, and Lindsley, D.H., 1985. Thermodynamic analysis of quadrilateral pyroxenes. Part II. Model calibration from experiments and applications to geothermometry. Contrib. Mineral. Petrol., 91, 390-404.

Davies, G., and Tredoux, M., 1985. The platinum-group element and gold contents of the marginal rocks and sills of the Bushveld Complex: Econ. Geol., 80 838-848.

de Jongh, W.K., 1973. X-ray fluorescence analysis applying theoretical matrix corrections. Stainless Steel. X-ray Spectrom., 2, 151-157.

Deer, W.A., Howie, R.A., and Zussman, J., 1966. An introduction to rock - forming minerals, Longmans, 528pp.

Dick, H.J.B., 1977. Partial melting in the Josephine Peridotite I. The effect of mineral composition and its consequence for geobarometry and geothermometry. Am. J. Sci., 277, 801-832.

Dick, H.J.B., 1984. Abyssal plagioclase peridotites and melt storage in the mantle beneath mid-ocean ridges (abstract). Trans. Am. Geoph. Union, EOS, 16, 487.

Dick, H.J.B., 1989. Abyssal peridotites, very slow spreading ridges and ocean ridge magmatism. In: Saunders, A.D., and Norry, M.J., (eds). Magmatism in the ocean basins, Geol. Soc. Spec. Publication No 42, 71-105.

Dick, H.J.B., and Bullen, T., 1984. Chromian spinel as a petrogenetic indicator in abyssal and alpine - type peridotites and spatially associated lavas. Contrib. Mineral. Petrol., 86, 54-76.

Dick, H.J.B., and Fisher, R.L, 1984. Mineralogic studies of the residues of mantle melting: Abyssal and alpine-type peridotites. In: Kornprobst, J., (ed). Kimberlites II: The mantle and crust-mantle relationships, Elsevier, 295-308.

Dick, H.J.B., Fisher, R.L, and Bryan, W.L., 1984. Mineralogic variability of the uppermost mantle along mid-ocean ridges. Earth Planet. Sci. Lett., 69, 88-106.

Duncan, R.A., and Green, D.H., 1987. The genesis of refractory melts in the formation of oceanic crust. Contrib. Mineral. Petrol., 96, 326-342.

Duncumb, P., and Jones, E.M., 1969. Tube Investments Company Report, No. 260.

Duncumb, P., and Reed, S.J.B., 1968. Quantitative electron probe microanalysis. National Bureau of Science Special Publication, 298, 133-154.

Dyar, M.D., McGuire, A.V., and Ziegler, R.D., 1989. Redox equilibria and crystal chemistry of coexisting minerals from spinel lherzolites mantle xenoliths. Am. Mineral., 74, 969-980.

Eckstrand, O.R., 1975. The Dumont serpentinite: A model for control of nickeliferous opaque mineral assemblages by alteration reactions in ultramafic rocks. Econ. Geol., 70, 183-201.

Economou, M., 1983. Platinum group metals in chromite ores from the Vourinos ophiolite complex, Greece, Ofioliti, 8, 339-356.

Edwards, S.J., 1990. Harzburgites and refractory melts in the Lewis Hill massif, Bay of Islands ophiolite complex: The base-metals and precious-metals story. Can. Mineral., 28, 537-552.

Elthon, D., 1983. Isomolar and isostructural pseudo-liquidus diagrams for oceanic basalts. Am. Mineral., 68, 506-511.

Elthon, D., 1991. Geochemical evidence for formation of the Bay of Islands ophiolite above a subducyion zone. Nature, 354, 140-143.

Elthon, D., and Ridley, W.I., 1979. Comments on: "The partitioning of nickel between olivine and silicate melt" by S.R. Hart and K.E. Davis. Earth Planet. Sci. Lett., 44, 162-164.

Elthon, D., and Scarfe, C.M., 1984. High-pressure phase equilibria of a high-magnesia basalt and the genesis of primary oceanic basalts. Am. Mineral., 69, 1-15.

Engi, M., 1983. Equilibria involving Al-Cr spinels: Mg-Fe exchange with olivine. Experiments, thermodynamic analysis and consequences for geothermometry. Am. J. Sci., 283-A, 29-71.

Engin, T., and Hirst, D.M., 1970. Serpentinization of harzburgites from the Alpine peridotite belt of southwest Turkey. Chem. Geol., 6, 281-295.

England, R.N., and Davies, H.L., 1973. Mineralogy of ultramafic cumulates and tectonites from eastern Papua. Earth Planet. Sci. Lett., 17, 416-425.

Ernst, W.G., and Piccardo, G.B., 1979. Petrogenesis of some Lingurian peridotites - I. Mineral and bulk rock chemistry. Geochim. Cosmochim. Acta, 43, 219-237.

Evans, C.A., 1985. Magmatic 'metasomatism' in peridotites from the Zambales ophiolite. Geology, 13, 166-169.

Evans, C.A., and Girardeau, J., 1988. Galicia margin peridotites: Undepleted abyssal peridotites from the North Atlantic. In: Boillot, G., Winterer, E.L., et al., Proc. Ocean Drill. Prog., Sci. Results, 103, 195-207

Fabriès, J., 1979. Spinel - olivine geothermometry in peridotites from ultramafic complexes. Contrib. Mineral. Petrol., 69, 329-336.

Falloon, T.J., and Green, D.H., 1987. Anhydrous melting of MORB pyrolite and other peridotite compositions at 10 kb: Implications for the origin of primitive MORB glasses. Mineral. Petrol., 37, 181-219.

Falloon, T.J., and Green, D.H., 1988. Anhydrous partial melting of peridotite from 8 to 35 kb and the petrogenesis of MORB. J. Petrology Special Lithospheric Issue, 379-414.

Falloon, T.J., Green, D.H., Hatton, C.J., and Harris, K.L., 1988. Anhydrous melting of a fertile and depleted peridotite from 2 to 30 kb and application to basalt petrogenesis. J. Petrology, 29, 6, 1257-1282.

Fisk, M.R., and Bence, A.E., 1980. Experimental crystallization of chrome spinel in FAMOUS basalt 527-1-1. Earth Planet. Sci. Lett., 48, 111-123.

Fleet, M.., and Stone, W.E., 1991. Partitioning of platinum-group elements in the Fe-Ni-S system and their fractionation in nature. Geochim. Cosmochim. Acta, 55, 245-253.

Frenkel, M.Y., and Ariskin, A.A., 1985. Computer simulation of basalt-magma equilibrium and fractional crystallization. Geochem. International, 22, 73-84.

Fujii, T., and Bugault, H., 1983. Melting relations of a magnesian abyssal tholeiite and the origin of MORBs. Earth Planet. Sci. Lett., 62, 283-295.

Fujii, T., 1976. Solubility of Al_2O_3 in enstatite coexisting with forsterite and spinel, Carnegie Inst. Wash. Yearbook, 75, 565-571.

Fujii, T., 1977. Pyroxene equilibria in spinel lherzolite, Carnegie Inst. Wash. Yearbook, 76, 569-572.

Fujii, T., 1977. Fe-Mg partitioning between olivine and spinel. Carnegie Inst. Wash. Yearbook, 76, 563-568.

Fujii, T., 1990. Petrology of peridotites from Hole 670A, Leg 109., In: Detrick, R., Honnorez, J., Bryan, W.B., Juteau, T., et al., Proc. Ocean Drill. Prog., Sci. Results, 106/109, 19-25.

Furnes, H., Pedersen, R.G., and Stillman, C.J., 1988. The Leka ophiolite complex, central Norwegian Caledonides: Field characteristics and geotectonic significance. J. Geol. Soc. Lond., 145, 401-412.

Garuti, G., Gorgoni, C., and Sighinolfi, G.P., 1984. Sulphide mineralogy and chalcophile and siderophile element abundances in the Ivrea-Verbano mantle peridotites (western Italian Alps). Earth Planet. Sci. Lett., 70, 69-87.

Gasparic, T., 1984. Two - pyroxene thermobarometry with new experimental data in the system CaO - MgO - Al_2O_3 - SiO_2. Contrib. Mineral. Petrol., 87, 87-97.

Gasparic, T., and Newton, R.C., 1984. The alumina contents of orhtopyroxene in equilibrium with spinel and forsterite in the system $MgO-Al_2O_3-SiO_2$. Contrib. Mineral. Petrol., 85, 186-196.

Gass, I.G., 1968. Is the Troodos massif of Cyprus a fragment of Mesozoic ocean floor? Nature, 220, 39-42.

Gass, I.G., and Masson Smith, D., 1963. The geology and gravity anomalies of the Troodos massif, Cyprus. Phil. Trans. Roy. Soc. Lond., A255, 417-467.

Gass, I.G., and Smewing, J.D., 1981. Ophiolites: Obducted oceanic lithosphere. In: Emiliani, C., (ed). The sea, Vol. 7, 339-361.

Gast, P.W., 1968. Trace element fractionation and the origin of tholeiitic and alkaline magma types. Geochim. Cosmochim. Acta, 32, 1057-1086.

Gauthier, M., Corrivaux, L, Trottier, L.J., Cabri, J., Laflamme, J.H.G., and Bergeron, M., 1990. Chromitites platinifères des complexes ophiolitiques de l' Estrie-Beauce, Appalaches du Sud du Québec. Mineralium Deposita, 25, 169-178.

Gijbels, R., Henderson, P., and Zels, 1976. Geochemisrty of some trace elements in mineral separates from Rhum, Inner Hebrides, with special emphasis on iridium. Econ. Geol., 71, 1364-1370.

Ginzburg, S.I., Ezerskaya, N.A., Prokof'eva, I.V., Fedorenko, N.V., Shlenskaya, V.I., and Bel'skii, N.K., 1975. Analytical chemistry of platinum metals, Kaner, N., (Transl.), Shelnitz, P., (ed). J. Wiley and Sons, New York, 673 pp.

Govindaraju, K., 1989. Compilation of working values and sample description for 272 geostandards. Geostandards Newsletter, Spec. Issue 13, 113pp.

Green, D.H., 1964. The petrogenesis of the high - temperature peridotite intrusion in the Lizard area, Cornwall. J. Petrology, 5, 134-188.

Green, D.H., 1973. Experimental melting studies on a model upper mantle composition at high pressure under water-saturated and water-undersaturated conditions. Earth Planet. Sci. Lett., 19, 37-53.

Green, D.H., 1976. Experimental testing of "equilibrium" partial melting of peridotite under water-saturated, high-pressure conditions. Can. Mineral., 14, 255-268.

Green, D.H., and Ringwood, 1967. The genesis of basaltic magmas. Contrib. Mineral. Petrol., 15, 103-190.

Green, D.H., Falloon, T.J., and Taylor, W.R., 1987. Mantle-derived magmas - roles of variable source peridotite and variable C-H-O fluid compositions. In: Mysen, B.O., (ed). Magmatic processes: Physicochemical principles. Sp. Publ. Geochem. Soc., 1, 139-154.

Greenbaum, D., 1972. Magmatic processes at ocean ridges, evidence from the Troodos massif, Cyprus. Nat. Phy. Sci., 288, 18-2.

Greenough, J.D., and Fryer, B.J., 1990. Distribution of gold, palladium, platinum, rhodium, ruthenium, and iridium in Leg 115 hotspot basalts: Implications for magmatic

processes. In: Duncan, R.A., Backman, J., Peterson, L.C., et al., Proc. Ocean Drill. Prog., Sci. Results, 115, 71-84.

Grove, T.L., and Bryan, W.B., 1983. Fractionation of pyroxene-phyric MORB at low pressure: An experimental study. Contrib. Mineral. Petrol., 84, 293-309.

Grove, T.L., Kinzler, R.J., Bryan, W.B., 1990. Natural and experimental phase relations of lavas from Serocki volcano. In: Detrick, R., Honnorez, J., Bryan, W.B., Juteau, T., et al., Proc. Ocean Drill. Prog., Sci. Results, 106/109, 9-17.

Hamlyn, P.R., and Bonatti, E., 1980. Petrology of mantle-derived ultramafics from the Owen Fracture Zone, northwest Indian ocean: Implications for the nature of the oceanic upper mantle. Earth Planet. Sci. Lett., 48, 65-79.

Hamlyn, P.R., Keays, R.R., Cameron, W.E., Crawford, A.J., and Waldron, H.M., 1985. Precious metals in magnesian low-Ti lavas: Implications for metallogenesis and sulfur saturation in primary magmas. Geochim. Cosmochim. Acta, 49, 1797-1811.

Hanson, G.N., and Langmuir, C.H., 1978. Modelling of major elements in mantle-melt systems using trace element approaches. Geochim. Cosmochim. Acta, 725-741.

Harkins, M.E., Green, H.W., and Moores, E.H., 1980. Multiple intrusive events documented from the Vourinos ophiolite, northern Greece. Am. J. Sci., 280-A, 284-295.

Harper, G.D., 1984. The Josephine ophiolite, northwestern California. Geol. Soc. Am. Bull., 95, 1009-1026.

Hart, S.R., and Davis, K.E, 1978. Nickel partitioning between olivine and silicate melt. Earth Planet. Sci. Lett., 40, 203-220.

Hart, S.R., and Davis, K.E., 1979. Reply to D, B, Clarke and M, J, O'Hara, "Nickel, and the existence of high-MgO liquids in nature". Earth Planet. Scl. Lett., 44, 159-161.

Hart, S.R., and Zindler, A., 1986. In search of a bulk earth composition. Chem. Geol., 57, 247-267.

Haughton, D.R., Roeder, P.L., and Skinner, B.J., 1974. Solubility of sulphur in mafic magmas. Econ. Geol., 69, 451-467.

Heinrich, K.F.J., 1967. 2nd national conference on electron-probe microanalysis, Boston, USA. Paper no. 7.

Helz, R.T., 1977. Determination of the P-T dependence of the first appearance of FeS-rich liquid in natural basalts to 20 kb, (abstract), Trans. Am. Geoph. Union, EOS, 58, 523.

Hemley, J.J., Montoya, J.W., Christ, C.L, and Hostetler, P.B., 1977a. Mineral equilibria in the $MgO-SiO_2-H_2O$ system: I Talc-chrysotile-forsterite-brucite stability relations. Am. J. Sci., 277, 322-351.

Hemley, J.J., Montoya, J.W., Shaw, D.R., and Luce, R.W., 1977b. Mineral equilibria in the $MgO-SiO_2-H_2O$ system: II Talc-antigorite-forsterite-anthophyllite-enstatite stability relations and some geologic implications in the system. Am. J. Sci., 277, 353-383.

Henderson, P., and Wood, R.J., 1981. Reaction relationships of chrome-spinels in igneous rocks - Further evidence from the layered intrusions of Rhum and Mull, Inner Hebrides, Scotland. Contrib. Mineral. Petrol., 78, 225-229.

Henry, D.J., and Medaris, L.G., 1980. Application of pyroxene and olivine - spinel geothermometers to spinel peridotites in southwestern Oregon. Am. J. Sci., 280A, 211-231.

Hertogen, J., and Gijbels, R., 1976. Calculation of trace element fractionation during partial melting. Geochim. Cosmochim. Acta, 40, 313-322.

Hertogen , J., Janssens, M-J., and Palmer, H., 1980. Trace elements in ocean ridge basalt glasses: implications for fractionations during mantle evolution and petrogenesis. Geochim. Cosmochim. Acta, 44, 2125-2143.

Herzberg, C.T., 1978. Pyroxene geothermometry and geobarometry: experimental and thermodynamic evaluation of some subsolidus phase relations involving pyroxenes in the system $CaO-MgO-Al_2O_3-SiO_2$. Geochim. Cosmochim. Acta, 42, 945-957.

Hess, H.H., 1964. The oceanic crust, the upper mantle, and the Mayaguez serpentinized peridotite. Natl. Acad. Sci. Natl. Res. Council Publ. 1118, 169-175.

Hiemstra, G.H., 1980. The role of collectors in the formation of platinum deposits in the Bushveld Complex. Can. Mineral., 17 469-482.

Hill, R., and Roeder, P., 1974. The crystallisation of spinel from basaltic liquid as a function of oxygen fugacity. J. Geol., 82, 709-729.

Hoffman, E.L., Naldrett, L.A., Van Loon, J.C., Hancock, R.G.V., and Manson, A., 1978.The determination of all the platinum group elements and gold in rocks and ore by neutron activation analysis after preconcentration by a nickel sulphide fire-assay technique on large samples. Anal. Chim. Acta, 102, 157-166.

Irvine, T.N., 1965. Chromian spinel as a petrogenetic indicator, Part 1 : Theory. Can. J. Earth Sci., 2, 648-671.

Irvine, T.N., 1967. Chromian spinel as a petrogenetic indicator, Part 2 : Petrologic applications. Can. J. Earth Sci., 4, 71-103.

Ishii, T., Robinson, , Maekawa, H., and Fiske, R., (in press). Petrological studies of peridotites from serpentinite diapiric seamounts in the Izu-Ogasawara-Mariana forearc. ODP Leg 125.

Ishiwatari, A., 1985/1986. Alpine ophiolites: product of low-degree mantle melting in a Mesozoic transcurrent rift zone. Earth Planet. Sci. Lett., 76, 93-108.

Ito, K., 1973. Analytical approach to estimating the source rock of basaltic magmas: Major elements. J. Geoph. Res., 78, 412-431.

Jackson, S.E., Fryer, B.J., Gosse, W., Healy, D.C., Longerich, H.P., and Strong, D.F., 1990. Determination of the precious metals in geological materials by inductively coupled plasma-mass spectrometry (ICP-MS) with nickel sulphide fire assay collection and tellurium co-precipitation. Chem. Geol., 83, 119-132.

Jagoutz, E., Palme, H., Baddenhausen, H., Blum, K., Cendales, M., Dreibus, G., Spettel, B., Lorenz, V., and Wanke, H., 1979. The abundances of major, minor and trace elements in the earth's mantle as derived from primitive ultramafic nodules. Proc. Lunar Plan. Sci. Conf. 10th, 2031-2050.

Janecky, D.R., and Seyfried, W.E.Jr., 1986. Hydrothermal serpentinization of peridotite within the oceanic crust: Experimental investigations of mineralogy and major element chemistry. Geochim. Cosmochim. Acta, 50, 1357-1378.

Jaques, A.L., 1980. Petrologic and experimental studies on the petrogenesis of Papua New Guinea ophiolites, Unpubl. Ph.D. thesis, University of Tasmania.

Jaques, A.L., and Green, D.H., 1980. Anhydrous melting of peridotite at 0-15 kb pressure and the genesis of tholeiitic basalts. Contrib. Mineral. Petrol., 73, 287-310.

Jenkins, D.M., 1981. Experimental phase relations of hydrous peridotites modelled in the system H_2O-CaO-MgO-Al_2O_3-SiO_2. Contrib. Mineral. Petrol., 77, 166-176.

Jenkins, R., and de Vries, J.L., 1970. Practical X-ray spectrometry. Macmillan.

Johan, J., and Augé, T., 1986. Ophiolitic mantle sequences and their evolution: Mineral chemistry constraints. In: Gallagher, M.J., Ixer, R.A., Neary, C.R., and Prichard, H.M., (eds). Metallogeny of basic and ultrabasic rocks. Inst. Miner. Metal., 305-317.

Johannes, W., 1969. An experimental investigation of the system MgO-SiO_2-H_2O-CO_2. Am. J. Sci., 267, 1083-1104.

Johannes, W., 1968. Experimental investigation of the reaction forsterite + water = serpentine + brucite. Contrib. Mineral. Petrol., 19, 309-315.

Jones, G., 1990. Tectonostratigraphy and evolution of the Mesozoic Pindos ophiolite and related units, northwestern Greece. Unpubl. PhD thesis, University of Edinburgh.

Jones, J.H., and Drake, M.J., 1986. Geochemical constraints on core formation in the earth. Nature, 322, 221-228.

Jurewicz, A.J.G., and Watson., E.B., 1988. Cations in olivine, Part 1: Calcium partitioning and calcium-magnesium distribution between olivines and coexisting melts, with petrologic applications. Contrib. Mineral. Petrol., 99, 176-185.

Juteau, T., Berger, E., and Cannat, M., 1990. Serpentinized, residual mantle peridotites from the M.A.R. Median Valley, ODP Hole 670A (21°10'N, 45°02'W, Leg 109): Primary mineralogy and geothermometry. In: Detrick, R., Honnorez, J., Bryan, W.B., Juteau, T., et al., Proc. Ocean Drill. Prog., Sci. Results, 106/109, 27-45.

Kantza, A., (in prep.). Hydrothermal alteration processes in the Pindos ophiolite, NW Greece. PhD thesis, University of Newcastle upon Tyne.

Karup-Møller, S., and Makovicky, E., 1986. The system Pd-Co-S at 1000°, 800°, 600°, and 400°C. Econ. Geol., 81, 1986. 1049-1055.

Keays, R.R., and Campbell, I.H., 1981. Precious metals in the Jimberlana Intrusion, Western Australia. Implications for genesis of platiniferous ores in layered intrusions: Econ. Geol., 76 1118-1141.

Keays, R.R., and Crocket, J.H., 1970. A study of precious metals in the Sudbury nickel irruptive ores. Econ. Geol., 65, 438-450.

Keays, R.R., Sewell, K., and Mithell, R.H., 1981. Platinum and palladium minerals in upper-mantle derived lherzolites. Nature, 294, 646-648.

Keays, R.R., Nickel, E.H., Groves, D.I., and McGoldrick, P.J., 1982. Iridium and palladium as discriminants of volcanic-exhalative hydrothermal and magmatic nickel sulphide mineralization. Econ. Geol., 77 1535-1547.

Kelemen, P.B., Joyce, D.B., Webster, J.D., and Holloway, J.R., 1990. Reaction between ultramafic rock and fractionating basltic magma II. Experimental investigation of reaction between olivine tholeiite and harzburgite at 1150-1050°C and 5 kb. J. Petrol., 31, 99-134.

Kemp, A.E.S., and McKaig, A., 1984. Origins and significance of rocks in an imbricate thrust zone beneath the Pindos ophiolite, northwestern Greece. In: Dixon, J.E., and Robertson, A.H.F., (eds). The geological evolution of the Eastern Mediterranean, Sp. Publ. Geol. Soc. Lond., 17, 569-580.

Kilinc, A., Carmichael, I.S.E., Rivers., M.L., and Sack.R.O., 1983. The ferric-ferrous ratio of natural silicate liquids equilibrated in air. Contrib. Mineral. Petrol., 83, 136-140.

Kimball, K.I., 1988. High-temperature hydrothermal alteration of ultramafic cumulates from the base of the sheeted dikes in the Josephine ophiolite, NW California. J. Geoph. Res., 93, 4675-6487.

Kimball, K.I., 1990. Effects of hydrothermal alteration on the compositions of chromian spinels. Contrib. Mineral. Petrol., 105, 337-346.

Kinzler, R.J., and Grove, T.L., 1985. Crystallization and differentiation of Archean komatiite lavas from northeast Ontario: phase equilibrium and kinetic studies. Am. Mineral., 70, 40-51.

Kinzler, R., J., Grove, T., L, and Recca, S., I., 1988. Experimental study of the effect of Fe on Ni partitioning between olivine and melt (abstract). Trans. Am. Geoph. Union, EOS, 69, 512.

Kirby, G.A., 1979. The Lizard Complex as an ophiolite. Nature, 282, 58-61.

Klein, E., M., and Langmuir., C., H., 1987. Global correlations of ocean ridge basalt chemistry with axial depth and crustal thickness. J. Geoph. Res., 92, 8089-8115.

Köhler, T.P., and Brey, G.P., 1990. Calcium exchange between olivine and clinopyroxene calibrated as a geothermobarometer for natural peridotites from 2 to 60 kb with applications. Geochim. Cosmochim. Acta, 54, 2375-2388.

Kostopoulos, D.K., 1988. Geochemistry, petrogenesis and tectonic setting of the Pindos ophiolite, NW Greece, Unpubl. Ph.D. thesis, University of Newcastle upon Tyne, 528pp.

Kostopoulos, D.K., 1991. Melting of the shallow upper mantle: A new perspective. J. Petrology, 32, 671-699.

Kostopoulos, D.K., (in press). Topology of partial melts generated in static and rising mantle: Implications for the origin of Mg-MORB. submitted to Contrib. Mineral. Petrol.

Kostopoulos, D.K., and James, S.D., (in press)., Parameterization of partial melting processes in the shallow upper mantle and the effects of variable lithospheric stretching on mantle modal stratification and trace element concentrations in magmas. submitted to J. Petrology.

Krauskopf, K., 1979. Introduction to goechemistry. McGraw-Hill.

Kushiro, I., Yoder, H.S., and Nishikawa, M., 1968. Effect of water on the melting of enstatite. Geol. Soc. Am. Bull., 79, 1685-1962.

Leblanc, M, Dupuy, C and Merlet, C, 1984. Nickel content of olivine as discriminatory factor between tectonite and cumulate peridotite in ophiolites. Sci. Géol. Bull., 37, 131-135.

Legendre, O., and Augé, T., 1985. Mineralogy of platinum-group mineral inclusions in chromitites from different ophiolitic complexes. In: Gallagher, M.J., Ixer, R.A., Neary, C.R., and Prichard, H.M., (eds). Metallogeny of basic and ultrabasic rocks, 361-372.

Lehman, J., 1983. Diffusion berween olivine and spinel: Application to geothermometry. Earth Planet. Sci. Lett., 64, 123-138.

Liang, Y., and Elthon, D., 1990. Evidence from chromium abundances in mantle rocks for extraction of picrite and komatiite melts. Nature, 343, 551-553.

Lindsley, D.H., and Andersen, D.J., 1983. A two-pyroxene thermometer. J. Geoph. Res., Suppl., 88, A887-A906.

Loney, R, A., Himmelberg, G, R and Coleman, R, G, 1971. Structure and petrology of the alpine-type peridotite at Burro Mountain, California, USA. J. Petrology, 12, 245-309.

Longhi, J., Walker, D., and Hays, J.F., 1978. The distribution of Fe and Mg between olivine and lunar basaltic liquids. Geochim. Cosmochim. Acta, 42, 1545-1558.

Longhi, J., Wooden, J.L., and Coppinger, K.D., 1983. The petrology of high-Mg dykes from the Beartooth Mountains, Montana: A search for the parent magma of the Stillwater complex. J. Geoph. Res., 88, Suppl., B53-B69.

Lorand, J.P., 1987. Cu-Fe-Ni-S mineral assemblages in the upper-mantle peridotites from the Table Mountain and Blow-Me-Down Mountain ophiolite massifs (Bay of Islands are, Newfoundland): Their relationships with fluids and silicate melts. Lithos, 20, 59-76.

Lorand, J.P., 1989. Abundance and distribution of Cu-Fe-Ni-S sulphides, sulphur, copper, and platinum-group elements in orogenic-type spinel lherzolite massifs of Ariège (northeastern Pyrenees, France). Earth Planet. Sci. Lett., 93, 50-64.

Lorand, J.P., 1990. Are spinel lherzolite xenoliths representative of the abundance of sulphur in the upper mantle? Geochim. Cosmochim. Acta, 54, 1487-1492.

Lorand, J.P., and Pinet, M., 1984. L' orcelite des peridotites de Beni Bousera (Maroc), Ronda (Espagne), Table Mountain et Blow-Me-Down Mountain (Terre Neuve) et du Pinde Septentrional (Grèce). Can. Mineral., 22, 553-560.

Loughnan, F.C., 1969. Chemical weathering of the silicate minerals, Elsevier, 154pp.

Maaløe, S., 1976. Quantitative aspects of fractional crystallization of major elements. J. Geol., 84, 81-96.

Maaløe, S., and Aoki, K., 1977. The major elements composition of the upper mantle estimated from the composition of lherzolites. Contrib. Mineral. Petrol., 64, 161-173.

Maaløe, S., and Steel, R., 1980. Mantle composition derived from the composition of lherzolites. Nature, 285, 321-322.

MacGregor, I.D., 1974. The system $MgO-Al_2O_3-SiO_2$: solubility of Al_2O_3 in enstatite for spinel and garnet peridotite compositions. Am. Mineral., 59, 110-119.

MacLean, W.H., 1969. Liquidus phase relations in the $FeS-FeO-Fe_3O_4-SiO_2$ system, and their application in geology. Econ. Geol., 64, 865-884.

McTaggart, K.C., 1971 On the origin of ultramafic rocks. Geol. Soc. Am. Bull., 83, 41-58.

Magaritz, M., and Taylor, H.P. Jr., 1974. Oxygen and hydrogen isotope studies of serpentinization in the Troodos ophiolite complex, Cyprus. Earth Planet. Sci. Lett., 23, 8-14.

Malpas, J., 1978. Magma generation in the upper mantle, field evidence from ophiolite suites and application to the generation of oceanic lithosphere. Phil. Trans. Roy. Soc. Lond., 288, 527-546.

Mathez, E.A., 1976. Sulfur solubility and magmatic sulphides in submarine volcanic glass, J. Geoph. Res., 81, 4269-4275.

Mattioli, G.S., and Wood, B.J., 1986. Upper mantle oxygen fugacity recorded by spinel lherzolites. Nature, 322, 626-628.

Mattioli, G.S., and Wood, B.J., 1988. Magnetite activities across the $MgAl_2O_4-Fe_3O_4$ spinel join, with application to thermobarometric estimates of upper mantle oxygen fugacities. Contrib. Mineral. Petrol., 98, 148-162.

Maurel, C., and Maurel, P., 1982a, Etúde experimentale des conditions de cristallisation de spinelle chromifere dans des bains silicates basiques, en presence d' olivine et de clinopyroxene. C, R, Acad. Sc. Paris, 295, Serie II, 489-491.

Maurel, C., and Maurel, P., 1982b, Etúde experimentale de la solubilite du chrome dans les bains silicates basiques et de sa distribution entre liquide et mineraux coexistants: conditions d' existence du spinelle chromifere. Bull. Mineral., 105, 640-647.

McKenzie, D., 1984. The generation and compaction of partially molten rock. J. Petrology, 25, 713-765.

McKenzie, D., and Bickle, M.J., 1988. The volume and composition of melt generated by extension of the lithoshpere. J. Petrology, 29, 625-679.

McKenzie, D., and O'Nions, R.K., 1991. Partial melt distributions from inversion of rare earth element concentrations, J. Petrol., 32, 1021-1091.

Melidonis, K., and Dimou, E., 1978. On the occurrence of massive sulphides from Pindos, Distrato-Armata area, Konitsa, I.G.M.E., Athens, Internal Report.

Menzies, M., and Allen, C., 1974. Plagioclase lherzolite - residual mantle relationships within two Eastern Mediterranean ophiolites. Contrib. Mineral. Petrol., 45, 197-213.

Mercier, J.-C.C., 1976. Single - pyroxene geothermometry and geobarometry. Am. Mineral., 61, 603-615.

Mercier, J.-C.C., 1980. Single - pyroxene thermobarometry. Tectonophysics, 70, 1-37.

Mercier, J.-C.C., and Nicolas, A., 1975. Textures and fabrics of upper-mantle peridotites as illustrated by xenoliths from basalts. J. Petrol., 16, 454-487.

Mercier, J.-C.C., Benoit, V., and Girardeau, J., 1984. Equilibrium state of diopside-bearing harzburgites from ophiolites: geobarometric and geodynamic implications. Contrib. Mineral. Petrol., 85, 391-403.

Michael, P.J., and Bonatti, E., 1985a. Peridotite composition from the North Atlantic: regional and tectonic variations and implications for partial melting. Earth Planet. Sci. Lett., 73, 91-104.

Michael, P.J., and Bonatti, E., 1985b. Petrology of ultramafic rocks from Sites 556, 558, and 560 in the North Atlantic. In: Bougault, H., Cande, S.C., et al., Init. Repts. Deep Sea Drill. Project, 82.

Miller, R.B., and Mogk, D.W., 1987. Ultramafic rocks of a fracture-zone ophiolite, north Cascades, Washington. Tectonophysics, 142, 261-289.

Mitchell, R.H., and Keays, R.R., 1981. Abundance and distribution of gold, palladium and iridium in some spinel and garnet lherzolites: Implications for the nature and origin of precious metal-rich intergranular components in the upper mantle. Geochim. Cosmochim. Acta, 45, 2425-2442.

Miyashiro, A., 1973. The Troodos complex was probably formed in an island arc. Earth Planet. Sci. Lett., 25, 217-22.

Miyashiro, A., Shido, F., and Ewing, M., 1969. Composition and origin of serpentinites from the Mid - Atlantic Ridge near 24° and 30° North Latitude. Contrib. Mineral. Petrol., 23, 117-127.

Moody, J.B., 1976a. An experimental study on the serpentinization of iron-bearing olivines. Can. Mineral., 14, 462-478.

Moody, J.B., 1976b. Serpentinization: a review, Lithos, 9, 125-138.

Moores, E.M., 1969. Petrology and structure of the Vourinos ophiolite complex of northern Greece. Geol. Soc. Am. Spec. Paper, 118, 1-74.

Moores, E.M., and Vine, F.J., 1971. Troodos massif, Cyprus and other ophiolites as oceanic crust: Evaluation and implications. Phil. Trans. Roy. Soc. Lond., A268, 443-466.

Morgan, J.W., Wandless, G.A., Petrie, R.K., and Irving, A.J., 1981. Composition of the earth's upper mantle, I. Siderophile trace elements in ultramafic nodules. Tectonophysics, 75, 47-67.

Morgan, J.W., 1986. Ultramafic xenoliths: Clues to the earth's late accretionary history. J. Geoph. Res., 91, 12375-12387.

Murck, B.W., and Campbell, I.H., 1986. The effects of temperature, oxygen fugacity and melt composition on the behaviour of chromium in basic and ultrabasic melts. Geochim. Cosmochim. Acta, 50, 1871-1909.

Mutschler, F.E., Rougon, D.J., and Lavin, O.P., 1976. PETROS - A data bank of major element chemical analysis of igneous rocks for research and teaching. Computers and Geoscience, 2, 51-57.

Mysen, B.O., 1979. Nickel partitioning between olivine and silicate melt: Henry's Law revisited. Am. Mineral., 64, 1107-1114.

Mysen, B.O., 1981. Nickel partitioning between olivine and liquid in natural basalts: Henry's Law behavior - Comment on a paper by P.I. Nabelek. Earth Planet. Sci. Lett., 52, 222-224.

Mysen, B.O., 1982. Partitioning of Ni between olivine and silicate melt: the "Henry's Law" problem reexamined: Discussion. Geochim. Cosmochimim. Acta, 46, 297-298.

Mysen, B.O., 1986. Structure and petrologically important properties of silicate melts relevant to natural magmatic liquids. In: Scarfe, C.M., (ed). Short course in silicate melts. Miner. Assoc. Can., 180-209.

Mysen, B.O., and Boettcher, A.L., 1975. Melting of a hydrous mantle: II. Geochemistry of crystals and liquids formed by anatexis of mantle peridotite at high pressures and high temperatures as a function of controlled activities of water, hydrogen, and carbon dioxide. J. Petrol., 16, 549-5 93.

Nagata, J., Goto, A., and Obata, M., 1983. The parabolic pattern of chromium partitioning observed between pyroxenes and spinel from ultramafic rocks and its petrologic significance. Contrib. Mineral. Petrol., 82, 42-51.

Naldrett, A.J., 1969. A portion of the system Fe-S-O between 900 and 1080°C and irs application to sulphide ore magmas. J. Petrology, 10, 2, 171-201.

Naldrett, A.J., 1981a. Nickel sulphide deposits: classification, composition and genesis. Econ. Geol., 75, 628-655.

Naldrett, A.J., 1981b. Platinum-group element deposits. Can. Inst. Miner. Metal., Spec. Iss. 23, 197-232.

Naldrett, A.J., Hoffman, E.L., Green, A.H., Chou, C.-L., Naldrett, S.R., and Alcock, R.A., 1979. The composition of Ni-sulphide ores, with particular reference to their content of PGE and Au. Can. Mineral., 17, 403-415.

Nell, J., and Wood, B.J., 1989. Thermodynamic properties in a multicomponent solid solution involving cation disorder: Fe_3O_4-$FeCr_2O_4$-Mg-$FeAl_2O_4$ spinels. Am. Mineral., 74, 1000-1015.

Nell, J., and Wood, B.J., 1991. High temperature electric measurements and thermodynamic properties of the Fe_3O_4-$FeCr_2O_4$-$MgCr_2O_4$-$FeAl_2O_4$ spinel. Am. Mineral., 76, 427-444.

Nicholls, I.A., 1974. Liquids in equilibrium with peridotitic mineral assemblages at high water pressures, Contrib. Mineral. Petrol., 45, 289-316.

Nicholls, I.A., Ferguson, J., Jones, H., Marks, G.P., and Mutter, J.C., 1981. Ultramafic blocks from the ocean floor southwest of Australia. Earth Planet. Sci. Lett., 56, 362-374.

Nickel, K.G., and Green, D.H., 1985. Empirical geothermobarometry for garnet peridotites and implications for the lithosphere, kimberkites and diamonds. Earth Planet. Sci. Lett., 73, 158-170.

Nicolas, A., 1989a. Analyse preliminaire des donnes structurales du Vourinos. Inst. Geol. Min. Res. (Greece), Int. Rept., 14 pp.

Nicolas, A., 1989b. Structures of ophiolites and dynamics of oceanic lithosphere. Kluwer Academic Publishers, 367pp.

Nicolas, A., Boudier, F., and Bouchez, J., 1980. Interpretation of peridotite structures from ophiolitic and oceanic environments. Am. J. Sci., 280A, 192-210.

Nicolas, A., and Dupuy, C., 1984. Origin of ophiolitic and oceanic lherzolites. Tectonophysics, 110, 177-187.

Nicolas, A., and Poipier, J., 1976. Crystalline plasticity and solid state flow in metamorphic rocks. J. Wiley Interscience Publ., London, 444 pp.

Nicolas, A., and Prinzhofer, A., 1983. Cumulative or residual origin for the transition zone in ophiolites: Structural evidence. J. Petrol., 24, 188-206.

Nicolas, A., Boudier, F., and Bouchez, J.-L., 1980. Interpretation of peridotite structures from ophiolitic and oceanic environments. Am. J. Sci., 280-A, 192-210.

Nielsen, R.L., 1985. EQUIL: A program for the modelling of low-pressure differentiation processes in natural mafic magma bodies. Computers and Geoscience, 11, 531-546.

Nielsen, R.L., and Drake, M.J., 1979. Pyroxene-melt equilibria. Geochim. Cosmochim. Acta, 43, 1259-1272.

Niu, Y., and Batiza, R.J., (in press). An empirical method for calculating melt compositions produced beneath mid-ocean ridges: Applications for axis and off-axis (seamounts) melting. Submitted to the J. Geoph. Res.

Noiret, G., Montigny, R., and Allègre, C.J., 1981. Is the Vourinos complex an island arc ophiolite? Earth Planet. Sci. Lett., 56, 375-386.

O'Hara, M.J., 1968. The bearing of phase equilibria studies in synthetic and natural systems on the origin and evaluation of basic and ultrabasic rocks. Earth Sci. Rev., 4, 69-133.

O'Neill, H.St.C., 1987. The quartz-fayalite-iron and quartz-fayalite-magnetite equilibria and the free energies of formation of fayalite (Fe_2SiO_4) and magnetite (Fe_3O_4). Am. Mineral., 72, 67-75.

O'Neill, H.St.C., and Wall, V.J., 1987. The olivine-orthopyroxene-spinel oxygen geobarometer, the nickel precipitation curve, and the oxygen fugacity of the earth's upper mantle. J. Petrology 28, 1169-1191.

Ono, A., 1983. Fe-Mg partitioning between spinel and olivine. J. Japan. Assoc. Miner. Petr. Econ. Geol., 78, 115-122.

Oshin, I.O., and Crocket, J.H., 1982. Noble metals in Thetford Mines ophiolites, Quebec. Canada. Part I: Distribution of gold, iridium, platinum, and palladium in the ultramafic and gabbroic rocks. Econ. Geol, 77, 1556-1570.

Page, N.J., Rowe, J.J., and Haffty, J., 1976. Platinum metals in the Stillwater complex, Montana. Econ. Geol., 71, 1352-1363.

Page, N.J., Pallister, J.S., Brown, M.A., Smewing, J.D., and Haffty, J., 1982a. Palladium, platinum, rhodium, iridium and ruthenium in chromite-rich rocks from the Samail ophiolite, Oman. Can. Mineral., 20, 537-548.

Page, N.J., Cassard, D., and Haffty, J., 1982b. Palladium, platinum, rhodium, ruthenium, and iridium in chromitites from the Massif du Sud and Tiébaghi Massif, New Caledonia. Econ. Geol., 77, 1571-1577.

Page, N.J., Singer, D.A., Moring, B.C., and Carlson, C.A., 1986. Platinum-group element resources in podiform chromitites from California to Oregon. Econ. Geol., 37, 1261-1271.

Page, N.J., Pallister, J.S., Brown, M.A., Smewing, J.D., and Haffty, J., 1982c. Platinum, rhodium, iridium and ruthenium in chromite-rich rocks from the Samail ophiolite, Oman. Can. Mineral., 20, 537-548.

Page, N.J., and Talkington, R.W., 1984. Palladium, platinum, rhodium, ruthenium and iridium in peridotites and chromitites from ophiolite complexes in Newfoundland. Can. Mineral., 22, 137-149.

Page, N.J., Myers, J.S., Haffty, J., Simon, F.O., and Aruscavage, P.J., 1980. Platinum, palladium and rhodium in the Fiskenaesset Complex, Southwestern Greenland. Econ. Geol., 75 907-915.

Paraskevopoulos, G.M., 1975. Cumulate cyclicity as crystallization product in layered gabbroic sequences, southern Pindos complex. Proc. Acad. Athens, 50, 429-442.

Parry, S.J., Sinclair, I.W., and Asif, M., 1988. Evaluation of the nickel sulphide bead method of fire-assay for the platinum-group elements using neutron activation analysis. In: Prichard, H.M., Potts, P.J., Bowles, J.F.W., and Cribb, S., (eds). Geoplatinum 87, Elsevier, Barking, 21-28.

Peach, C.L., Mathez, E.A., and Keays, R.R., 1990. Sulphide melt-silicate melt distribution coefficients for noble metals and other chalcophile elements as deduced from MORB: Implications for partial melting. Geochim. Cosmochim. Acta, 54, 3379-3389.

Pearce, J.A., and Cann, J.R., 1973. Tectonic setting of basic volcanic rocks determined using trace element analyses. Earth Planet. Sci. Let., 19, 290-300.

Pearce, J.A., and Norry, M.J., 1979. Petrogenetic implications of Ti, Zr, Y and Nd variations in volcanic rocks. Contrib. Mineral. Petrol., 69, 33-47.

Pearce, J.A., Lippard, S.J., and Roberts, S., 1984. Characteristics and tectonic significance of supra-subduction zone ophiolites. In: Kokellar, B.P., and Howells, M.F., (eds). Marginal basin geology. Spec. Publ. Geol. Soc. Lond., 16, 77-94.

Philibert, J., 1963. X-ray optics and X-ray microanalysis: 3rd International Symposium. Academic Press, 379-392.

Pike, N.J.E., and Schwarzman, E.C., 1977. Classification of textures in ultramafic xenoliths. J. Geol., 85, 49-61.

Pistorius, C.W.F.T., 1963. Some phase relations in the system MgO-SiO_2-H_2O to high pressures and temperatures. Neues J. Miner. Monatsh., 11, 283-293.

Poulson, S.R., and Ohmoto, H., 1990. An evaluation of the solubility of sulphide sulphur in silicate melts from experimental data and natural samples. Chem. Geol., 85, 57-75.

Powell, R., 1978. The thermodynamics of pyroxenes geotherms. Phill. Trans. Roy. Soc. Lond., A288, 457-469.

Presnall, D.C., 1969. The geometrical analysis of partial fusion. Am. J. Sci., 267, 1180-1194.

Presnall, D.C., and Hoover, J.D., 1984. Composition and depth of origin of primary mid-ocean ridge basalts. Contrib. Mineral. Petrol., 87, 170-178.

Prichard, H.M., 1979. A petrographic study of the process of serpentinization in ophiolites and the ocean crust. Contrib. Mineral. Petrol., 68, 231-241.

Prichard, H.M., Potts, P.J., and Neary, C.R., 1981. Platinum group element minerals in the Unst chromite, Shetland Isles: Inst. Miner. Metall., 90, B186-B188.

Prichard, H.M., Neary, C.R., and Potts, P.J., 1985. Platinum group minerals in the Shetland Ophiolite, In: Gallagher, M.J., Ixer, R.A., Neary, C.R., and Prichard, H.M., (eds). Metallogeny of basic and ultrabasic rocks, 395-414.

Prichard, H.M., and Lord, R.A., 1990. Platinum and palladium in the Troodos ophiolite complex, Cyprus. Can. Mineral., 28, 607-617.

Prichard, H.M., Potts, P.J., Neary, C.R. Lord, R.A., and Ward, G.R., 1989. Development of techniques for the determination of the platinum-group elements in ultramafic rock complexes of potential economic significance: mineralogical studies. Commision European Communities, Report No EUR 11631, 163pp.

Prinzhofer, A., and Allègre, C.J., 1985. Residual peridotites and the mechanisms of partial melting. Earth Plan. Sci. Lett., 74, 251-265.

Rassios, A., 1989. Internal structure of the Dramala peridotite, Pindos ophiolite, Greece (abstract). Tethyan Working Group Meeting, Edinburgh.

Rassios, A., and Grivas, E., 1988. Peridotite as potential host of chromite deposits in Pindos. Preliminary findings. Inst. Geol. Min. Res. (Greece), Int. Rept., 21 pp.

Reed, S.J.B. 1965. Characteristic fluorescence corrections in electronprobe microanalysis. British Journal of Applied Physics, 16, 913-926.

Ringwood, A.E., 1975. Composition and petrology of the Earth's mantle. McGraw Hill, 618 pp.

Robèrt, R.V.D., Van Wyk, E., Palmer, R., and Steele, T.W., 1971. Concentration of the noble metals by a fire-assay technique using nickel sulphide as the collector. South Africa, Natl. Inst. Metallurgy Rept. 1371, 20pp.

Roberts, S., 1986. The role of igneous processes in the formation of ophiolitic chromitite. Unpubl. PhD thesis, Open University, 261pp.

Roeder, P.L., and Emslie, R.F., 1970. Olivine-melt equilibrium. Contrib. Mineral. Petrol., 29, 275-289.

Roeder, P.L., Campbell, I.H., and Jamieson, H.E., 1979. A re-evaluation of the olivine spinel geothermometer. Contrib. Mineral. Petrol., 68, 325-335.

Roeder, P.L., and Reynolds, I., 1991. Crystallization of chromite and chromium solubility in basaltic melts, J. Petrol., 32, 909-934.

Ross, J., and Zimmermanm J., 1982. The Pindos ophiolite complex: Evolution and tectonic significance of the tectonite suite (abstract). Geol. Eastern Mediterranean, Athens, 95.

Ross, J., Mercier, J.-C., Ave Lallemant, H., and Carter, N., 1980. The Vourinos ophiolite complex, Greece: The tectonite suite. Tectonophysics, 70, 63-83.

Ross, J.R., and Keays, R.R., 1979. Precious metals in volcanic-type nickel sulphide deposits in Western Australia. I. Relationship with the composition of the ores and their host rocks. Can. Mineral., 17, 417-435.

Sachtleben, T., and Seck, H.A., 1981. Chemical control of Al - solubility in orthopyroxene and its implication on pyroxene geothermometry. Contrib. Mineral. Petrol., 78, 157-165.

Sack, R.O., and Ghiorso, M.S., 1989. Importance of considerations of mixing properties in establishing an internally consistent thermodynamic database: thermochemistry of minerals in the system Mg_2SiO_4-Fe_2SiO_4-SiO_2. Contrib. Mineral. Petrol., 102, 41-68.

Sack, R.O., and Ghiorso, M.S., 1991. Chromian spinel as a petrogenetic indicator: Thermodynamics and petrological applications. Am. Mineral., 76, 827-847.

Sato, H., 1977. Nickel content of basaltic magmas: identification of primary magmas and a measure of the degree of olivine fractionation. Lithos, 10, 113-120.

Schreiber, H.D., 1977. Redox states of Ti, Zr, Hf, Cr, and Eu in basaltic magmas. An experimental study. Proc. Lunar Sci. Conf., 8th, 1785-1807.

Schreiber, H.D., and Haskin, L.A., 1976. Chromium in basalts: Experimental determination of redox states and partitioning among synthetic silicate phases. Proc. Lunar Sci. Conf., 7th, 1221-1259.

Sen, G., and Jones, R., 1989. Experimental equilibration of multicomponent pyroxenes in the spinel peridotite field: Implications for practical thermometers and a possible barometer. J. Geoph. Res., 94, 17871-17880.

Seyfried, W.E.Jr., and Dibble, W.E.Jr., 1980. Seawater-peridotite interaction at 300°C and 500 bars: implications for the origin of oceanic serpentinites. Geochim. Cosmochim. Acta, 44, 309-321.

Shaw, D.M., 1970. Trace element fractionation during anatexis. Geochim. Cosmochim. Acta, 34, 237-243.

Shazali, I., Van't Dack, L., and Gijbels, R., 1988. Preconcentration of precious metals by tellurium sulphide fire-assay followed by instrumental neutron activation analysis. In: Prichard, H.M., Potts, P.J., Bowles, J.F.W., and Cribb, S., (eds). Geoplatinum 87, Elsevier, Barking, 29-42.

Shibata, T., and Thompson, G., 1986. Peridotites from the Mid-Atlantic Ridge at 43°N and their petrogenetic relation to abyssal tholeiites. Contrib. Mineral. Petrol., 93, 144-159.

Sideris, C.G., 1968. Notes on the chemistry of spilitic pillow lavas from central Othris and Avdela (Smolikas). Proc. Acad. Athens, 43, 377-389.

Sideris, C., and Baltatzis, E., 1979. Petrography and trace element geochemistry of some Greek spilites. Ann. Geol. Pays Hellen., 30, 69-83.

Sideris, C., Skounakis, S., Laskou, M., and Economou, M., 1984. Brecciated pipeform diabase from Pindos ophiolite complex. Chem. Erde, 43, 189-195.

Sinton, J.M., 1978. Petrology of (alpine-type) peridotites from Site 395, DSDP Leg 45. In: Melson, W.G., and Rabinowitz, P.D., et al., Init. Rep. Deep Sea Drill. Project, 45, Washington, 595-602.

Skinner, B.J., Luce, F.D., Dill, J.A., Ellis, P.E., Hagan, H.A., Lewis, D.M., Odell, D.A., Sverjensky, D.A and Williams, N., 1976. Phase relationships in ternary portions of the system Pt-Pd-Fe-As-S. Econ. Geol., 71 1469-1475.

Skounakis, S., Sideris, C., and Economou, M., 1982. A natural occurrence of Co_9S_8 in pyrrhotite ore from the ophiolite complex of Pindos, Greece. N. Jb. Miner. Mh., H4, 169-174.

Soliman, H.A., and Zygoyiannis, N., 1979. Foraminiferal assemblages from the Eocene of Mesohellenic Basin, northern Greece, 6th Colloquium of the geology of Greece, Athens.

Spray, J.G., Bebien, J., Rex, D.C., and Roddick, J.C., 1984. Age constraints on the igneous and metamorphic evolution of the Hellenic-Dinaric ophiolites. In: Dixon, J.E., and Robertson, A.H.F., (eds). The geological evolution of the Eastern Mediterranean, Sp. Publ. Geol. Soc. Lond. 17, 619-627.

Spry, A., 1969. Metamorphic textures. Pergamon Press, Oxford, 350pp.

Steinman, G., 1927. Die ophiolitischen zonen in dem Mediterranean Kettengebirge. 14th Intern. Geol. Congr. Madrid, 2, 638-667.

Stockman, H.W., and Hlava, P.F, 1984. Platinum-group minerals in alpine chromitites from southwestern Oregon. Econ. Geol., 79, 491-508.

Stolper, E., 1980. A phase diagram for mid-ocean ridge basalts: Preliminary results and implications for petrogenesis. Contrib. Mineral. Petrol., 74, 13-27.

Stone, W.E., and Fleet, M.E., 1991. Platinum-iron alloy (Pt_3Fe) in kimberlite from Fayette County, Pennsylvania. Am. Mineral., 75, 881-885.

Stone, W.E., Crocket, J.H., and Fleet, M.E., 1990. Partitioning of palladium, iridium, platinum, and gold between sulphide liquid and basalt melt at 1200°C. Geochim. Cosmochim. Acta, 54, 2341-2344.

Stroh, J.M., 1976. Solubility of alumina in orthopyroxene plus spinel as a geobarometer in complex systems. Applications to spinel-bearing Alpine-type peridotites. Contrib. Mineral. Petrol., 54, 173-188.

Sun, S.-S., 1982. Chemical composition and origin of the earth's primitive mantle. Geochim. Cosmochim. Acta, 46, 179-192.

Takahashi, E., 1980. Melting relations of an alkali-olivine basalt to 10 kbar, and their bearing on the origin of alkali basalt magmas. Carnegie Inst. Wash. Yearbook, 79, 271-276.

Takahashi, E., 1985. Melting of a dry peridotite KLB-1 up to 14 GPa: Implications on the origin of peridotitic upper mantle. Tech. Rep. Ser. A, No. 3, Inst. Study Earth's Inter., Okoyama Univ., Misasa, Tottori-Ken, Japan, 1-32.

Takahashi, E., 1986. Melting of a dry peridotite KLB-1 up to 14 GPa: Implications on the origin of peridotitic upper mantle. J. Geoph. Res., 91, 9367-9382.

Takahashi, E., and Kushiro, I., 1983. Melting of a dry peridotite at high pressures and basalt magma genesis. Am. Mineral., 68, 859-879.

Talkington, R.W., and Watkinson, D.H., 1985. Whole rock platinum-group elements trends in chromite-rich rocks in ophiolitic and stratiform igneous complexes. In: Gallagher, M.J, Ixer, R.A., Neary, C.R., and Prichard, H.M., (eds). Metallogeny of basic and ultrabasic rocks, 427-440.

Tanguay, S., Herbert, R., and Bergeron, M., 1990. Distribution of PGE in pyroxene-bearing ultramafic cumulates in the Thetford Mines ophiolitic complex, Quebec. Can. Mineral., 28, 597-605.

Terry, J., 1971. Sur l' âge triassique de laves associees a la nappe ophiolitique du Pinde septentrional (Epire et Macedoine, Grèce). C. R. Somm. Soc. geol. Fr., fasc. 7, 384-385.

Terry, J.P., 1972. Sur l' origin polyphasee des ophiolites du Pinde septentrional (Epire et Macedoine, Grèce). C.R.Som.S.G.F., fasc. 2, 12.

Terry, J.P., 1973. A propos d'un metamorphisme anterieur aux deformations tangentielles dans les ophiolites du Pinde septentrional (Grèce). C.R.Ac.Sci., Paris.

Terry, J.P., 1974. Ensembles lithologiques et structures internes du cortège ophiolitique du Pinde septentrional (Grèce). Construction d'un modèle pétrogénétique. B.S.G.F., 7, 16.

Terry, J.P., 1975. Echo d' une tectonique jurassique: les phenomenes de resedimentation dans le secteur de la nappe des ophiolites du Pinde septentrional (Grèce). C.R.Som.S.G.F., fasc. 2, 49-51.

Terry, J.P., 1979. Distinction geochimique de plusieurs groupes dans les ensembles volcaniques de la nappe ophiolitique du Pinde septentrional (Grèce). B.S.G.F., 21, 6, 727-735.

Thayer, T.P., 1960. Some critical differences between alpine-type and stratiform peridotite-gabbro complexes. Mineral. Soc. Am. Spec. Paper, 1, 55-61.

Thayer, T.P., 1964. Principle features and origin of podiform chromite deposits, and some observations on the Canleman-Soridag district, Turkey. Econ. Geol., 59, 1497-1524.

Thayer, T.P., 1967. Chemical and structural relations of ultramafic and feldspathic rocks in Alpine intrusive complexes. In: Wyllie, P.J., (ed), Ultramafic and related rocks. John Wiley and Sons, 222-239.

Tormey, D.R., Grove, T.L., and Bryan, W.B., 1987. Experimental petrology of normal MORB near the Kane Fracture Zone: 22°-22°N, mid-Atlantic ridge. Contrib. Mineral. Petrol., 96, 121-139.

Trommsdorf, V., and Conolly, J.A., D, 1990. Constraints on phase diagram topology for the system $CaO-MgO-SiO_2-CO_2-H_2O$. Contrib. Mineral. Petrol., 104, 1-7.

Umino, S., and Kushiro, I., 1989. Experimental studies on boninite petrogenesis. In: Crawford, A.J., (ed). Boninites and Related Rocks, Elsevier, 89-111.

Valsami, E., 1991. Geochemistry and petrology of hydrothermal discharge zones in the Pindos and Othrys ophiolites, Greece. Unpubl. PhD thesis, University of Newcastle upon Tyne, 359 pp.

Van der Laan, S.R., Flower, M.F.J., and Koster van Groos, A.F., 1989. Eutectic- and peritectic-type boninites: The role of water in olivine-orthopyroxene saturation. In: Crawford, A.J., (ed). Boninites and Related Rocks, Elsevier, 112-147.

Walker, D., Shibata, T., DeLong, S.E., 1979. Abyssal tholeiites from the Oceanographer Fracture Zone. Contrib. Mineral. Petrol., 70, 111-125.

Watson, E.B., 1977. Partitioning of manganese between forsterite and silicate liquid. Geochim. Cosmochim. Acta, 41, 1363-1374.

Watson, E.B., 1985. Henry's law behaviour in simple systems and in magmas: Criteria for discerning concentration-dependent partition coefficients in nature. Geochim. Cosmochim. Acta, 49, 917-923.

Weaver, J.S., and Langmuir, C.H., 1990. Calculation of phase equilibrium in mineral-melt systems, Computers and Geoscience, 16, 1-19.

Webb, S.A., and Wood, B.J., 1986. Spinel-pyroxene-garnet relationships and their dependence on Cr/Al ratio. Contrib. Mineral. Petrol., 92, 471-480.

Wells, P.R.A., 1977. Pyroxene thermometry in simple and complex systems. Contrib. Mineral. Petrol., 62, 129-139.

Wendlandt, R.F., 1982. Sulphide saturation of basalt and andesite melts at high pressures and temperatures. Am. Mineral., 67, 877-885.

Wenner, D.B., and Taylor, H.P.Jr., 1973. Oxygen and hydrogen isotope studies of the serpentinization of ultramafic rocks in oceanic environments and continental ophiolite complexes. Am. J. Sci., 273, 207-239.

Westland, A.D., 1981. Inorganic chemistry of the platinum-group elements. In: Cabri, L.J., (ed). Platinum-group elements: mineralogy, geology, recovery. Can. Inst. Miner. Metal., Spec. Iss. 23, 5-18.

Wicks, F.J., and O'Hanley, D.S., 1988. Serpentine minerals: Structures and petrology. In: Baily, S.W., (ed). Reviews in Mineralogy 25. Hydrous phyllosilicates (exclusive of micas). Mineral. Soc. Am., 698pp.

Wicks, F.J., and Whittaker, E.J.W., 1977. Serpentine textures and serpentinization. Can. Mineral., 15, 459-488.

Wicks, F.J., Whittaker, E.J.W., and Zussman, J., 1977. An idealized model for serpentine textures after olivine. Can. Mineral., 15, 446-458.

Will, T.M., Powell, R., and Holland, T.J.B., 1990. A calculated petrogenetic grid for ultramafic rocks in the system $CaO-FeO-MgO-Al_2O_3-SiO_2-CO_2-H_2O$ at low pressures. Contrib. Mineral. Petrol., 105, 347-358.

Wilson, G.C., Kilius, L.R., and Rucklidge, J.C., 1991. In situ analysis of precious metals in polished mineral samples and sulphide "standards" by accelerator mass spectrometry at concentrations of parts-per-billion. Geochim. Cosmochim. Acta, 55, 2241-2251.

Witt-Eikschen, G., and Seck, H.A., 1991. Solubility of Ca and Al in orthopyroxene from spinel peridotite: An improved version of an empirical geothermometer. Contrib. Mineral. Petrol., 106, 431-439.

Wood, B.J., 1991. The oxidation state of the mantle and its relationship to tectonic environments. (abstract). Terra Abstr., 3, 421.

Wood, B.J., and Banno, S., 1973. Garnet-orthopyroxene and orthopyroxene-clinopyroxene relationships in simple and complex systems. Contrib. Mineral. Petrol., 42, 109-124.

Wood, B.J., and Fraser, D.G., 1976. Elementary thermodynamics for geologists. Oxford University Press, 303 pp.

Wood, B.J., and Virgo, D., 1989. Upper mantle oxidation state: Ferric iron contents of lherzolite spinels by [57]Fe Mössbauer spectroscopy and resultant oxygen fugacities. Geochim. Cosmochim. Acta, 53, 1277-1291.

Yakowitz, H., Myklebust, R.L., and Heinrich, K.J.F., 1973. FRAME: An on-line correction procedure for quantitative electronprobe microanalysis. National Bureau of Science Technical Note, 796.

Yoder, H.S.Jr., and Tilley, C.E., 1962. Origin of basalt magmas: An experimental study of natural and synthetic rock systems. J. Petrol., 3, 342-532.